PRAMANA

journal of physics

Vol. 44 No. 4
April 1995

BANGALORE-560

INDIAN ACADEMY OF SCIENCES
Indian National Science Academy
Indian Physics Association

Pramana – journal of physics

Editor

R Nityananda
Raman Research Institute, Bangalore

Associate Editor

H R Krishnamurthy
Indian Institute of Science, Bangalore

Editorial Board

G S Agarwal, *University of Hyderabad, Hyderabad*
V Balakrishnan, *Indian Institute of Technology, Madras*
M Barma, *Tata Institute of Fundamental Research, Bombay*
P Chaddah, *Centre for Advanced Technology, Indore*
B M Deb, *Panjab University, Chandigarh*
P K Kaw, *Institute for Plasma Research, Gandhinagar*
H S Mani, *Indian Institute of Technology, Kanpur*
N Mukunda, *Indian Institute of Science, Bangalore*
T Padmanabhan, *Inter-University Centre for Astronomy and Astrophysics, Pune*
J C Parikh, *Physical Research Laboratory, Ahmedabad*
G Rajasekaran, *Institute of Mathematical Sciences, Madras*
V S Ramamurthy, *Institute of Physics, Bhubaneswar*
R Ramaswamy, *Jawaharlal Nehru University, New Delhi*
K R Rao, *Bhabha Atomic Research Centre, Bombay*
Probir Roy, *Tata Institute of Fundamental Research, Bombay*
A K Sood, *Indian Institute of Science, Bangalore*

Editor of Publications of the Academy

V K Gaur
C-MMACS, NAL, Bangalore

RAMAN RESEARCH INSTITUTE
BANGALORE - 80.
CLASS NO.
ACC NO. 26998

Subscription Rates
(Effective from 1989)

All countries except India	1 year	3 years	5 years
(Price includes AIR MAIL charges)	US$ 175	$ 470	$ 700
India	1 year Rs. 100	10 years (1989–1998 only) Rs. 500	

All correspondence regarding subscription should be addressed to the **Circulation Department** of the Academy

---

Editorial Office

Indian Academy of Sciences, C V Raman Avenue,
P.B. No. 8005, Bangalore 560080, India

Telephone: 334 2546
Telex: 845-2178 ACAD IN
Telefax: 91-80-334 6094

© 1995 by the Indian Academy of Sciences. All rights reserved.

"Information for contributors" is printed in the last issue of every volume.

Regd. No. KRN-A 64

Pramana journal of physics Vol. 44 (No. 4), April 1995

Contents

Patterned chaos in a system of three coupled identical unidirectional ring lasers……*J Jose and S Dutta Gupta* 281

Invariants of chaotic Hamiltonian systems……*B R Sitaram* 295

On singularity-free spacetimes……*Naresh Dadhich, L K Patel and R Tikekar* 303

Exact solutions of Einstein and Einstein-scalar equations in $2+1$ dimensions……*K S Virbhadra* 317

Charge screening in a two potential theory of electromagnetism……*C Wolf* 323

Dual nature of Ricci scalar and creation of spinless particles……*K P Sinha and S K Srivastava* 333

Two-loop Majorana neutrino mass and magnetic moment in a gauge model……*Jyoti Dhar, Umesh Pandey and S Dev* 347

S-wave baryons in an equally mixed scalar-vector square root potential model of independent quarks……*S N Jena and M R Behera* 357

Shape transitions in even Mo and Sm isotopes: Study in a new microscopic interacting boson model scheme……*Subrata Sarangi and Jitendra C Parikh* 375

Rapid Communication

Giant magnetoresistance in bulk samples of $LaMnO_3$ with varying Mn^{4+} content……*R Mahendiran, R Mahesh, A K Raychaudhuri and C N R Rao* L393

RAMAN RESEARCH INSTITUTE LIBRARY BANGALORE-80.

MAY 1995

Indexed in CURRENT CONTENTS ISSN 0304–4289

Edited and published by V K Gaur for the Indian Academy of Sciences, Bangalore 560080. Typeset at Thomson Press (I) Ltd., New Delhi 110001 and printed at Macmillan India Press, Madras 600041.

Regd. No. KRN-A 64

Pramana journal of physics Vol. 44 (No. 5), May 1995

Contents

Effect of nonlocal elasticity on internal friction peaks observed during martensite transformation .... *Ali Doğan* 397

Dielectric study of aqueous solution of acetonitrile .... *S N Helambe, M P Lokhande, A C Kumbharkhane, S C Mehrotra and S Doraiswamy* 405

Structural and dielectric properties of $Pb(Li_{1/4}Dy_{1/4}W_{1/2})O_3$ .... *S Bera and R N P Choudhary* 411

Phonon properties of rare earth ytterbium pnictides .... *Prafulla K Jha and Sankar P Sanyal* 419

Lattice vibronics of bcc phase metals (Ti, Zr and Hf) at higher temperatures .... *S K Saxena, R M Agrawal and R P S Rathore* 429

Temperature variation of electric field gradient in scandium metal .... *B B Panigrahi and N C Mohapatra* 443

Composite Anderson–Newns model and chemisorption characteristics of nickel-hydrogen system .... *Ravinder Guleria, P K Ahluwalia and K C Sharma* 453

Vibrational analysis of $NaM_2OH(H_2O)(MoO_4)_2/D_2O[M = Ni, Zn]$ .... *R Ratheesh, G Suresh and V U Nayar* 461

Measurement of cross-section of excitation transfer from $3s_2$ to $4s_1$ and $5s_1$ energy levels of neon .... *R K Garg and Vasant Dandawate* 471

Fringe formation theory for real-time holographic interferometry using $Bi_{12}SiO_{20}$ .... *C S Narayanamurthy* 481

RAMAN RESEARCH INSTITUTE LIBRARY BANGALORE-80.
21 JUL 1995

Indexed in CURRENT CONTENTS ISSN 0304–4289

Edited and published by V K Gaur for the Indian Academy of Sciences, Bangalore 560080. Typeset at Thomson Press (I) Ltd., New Delhi 110001 and printed at Macmillan India Press, Madras 600041.

Regd. No. KRN-A 64

Pramana journal of physics Vol. 44 (No. 6), June 1995

Contents

Quantal behaviour of magnetically kicked electron .... *A K Sikri and M L Narchal* 489

Higher dimensional spherically symmetric inhomogeneous cosmological model with heat flow .... *Subenoy Chakraborty and Md. Firoj Shah* 495

Supersymmetry in complex space-time .... *Shuchi Bora and B S Rajput* 501

Cosmic strings in Bianchi III spacetime: Integrable cases .... *S D Maharaj, P G L Leach and K S Govinder* 511

Static and dynamic properties of pseudoscalar mesons .... *D K Choudhury, Pratibha Das, D D Goswami and J K Sarma* 519

Measurement and analysis of alpha particle induced reactions on gold .... *D J Shah, H B Patel, N L Singh, S Mukherjee and S N Chintalapudi* 535

Elastic scattering of 81 keV γ-rays by aluminium, nickel, tantalum, gold and lead .... *G Basavaraju, P P Kane, Lynn Kissel and R H Pratt* 545

Collision cross-sections for scattering of electrons from NO molecule .... *Arvind Kumar Jain, Pradeep Kumar and A N Tripathi* 555

Electron impact ionization of Ba, Ba^+ and Ba^{2+} .... *Gopaljee, S K Shrivastava and B N Roy* 563

Subject Index 569

Author Index 574

Information for contributors

21 JUL 1995

RAMAN RESEARCH INSTITUTE
LIBRARY
BANGALORE-80.

Indexed in CURRENT CONTENTS ISSN 0304–4289

Edited and published by V K Gaur for the Indian Academy of Sciences, Bangalore 560080. Typeset at Thomson Press (I) Ltd., New Delhi 110001 and printed at Macmillan India Press, Madras 600041.

[redacted]

PRAMANA
— journal of
physics

© Printed in India

Vol. 44, No. 4,
April 1995
pp. 281–293

BANGALORE-80.

Patterned chaos in a system of three coupled identical unidirectional ring lasers

J JOSE and S DUTTA GUPTA
School of Physics, University of Hyderabad, Hyderabad 500 134, India

MS received 10 November 1994

Abstract. Three coupled identical unidirectional B-type ring lasers are considered and the dynamics for varying coupling parameter investigated. For given system parameters like pumping, cavity damping etc. the system is characterized by three distinct types of steady states. The linear stability of these steady states is investigated in detail which are unstable beyond a critical value of the coupling parameter. For a certain range of the coupling parameter chaotic behaviour of the system is demonstrated. The dynamical variables are mapped on to a complex variable reflecting the symmetry of the system. The plot of the real vs. the imaginary part of this complex variable exhibits patterns with threefold symmetry. The largest Lyapunov exponent as well as the power spectra corresponding to the chaotic attractors are also calculated.

Keywords. Coupled ring laser; chaotic dynamics.

PACS No. 42·65

In recent years there has been a lot of interest in coupled lasers [1,2]. Studies on coupled laser systems were motivated by the fact that by means of coupling one can relatively simply increase the output power. Very recently a very different aspect of coupled identical systems has been reported. The inherent symmetries of such systems can lead to symmetric chaos [3]. Namely, in a dynamical system with symmetry, chaotic attractors may themselves possess a degree of symmetry. The symmetry aspects of three coupled identical oscillators were investigated in detail by Ashwin *et al* [4]. An almost simultaneous experiment by Ashwin [5] confirmed the theoretical predictions. However, to the best of our knowledge, similar concepts have not yet been tested for optical systems. In this paper we concentrate on an optical system with inbuilt cyclic permutation symmetry. Namely, we consider three identical unidirectional ring lasers. The choice of lasers as the constitutive element is obvious since they are known to lead to a variety of dynamical behaviour including self pulsing [6] and chaos [7]. We restrict our attention only to B-type lasers. It is well known that an isolated B-type laser is essentially a two dimensional system, and by virtue of Poincare-Bendixson theorem cannot exhibit chaotic dynamics. First ever demonstration of chaotic dynamics in such lasers was achieved by modulating the cavity damping of the lasers [8]. Later, insertion of phase sensitive elements in such laser cavities was shown to lead to additional attractors [9]. In the context of the problem of coupled B-type lasers, the important questions that can be addressed are the following: a) can coupling lead to chaotic dynamics when the individual isolated components show regular dynamics, b) does the attractor reflect the symmetries of the system after proper mapping of the dynamical variables. It is quite clear that since the dimension of the coupled system is now higher, chaos is not ruled out. In order to provide answer to the above questions we proceed in a systematic fashion, first by looking at the steady states and investigating their linear stability. The coupling parameter is used as the control parameter and the change of stability is investigated as the coupling strength is varied. We show that beyond a critical value of the coupling parameter, all the steady states become unstable. In the domain where the steady states are unstable we integrate the equations of motion numerically. We show the existence of a window in the values of the coupling strength where the system exhibits chaotic response. In order to have direct evidence of the chaotic dynamics, we calculate the largest Lyapunov exponent and show its positivity. Moreover, we look at the power spectra which shows broad band features. To extract the symmetry features of the chaotic attractor, following ref. [4] we construct a complex dynamical variable which retains the symmetry of the system. The depiction of the variable on the complex plane exhibits the symmetries of the attractor.

Consider a system of three coupled B-type ring lasers. The lasers are assumed to be identical and unidirectional such that the output of the second laser is fed to the first and that of first is fed to the third and so on. Such a system can be described by the following set of equations [9, 1]

$$\frac{\mathrm{d}e_1}{\mathrm{d}\tau} = -\bar{\kappa}[e_1(1-d_1)+\beta e_2], \tag{1}$$

$$\frac{\mathrm{d}e_2}{\mathrm{d}\tau} = -\bar{\kappa}[e_2(1-d_2)+\beta e_3], \tag{2}$$

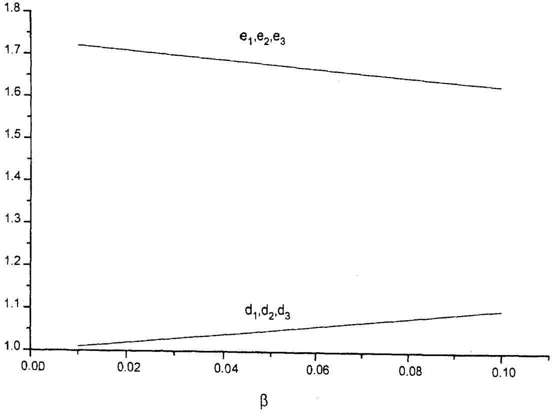

Figure 1. Steady state values of e_j, $d_j (j = 1,3)$ as functions of coupling parameter β. The state depicting equal field and inversion for all the lasers. Parameters used for calculation are as follows: $\kappa = 100, d_0 = 4{\cdot}0$.

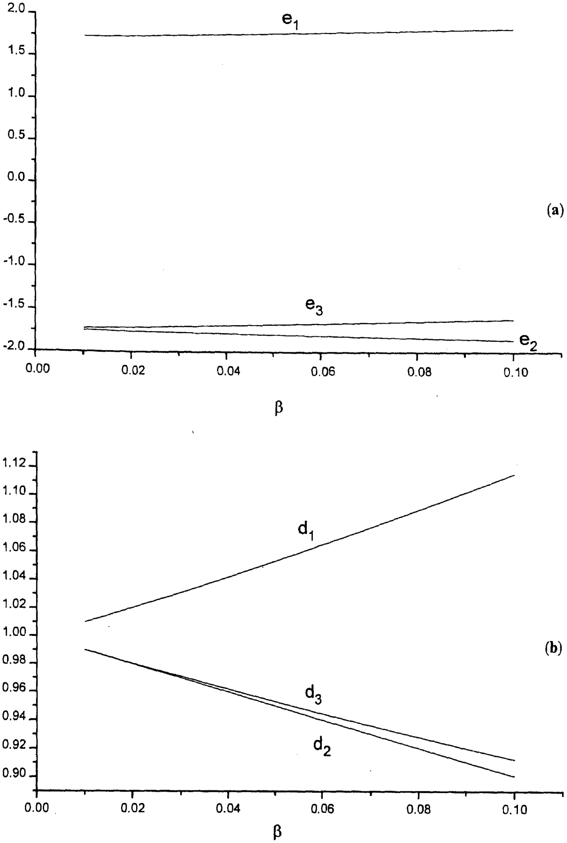

Figure 2. Steady state values of (**a**) e_j and (**b**) d_j, $(j = 1,3)$, when all the three lasers have distinct fields and inversion. Other parameters are as in figure 1.

$$\frac{\mathrm{d}e_3}{\mathrm{d}\tau} = -\tilde{\kappa}[e_3(1-d_3)+\beta e_1], \tag{3}$$

$$\frac{\mathrm{d}d_i}{\mathrm{d}\tau} = -[d_j - d_0 + e_j^2 d_j], \quad j = 1,2,3 \tag{4}$$

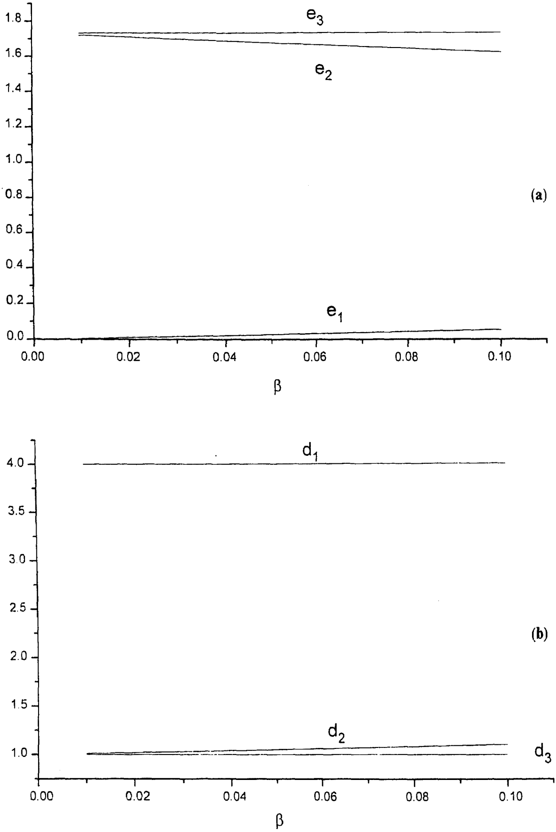

Figure 3. Steady state values of (**a**) e_j and (**b**) $d_j (j = 1, 3)$, when one of the lasers is almost off. Other parameters are as in figure 1.

where, $\bar{\kappa} = \kappa/\gamma_{\|}$, is the normalized (to longitudinal decay rate $\gamma_{\|}$) cavity damping $\tau = \gamma_{\|}\ t$ is the dimensionless time, and β is the coupling parameter. In all our calculations we have assumed β to be real for simplicity. In (1)–(4), e_j (d_j) denotes the dimensionless field envelope (inversion) of the jth laser. e_js, for example, are normalized to the saturation amplitude, whereas, d_js are normalized to the corresponding steady state value of an isolated B-type system. Note also the invariant character of the system (1)–(4) under cyclic permutation of the indices 1,2,3.

We first look at the steady states and investigate their linear stability. The steady states are obtained by setting the time derivative to be zero in (1)–(4). One of the steady states, trivially obtained, is given by the following:

$$\bar{d}_j = 1 + \beta, \tag{5}$$

$$\bar{e}_j^2 = \frac{d_0}{1+\beta} - 1. \tag{6}$$

In (5) and (6) overbars denote the steady states. The steady states given by (5) and (6) represent the state of the system where all the three lasers have the same amplitude as well as inversion. Unfortunately other steady states could not be obtained by simple analytical methods. We resorted to numerical methods in order to obtain the other steady states of the system. The results for all the steady states are shown in figures 1–3. In these figures we have plotted the different possible steady state values of e_j and $d_j (j = 1\text{–}3)$ as functions of the coupling parameter β which was varied in the range 0·01 to 0·10. For numerical calculations we have chosen the other parameters as follows: $d_0 = 4{\cdot}0, \bar{\kappa} = 100$. It is clear from figures 1–3 that three distinct types of

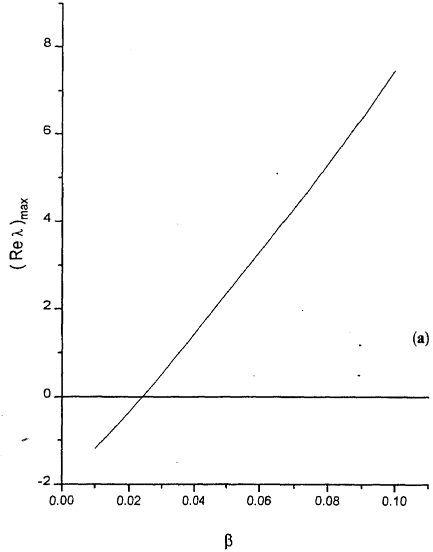

Figure 4a.

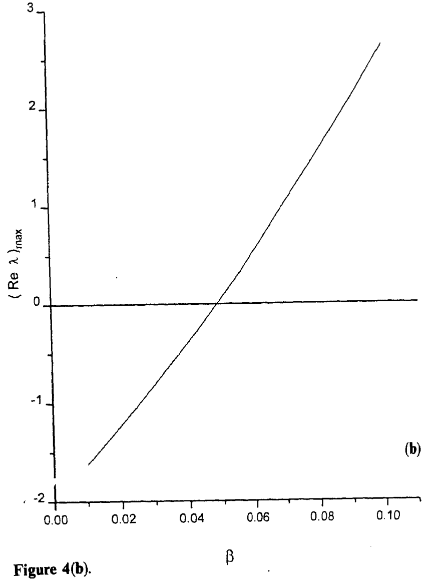

Figure 4(b).

Figure 4. Largest positive real part $[\mathrm{Re}(\lambda)]_{\max}$ of the eigenvalues of matrix A(see eq. (9)) for the steady state depicted (**a**) in figure 1 and (**b**) in figure 2.

steady states are possible. The first one is characterized by equal fields and inversions for each laser. The second one is characterized by all three lasers oscillating with non zero and distinct amplitudes (figures 2a and 2b), whereas, the third one depicts the situation when two lasers are on with the third laser close to the zero field state (figures 3a and 3b). Note that inversion corresponding to the almost "off" laser is slightly perturbed from the d_0 value meaning thereby that the inital inversion remains unburnt. Note also that similar results hold when the indices are permuted in a cyclic fashion (i.e. 1,2,3 → 2,3,1 → 3,1,2). In what follows we present results pertaining to the linear stability of the solutions. The temporal evolution of small perturbations around the steady state values can be described by the following equation:

$$\frac{\mathrm{d}(\delta X)}{\mathrm{d}\tau} = A\,\delta X, \tag{7}$$

where δX represents the column vector of perturbations

$$\delta X = (\delta e_1, \delta e_2, \delta e_3, \delta d_1, \delta d_2, \delta d_3)^t \tag{8}$$

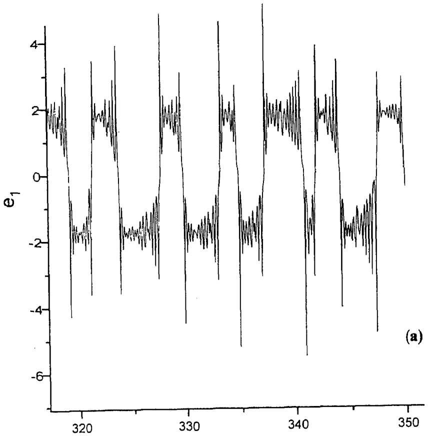

Figure 5a.

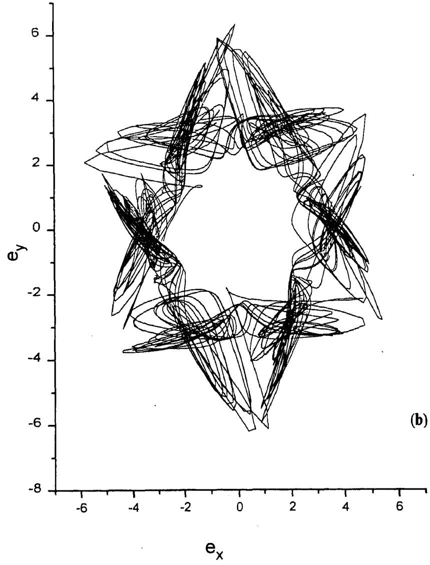

Figure 5b.

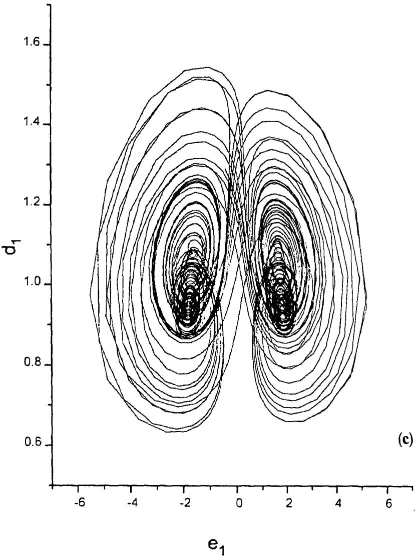

Figure 5. (**a**) e_1 as a function of dimensionless time τ, (**b**) e_y as a function of e_x and (**c**) e_1 as a function of d_1 for $\beta = 0{\cdot}05$. Other parameters are as in figure 1.

and the matrix A is given by

$$\begin{bmatrix} -\bar{\kappa}(1-\bar{d}_1) & -\bar{\kappa}\beta & 0 & \bar{\kappa}\bar{e}_1 & 0 & 0 \\ 0 & -\bar{\kappa}(1-\bar{d}_2) & -\bar{\kappa}\beta & 0 & \bar{\kappa}\bar{e}_2 & 0 \\ -\bar{\kappa}\beta & 0 & -\bar{\kappa}(1-\bar{d}_3) & 0 & 0 & \bar{\kappa}\bar{e}_3 \\ -2\bar{e}_1\bar{d}_1 & 0 & 0 & -(1+\bar{e}_1^2) & 0 & 0 \\ 0 & -2\bar{e}_2\bar{d}_2 & 0 & 0 & -(1+\bar{e}_2^2) & 0 \\ 0 & 0 & -2\bar{e}_1\bar{d}_3 & 0 & 0 & -(1+\bar{e}_3^2) \end{bmatrix} \tag{9}$$

The real part of the eigenvalues of matrix A determines whether the steady state under consideration is stable or not. Presence of the positive real part of any eigenvalue heralds the instability of the fixed point. We have calculated numerically the eigenvalues of the matrix A for all steady states. We have extracted the largest real part of the eigenvalues and investigated their dependence on the coupling parameters. The results are shown in figures 4a and 4b. Figure 4a, for example, depicts the stability aspect of the steady state solution of figure 1a. It is clear from figure 4a that with an

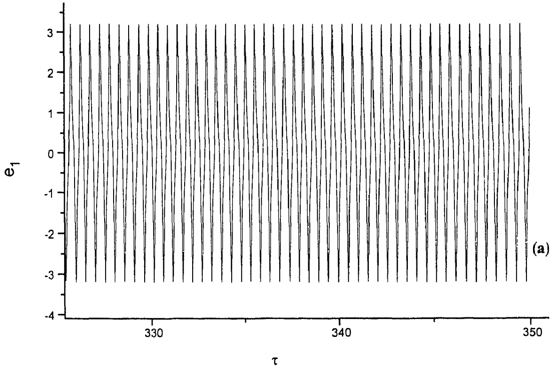

Figure 6a.

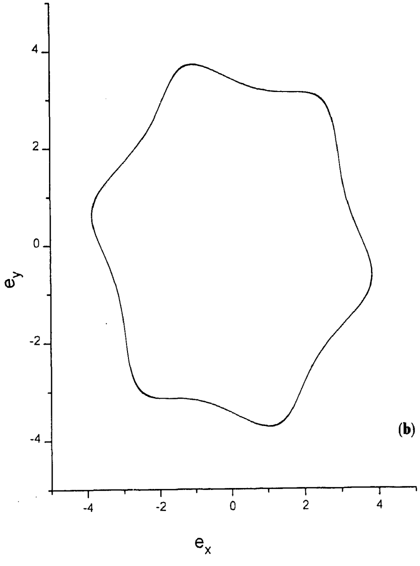

Figure 6b.

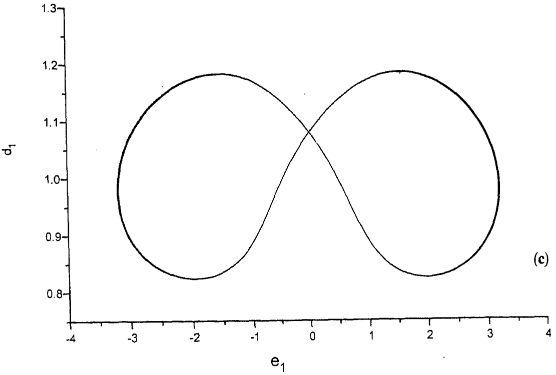

Figure 6c. Same as in figure 5 except that now $\beta = 0{\cdot}069$.

increase in β the largest real part of eigenvalue $[\mathrm{Re}(\lambda)]_{\max}$ increases from negative values crossing zero at about $\beta = 0{\cdot}024$. Thus the state of equal fields and equal inversion for all the lasers becomes unstable when β crosses this value. The stability results for the steady state depicted in figures 2a and 2b are given in figure 4b and these steady states become unstable when β exceeds the value 0·046. So far as the other type of steady states (with one of the lasers almosts off) is concerned, it is unstable over the range of β values considered. Thus for $\beta > 0{\cdot}046$ no stable fixed points exist and the system exhibits a richer temporal dynamics.

In the domain where there are no stable fixed points we integrated the set of equations (1)–(4) numerically. Caution was taken in view of the stiff character of the equations. In order to see the symmetry aspects of the attractor following [4], we constructed a complex dynamical variable e as follows:

$$e = e_1 \exp(2\pi i/3) + e_2 \exp(4\pi i/3) + e_3. \tag{10}$$

The imaginary part e_y of e as a function of the real part e_x reflects the inherent symmetries of the dynamics. In our numerical calculation we used a wide range of values of β. For a range of β values namely $0{\cdot}049 \leqslant \beta \leqslant 0{\cdot}054$ chaotic dynamics was observed in the system. Below and above this window the dynamics was predominantly quasi periodic or periodic. In figure 5 we have shown the case corresponding to well developed chaos for $\beta = 0{\cdot}05$. In figure 5a we have shown the temporal evolution of the field in one of the lasers. Figure 5b shows e_y as a function of e_x, whereas in figure 5c e_1 is plotted as a function of d_1. The three-fold symmetry of the attractor shown in figure 5b is easily noticed. In order to compare with the regular

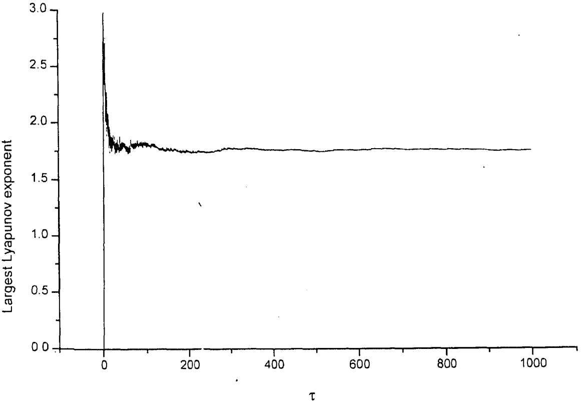

Figure 7. Convergence of largest Lyapunov exponent for $\beta = 0{\cdot}05$.

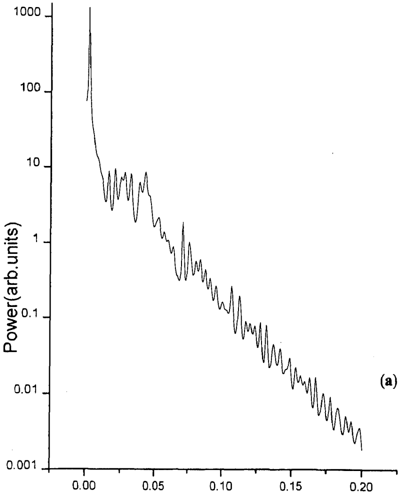

Figure 8a.

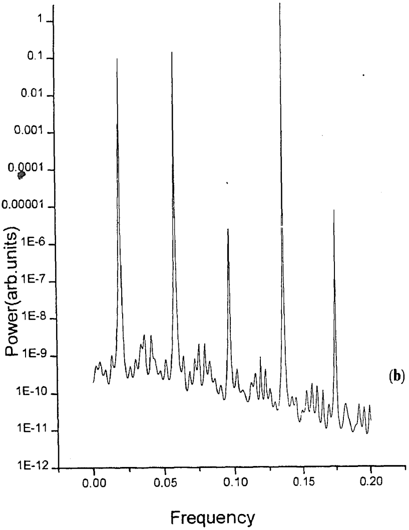

Figure 8(b).

Figure 8. Power spectrum for (**a**) $\beta = 0{\cdot}05$ and (**b**) $\beta = 0{\cdot}069$. Other parameters are as in figure 1.

dynamics we have also produced the curves for $\beta = 0{\cdot}069$. It is clear from figures 6a–c that the temporal dynamics is periodic for $\beta = 0{\cdot}069$. We have also investigated the effect of negative values of coupling. Negative coupling has a stabilizing effect on the system and all the lasers after some relaxation oscillations settle down to the steady state values.

In order to have a convincing evidence of the chaotic behaviour of the system for example, for $\beta = 0{\cdot}05$ we calculated the largest Lyapunov exponent. The results are shown in figure 7 which demonstrates the convergence of the largest exponent to the value 1·74. The positive character of the largest Lyapunov exponent is a convincing proof of the chaotic dynamical behaviour of a system for $\beta = 0{\cdot}05$. We have also calculated the power spectra by maximum entropy method [10] corresponding to the chaotic and the regular attractor in the positive Nyquist interval. The results corresponding to the chaotic (regular) attractor of figure 5 (figure 6) are shown in figure 8a (figure 8b). The broad band features in the chaotic case (figure 8a) are easily distinguished from the spiked ones (figure 8b) corresponding to the regular dynamics.

In conclusion, we have carried out a detailed investigation of three coupled identical ring lasers. We have shown that though the individual isolated lasers are incapable of exhibiting chaotic dynamics, the same is possible in the coupled system. With proper mapping of the dynamical variables the attractor reflects the inherent symmetries of the system. We have carried out a detailed study of the steady states (fixed points) of the system. We have also characterized the attractors by calculating the largest Lyapunov exponent as well as the power spectra. There are still some open questions. We could not find a definitive answer as regards the route to chaos. Moreover, deviation from real character of the coupling constant complicates the problem to a large extent and phase of the coupling constant may play a significant role in determining the dynamics. These questions are under investigation and will be reported elsewhere.

Acknowledgements

One of the authors (SDG) is thankful to the Department of Science and Technology for supporting this work. He is also thankful to Prof. M Lakshmanan for bringing to his notice refs [4] and [5] which motivated this work.

References

[1] V V Likhanskii and A P Napartovich, *Usp. Fiz. Nauk* **160**, 101 (1990)
[2] P Mandel and L Ruo-ding, *Phys. Rev.* **A39**, 2502 (1989)
[3] G King and L Stewart, In *'Nonlinear equations in the Applied Sciences'*. edited by N F Ames and C Rogers (Academic, New York, 1992) p. 257
[4] P Ashwin, G P King and J W Swift, *Nonlinearity*, **3**, 585 (1990)
[5] P Ashwin, *Nonlinearity*, **3**, 603 (1990)
[6] H Risken and K Nummedal, *Phys. Lett.* **A26**, 275 (1968)
[7] H Haken, *Phys. Lett.* **A53**, 77 (1975)
[8] F T Arecchi, R Meucci, G P Puccioni and J R Tredicce, *Phys. Rev. Lett.* **49**, 1217 (1982)
[9] S Dutta Gupta and M B Pande, *J. Mod. Opt.* **39**, 1643 (1992)
[10] *Numerical recipes, the art of scientific computing.* edited by W H Press, B P Flannery, S T Teukolsky and W T Vetterling (Cambridge University Press, Cambridge, 1986) p. 420

[redacted]

PRAMANA
— journal of
physics

© Printed in India

Vol. 44, No. 4,
April 1995
pp. 295–302

Invariants of chaotic Hamiltonian systems

B R SITARAM
Physical Research Laboratory, Navrangpura, Ahmedabad 380 009, India

MS received 19 April 1994; revised 6 December 1994

Abstract. The invariants of chaotic bounded Hamiltonian systems and their relation to the solutions of the first variational equations of the equations of motion are studied. We show that these invariants are characterized by the fact that they either lose the property of differentiability as functions on phase space or that a certain formal power series defined in terms of the derivatives of the invariants has zero radius of convergence. For a specific example, we show that the former possibility appears to apply.

Keywords. Integrability; Liapunov exponents; chaos; Hamiltonian systems.

PACS Nos 03·20; 02·40

The problem of determining invariants for a Hamiltonian system has an old history. The motivation for looking for such invariants is that they help in reducing the number of degrees of freedom and thereby enable us to solve the equations of motion in terms of quadrature. Recent studies [1–4], have attacked the problem of invariants which are complex analytic functions on phase space. It is not very clear, however, why complex analyticity is required; it is thus worthwhile to see whether any light can be thrown on the structure of invariants, assuming only that they are once differentiable as functions on phase space. (The once differentiability property is of course required as invariants have to satisfy the first order PDE $\{I, H\} = 0$). We show here that the information obtained from Liapunov exponents can be used to draw certain conclusions regarding the structure of invariants in chaotic systems.

Let $\xi_i, i = 1\ldots 2n$ denote canonical coordinates on R^{2n} and let H be a Hamiltonian function such that (i) all the orbits of H are compact and (ii) for at least one orbit, one or more of the Liapunov exponents [5] are positive. We study here the problem of determining invariants for such systems and what we can learn about the properties of such invariants by looking at the Liapunov exponents.

Considered as a set of differential equations (without taking into account the special features of symplecticity), an invariant for Hamilton's equations is any solution of the equation

$$\frac{\mathrm{d}F}{\mathrm{d}t} = 0. \tag{1}$$

For a system with n degrees of freedom, to completely solve the problem of integrating the equations of motion, we need $2n$ functionally independent solutions of (1); of these invariants, at least one must necessarily depend on t. If we take into account the important fact that Hamilton's equations are symplectic, then, according to Liouville's theorem [6] we need to only determine n mutually involutive invariants.

(Usually, Liouville's theorem is stated in the form that n *time independent* mutually involutive invariants are required, which therefore satisfy the equation

$$\{F,H\}=0. \tag{2}$$

However, by extending phase space to include t and a conjugate variable T, and redefining H by $H+T$, we get an equivalent dynamical system and Liouville's theorem in the form usually stated applies.) In such a case, Liouville's theorem allows us to construct the remaining n invariants in a step by step manner. The converse of Liouville's theorem is also true in R^{2n}: given $2n$ independent solutions of (1), Darboux's theorem [7] allows us to choose a subset whose elements are mutually involutive.

It is easy to see that the existence of an invariant implies the existence of an exact solution of the first variational equations (the Liapunov equations). To see this, consider Hamilton's equations,

$$\frac{\mathrm{d}\xi_i}{\mathrm{d}t}=\omega_{ij}\frac{\partial H}{\partial \xi_j}\equiv\omega_{ij}H_j, \tag{3}$$

where ω is the Poisson bracket matrix. The first variational equations, whose solutions provide the Liapunov exponents, are given by,

$$\frac{\mathrm{d}\eta_i}{\mathrm{d}t}=\omega_{ij}H_{jk}\eta_k. \tag{4}$$

While solving these equations, we choose a specific solution $\xi_i(t)$ of Hamilton's equations, insert it into the rhs of (4) and determine $\eta_i(t)$; obviously, the solution so obtained will depend on the choice of orbit. Alternatively, we can look at (4) as the equations along the characteristic of the partial differential equations,

$$\frac{\partial\eta_i}{\partial t}+\omega_{jk}\frac{\partial\eta_i}{\partial\xi_j}H_k=\omega_{ij}H_{jk}\eta_k, \tag{5}$$

where, we consider η as a function of ξ and t. Knowing a solution of (4) for every orbit and for a suitable choice of initial conditions for η is equivalent to solving (5).

Now, let F be a solution of (1) and define

$$\eta_i=\omega_{ij}\frac{\partial F}{\partial\xi_j}. \tag{6}$$

A simple substitution of this in the Liapunov equation shows that the equation is indeed valid. If F satisfies (i) F is C^∞ as a function on phase space (ii) the formal series,

$$\sum_{n=0}^{n=\infty}\varepsilon^n Ad_F^{(n)}(\xi,t), \tag{7}$$

where

$$Ad_F^{(n)}(\xi,t)=\{F,Ad_F^{(n-1)}(\xi,t)\},\ Ad_F^{(1)}(\xi,t)=\{F,\xi\}, \tag{8}$$

converges in some circle in the complex ε plane around $\varepsilon=0$ for all ξ, then F defines a canonical transformation for each sufficiently small ε. This transformation has the property that it is compact; hence the corresponding Liapunov exponent is 0.

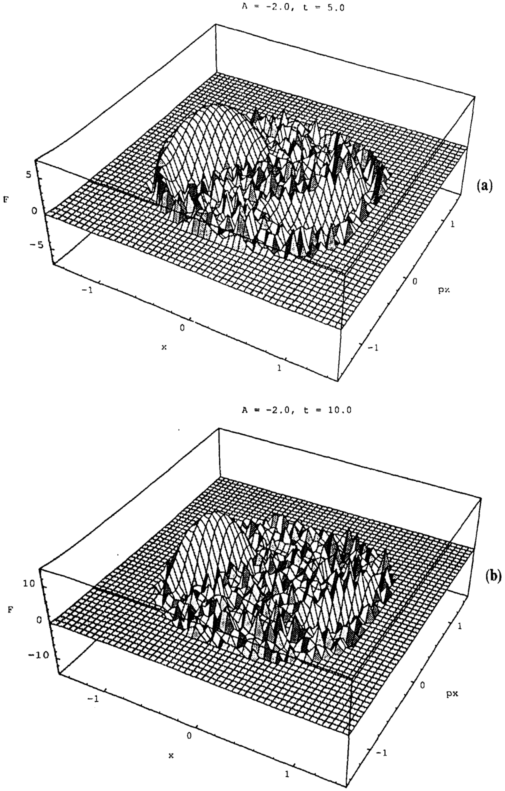

Figures 1a and 1b. Plot of F versus x and px for the Hamiltonian given by (13), with $y = 0$ and $E = 1$, for times $t = 5$ and 10 respectively. The parameter A has been chosen as -2 corresponding to the chaotic regime.

The converse of the relationship between invariants and solutions of the Liapunov equations is also true: Given a solution $\eta_i(\xi, t)$, we can construct an invariant function $F(\xi, t)$ by

$$\frac{\partial F}{\partial \xi_i} = \boldsymbol{\Omega}_{ij}\eta_j, \quad \frac{\partial F}{\partial t} = H_j\eta_j, \tag{9}$$

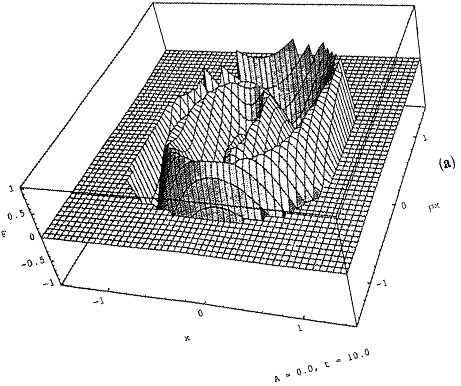

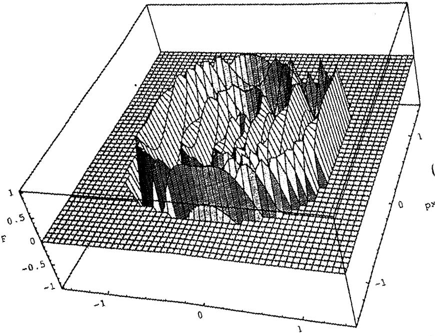

Figures 2a and 2b. Same as figures 1a and 1b, with $A = 0$ (integrable cas

where Ω is the inverse matrix of ω. By construction, F is invariant, i.e., it sa
This construction is possible, provided the matrix C_{ab} defined by

$$C_{ab} = \Omega_{aj}\frac{\partial \eta_j}{\partial \xi_b} - \Omega_{bj}\frac{\partial \eta_j}{\partial \xi_a}$$

vanishes. This condition is satisfied, provided C_{ab}, which is a functi

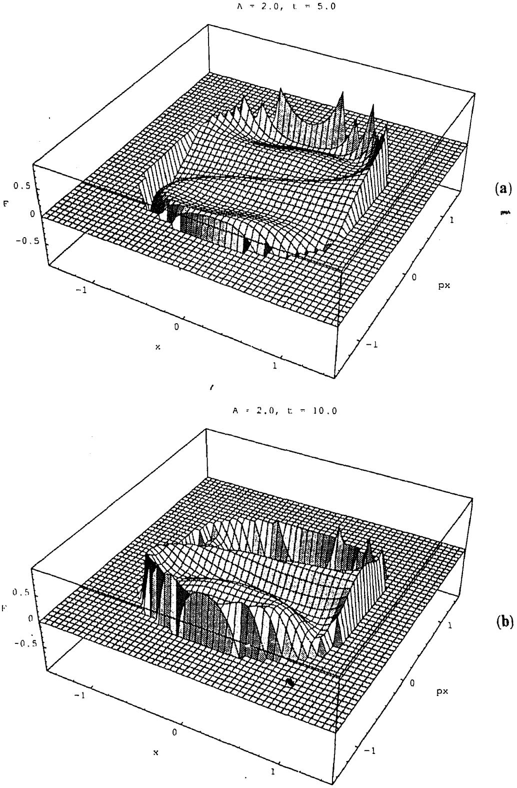

Figures 3a and 3b. Same as figures 1a and 1b, with $A = 2$ (integrable case).

vanishes for $t = 0$, as the evolution equation for C is given by

$$\frac{\mathrm{d}C_{ab}}{\mathrm{d}t} = C_{aj}H_{jb} - C_{bj}H_{ja}. \tag{11}$$

We thus conclude that every solution of the Liapunov equations leads to an invariant, provided the initial conditions are chosen suitably. This can always be

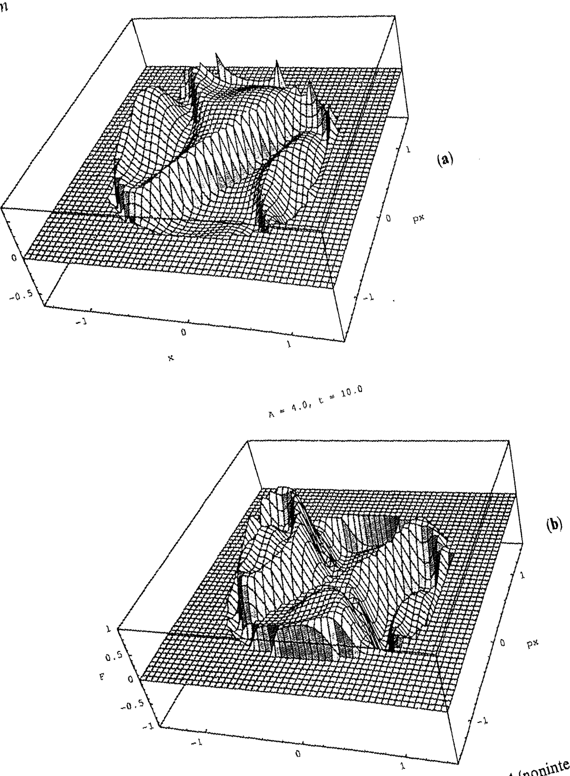

Figures 4a and 4b. Same as figures 1a and 1b, with $A = 4$ (noninteg

done; e.g., if the ξ are cartesian coordinates on phase space, a cor
is $\eta_i(\xi, t = 0) = \delta_{ij}$ for fixed j, which corresponds to the initial conditi
$\Omega_{ik}\delta_{kj}$. Since the Liapunov equations are linear, if the initial condi
to be linearly independent, so are the solutions for all time. But, *lin*
of the solutions of the Liapunov equations in fact correspo
independence of the invariants. Thus, this completes the const

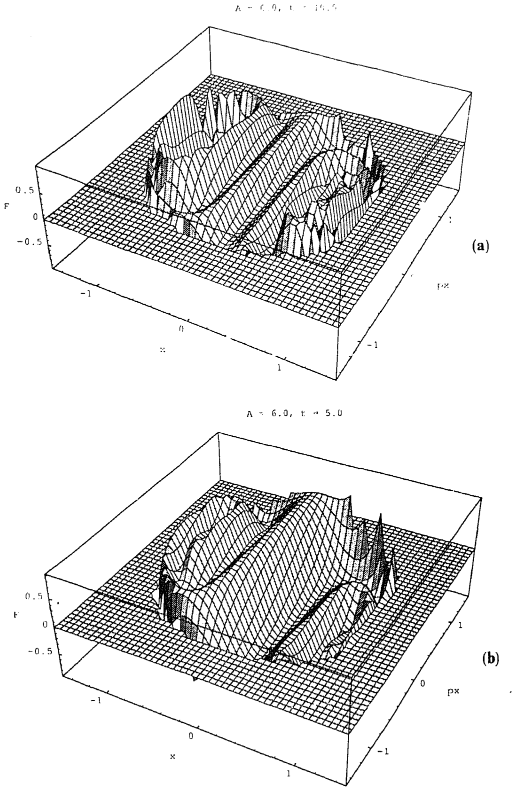

Figures 5a and 5b. Same as figures 1a and 1b, with $A = 6$ (integrable case).

as, choosing $2n$ different initial conditions allows us to construct $2n$ functionally independent F's.

From the assumptions made regarding the non-vanishing of at least one of the Liapunov exponents, it is clear that at least one of the invariants so constructed must violate one of the two conditions given above, i.e., the invariant must be non-C^∞ as a function on phase space or the formal power series must have zero radius of convergence. (The second condition can be re-expressed in the form that the solutions of the equations:

$$\frac{\mathrm{d}\xi(\varepsilon)}{\mathrm{d}\varepsilon} = \{F, \xi(\varepsilon)\}, \tag{12}$$

are singular at $\varepsilon = 0$.)

We have studied the above problem numerically for the quartic oscillator in 2 dimensions, defined by the Hamiltonian [8]

$$H = px^2 + py^2 + x^4 + y^4 + Ax^2y^2. \tag{13}$$

As is well known, the system is integrable for $A = 0, 2, 6$ and becomes increasingly chaotic as $A \to -2$. For this system, (1) was directly integrated using the initial conditions $F(x, y, px, py, t = 0) = x$, corresponding to the initial conditions $\eta_i(t = 0) = \delta_{i1}$. This choice of initial conditions can be motivated by the fact that if there is a non-zero Liapunov exponent, then we would expect almost all solutions of the Liapunov equations to be dominated by the particular solution corresponding to the positive Liapunov exponent. The values of the invariant function have been plotted on the Poincare surface defined by x, px and $y = 0$ for various times t and parameters A for the energy $E = 1$. (The Hamiltonian under consideration exhibits scaling, so that it is adequate to study one energy). As can be seen, for values of A corresponding to chaotic regimes, the values show increasing jaggedness, indicative of the fact that the phase space derivatives of F become larger and larger. We interpret this result as showing that the function eventually ceases to be analytic on phase space.

Acknowledgements

We would like to thank the referee for some useful comments.

References

[1] S L Ziglin, *Funct. Anal. Appl.* **16**, 181 (1983a)
[2] S L Ziglin, *Funct. Anal. Appl.* **17**, 6 (1983b)
[3] H Ito, *Kodai Math. J.* **8**, 120 (1985)
[4] H Yosida, *Physica* **D29**, 128 (1987)
[5] G Benettin, L Gaglani and J M Strelcyn, *Phys. Rev.* **A14**, 2338 (1976)
[6] V I Arnol'd and A Avez, *Ergodic problems of classical mechanics*, (Benjamin, New York, 1968)
[7] Y Choquet-Bruhat, C de Witt-Morette and M Dillard-Bleick, *Analysis, manifolds and physics* (North Holland, Amsterdam, 1977)
[8] M Lakshmanan and R Sahadevan, *Phys. Rep.* **224**, 1 (1993)

PRAMANA
— journal of
physics

© Printed in India

Vol. 44, No. 4,
April 1995
pp. 303–316

On singularity-free spacetimes

NARESH DADHICH, L K PATEL* and R TIKEKAR**
Inter University Centre for Astronomy and Astrophysics, Post Bag 4, Ganeshkhind, Pune 411 007, India
* Permanent address: Department of Mathematics, Gujarat University, Ahmedabad 380 009, India
** Permanent address: Department of Mathematics, Sardar Patel University, Vallabh–Vidyanagar 358 120, India

MS received 27 September 1994; revised 21 January 1995

Abstract. We consider here the metric for the singularity-free family of fluid models. The metric is unique for cylindrically symmetric space-time with metric potentials being separable functions of radial and time coordinates in the comoving coordinates. It turns out that fluid models separate out into two classes, with $\rho \neq \mu p$ in general but $\rho = 3p$ in particular and $p = \rho$. It is shown that in both the cases radial heat flow can be incorporated without disturbing the singularity-free character of the spacetime. The geodesics of the singularity-free metric are studied and the geodesic completeness is established. Several previously known solutions are derived as particular cases.

Keywords. General relativity; singularity-free models; exact solutions.

PACS Nos **04·20; 98·80**

1. Introduction

The standard view, the Universe had a big-bang singular origin predicted by the standard Friedman–Robertson–Walker (FRW) model, was supported on the formal grounds by the strong singularity theorems [1]. That occurrence of singularity is inescapable if we adhere to reasonable energy and causality conditions and to general relativity (GR). To handle the cosmic singularity several attempts have been made by several authors. They include modification of GR, invoking quantum effects and new fields, ascribing unusual properties to matter etc. By sacrificing energy conditions and other physical properties, it is easy to construct a singularity free model, the most well-known example of this class is the deSitter universe. That is there exists a large number of such models where acceptable physical behaviour of matter has been traded off for avoidance of singularity.

Under this background Senovilla's singularity-free solution [2] is remarkable that it satisfies the energy conditions and has very acceptable equation of state $\rho = 3p$. This is the first solution of its kind that is free of singularity with physically reasonable behaviour of matter. Further Ruiz and Senovilla [3] have discussed the singularity-free character of inhomogeneous cylindrically symmetric spacetime and have separated out a family of singularity-free perfect fluid models. It has been shown [4] that these solutions are geodetically complete and are able to escape the singularity theorems because they do not obey the assumption of existence of causal compact trapped surfaces.

From the point of view of general study of singularity-free cosmology it would be of relevance to examine how robust is the singularity-free character of the spacetime? That is, can we generate singularity-free vacuum solutions or can we introduce heat flow, viscosity etc. retaining the singularity-free character? In this context we have [5] considered viscous fluid and found that it is not possible to have viscosity non-negative for all times while heat flow [6] can be incorporated easily. We give the heat flow generalizations of the two classes of fluid models mentioned above.

In § 2 we obtain the singularity-free metric. We also consider the regularity of Weyl and Ricci curvatures for this metric. Section 3 is devoted to the study of perfect fluid models and the fluid models with radial heat flow. In § 4 we present a general study of geodesics of the singularity-free metric. We also explicitly exhibit the non-occurrence of compact trapped surfaces that makes the singularity theorems inapplicable to this family of metrics. We conclude in § 5 with discussion of the results obtained in the paper.

2. Singularity-free metric

Ruiz and Senovilla [3] have separated out a singularity-free family of solutions of Einstein's equations for perfect fluid. The spacetime has cylindrical symmetry. With metric potentials as separable functions of r and t the family is unique.

We begin with the general form of the metric

$$ds^2 = A^2(dt^2 - dr^2) - B^2 dz^2 - C^2 d\phi^2. \tag{1}$$

Here we have $A = A_1(t)A_2(r), B = B_1(t)B_2(r), C = C_1(t)C_2(r)$ and have used the coordinate freedom to write $g_{tt} = |g_{rr}|$. The metric admits two space-like Killing vectors $\partial/\partial z$ and $\partial/\partial\phi$ which are mutually as well as hypersurface orthogonal implying cylindrical symmetry. That means we should write $C_2(r) = rf(r)$ so as to satisfy the regularity conditions on the axis $r = 0$ and the elementary flatness condition in its vicinity.

The prime requirement for a metric to be singularity-free is that its coefficients have no zeroes for real values of the co-ordinates and Ricci and Weyl tensors are regular everywhere. Ricci curvatures for the metric (1) are given in the Appendix and they will be regular provided $\dot{A}/A$, A'/A etc. are regular. At the outset $C_2(r) = rf(r)$ would imply $A_1(t) = C_1(t)$ (by demanding: coefficient of $r^{-1} = 0$). This regularity condition has no reference to matter distribution.

Assuming the matter content of the spacetime to be perfect fluid we impose the fluid conditions, $R_{14} = 0$, and $R_{11} = R_{22} = R_{33}$ for the comoving velocity field

$$\mathbf{u} = A dt. \tag{2}$$

After some calculations it can be shown that $R_{14} = 0$ implies that $A_1(t) = C_1(t) = T^{\alpha}(t)$, $B_1(t) = T^{\beta}(t)$ and $A_2(r) = B_2^q(r)$. That is the time variation in the metric stems from one singile function. Subsequently $R_{11} = R_{22} = R_{33}$ (from Appendix) will imply

$$\frac{\ddot{T}}{T} + (\alpha + \beta - 1)\frac{\dot{T}^2}{T^2} = k^2, \tag{3}$$

$$\frac{C_2''}{C_2} - \frac{B_2''}{B_2} = (\alpha - \beta)k^2, \tag{4}$$

$$C_2 = B_2' B_2^{(\alpha-\beta)/\beta}. \tag{5}$$

Equation (3) admits the general singularity-free solution

$$T(t) = K_1 [C(\lambda kt) + t_0)]^{1/\lambda^2} = C^{1/\lambda^2}(\lambda kt), \tag{6}$$

where we have chosen the integration constants $K_1 = 1$, $t_0 = 0$ and written $\alpha + \beta = \lambda^2$, $C(x) = \cosh(x)$. The other solutions for $\lambda^2 \leqslant 0$ have been ruled out by the singularity-free and positivity of density conditions.

In [3] it was assumed that $\alpha + \beta = 1$ and the time dependence stemming from the same function $T(t)$ which we have shown above has to follow from $R_{14} = 0$. It turns out that there is no loss of generality in the former assumption either, for it would just imply an overall scaling in the expressions for density and pressure (i.e. $C^\alpha(kt) \to C^{\alpha/\lambda^2}(\lambda kt)$). We can hence take $\alpha + \beta = \lambda^2 = 1$. For space-dependance Ruiz and Senovilla employ four arbitrary functions ($g_{44} \neq |g_{11}|$) and obtain the general solution of the system of equations (4) and (5) with the condition $\alpha + \beta = 1$. The solution in our notation, will read as

$$MX' = C_2/B_2,\ B_2 = X^{(1-\alpha)/(2\alpha-1)}$$
$$C_2^2 = B_2^2[(2\alpha - 1)^2 k^2 M^2 X^2 + NX^{(4\alpha-3)/(2\alpha-1)} - L]$$

where $X = X(r)$ and M, N, L are constants of integration. This family is cylindrically symmetric and contains a sub-family which is non-singular. This family can be shown to be unique for the general orthogonal metric separable in space and time variables [7]. In Ruiz-Senovilla case $X(r)$ is arbitrary which gets determined for us because of the choice $g_{44} = |g_{11}|$. It turns out that for non-singular family we can integrate for X in terms of elementary regular functions, only for $N = 0$ to give the general solution

$$B_2 = C^b(mr),\ C_2 = m^{-1} S(mr) C^c(mr)$$

where $S(mr) = \sinh(mr)$ and $A_2 = B_2^q = C^a(mr)$. The fluid consistency equations (4), (5) and the equation $R_{14} = 0$ will give relations between the parameters a, b, c, m, k and α.

Thus we obtain the metric for singularity free space-time as

$$\begin{aligned} \mathrm{d}s^2 = {} & C^{2\alpha}(kt) C^{2a}(mr)(\mathrm{d}t^2 - \mathrm{d}r^2) - C^{2\beta}(kt) C^{2b}(mr)\mathrm{d}z^2 \\ & - m^{-2} S^2(mr) C^{2c}(mr) C^{2\alpha}(kt)\, \mathrm{d}\phi^2 \end{aligned} \tag{7}$$

which is unique for perfect fluid distribution with appropriate relations between free parameters.

If we do not use the co-ordinate freedom to write $g_{44} = |g_{11}|$, then the most general unique singularity-free metric is [3]

$$\begin{aligned} \mathrm{d}s^2 = {} & C^{1+n}(kt) C^{n-1}(nkr)\left[\mathrm{d}t^2 - \frac{S^2(nkr)}{P^2}\mathrm{d}r^2\right] - C^{1-n}(kt) C^{(n-1)/n}(nkr)\mathrm{d}z^2 \\ & - C^{1+n}(kt) \frac{P^2}{n^2 k^2 L^2 C^{(n-1)/n}(nkr)} \mathrm{d}\phi^2 \end{aligned} \tag{8}$$

where $L = M - (M-1)/2n$, $P^2 = C^2(nkr) + (M-1) C^{(2n-1)/n}(nkr) - M$; n, k and M being constants. The metric (8) satisfies Einstein field equations for a perfect fluid distribution. The metric (7) follows from (8) when $M = 1$. We [8] have shown elsewhere that the metric (7) can be deduced through a natural anisotropization and inhomogeneisation of the FRW metric with negative curvature. We shall not give these details here.

The kinematic parameters expansion θ, shear σ^2 and acceleration $\dot{u}_r$ for the metric (7) are given by

$$\theta = (\alpha + 1)kS(kt)\,C^{-\alpha-1}(kt)\,C^{-a}(mr) \tag{9}$$

$$\sigma^2 = \frac{2}{3}(2\alpha - 1)^2 k^2 S^2(kt)\,C^{-2(\alpha+1)}(kt)\,C^{-2a}(mr) \tag{10}$$

$$\dot{u}_r = -\,amS(mr)\,C^{-\alpha}(kt)\,C^{-a-1}(mr). \tag{11}$$

They are all regular and finite throughout the spacetime. The Ricci and Weyl curvatures will also be regular as they involve $\dot{A}/A, A'/A$ etc. which are all regular and finite for the metric (7). This would also imply the regular behaviour for the physical parameters ρ and p. There would however be some conditions on the parameters.

It is the non-vanishing of acceleration and shear that is responsible for avoidance of singularity. It is physically conceivable that acceleration and shear do not let the fluid congruence to focus into small enough a region to form trapped surfaces leading to singularity. Acceleration of congruence viewed as spatial *pressure gradient* which opposes gravitational attraction and provides the bounce to transform contraction into expansion at $t = 0$. For the metric (1) acceleration can be non-zero only if shear is non-zero [7]. The shear makes geodesics of the congruence to slip through without letting them converge into a small region. It helps in defocussing of the congruence. It is however obvious that their presence alone is not sufficient to avoid singularity as we can easily check by letting $C(kt) \to S(kt)$ in (7). Then the spacetime is singular at $t = 0$ with acceleration and shear non-zero. Hence it may be a necessary condition but not sufficient. For sufficiency we should have regularity of the metric and curvatures. Then energy conditions will have to be satisfied.

For the metric (7) we give below the Ricci and Weyl curvatures to show explicitly that they are regular. The expressions read as follows:

$$\begin{aligned} 2(\psi_0 + \psi_4)A^2 &= m^2(2a - 3c + b - 1) - k^2(\alpha - \beta) + 2\alpha(\alpha - \beta)k^2\,T^2(kt) \\ &\quad + m^2[2a(c - b) + (b - c)(b + c - 1)]\,T^2(mr) \end{aligned} \tag{12}$$

$$\begin{aligned} 2(\psi_0 - \psi_4)A^2 &= mk(\alpha + \beta - 1)\,T(kt)\,T^{-1}(mr) + \\ &\quad \{2\alpha(c - b) + \alpha(2a - b - c) + \beta(b + c - 2a) + (b - c)\}\,T(mr) \end{aligned} \tag{13}$$

$$\begin{aligned} 2\psi_2 A^2 &= k^2(1 - 2\alpha) + m^2(2a + b - 3c - 1) \\ &\quad + (b + c - 2a + 2bc - b^2 - c^2)m^2\,T^2(mr) \\ &\quad + (2\alpha + \alpha^2 + \beta^2 - 2\alpha\beta - 1)k^2\,T^2(kt) \end{aligned} \tag{14}$$

$$\begin{aligned} A^2 R_{11} &= m^2(1 + b + 3c) - \alpha k^2 + \{b(b - 1) + c(c - 1) - a(b + c + 1)\}m^2\,T^2(mr) \\ &\quad - \{\alpha(\alpha + \beta - 1)\}k^2\,T^2(kt) \end{aligned} \tag{15}$$

$$A^2 R_{22} = 2bm^2 - \beta k^2 - \beta(\alpha + \beta - 1)k^2\,T^2(kt) + \{b(b - 1) + bc\}m^2\,T^2(mr) \tag{16}$$

$$A^2 R_{33} = m^2(b+3c+1) - \alpha k^2 - \alpha(\alpha+\beta-1)k^2\ T^2(kt) + \{c(c-1)+bc\} m^2\ T^2(mr) \tag{17}$$

$$A^2 R_{44} = (2\alpha+\beta)k^2 - 2am^2 + a(1-b-c)m^2\ T^2(mr) + \{\beta(\beta-1)+\alpha(\alpha-1)-\alpha(\alpha+\beta+1)\} k^2\ T^2(kt) \tag{18}$$

$$A^2 R_{14} = mk[\beta(b-a) - \alpha(a+b)]\ T(kt)\ T(mr) \tag{19}$$

where

$$A^2 = C^{2\alpha}(kt) C^{2a}(mr),\ T(x) = \tanh(x). \tag{20}$$

The above quantities will be singularity-free if the coefficients of $T^{-1}(mr)$ vanish, so we obtain the condition

$$\alpha + \beta = 1. \tag{21}$$

With α, β as restrained above, Ricci and Weyl curvatures are regular and finite everywhere indicating that the metric is free of any kind of singularity. Now we can introduce matter to determine other parameters occurring in R_{ik} consistent with the energy conditions.

The conditions for perfect fluid $R_{14} = 0$ and $R_{11} = R_{22} = R_{33}$ would imply

$$(\alpha-\beta)(\alpha+\beta-1) = 0 \tag{22}$$

$$(\beta-\alpha)k^2 = (b-1-3c)m^2 \tag{23}$$

$$(b-c)(b+c-1) = 0 \tag{24}$$

$$a(b+c+1) = b(b-1-c) \tag{25}$$

$$\alpha(a+b) = \beta(b-a). \tag{26}$$

The first condition is satisfied in view of (21) which has to be obeyed always as it is dictated by the regularity of Weyl tensor.

The remaining conditions give rise to the following two cases (i) $b = c$, (ii) $b + c = 1$. These are the only two possibilities for singularity-free fluid models satisfying the energy conditions. The former in general represents a fluid without an equation of state. Only when $b = -1/3$, it represents Senovilla's [2] radiation model with $\rho = 3p$. The latter will always have $\rho = p$, representing stiff fluid model [9]. In this case when we put $\rho = 0$, we get two distinct vacuum solutions as its matter free limit. The point to be noted is that these are all general unique solutions for the singularity-free form (7). It is also interesting that the two cases $\rho \neq \mu p$ in general (but $\rho = 3p$ in particular) and $\rho = p$ separate out nicely.

3. Fluid models

We shall consider the perfect fluid and fluid with radial heat flux models. It is possible to introduce heat flux in both the cases considered above.

3.1 *Perfect fluid*

Einstein's equations for non-empty spacetime are

$$R_{ik} = -8\pi(T_{ik} - \tfrac{1}{2}Tg_{ik}) \tag{27}$$

where for perfect fluid

$$T_{ik} = (p + \rho)u_i u_k - pg_{ik}, \quad u_i u^i = 1. \tag{28}$$

Case (*i*) $b = c$

We write from eqs (23)–(26)

$$\alpha = (1 + b)(1 + 2b)^{-1}, \quad a = -b(1 + 2b)^{-1}, \quad \frac{m}{k} = n = (1 + 2b)^{-1}. \tag{29}$$

This determines the metric (7) in terms of the two free parameters b and k, say.

The pressure and density have the expressions:

$$8\pi pA^2 = \frac{b^2(1 - 2b)}{(1 + 2b)^3}k^2 C^{-2}(nkr) - \frac{(3b + 1)(b + 1)}{(1 + 2b)^2}k^2 C^{-2}(kt) \tag{30}$$

$$8\pi\rho A^2 = \frac{b(2b - 1)(2 + 3b)}{(1 + 2b)^3}k^2 C^{-2}(nkr) - \frac{(3b + 1)(b + 1)}{(1 + 2b)^2}k^2 C^{-2}(kt) \tag{31}$$

where $A = C^{\alpha}(kt)C^{a}(nkr)$. This is the Ruiz-Senovilla [3] model. For satisfaction of the energy conditions we shall require $-\frac{1}{2} < b \leqslant -\frac{1}{3}$ and the Senovilla radiation model results for $b = -\frac{1}{3}$. With b so restricted, ρ and p are positive for entire spacetime. For $b \neq -\frac{1}{3}$, there is no equation of state of the type $\rho = \mu p$. The maximum density would occur at $t = 0$ and $r = 0$ which decreases to zero as $t \to \pm\infty$ and $r \to \infty$. The parameter k can be identified with $\rho_{\max}$ which can be freely chosen. At a given t, ρ is largest at the origin $r = 0$ and at given r, it is largest at $t = 0$.

Case (*ii*) $b + c = 1$

In this case we have

$$\alpha = \tfrac{1}{2}(2 - b), \quad a = b(b - 1), \quad c = 1 - b, \quad n^2 = \frac{m^2}{k^2} = \frac{1}{4} \tag{32}$$

and we get the stiff fluid [5] model with

$$8\pi\rho = 8\pi p = \left(\frac{b^2 - 4}{4A^2}\right)k^2 C^{-2}(kt). \tag{33}$$

Clearly the energy condition will be obeyed for $b^2 \geqslant 4$, i.e. b lying outside the interval $-2 \leqslant b \leqslant 2$, the end points of which give the two distinct vacuum cosmological solutions [9]. These solutions are given as follows:

For $b = 2$

$$\mathrm{d}s^2 = C^4(mr)(\mathrm{d}t^2 - \mathrm{d}r^2 - C^2(2mt)\mathrm{d}z^2) - m^{-2}S^2(mr)C^{-2}(mr)\mathrm{d}\phi^2. \tag{34}$$

For $b = -2$

$$ds^2 = C^4(2mt)[C^{12}(mr)(dt^2 - dr^2) - C^6(mr)m^{-2}S^2(mr)d\phi^2] - C^{-2}(2mt)C^{-4}(mr)dz^2. \tag{35}$$

It can be easily verified from eqs (12)–(14) that both the solutions are Petrov type I. The former (34) is static as Weyl scalars have no time dependence, while the latter can asymptotically represent a plane gravitational wave. Since there are no obvious localized sources for the solutions, hence the only possible source can be gravitational radiation. However, one knows that in realistic situation the metric for gravitational radiation is of type I almost everywhere [10].

3.2 *Fluid with heat flow*

The energy momentum tensor for fluid with heat flow is given by

$$T_{ik} = (p + \rho)u_i u_k - p g_{ik} + (q_i u_k + q_k u_i), \quad u_i u^i = 1, \quad u_i q^i = 0. \tag{36}$$

Here q_i is the heat flow vector. Here we are relaxing the condition (26) by taking radial heat flow. We take the tetrad components of q_i as $q_a = (q, 0, 0, 0)$. The parameters ρ, p and q are given by

$$8\pi\rho A^2 = (a - 3b)m^2 + (\beta - \alpha)k^2 + (\beta^2 + 2\alpha\beta + \alpha - \beta)k^2 T^2(kt) + \tfrac{1}{2}(a - 3b)(b + c - 1)m^2 T^2(mr) \tag{37}$$

$$8\pi p A^2 = (a + b)m^2 - (\alpha + \beta)k^2 + (\alpha + \beta - \beta^2)k^2 T^2(kt) + \tfrac{1}{2}(a + b)(b + c - 1)m^2 T^2(mr) \tag{38}$$

$$8\pi q A^2 = mk[\alpha(a + b) - \beta(b - a)]\, T(kt)\, T(mr) \tag{39}$$

where $A = C^\alpha(kt)C^a(mr)$.

Case (*i*) $b = c$

In this case we have

$$b = c, \alpha = 1 - \beta, a = -\frac{b}{1 + 2b}, n^2 = \frac{m^2}{k^2} = \frac{1 - 2\beta}{1 + 2b}. \tag{40}$$

We treat b and n as arbitrary parameters. The physical parameters are then given by

$$8\pi q A^2 = \frac{k^2 nb}{(1 + 2b)}\{(n^2 - 1) + 4b(b + 1)n^2\}\, T(kt)\, T(nkr) \tag{41}$$

$$8\pi p A^2 = \frac{k^2}{4}(n^2 - 1)\{1 - n^2(1 + 2b)^2\} + \frac{b^2(1 - 2b)}{(1 + 2b)}n^2 k^2 C^{-2}(nkr) + \tfrac{1}{4}\{n^2(1 + 2b) - 3\}\{1 + n^2(1 + 2b)\}C^{-2}(kt) \tag{42}$$

$$8\pi\rho A^2 = \frac{k^2}{4}(3+n^2)\{1-n^2(1+2b)^2\}$$
$$-\frac{b(1-2b)(2+3b)}{(1+2b)}n^2k^2C^{-2}(nkr)$$
$$+\tfrac{1}{4}\{n^2(1+2b)-3\}\{1+n^2(1+2b)\}C^{-2}(kt). \tag{43}$$

From the above equations it can be easily seen that the physical requirements $p \geqslant 0, \rho \geqslant 0$ are satisfied for

$$-\frac{1}{2} < b \leqslant -\frac{1}{3}, \quad \frac{3}{1+2b} < n^2 \leqslant \frac{1}{(1+2b)^2}. \tag{44}$$

From (41) it is clear that $q = 0$ implies $n^2 = (1+2b)^{-2}$ and the model reduces to the perfect fluid (29). For $n = 3$ we have the heat flow generalization of the Senovilla radiation model [6].

Case (ii) $b + c = 1$

Here we write

$$a = b(b-1), \quad C = 1-b, \quad \alpha = 1-\beta, \quad n^2 = \frac{m^2}{k^2} = \frac{2\beta-1}{4(b-1)} \tag{45}$$

and obtain

$$8\pi q A^2 = b(b-1)(4n^2-1)nk^2\, T(kt)\, T(nkr) \tag{46}$$

$$8\pi p A^2 = \frac{k^2}{4}(4n^2-1)\{1-4n^2(b-1)^2\}$$
$$+\frac{k^2}{4}[4n^2(b-1)-1][4n^2(b-1)+3]C^{-2}(kt) \tag{47}$$

$$8\pi\rho A^2 = -\frac{k^2}{4}[4n^2-1][3+4n^2(b-1)^2]$$
$$+\frac{k^2}{4}[4n^2(b-1)-1][4n^2(b-1)+3]C^{-2}(kt). \tag{48}$$

The physical requirements $\rho > 0$ and $p \geqslant 0$ restrict n and b to the ranges

$$0 < n^2 \leqslant \tfrac{1}{4}, \quad 1 < b < 2. \tag{49}$$

For $n^2 = \frac{1}{4}$, it reduces to the stiff fluid model (32). The phenomenological expression for the heat conduction is given by

$$q_k = \psi\left(\frac{\partial F}{\partial x^i} + F\dot{u}_i\right)(\delta^i_k - k^i u_k) \tag{50}$$

where ψ is the thermal conductivity and F is the temperature. For the cases under consideration only radial flow is retained. Hence eq. (50) can be integrated if ψ is a function of t alone to give

$$F = l(t)C^{a}(nkr) - \frac{k}{16\pi a\psi}\{\alpha(a+b) - \beta(b-a)\}C^{-a}(nkr)C^{-\alpha}(kt)\ T(kt) \tag{51}$$

where $l(t)$ is an arbitrary function of t. Thus temperature distributions for the cases (i) and (ii) can be obtained.

The heat flux has been considered in the evolution of the cosmological models by several authors (see [6]). Here it should be noted that the metric (7) has been considered by Tikekar *et al* [11] in connection with inhomogeneous string models.

4. Geodesics

To demonstrate the geodesic completeness of the metric, we should show that all non-spacelike geodesics can be extended to arbitrary values of the affine parameter. For this let us write the geodesics of the metric (7) following the standard procedure and they would read as follows:

$$C^{2\alpha}(kt)\,C^{2a}(mr)(\dot{t}^2 - \dot{r}^2) - L^2C^{-2\beta}(kt)C^{-2b}(mr) - m^2M^2S^{-2}(mr)C^{-2\gamma}(kt)C^{-2c}(mr) = \delta, \tag{52}$$

$$C^{2\beta}(kt)\,C^{2b}(mr)\dot{z} = L, \tag{53}$$

$$m^{-2}S^{2}(mr)C^{2\gamma}(kt)C^{2c}(mr)\dot{\phi} = M, \tag{54}$$

$$\ddot{r} + amT(mr)(\dot{t}^2 + \dot{r}^2) + 2\alpha kT(kt)\dot{t}\dot{r} - M^2m^3S^{-3}(mr)C^{-2(\gamma+\alpha)}(kt)C^{-2(c+a)+1}(mr)(1 + cT^2(mr)) - L^2bmS(mr)C^{-2(\beta+\alpha)}(kt)C^{-2(b+a)-1}(mr) = 0, \tag{55}$$

$$\ddot{t} + \alpha kT(kt)(\dot{t}^2 + \dot{r}^2) + 2amT(mr)\dot{t}\dot{r} + \gamma km^2M^2S^{-2}(mr)S(kt)C^{-2(\gamma+\alpha)-1}(kt)C^{-2(c+a)}(mr) + \beta kL^2S(kt)C^{-2(\beta+\alpha)-1}(kt)C^{-2(b+a)}(mr) = 0. \tag{56}$$

A dot denotes derivative with respect to the affine parameter, and L and M are the two constants of motion corresponding to the two Killing vectors representing the conserved z and ϕ momenta. The another constant of motion is δ due to the rest mass which is one for timelike and zero for null geodesics. Since all the terms in (52)–(56) are non-singular hence the solutions to the equations will exist and they will be unique.

We shall now examine the behaviour of first and second derivatives of the coordinates relative to the affine parameter. We should put finite bounds on the first derivatives [12] which will imply that the geodesics are complete. However, the second derivatives should not be singular to ensure that the field is overall non-singular. Without any loss of generality we can restrict to the future pointing geodesics. In this discussion, we do not restrict to fluid distributions, i.e. the parameters $\alpha, \beta, \gamma, a, b, c, m, k$ are treated as arbitrary. Following [4], we shall first consider the particular geodesics and then come to the general case.

(*a*) *Fluid congruence*: The simplest geodesics are the ones associated with the fluid congruence. For these we have $\dot{r} = \dot{\phi} = \dot{z} = 0$. It follows from (2) that the only geodesic possible in this case has to lie on the axis $r = 0$ and it is given by

$$\dot{t} = C^{-\alpha}(kt) \leqslant 1 \quad \text{for} \quad \alpha \geqslant 0.$$

That means α must be non-negative and then the geodesics are obviously complete.

(*b*) *Axial geodesics*: For the geodesics lying on the axis we have $\dot{r} = 0 = \dot{\phi}, r = 0$ and so we write

$$\dot{z} = LC^{-2\beta}(kt),$$
$$\dot{t} = C^{-\alpha}(kt)[L^2 C^{-2\beta}(kt) + \delta]^{1/2} \leqslant (L^2 + \delta)^{1/2},$$

provided $\alpha + \beta \geqslant 0$. Then the derivatives will be bounded everywhere and the geodesics will be complete. Note that the coordinate t attains infinite value only when so does the affine parameter. This property will be shared by all the geodesics and will not be referred to henceforth.

(*c*) *Radial null geodesics*: Here $\dot{z} = 0 = \dot{\phi}, \delta = 0$, the first integrals give

$$\dot{t} = |\dot{r}|, \quad \dot{t} = hC^{-2\alpha}(kt)\, C^{-2a}(mr), \quad h = \text{constant}.$$

It is clear that $|\dot{r}| = \dot{t} \leqslant h$ provided $\alpha \geqslant 0, a \geqslant 0$ and then the geodesics will be complete. The geodesics with fixed ϕ comfortably continue along $\pi + \phi$ after crossing the axis.

(*d*) *Radial timelike geodesics*: Here $\delta = 1$, $\dot{z} = 0 = \dot{\phi}$. Let us parametrize $\dot{t}$ and $\dot{r}$ by writing

$$\dot{t} = C(v)A(r,t), \quad \dot{r} = S(v)A(r,t), \dot{v} = B(r,t,v)A(r,t)$$

where $A = C^{-\alpha}(kt)\, C^{-a}(mr)$. Then

$$B = -[amT(mr)C(v) + \alpha kT(kt)S(v)].$$

We have $a \geqslant 0, \alpha \geqslant 0$ and take $k, m \geqslant 0$ which will imply $\dot{v} \leqslant 0$. We shall consider the role of the second derivatives in the end. The same reasoning will apply here to show that geodesics are complete.

(*e*) *Null geodesics with zero angular momentum*: In this case we have $\dot{\phi} = 0, \delta = 0$ and as before we write

$$\dot{t} = C(v)E(r,t), \dot{r} = S(v)E(r,t),$$

and

$$\dot{v} = E(r,t)F(r,t,v).$$

Then we obtain

$$E = |L|\, C^{-(\alpha+\beta)}(kt)\, C^{-(a+b)}(mr),$$
$$F = -[k(\alpha - \beta)\; T(kt)S(v) + m(a-b)\; T(mr)C(v)]$$

RAMAN RESEARCH INSTITUTE 26998

We shall require $\alpha + \beta \geqslant 0, a + b \geqslant 0, \alpha \geqslant \beta$ and $a \geqslant b$ for $\dot{v} \leqslant 0$.

(*f*) *Null geodesics on the hypersurfaces* $z = constant$: These are defined by $\dot{z} = 0, \delta = 0$, and as before we have

$$\dot{t} = C(v)P(r,t), \dot{r} = S(v)P(r,t)$$

and

$$\dot{v} = P(r,t)D(r,v)$$

where

$$P = |M| m S^{-1}(mr) C^{-(\gamma+\alpha)}(kt) C^{-(a+c)}(mr),$$

$$D = k(\gamma - \alpha)\, T(kt) S(v) + mC(v)[(c-a)\, T(mr) + T^{-1}(mr)].$$

As has been noted earlier that the regularity of the Ricci tensor requires $\alpha = \gamma$. Hence $D = D(r, v)$ as assumed.

In this case we can obtain one of the equations of the orbit that on integration yields

$$C(v) = N^{-1} S(mr) C^{c-a}(mr), \quad N = \text{constant} > 0.$$

Since $C(v) \geqslant 1$, the coordinate r is bounded between the roots of $S(mr)C^{c-a}(mr) = N$. Clearly $|v|$ is bounded and the geodesics are complete. Among them there could be a circular geodesic, corresponding to the double root, which will go around the axis at the fixed radius.

(*g*) *General non-spacelike geodesics*: Now we come to the general case. From (55) it follows that $\ddot{r}$ will be negative for positive t and increasing r provided $b \leqslant 0$ (for large r the term with L^2 will dominate over that with M^2). With $\ddot{r} < 0$, the r-coordinate cannot diverge to infinity in a finite proper time. As r decreases the $\dot{t}\dot{r}$ terms will dominate over the $(\dot{t}^2 + \dot{r}^2)$ term while the L^2 term will tend to zero as $r \to 0$. In the vicinity of the axis $r = 0, \ddot{r} > 0$ for decreasing r and $t > 0$. Thus the geodesics cannot collapse quickly enough into the axis to become singular. It is this feature that really provides the *bounce off* to the universe, turning contraction to expansion at $t = 0$.

The above arguments will apply to the cases (d) and (e) above and hence the geodesics will be complete for them. As regards the t-coordinate, $\ddot{t}$ should be negative for large values of t, so that it keeps its growth in check, not letting it diverge to infinity for finite values of the affine parameter. From (56), it can be seen that this will be so even if $\beta \leqslant 0$ because the $(\dot{t}^2 + \dot{r}^2)$ will always be the dominant term (for decreasing r the $\dot{t}\dot{r}$ term will not be relevant). $\dot{z}$ is always regular so long as t and r are regular. $\dot{\phi}$ diverges as $r \to 0$ but with $\dot{\phi} \neq 0$, the geodesics can never reach $r = 0$ as has been demonstrated in (f) above. In the neighbourhood of the axis eq. (54) simply represents the centrifugal effect.

It is straightforward to carry out the similar calculations as done in the previous cases but they are very cumbersome and not very enlightening and hence we will not report them here. It can be verified that the general geodesics are also complete. Let us now collect together all the restrictions prescribed by the above considerations on the parameters and they are

$$\alpha \geqslant 0, \alpha + \beta \geqslant 0, \alpha \geqslant \beta$$

$$a \geqslant 0, a + b \geqslant 0, a \geqslant b, b \leqslant 0, k \geqslant 0, m \geqslant 0$$

and $\alpha = \gamma$ implied by the regularity of the Ricci tensor. It is interesting to note that α, β and a, b satisfy the similar conditions. All this follows purely by requiring the geodesics to be complete without any reference to the matter distribution. That is in this framework one can *a priori* ensure the geodesic completeness by adhering to the above conditions on the parameters. The singularity-free perfect fluid models discussed above satisfy all these restrictions.

5. Discussion

If one were to write a singularity-free metric, without reference to anything else, the natural choice for metric functions would have been hyperbolic or quadratic functions without zeros. The amazing thing is that this obvious choice is the right and the only choice. However, one has to take cylindrical symmetry in place of the usual spherical symmetry.

For the avoidance of singularity acceleration and shear play the crucial role. In our case, the former cannot exist without the latter [7]. The former provides the bounce to the universe at $t = 0$ where contraction turns into expansion while the latter makes the fluid geodesic congruence to slip through without letting them to focus in a small enough region to form compact surfaces leading to singularity. The overall scenario is: universe has very low density tending to zero at $t \to -\infty$, wherefrom it starts contracting and attains the dense state at $t = 0$ where contraction changes to expansion and it expands to low density again at $t \to \infty$. The momentum gained during the contraction phase takes the universe through $t = 0$ to the expanding phase. The maximum density at $t = 0$ and $r = 0$ can be made as large or small as one pleases by choosing the parameter k. All physical and kinematic parameters remain regular and finite throughout the universe. The presence of acceleration and shear may be necessary but by no means sufficient to avoid singularity. In addition the spacetime should be regular.

It follows from the analysis of § 4 that all the conclusions drawn in [4] for the geodesics of radiation model [2] remain true for our general case as well. We shall now demonstrate that the space-time does not admit trapped surfaces.

For this we should compute trace of the two null second fundamental forms [1] and that is given by

$$(g^{ab}X_{ab}) = \frac{1}{\sqrt{2}} C^{-\alpha}(kt)\, C^{-a+1}(mr) S^{-1}(mr) \times$$

$$[\mp m \mp m(b+c)\, T^2(mr) - k(\gamma+\beta)\, T(kt)\, T(mr)].$$

It is clear that $(X^a_a)_- \leqslant 0$ provided $b + c - 1 \geqslant 0$ and $(X^a_a)_+ \geqslant 0$ for $m(b + c + 1) \geqslant k(\alpha + \beta)$. Since the traces have opposite signs, there exist no closed trapped surfaces. This means that the outgoing and incoming radial null geodesics are respectively expanding and contracting everywhere. For existence of a closed trapped surface, in some region they should all be contracting, i.e. the trace should be positive for both in some region. It can be verified that the singularity-free models for § 3 satisfy the conditions just deduced. Thus there occur no closed trapped surface in the singularity-free family of metrics.

Let us recall that $\alpha = \gamma$ was dictated by the cylindrical symmetry while $\alpha + \beta = 1$ for the metric (7) is demanded by the Weyl regularity. These two are general conditions without reference to any matter field. That is of the three α, β, γ only one is free for the singularity-free spacetime. It may be noted that all the fluid models (which are the only ones for the metric (7)) discussed in § 3 obey the conditions, $\alpha \geqslant 0, \alpha + \beta \geqslant 0, \alpha \geqslant \beta, a \geqslant 0, a + b \geqslant 0, a \geqslant b$ and $b \leqslant 0$, obtained for completeness of geodesics.

The most important question for the singularity-free models is how to evolve them into the standard FRW model which successfully describes the present day universe. The affirmative answer to this question will bring these models into the active arena of cosmology and would perhaps have very significant role to play in the early universe cosmology. The main difficulty here is that the anisotropy measure (σ/θ) of the metric (7) is constant which means it remains anisotropic for all times. It would be interesting to find a singularity-free solution with σ/θ decreasing with t so that it can isotropise at late times to go over to FRW model. The uniqueness of the metric (8) has been established for a general orthogonal metric, separable in space and time in comoving coordinates [7]. That means to get a singularity-free model with $\sigma/\theta \neq$ constant, we will have to give up orthogonality or separability. Then the problem becomes almost unmanageable. It may however be worth its while to invest some effort on this very difficult problem.

Acknowledgement

The authors, LKP and RT, express their thanks to IUCAA, Pune for hospitality.

Appendix

For the metric (1) we introduce the tetrad $\theta^1 = A\mathrm{d}r, \theta^2 = B\mathrm{d}z, \theta^3 = C\mathrm{d}\phi, \theta^4 = A\mathrm{d}t$. The non-vanishing tetrad components R_{ab} of the Ricci tensor for (1) are given by

$$R_{14} = \frac{1}{A^2}\left[\frac{\dot{B}'}{B} + \frac{\dot{C}'}{C} - \frac{\dot{A}}{A}\left(\frac{B'}{B} + \frac{C'}{C}\right) - \frac{A'}{A}\left(\frac{\dot{B}}{B} + \frac{\dot{C}}{C}\right)\right]$$

$$R_{44} = \frac{1}{A^2}\left[\frac{\ddot{A}}{A} + \frac{\ddot{B}}{B} + \frac{\ddot{C}}{C} - \frac{\dot{A}}{A}\left(\frac{\dot{A}}{A} + \frac{\dot{B}}{B} + \frac{\dot{C}}{C}\right) - \frac{A''}{A} + \frac{A'}{A}\left(\frac{A'}{A} - \frac{B'}{B} - \frac{C'}{C}\right)\right],$$

$$R_{11} = \frac{1}{A^2}\left[\frac{A''}{A} + \frac{B''}{B} + \frac{C''}{C} - \frac{A'}{A}\left(\frac{A'}{A} + \frac{B'}{B} + \frac{C'}{C}\right) - \frac{\ddot{A}}{A} - \frac{\dot{A}}{A}\left(\frac{\dot{B}}{B} + \frac{\dot{C}}{C} - \frac{\dot{A}}{A}\right)\right],$$

$$R_{22} = \frac{1}{A^2}\left[\frac{B''}{B} + \frac{B'C'}{BC} - \frac{\ddot{B}}{B} - \frac{\dot{B}\dot{C}}{BC}\right]$$

$$R_{33} = \frac{1}{A^2}\left[\frac{C''}{C} + \frac{B'C'}{BC} - \frac{\ddot{C}}{C} - \frac{\dot{B}\dot{C}}{BC}\right]$$

A prime and a dot indicate differentiation with respect to r and t respectively.

References

[1] S W Hawking and G F R Ellis, *The large scale structure of space-time* (Cambridge University Press, Cambridge, 1973)

[2] J M M Senovilla, *Phys. Rev. Lett.* **64**, 2219 (1990)

[3] E Ruiz and J M M Senovilla, *Phys. Rev.* **D45**, 1995 (1992)

[4] F J Chinea, L Fernandez-Jambrina and J M M Senovilla, *Phys. Rev.* **D45**, 481 (1992)

[5] L K Patel and N Dadhich, IUCAA-21/92 Preprint (1992)

[6] L K Patel and N Dadhich, *Class. Quantum Gravit.* **10**, L85 (1993)

[7] N Dadhich and L K Patel, *On Uniqueness of non-singular inhomogeneous perfect fluid models*, submitted for publication

[8] N Dadhich, R Tikekar and L K Patel, *Curr. Sci.* **65**, 9 (1993)

[9] L K Patel and N Dadhich, IUCAA-1/93 Preprint (1993)

[10] F A E Pirani, *Gravitation: An introduction to current research*, edited by L Witten (John Wiley, New York, 1962)

[11] R Tikekar, L K Patel and N Dadhich, *Gen. Relativ. Gravit.* **26**, 647 (1994)

[12] A I Arnold, *Ordinary differential equations* (MIT press, Cambridge, 1973)

PRAMANA
— journal of
physics

© Printed in India

Vol. 44, No. 4,
April 1995
pp. 317–322

Exact solutions of Einstein and Einstein-scalar equations in 2 + 1 dimensions

K S VIRBHADRA
Departamento de Física Teórica, Universidad del País Vasco, Apartado 644, 48080 Bilbao, Spain
Present address: Theoretical Astrophysics Group, Tata Institute of Fundamental Research, Homi Bhabha Road, Bombay 400005, India

MS received 18 October 1994

Abstract. A nonstatic and circularly symmetric exact solution of the Einstein equations (with a cosmological constant Λ and null fluid) in $2+1$ dimensions is given. This is a nonstatic generalization of the uncharged spinless BTZ metric. For $\Lambda = 0$, the spacetime is though not flat, the Kretschmann invariant vanishes. The energy, momentum, and power output for this metric are obtained. Further a static and circularly symmetric exact solution of the Einstein-massless scalar equations is given, which has a curvature singularity at $r = 0$ and the scalar field diverges at $r = 0$ as well as at infinity.

Keywords. Lower dimension gravity; BTZ metric; Einstein-scalar equations; energy-momentum pseudotensor.

PACS No. 04·20

In recent years there has been considerable interest in studying the Einstein theory of gravity in $2+1$ spacetime dimensions. Due to the smaller number of dimensions it has tremendous mathematical simplicity. The use of three dimensional gravity has been suggested as a test bed for the quantization of gravity [1]. The lowest spacetime dimension in which the Einstein theory of gravitation exists is three and it possesses some strange features. In three dimensions the number of independent components of the Riemann curvature tensor and the Einstein tensor are the same (six) and the Riemann tensor can be expressed in terms of the Einstein tensor. Consequently, the spacetime described by the vacuum solutions to the Einstein equations in $2+1$ dimensions are locally flat and there are no gravitational waves and no interaction between masses. However, in Newton's theory of gravitation in three dimensions a point mass produces an acceleration which falls off like $1/r$ [2]. Unlike the case in $3+1$ dimensions, the Einstein theory of gravitation has no Newtonian limit in $2+1$ dimensions. Therefore, the Einstein gravitational constant is undetermined in three dimensions.

Deser and Mazur [3] obtained the gravitational and Coulomb fields of a massive point charge in $2+1$ dimensional Einstein–Maxwell (EM) theory. As opposed to the case of $3+1$ dimensional EM theory, the Coulomb field behaves asymptotically as $1/r$ and the stress tensor is nonvanishing everywhere. The total energy diverges. The Kretschmann invariant diverges at $r = 0$ as well as at infinity [3]. There exists a static multi-charge solution in $3+1$ dimensional EM theory [4]. However, there are no static solutions corresponding to two or more charges in $2+1$ dimensions [3].

Arguing that the light emitted from the surface of a star will always escape to the infinity because there is no gravity outside matter (or energy), Giddings *et al* concluded that black holes do not exist in three dimensional Einstein theory of gravitation [5]. However, Bañados *et al* (BTZ) [6] have recently discovered a black hole solution to the EM equations (with a negative cosmological constant) in $2+1$ dimensions, which is characterized by mass, angular momentum, and charge parameters. The $2+1$ dimensional uncharged BTZ black hole solution has fascinated many physicists minds ([7] and references therein). Unlike the Kerr metric it is not asymptotically flat and there is no curvature singularity. However, it shares many features of its $3+1$ dimensional counterpart. For instance, it has an ergosphere, upper bound in angular momentum (for a given mass) and has similar thermodynamical properties [8].

In this paper we give two exact solutions: (*a*) a nonstatic and circularly symmetric solution of the Einstein equations with a cosmological constant and null fluid, which is a nonstatic generalization to the spinless uncharged BTZ metric and (*b*) a static and circularly symmetric solution of the Einstein-massless scalar equations. We obtain the energy, momentum, and power output for the nonstatic circularly symmetric metric (with zero cosmological constant) and compare the results with its $3+1$ dimensional counterpart. We use the geometrized units and follow the convention that Latin (Greek) indices take values 0 to 2 (1 to 2). x^0 stands for the time coordinate.

The Einstein field equations with a cosmological constant Λ and the null fluid present are

$$R_{ij}-\frac{1}{2}R\,g_{ij}+\Lambda g_{ij}=\kappa N_{ij}. \tag{1}$$

R_{ij} is the Ricci tensor and R is the Ricci scalar. κ is the Einstein gravitational constant. N_{ij} is the energy-momentum tensor due to the null fluid, which is given by

$$N_{ij}=V_i\,V_j, \tag{2}$$

where V_i is the null fluid current vector satisfying

$$V_i\,V^i=0. \tag{3}$$

A nonstatic and circularly symmetric exact solution of the above equations in $2+1$ dimensions is given, in coordinates $x^0=u, x^1=r, x^2=\varphi$, by the line element

$$ds^2=-(-m(u)-\Lambda r^2)du^2-2du\,dr+r^2d\varphi^2. \tag{4}$$

The nonvanishing component of the energy-momentum tensor of the null fluid is

$$N_0^1=\frac{\dot m}{2\kappa r}. \tag{5}$$

The dot denotes the derivative with respect to the time coordinate u. The null fluid current vector is

$$V^i=g_1^i\sqrt{\frac{-\dot m}{2\kappa r}}. \tag{6}$$

The nonvanishing components of the Riemann curvature tensor are

$$\begin{aligned} R_{1220} &= \Lambda r^2, \\ R_{1010} &= -\Lambda, \\ R_{2020} &= \frac{2m\Lambda r^2 + r(-\dot{m} + 2\Lambda^2 r^3)}{2}, \end{aligned} \tag{7}$$

and the Kretschmann invariant is

$$R^{abcd} R_{abcd} = 12\Lambda^2. \tag{8}$$

The spacetime described by the line element (4) with $\Lambda = 0$ is though not flat, the Kretschmann invariant vanishes. When m is a constant, (4) gives the uncharged spinless BTZ metric.

Lindquist *et al* [9] obtained the energy, momentum and power output for the Vaidya metric. It is of interest to obtain the same for the circularly symmetric nonstatic metric (with $\Lambda = 0$) and compare the results with its $3+1$ dimensional counterpart. There are several prescriptions for calculating the energy, momentum and power output for a nonstatic general relativistic system. For example, one can use the Landau and Lifshitz (LL) pseudotensor [10]

$$L^{mn} = L^{nm} = \frac{1}{2\kappa} S^{mjnk}{}_{,jk}, \tag{9}$$

where

$$S^{mjnk} = -g(g^{mn} g^{jk} - g^{mk} g^{nj}). \tag{10}$$

S^{mjnk} has the symmetries of the Riemann tensor. The LL pseudotensor satisfies the local conservation laws:

$$\frac{\partial L^{mn}}{\partial x^m} = 0. \tag{11}$$

L^{00} and $L^{0\alpha}$ are, respectively, the energy density and momentum (energy current) density components. It is known that the LL pseudotensor gives the correct result if calculations are carried out in "Cartesian coordinates". Therefore, we transform the line element (4), with $\Lambda = 0$, to these coordinates, which is given by

$$\mathrm{d}s^2 = -\mathrm{d}t^2 + \mathrm{d}x^2 + \mathrm{d}y^2 + (1 + m(u))\left[\mathrm{d}t - \frac{x\mathrm{d}x + y\mathrm{d}y}{r}\right]^2. \tag{12}$$

The coordinates u, r, φ in (4) and t, x, y in (12) are related through

$$\begin{aligned} u &= t - r, \\ x &= r\cos\varphi, \\ y &= r\sin\varphi. \end{aligned} \tag{13}$$

The determinant $g \equiv |g_{ij}|$ is

$$g = -1 \tag{14}$$

and the contravariant components of the metric tensor are

$$\begin{aligned}
g^{00} &= -m-2,\\
g^{11} &= \frac{-mx^2+y^2}{r^2},\\
g^{22} &= \frac{-my^2+x^2}{r^2},\\
g^{01} &= -\frac{x(1+m)}{r},\\
g^{02} &= -\frac{y(1+m)}{r},\\
g^{12} &= -\frac{xy(1+m)}{r^2}.
\end{aligned} \tag{15}$$

We are interested in calculating the energy and momentum density components and therefore the required components of S^{mjnk} are

$$\begin{aligned}
S^{0101} &= \frac{-y^2(1+m)-r^2}{r^2},\\
S^{0202} &= \frac{-x^2(1+m)-r^2}{r^2},\\
S^{0102} &= \frac{xy(1+m)}{r^2},\\
S^{0112} &= \frac{y(1+m)}{r},\\
S^{0212} &= \frac{-x(1+m)}{r}.
\end{aligned} \tag{16}$$

Substituting (16) in (9), we get the energy and momentum (energy current) density components

$$\begin{aligned}
L^{00} &= \frac{m'}{2\kappa r},\\
L^{01} &= -\frac{\dot{m}x}{2\kappa r^2},\\
L^{02} &= -\frac{\dot{m}y}{2\kappa r^2}
\end{aligned} \tag{17}$$

(m' stands for $\partial m/\partial r$). Therefore, the energy and momentum components are

$$\begin{aligned}
E &= m\frac{\pi}{\kappa},\\
P_x &= P_y = 0,
\end{aligned} \tag{18}$$

and the power output is

$$W = -\frac{\pi}{\kappa}\frac{\mathrm{d}m}{\mathrm{d}u}. \tag{19}$$

For the Vaidya metric, Lindquist *et al* found $E = M, P_x = P_y = P_z = 0$, and $W = -\,\mathrm{d}M/\mathrm{d}u$, where M is the mass parameter in the Vaidya metric. Thus, we get similar results in its $2+1$ dimensional counterpart (κ is not known due to the lack of a Newtonian limit). This supports the importance of the study of lower dimension gravity as a toy model.

The exact solutions of the Einstein-massless scalar equations in $3+1$ spacetime dimensions are known in the literature [11]. It is of interest to obtain a static and circularly symmetric exact solution of these equations in $2+1$ dimensions. The Einstein-massless scalar field equations are [11]

$$R_{ij} - \frac{1}{2} R\, g_{ij} = \kappa S_{ij}, \tag{20}$$

where S_{ij}, the energy-momentum tensor of the massless scalar field, is given by

$$S_{ij} = \Phi_{,i}\Phi_{,j} - \frac{1}{2} g_{ij} g^{ab} \Phi_{,a}\Phi_{,b}, \tag{21}$$

and

$$\Phi_{,i}^{;i} = 0. \tag{22}$$

Φ stands for the massless scalar field.

A static and circularly symmetric exact solution of the above equations is given by the line element

$$\mathrm{d}s^2 = -\,B\,\mathrm{d}t^2 + B\,\mathrm{d}r^2 + r^2\,\mathrm{d}\varphi^2 \tag{23}$$

with

$$B = (1-q)\,\mathscr{R}^q, \tag{24}$$

and the scalar field

$$\Phi = \sqrt{\frac{q}{\kappa}}\ln \mathscr{R}, \tag{25}$$

where

$$\mathscr{R} = \frac{r}{r_0}. \tag{26}$$

q stands for the scalar charge. $q = 0$ gives the flat spacetime in $2+1$ dimensions. The nonvanishing components of the Einstein tensor and the energy-momentum tensor of the massless scalar field are given by

$$G_1^1 = -\,G_2^2 = -\,G_0^0 = \kappa S_1^1 = -\,\kappa S_2^2 = -\,\kappa S_0^0 = \frac{q}{2(1-q)\,\mathscr{R}^q r^2}. \tag{27}$$

The surviving independent components of the Riemann tensor are

$$R_{1212} = R_{2020} = \frac{q}{2},$$

$$R_{1010} = \frac{q(q-1)\mathscr{R}^q}{2r^2}, \tag{28}$$

and the Kretschmann invariant is

$$R^{abcd}R_{abcd} = \frac{3q^2}{(1-q)^2\mathscr{R}^{2q}r^4}. \tag{29}$$

The Kretschmann invariant diverges at $r = 0$ showing a curvature singularity there and it vanishes at infinity. However, the scalar field diverges at $r = 0$ as well as at infinity. The details of this paper will be given elsewhere. Upon completion of this work a preprint [12] came to our notice which has the nonstatic solution given here.

Acknowledgements

This work was supported in part by a Basque Government post-doctoral fellowship. Thanks are due to A Achúcarro, I Egusquiza, P S Joshi, and M A Valle for discussions.

References

[1] W G Unruh, *Int. J. Mod. Phys.* **D3**, 131 (1994)
E Witten, *Nucl. Phys.* **B311**, 46 (1988)
[2] J R Gott and M Alpert, *Gen. Relativ. Gravit.* **16**, 243 (1984)
[3] S Deser and P O Mazur, *Class. Quantum Gravit.* **2**, L51 (1985)
[4] A Papapetrou, *Proc. R. Irish Acad.* **51**, 91 (1947)
S D Majumdar, *Phys. Rev.* **72**, 390 (1947)
[5] S Giddings, J Abbott and K Kuchar, *Gen. Relativ. Gravit.* **16**, 751 (1984)
[6] M Bañados, C Teitelboim and J Zanelli, *Phys. Rev. Lett.* **69**, 1849 (1992)
[7] D Cangemi, M Leblanc and R B Mann, *Phys. Rev.* **D48**, 3606 (1993)
N Kaloper, *Phys. Rev.* **D48**, 2598 (1993)
A Achúcarro and M Ortiz, *Phys. Rev.* **D48**, 3600 (1993)
K Shiraishi and T Maki, *Class. Quantum Gravit.* **11**, 695 (1994)
A R Steif, *Phys. Rev.* **D49**, R585 (1994)
G Lifschytz and M Ortiz, *Phys. Rev.* **D49**, 1929 (1994)
S Hyun, G H Lee and J H Yee, *Phys. Lett.* **B322**, 182 (1994)
O B Zaslavskii, *Class. Quantum. Gravit.* **11**, L33 (1994)
[8] M Bañados, M Henneaux, C Teitelboim and J Zanelli, *Phys. Rev.* **D48**, 1506 (1993)
[9] R W Lindquist, R A Schwartz and C W Misner, *Phys. Rev.* **137**, B1364 (1965)
[10] L D Landau and E M Lifshitz, *The classical theory of fields* (Oxford, Pergamon Press, 1985) p. 280
[11] A I Janis, D C Robinson and J Winicour, *Phys. Rev.* **186**, 1729 (1969)
[12] J S F Chan, K C K Chan and R B Mann, *Interior structure of a charged spinning black hole in (2 + 1) dimensions* gr-qc/9406049 (1994)

PRAMANA
— journal of
physics

© Printed in India

Vol. 44, No. 4,
April 1995
pp. 323–332

Charge screening in a two potential theory of electromagnetism

C WOLF
Department of Physics, North Adams State College, North Adams, MA 01247, USA

MS received 3 June 1994; revised 28 November 1994

Abstract. By surrounding an Abelian Dyon with an axion-like domain wall we calculate the screening effects generated by the domain wall on the dyon degrees of freedom.

Keywords. Dyon; charge screening; two potential theory.

PACS No. 03·50

1. Introduction

In theories of elementary particle phenomena screening effects play an important role firstly because they determine the attractive, repulsive and confining properties of a gauge field [1] and secondly because screening effects alter secondary phenomena such as proton decay [2] and phase transitions such as the deconfinement transition and the chiral phase transition in QCD [3]. It is known in QED that a bare electric charge is screened by a vacuum polarized surrounding cloud of opposite charge to give rise to a renormalized finite charge [4] and in QCD a given coloured quark is screened by anti-coloured quarks but anti-screened by like coloured gluons to generate the confining QCD potential [5]. In a previous note [6] we have discussed a somewhat related but different phenomena, namely the screening of the electric charge degree of freedom of an Abelian dyon by an axion cloud. The analysis of that investigation showed that the electric charge could be screened, reversed in sign or anti-screened by a surrounding axion cloud depending on the boundary conditions of the axion field at the interior and exterior of the configuration.

In an interesting study Fischler and Preskill [7] have shown how monopoles might deplete the axion density to acceptable levels in the early universe so as not to overclose the universe by forcing (θ_{QCD}) the vacuum angle of QCD to approach 0. (Here θ_{QCD} is the coefficient of the topological CP violating term induced by the non-trivial vacuum structure of QCD). In that investigation the authors demonstrated that the axion field would screen the electric charge of a dyon but not its magnetic charge. Thus in addition to altering the properties of the dyon degree of freedom the interplay between the axion-like field and the dyon parameters may resolve problems in early universe cosmology that have no other solution.

In a subsequent note we have studied screening of a $U(1) \times U(1)$ gauge theory where each $U(1)$ group was represented by an electric-like and magnetic-like potential, the analysis demonstrated that screening and anti-screening were dependent on the strength of the coupling [8]. Following this note we discussed the screening of an Abelian dyon by a spherically symmetric domain wall where the positions of the degenerate minimum determine the screening effects of the domain wall [9]. As mentioned in [9], topological defects such as strings, monopoles and domain walls occur in a spontaneously broken gauge theory and the trapping of a monopole or dyon by a domain wall might be a likely occurrence in the early universe. It was also stressed that the screening of a dyon by a domain wall should have far ranging consequences in the space surrounding the exterior of the domain wall altering such phenomena as the catalysis of proton decay and plasma generated density perturbations that may serve as the origin of large scale structure. In the following note we discuss the screening of both electric and magnetic charge by a domain wall in a theory where the electromagnetic field is represented by a two potential theory (electric and magnetic potential) [10].

To-date there is no conclusive evidence that would either confirm or refute the two potential theory since magnetic monopole (magnetic charge) searches have to-date not produced any conclusive evidence for their existence [11]. Since monopoles are a necessary consequence of spontaneously broken gauge theories [12] their detection may be difficult due to their extraordinarily large masses. In a recent paper S Davidson and M Peskin [13] have discussed the existence of a paraphoton interacting with milli-charged particles and given astrophysical bounds on such particles. Holdom [14] has shown how a second photon can be a natural consequence of GUT models and can be produced in the laboratory via Compton scattering of normal photons. Possibly these developments might suggest that the existence of a second photon could be accommodated by a two potential theory. Actually, Callegari *et al* [15] have shown how a two potential theory of massive photons could be tested for by looking for corrections to the earth's magnetic field. One of the shortcomings of the two potential theory is that when electromagnetism interacts with fermions it leads to an effective non-linear lagrangian which implies a coupling between the electric like and magnetic like photons, this would suggest that high fields would necessarily generate magnetic like photons that would effect phenomena such as photon splitting in a magnetic field [16] which has been calculated to many orders of perturbation theory in normal QED and awaits experimental confirmation perhaps in the radiation coming from pulsars where the magnetic field is high. Using the two potential theory we calculate the screened values of the electric and magnetic charge as seen exterior to the domain wall as well as an approximate expression for the electric field, magnetic field and pseudo-scalar axion field within the wall. Finally, we develop an approximate expression for the mass of the domain wall in terms of the parameters in the lagrangian and the central dyon charges.

2. Electric and magnetic charge screening in a two potential theory

We begin our analysis by writing the following axion-like electromagnetic lagrangian of a pseudo-scalar field coupled to electromagnetism and gravity as

$$\begin{aligned}\mathscr{L} &= \frac{c^4}{16\pi G} R\sqrt{-g} + \left[\frac{\partial^\mu\phi\partial_\mu\phi}{2} - \frac{A_2}{4}\left(\phi^2 - \frac{A_1}{A_2}\right)^2\right]\sqrt{-g} \\ &\quad + \alpha\phi\left(\frac{\varepsilon^{\mu\nu\alpha\beta}F_{\alpha\beta}F_{\mu\nu}}{\sqrt{-g}}\right)\sqrt{-g} - \frac{1}{16\pi} + F_{\mu\nu}F^{\mu\nu}\sqrt{-g} \\ &= \mathscr{L}_G + \mathscr{L}_M\end{aligned} \tag{2.1}$$

where α is the coupling constant.

The kinetic term in (2.1) is the usual kinetic term in any scalar or pseudo-scalar theory and the potential has degenerate minimum at

$$\phi = \pm (A_1/A_2)^{1/2}$$

The phenomenological coupling between the pseudo-scalar field and the electromagnetic field is analogous to the axion electromagnetic interaction discussed by Peccei and Quinn [17], Weinberg [18], Wilczek [19] and Kim [20] which represents a low energy effective term after the heavy fields in the theory are integrated out. Here since α depends on the inverse mass of the heavy fields we expect it to be small and thus screening effects depending on α to be small. The last term is the usual kinetic term of electromagnetism.

For the metric in this problem we choose

$$(\mathrm{d}S)^2 = e^{\nu}(\mathrm{d}x^4)^2 - e^{\lambda}(\mathrm{d}r)^2 - r^2(\mathrm{d}\theta)^2 - r^2\sin^2\theta(\mathrm{d}\bar{\phi})^2$$

where e^{ν} e^{λ} depend only on r. The electromagnetic field is described by [10]

$$F_{\mu\nu} = \frac{\partial A_\mu}{\partial x^\nu} - \frac{\partial A_\nu}{\partial X^\nu} - \frac{\varepsilon_{\mu\nu}{}^{\alpha\beta}}{2\sqrt{-g}}\left(\frac{\partial B_\alpha}{\partial x^\beta} - \frac{\partial B_\beta}{\partial x^\alpha}\right)$$

where A_μ = electric four potential, B_μ = magnetic four potential, ϕ = pseudo-scalar field with the potential term containing degenerate minimum at

$$\phi = \pm (A_1/A_2)^{1/2}.$$

In the above expression for $F_{\mu\nu}$ we note we have two potentials A_μ, B_μ; this does not necessarily imply the existence of two photons since the theory is equivalent to the usual theory in the absence of magnetic charge and interactions. In the presence of magnetic charge and interactions quanta of the B field will be associated with the magnetic charge existing as virtual or free photons and possibly mixing with the normal photon.

Varying (2.1) with respect to ϕ gives

$$-\Box\phi - A_2\phi\left(\phi^2 - \frac{A_1}{A_2}\right) + \frac{\alpha\varepsilon^{\mu\nu\alpha\beta}F_{\alpha\beta}F_{\mu\nu}}{\sqrt{-g}} = 0 \tag{2.2}$$

Varying (2.1) with respect to A_μ gives

$$\frac{\partial}{\partial x^\nu}\left(\frac{1}{4\pi}\sqrt{-g}F^{\mu\nu}\right) - 4\alpha\frac{\partial}{\partial x^\nu}(\phi\varepsilon^{\mu\nu\alpha\beta}F_{\alpha\beta}) = 0 \tag{2.3}$$

Varying (2.1) with respect to B_μ gives

$$\frac{\partial}{\partial x^\nu}\left(\frac{1}{4\pi}\tilde{F}^{\mu\nu}\right) - 4\alpha\frac{\partial}{\partial x^\nu}\left(\frac{\phi\varepsilon^{\mu\nu\alpha\beta}\tilde{F}_{\alpha\beta}}{\sqrt{-g}}\right) = 0$$

$$\tilde{F}^{\mu\nu} = \frac{\varepsilon^{\mu\nu\alpha\beta}F_{\alpha\beta}}{2} \tag{2.4}$$

The energy momentum tensor for the pseudo-scalar field and EM field is from (2.1)

$$T_{\mu\nu}=\frac{2}{\sqrt{-g}}\frac{\partial L_M}{\partial g^{\mu\nu}}=\partial_\mu\phi\,\partial_\nu\phi-\frac{g_{\mu\nu}}{2}(\partial^\alpha\phi\,\partial_\alpha\phi)+g_{\mu\nu}\frac{A_2}{4}\left(\phi^2-\frac{A_1}{A_2}\right)^2$$

$$+\frac{1}{16\pi}g_{\mu\nu}(F_{\alpha\beta}F^{\alpha\beta})-\frac{1}{4\pi}F_{\mu\alpha}F^{\alpha}_{\nu}. \tag{2.5}$$

We now position an Abelian dyon of mass M and electric and magnetic charge e, q so that its centre is at $r=0$, we call the effective radius of the dyon R_D, for $R_D\leqslant r\leqslant R_1$ we have the minimum

$$\phi=-(A_1/A_2)^{1/2}.$$

Actually by (2.2) we have a variation of ϕ over the region $R_D\leqslant r\leqslant R_1$ but if R_1 and R_D are close to one another we may neglect the variation of ϕ over $R_D\leqslant r\leqslant R_1$ and set $\phi=-(A_1/A_2)^{1/2}$to a good approximation. At $r=R_2$ (outer boundary of domain wall) we set

$$\phi=(A_1/A_2)^{1/2}$$

and neglect the variation of ϕ for $r>R_2$ since ϕ will change very slowly by (2.2) if R_2 is far enough from the dyon centre where E,B will vary as $1/r^2$. Here R_1 and R_2 are arbitrary except for the fact that R_1 is close to R_D so as to ensure that the variation of the axion-like field is small for $R_D\leqslant r\leqslant R_1$ and R_2 is large enough so that the variation of ϕ for $r>R_2$ can be neglected. Thus

$$\phi=-(A_1/A_2)^{1/2}\ \text{for}\ R_D\leqslant r\leqslant R_1,$$

$$\phi=(A_1/A_2)^{1/2}\ \text{for}\ r>R_2$$

($R_1,R_2=$ inner and outer radii of domain wall respectively). The two degenerate minima are separated by a domain wall where the potential attains a maximum somewhere between R_1 and R_2. Also $F_{14}=E(r)$, $F_{23}=r^2\sin\Theta\,B(r)$. ($E,B=$ radial electric and magnetic field). For $R_D<r<R_1$ we may integrate (2.3) to give

$$\frac{r^2E}{4\pi}-8\alpha\phi r^2B=\frac{e}{4\pi} \tag{2.6}$$

and (2.4) integrates to give

$$\frac{r^2B}{4\pi}+8\alpha\phi r^2E=\frac{q}{4\pi} \tag{2.7}$$

where

$$\phi=-(A_1/A_2)^{1/2}\ \text{for}\ R_D<r\leqslant R_1.$$

(e and q are electric and magnetic charges of the central dyon.)
In (2.6) and (2.7) we have used $\lambda+\nu=0$ for $R_D<r<R_1$ which follows from the form of the energy momentum tensor ($T^1_1=T^4_4$) in (2.5) for $R_D<r<R_1$ and the Einstein equations.

Solving (2.6) and (2.7) gives

$$E=\frac{1}{r^2}\left(\frac{e-32\pi\alpha(A_1/A_2)^{1/2}q}{1+(32\pi\alpha(A_1/A_2)^{1/2})^2}\right)=\frac{\bar{e}}{r^2} \tag{2.8}$$

$$B=\frac{1}{r^2}\left(\frac{q-32\pi\alpha(A_1/A_2)^{1/2}e}{1+(32\pi\alpha(A_1/A_2)^{1/2})^2}\right)=\frac{\bar{q}}{r^2} \tag{2.9}$$

($\bar{e},\bar{q}$ are the effective electric and magnetic charge for $R_D<r\leqslant R_1$).
For $r>R_2$ we have upon integrating (2.3) and (2.4) and setting

$$\phi=(A_1/A_2)^{1/2}$$

$$E=\frac{1}{r^2}\left[\frac{e_E+32\pi\alpha(A_1/A_2)^{1/2}q_E}{1+(32\pi\alpha(A_1/A_2)^{1/2})^2}\right]=\frac{\bar{\bar{e}}}{r^2} \tag{2.10}$$

$$B=\frac{1}{r^2}\left[\frac{q_E+32\pi\alpha(A_1/A_2)^{1/2}e_E}{1+(32\pi\alpha(A_1/A_2)^{1/2})^2}\right]=\frac{\bar{\bar{q}}}{r^2} \tag{2.11}$$

($\bar{\bar{e}}, \bar{q}$ are the effective electric and magnetic charge seen for $r\geqslant R_2$).

In (2.10) and (2.11) we have again used $\lambda+v=0$ for $r>R_2$ which follows from (2.5) and the Einstein equation for $r>R_2$. Here e_E, q_E = exterior electric and magnetic charge seen for $r>R_2$ and correspond to the rhs in (2.6) and (2.7) for $r>R_2$.
Now integrating (2.3) and (2.4) between R_1 and R_2 with

$$\phi_{R_1}=(A_1/A_2)^{1/2},\ \phi_{R_2}=(A_1/A_2)^{1/2}$$

$$\bar{\bar{e}}-\bar{e}-32\pi\alpha(A_1/A_2)^{1/2}\bar{\bar{q}}-32\pi\alpha(A_1/A_2)^{1/2}\bar{q}=0 \tag{2.12}$$

$$\bar{\bar{q}}-\bar{q}-32\pi\alpha(A_1/A_2)^{1/2}\bar{\bar{e}}+32\pi\alpha(A_1/A_2)^{1/2}\bar{e}=0 \tag{2.13}$$

or

$$\bar{\bar{e}}-32\pi\alpha(A_1/A_2)^{1/2}\bar{\bar{q}}=32\pi\alpha(A_1/A_2)^{1/2}\bar{g}+\bar{e} \tag{2.14}$$

$$\bar{\bar{e}}(32\pi\alpha(A_1/A_2)^{1/2})+\bar{\bar{q}}=\bar{q}-32\pi\alpha(A_1/A_2)^{1/2}\bar{e}. \tag{2.15}$$

Solving (2.14) and (2.15) for $\bar{\bar{e}}$, $\bar{\bar{q}}$ gives

$$\bar{\bar{e}}=\frac{\bar{e}(1-(32\pi\alpha(A_1/A_2)^{1/2})^2)+64\pi\alpha(A_1/A_2)^{1/2}\bar{q}}{(1+(32\pi\alpha(A_1/A_2)^{1/2})^2)} \tag{2.16}$$

$$\bar{\bar{q}}=\frac{\bar{q}(1-(32\pi\alpha(A_1/A_2)^{1/2})^2)-64\pi\alpha(A_1/A_2)^{1/2}\bar{e}}{(1+(32\pi\alpha(A_1/A_2)^{1/2})^2)}. \tag{2.17}$$

Using (2.16), (2.17) along with (2.8), (2.9), (2.10) and (2.11) for the definitions of $\bar{e},\bar{q},\bar{\bar{e}},\bar{\bar{q}}$ we have upon solving for e_E, q_E in terms of e, q

$$e_E=e$$

$$q_E=q.$$

From (2.16) we see that the domain wall screens $\bar{e}$ through the first term in (2.16) and anti-screens $\bar{e}$ through the second term which contains the effective magnetic charge $\bar{q}$. If $32\pi\alpha(A_1/A_2)^{1/2}<1$ the dominant term is the anti-screening term in (2.16) which contains the effective magnetic charge $\bar{q}$.

From (2.17) we see that the effective magnetic charge $\bar{q}$ is screened by the effective electric charge $\bar{e}$ and the first term in (2.17) also screens the effective magnetic charge $\bar{q}$. If $32\pi\alpha(A_1/A_2)^{1/2} > 1$ then both the effective electric charge $\bar{e}$ and effective magnetic charge $\bar{q}$ can be screened through the first term in (2.16) and both terms in (2.17). If instead of the degenerate minima

$$\phi_{R_1} = -(A_1/A_2)^{1/2}$$

and

$$\phi_{R_2} = (A_1/A_2)^{1/2}$$

we have

$$\phi_{R_1} = (A_1/A_2)^{1/2}, \phi_2 = -(A_1/A_2)^{1/2}$$

then (2.16) and (2.17) would be altered by letting

$$(A_1/A_2)^{1/2} \to -(A_1/A_2)^{1/2}.$$

This would lead to a screening of the electric charge by the magnetic charge $\bar{q}$ and anti-screening of the magnetic charge by the electric charge for

$$32\pi\alpha(A_1/A_2)^{1/2} < 1.$$

This would be a reverse effect as that contained in (2.16) and (2.17). For

$$32\pi\alpha(A_1/A_2)^{1/2} > 1$$

again both electric charge and magnetic charge would be screened. This curious property of a transition from screening to anti-screening or anti-screening to screening brought about by interchanging the degenerate minimum of ϕ suggests that the symmetry $\phi \to -\phi$ enjoyed for a pure scalar field theory is broken locally in the lagrangian of (2.1) and globally by the effective dyon charges seen by a distant observer. In Ref. [9] we demonstrated that for a one potential theory the magnetic charge remains unscreened, but the electric charge is either screened or anti-screened depending on which degenerate minima of ϕ is on the interior of the domain wall and which is on the outside. In another investigation [21] we have discussed the screening of a $U(1) \times U(1)$ dyon in a theory with two scalar fields each having degenerate minimum of

$$\phi_1 = \pm(A_1/A_2)^{1/2}, \quad \phi_2 = \pm(\bar{A}_1/\bar{A}_2)^{1/2}$$

on either side of the domain wall, here we have four different possible configurations and we found if the negative minimum are on the interior of the wall, the electric-like charges of both $U(1)$ factors are anti-screened, if the positive minimum of ϕ_1, ϕ_2 are on the interior of the wall both electric-like charges are screened. Here for the actual magnitude of the screen charges we have four different possibilities since the interior of the wall can be at either

$$\phi_1 = \pm(A_1/A_2)^{1/2}, \quad \phi_2 = \pm(\bar{A}_1/\bar{A}_2)^{1/2}.$$

The strength of the coupling constant also effects the magnitude of the screened charges. Again, as in [ref. 9] the magnetic-like charges remained unscreened.

To test the above theories we would first have to identify a dyon in an astrophysical setting, if the magnetic charges of a series of dyons remain the same we would be driven to choose a one-potential theory. If however the magnetic charge varied for a series of similar dyons it would suggest a two potential theory. Phenomena sensitive to the screened charges include, Zeeman like splitting of atomic hydrogen in the field of a dyon, dyon induced plasma oscillations and photon splitting for high magnetic fields. The multiplicity of plasma frequencies, Zeeman like splittings and photon orientations from splitting phenomena could be used to distinguish amongst the above theories.

Also all elementary particle phenomena in the field of a dyon would be sensitive to high magnetic fields and this would lead to altered life-times, altered left right asymmetries and altered back-forth asymmetries which could be used to probe the dyon properties if cosmic rays from the dyon region could be analyzed. The reversal or transition from anti-screening to screening by adjustment of the coupling constant (α) and the vacuum expectation values $\pm(A_1/A_2)^{1/2}$ suggests that any cosmological conditions that alter the strength of α and $(A_1/A_2)^{1/2}$ can alter the electromagnetic effect of dyons and thus alter such phenomena as the catalysis of proton decay as well as dyon induced density fluctuations giving rise to the seeds of large scale structure.

To calculate the evolution of the pseudo-scalar field within the domain wall we first integrate (2.3) and (2.4) from R_1 to r within the domain wall to obtain (using the approximation $e^{\lambda} \approx e^{\nu} \approx 1$ for $R_1 \leqslant r \leqslant R_2$)

$$\frac{r^2 E(r)}{4\pi} - \frac{1}{4\pi}\bar{e} = 8\alpha\phi r^2 B(r) + 8\alpha(A_1/A_2)^{1/2} r^2 \frac{\bar{q}}{r^2} \tag{2.18}$$

$$\frac{r^2 B(r)}{4\pi} - \frac{1}{4\pi}\bar{q} = -8\alpha\phi E(r) r^2 - 8\alpha(A_1/A_2)^{1/2}\left(\frac{\bar{e}}{r^2}\right) r^2. \tag{2.19}$$

Solving (2.18) and (2.19) for E, B gives for $R_1 < r < R_2$

$$E(r) = \frac{\bar{e}\left(r^2 - 102\pi^2\alpha^2\phi(A_1/A_2)^{1/2} r^2\right) + \bar{q}\left(32\pi\alpha(A_1/A_2)^{1/2} r^2 + 32\pi\alpha\phi r^2\right)}{r^4 + 1023\pi^2\phi^2 r^4} \tag{2.20}$$

$$B(r) = \frac{\bar{q}\left(r^2 - 1024\pi^2\alpha^2 r^2 (A_1/A_2)^{1/2}\phi\right) - \bar{e}\left(32\pi\alpha\phi r^2 + 32\pi\alpha(A_1/A_2)^{1/2} r^2\right)}{r^4 + 1024\pi^2\alpha^2\phi^2 r^4} \tag{2.21}$$

To solve for ϕ within the wall we write out (2.2) as

$$\frac{\mathrm{d}}{\mathrm{d}r}(r^2\phi_{,r}) - r^2 A_2\phi(\phi^2 - A_1/A_2) - 8\alpha r^2 E(r) B(r) = 0. \tag{2.22}$$

For ϕ we have

$$\phi(r = R_1) = -(A_1/A_2)^{1/2}, \quad \phi(r = R_2) = (A_1/A_2)^{1/2} \tag{2.23}$$

we set

$$\frac{\mathrm{d}\phi}{\mathrm{d}r}(r = R_1) = K_0. \tag{2.24}$$

We may develop a power series solution for ϕ about $r = R_1$ as

$$\phi(r) = \phi(R_1) + \left(\frac{\mathrm{d}\phi}{\mathrm{d}r}\right)_{R_1}(r - R_1) + \frac{1}{2}\left(\frac{\mathrm{d}^2\phi}{\mathrm{d}r^2}\right)_{R_1}(r - R_1)^2 \ldots \tag{2.25}$$

by using $\phi(r = R_1)$ from (2.23) and K_0 for $\left(\frac{\mathrm{d}\phi}{\mathrm{d}r}\right)_{r=R_1}$ and calculating higher derivatives of ϕ at $r = R_1$ from Eq. (2.22) after substituting E, B from (2.20) and (2.21), in this way we may calculate ϕ to any order about $r = R_1$ from (2.25). To evaluate K_0 in an approximate manner we take a finite number of terms in (2.25) and set $\phi(r = R_2) = (A_1/A_2)^{1/2}$ and solve for K_0.

To obtain an approximate expression for the mass of the domain wall we have the energy momentum tensor from (2.5)

$$\begin{aligned} T^\mu_\nu = {} & \partial^\mu\phi\,\partial_\nu\phi - \frac{1}{2}\delta^\mu_\nu(\partial^\alpha\phi\,\partial_\alpha\phi) + \frac{\delta^\mu_\nu}{4}A_2\left(\phi^2 - \frac{A_1}{A_2}\right)^2 \\ & + \frac{1}{16\pi}\delta^\mu_\nu(F_{\alpha\beta}F^{\alpha\beta}) - \frac{1}{4\pi}F^\mu_\alpha F^\alpha_\nu. \end{aligned} \tag{2.26}$$

For $R_D < r < R_1$ we have using $\lambda + \nu = 0$ for $R_1 > r > R_D$

$$T^1_1 = T^4_4 = \frac{1}{8\pi}\left(\frac{\bar{e}^2}{r^4}\right) + \frac{1}{8\pi}\left(\frac{\bar{q}^2}{r^4}\right).$$

For $\infty > r > R_2$ we have using $\lambda + \nu$ for $\infty > r > R_2$.

$$T^1_1 = T^4_4 + \frac{1}{8\pi}\left(\frac{\bar{\bar{e}}^2}{r^4}\right) + \left(\frac{\bar{\bar{q}}^2}{R^4}\right).$$

For $R_2 > r > R_1$ we have using (2.26)

$$T^4_4 = \frac{1}{2}(\phi_{,r})^2 + \frac{A_2}{4}\left(\phi^2 - \frac{A_1}{A_2}\right)^2 + \frac{E^2}{8\pi} + \frac{B^2}{8\pi}. \tag{2.27}$$

Here we have approximated $e^\nu \approx e^\lambda \approx 1$ for $R_1 < r < R_2$.In (2.27) we substitute ϕ from (2.25) and E, B from (2.20) and (2.21). From the $\binom{4}{4}$ Einstein equation we have

$$\frac{\mathrm{d}}{\mathrm{d}r}(re^{-\lambda}) = 1 - \frac{8\pi G}{c^4}T^4_4 r^2$$

integrating between R_1 ad R_2 we have

$$(re^{-\lambda})_{R_2} - (re^{-\lambda})_{R_1} = R_2 - R_1 - \frac{8\pi G}{c^4}\int_{R_1}^{R_2} r^2 T^4_4\,\mathrm{d}r \tag{2.28}$$

here

$$(e^{-\lambda})_{R_1} = 1 - \frac{2GM}{R_1c^2} + \frac{G\bar{e}^2}{R_1^2c^4} + \frac{G\bar{q}^2}{R_1^2c^4} \tag{2.29}$$

$$(e^{-\lambda})_{R_2} = 1 - \frac{2G(M + M_D)}{R_1c^2} + \frac{G\bar{\bar{e}}^2}{R_2^2c^4} + \frac{G\bar{\bar{q}}^2}{R_2^2c^4}. \tag{2.30}$$

Equations (2.29) and (2.30) follow from the $\binom{4}{4}$ Einstein equations in the regions $R_D < r < R_1$ and $r > R_2$ respectively, here we have used the continuity of the metric at $r = R_1$ and R_2 and the expressions for T_4^4 in each region when we integrate the $\binom{4}{4}$ Einstein equation.

Also M_D = mass of domain wall and M = mass of central dyon. When (2.29), (2.30) and T_4^4 from (2.27) are substituted into (2.28) we may solve for M_D (mass of domain wall).

3. Conclusion

The two potential theory of electromagnetism coupled to the axion-like pseudo-scalar has led to electric charge anti-screening and magnetic charge screening for $32\pi\alpha(A_1/A_2)^{1/2} < 1$ and electric charge screening and magnetic charge screening for $32\pi\alpha(A_1/A_2)^{1/2} > 1$ from (2.16) and (2.17). The transition from screening to anti-screening may be determined by the cosmological conditions affecting α (the coupling constant in (2.1), thus the electric charge degree of freedom of a dyon may be more effective than the magnetic charge as the universe cools which in turn produces a delayed effect on particle phenomena such as the catalysis of proton decay (since the magnetic field is diminished) as well as plasma induced density perturbations stimulated by the dyon field. Our results here differ from previous results [Ref. 9] for a one potential electromagnetic theory which always produced an anti-screening effect on the electric charge for a domain wall with interior minimum at $-(A_1/A_2)^{1/2}$ and exterior minimum at $(A_1/A_2)^{1/2}$.

The fascinating feature of this investigation is that it offers us a test for a two potential theory because the magnetic charge is also effected by the domain wall. It might very well be that the domain wall transforms a quantized magnetic charge into a continuum of values (dependent on parameters of a wall) which could show up in exterior secondary phenomena sensitive to magnetic fields such as the rate of elementary particle interactions, magnetic charge plasma oscillations, and Zeeman like spliting of surrounding atomic hydrogen atoms in a dyon induced magnetic field. In closing, if dyons were discovered in an astrophysical setting, their properties probed external to the topological defect could not only distinguish between the one potential theory and two potential theory, but also serve to probe the precise nature of the gauge-field pseudo-scalar coupling.

Acknowledgement

The author would like to thank the Physics Departments at Williams College and Harvard University for the use of their facilities.

References

[1] M Creutz, *Phys. Rev.* **D21**, 2308 (1980)
[2] C G Callan Jr. *Phys. Rev.* **D26**, 2058 (1982)
[3] K G Wilson, *Phys Rev.* **D10**, 2445 (1974)
[4] A Euler and W Heisenberg, *Z. Phys.* **98**, 714 (1936)
[5] C Rebbi, *Lattice gauge theories and Monte Carlo simulations* (World Scientific Pub. Co., Singapore, 1983)
[6] C Wolf, *Acta Phys. Slovaca* **41, (No. 2)** 109 (1991)

[7] W Fischler and J Preskill, *Phys., Lett.* **B125**, 165 (1983)
[8] C Wolf, *An. Found. Louis de Broglie* **18**, 15 (1993)
[9] C Wolf, *Can. J. Phys,* **70**, 391 (1992)
[10] M Cabibbo and E Ferrari, *Il. Nuovo Cimento* **23**, 1147 (1962)
[11] W P Trower, *Phys. Rev.* **D50**, 1793 (1994)
[12] E W Kolb and M S Turner, *The early universe* (Addison-Wesley Pub. Comp., Reading Mass, 1990), pp. 233
[13] S Davidson and M Peskin, *Phys. Rev.* **D49**, 2114 (1994)
[14] B Holdom, *Phys. Lett.* **B166**, 196 (1986)
[15] P Callegari, P Fortini and D Tartari, *Acta Phys. Hung.* **67**, 359 (1990)
[16] S Adler, *Ann. Phys. (N.Y.)* **67**, 599 (1971)
[17] R Peccei and H Quinn, *Phys. Rev. Lett.* **38**, 1440 (1978)
[18] S Weinberg, *Phys. Rev. Lett.* **40**, 223 (1978)
[19] F Wilczek, *Phys. Rev. Lett.* **40**, 279 (1978)
[20] J E Kim, *Phys. Rev. Lett.* **43**, 103 (1979)
[21] C Wolf, *Pramana – J. Phys.* **39**, 37 (1992)

PRAMANA
— journal of
physics

© Printed in India

Vol. 44, No. 4,
April 1995
pp. 333–345

Dual nature of Ricci scalar and creation of spinless particles

K P SINHA and S K SRIVASTAVA*
Department of Physics, Indian Institute of Science, Bangalore 560 012, India
*Permanent address: Department of Mathematics, North Eastern Hill University Permanent Campus, Umshing, Shillong 793 022, India
*Present address: Centre for Theoretical Studies, Indian Institute of Science, Bangalore 560 012, India (short term visitor)

MS received 30 September 1994; revised 13 January 1995

Abstract. Manifestation of Ricci scalar like a matter field as well as a geometrical field, at high energy, has been noted earlier [9]. Here, its interaction with another scalar field is considered in four-dimensional curved space-time. This interaction leads to the production of a large number of pairs of spinless particle-antiparticle due to expansion of the early universe in the vacuum state (provided by temperature dependent Coleman-Weinberg like potential for Ricci field), where spontaneous symmetry breaking takes place.

Keywords. R^2 gravity; dual nature of Ricci scalar; early Universe; particle production.

PACS No. 98·80

1. Introduction

In spite of its success at low energy (long distance), Einstein's theory of gravity is problematic at high energy. According to Hawking–Penrose theorem [1], the field equations of Einstein's theory exhibit point-like singularities, where physical laws collapse. This is the first problem. The second problem is the failure of attempts to renormalize Einstein's theory of gravity. Hence this theory needs modification at least at high energy levels. In this context R^2-gravity [2]–[10] is very interesting which incorporates the general principle of covariance and reduces to Einsteinian gravity at low energy. R^2-gravity is obtained by adding R^2-terms (like R^2, $R_{\mu\nu}R^{\mu\nu}$ and $R_{\mu\nu\rho\sigma}R^{\mu\nu\rho\sigma}$, where R is Ricci scalar, $R_{\mu\nu}$ are components of Ricci tensor and $R_{\mu\nu\rho\sigma}$ are components of Riemann-Curvature tensor) to the Einstein-Hilbert lagrangian which is linear in R. According to the definition of R, $R_{\mu\nu}$ and $R_{\mu\nu\rho\sigma}$, one knows that these geometrical quantities involve second order derivatives of components of the metric tensor as well as square of the first order derivatives of the same with respect to space-time coordinates. Components of the metric tensor are defined as

$$ds^2 = g_{\mu\nu} dx^\mu dx^\nu, \tag{1.1}$$

where $\mu, \nu = 0, 1, 2, 3$. It is obvious from (1.1) that $g_{\mu\nu}$ are dimensionless. So, in natural units ($\hbar = c = k_B = 1$, where $\hbar$, c and k_B have their usual meaning), the dimension of R, $R_{\mu\nu}$ and $R_{\mu\nu\rho\sigma}$ is (mass)^2. Hence, R^2-terms are insignificant at low energy but are very important at high energy level. Importance of R^2-gravity was realized in the context of renormalizability of gravity and R^2-terms also appear as stringy correction to Einstein–Hilbert lagrangian [11]. Some authors [12] have considered lagrangian containing polynomial of R of order higher than two also and have obtained some interesting results. But in these theories, either coupling constants are not dimensionless or dimensionality of space-time is taken to be more than 4. In such cases, the theory is not renormalizable. The present paper deals with R^2-gravity with action given as

$$S_g = \int \mathrm{d}^4 x \sqrt{-g}\left[\frac{R}{16\pi G} + bR^2 + cR_{\mu\nu}R^{\mu\nu} + \mathrm{d}R_{\mu\nu\rho\sigma}R^{\mu\nu\rho\sigma}\right], \tag{1.2}$$

where G is the gravitational constant of dimension $(\text{mass})^{-2}$, g is the determinant of $g_{\mu\nu}$ and coupling constants (b, c and d) are dimensionless.

Taking the above action for gravity (S_g, given by (1.2)), it has been discussed earlier [9, 10] that, at high energy, R manifests itself not only as a geometrical field, but also as a spinless matter field. This kind of dual nature of R, at high energy, is very interesting as well as useful. In quantum field theory, fields describe elementary particles. So, Ricci scalar R is supposed to describe R-quanta, called as Riccions [10], which are spinless bosons.

In the present paper, taking the material aspect of the Ricci scalar, the main focus lies on interactions of spinless Bose field $\tilde{R} = \eta R$ (where η is a parameter of unit magnitude and length dimension) with another scalar field ϕ and its implications in the inflationary model obtained after spontaneous symmetry breaking in the theory with temperature dependent Coleman–Weinberg like potential for $\tilde{R}$. The interaction term is defined as $L_I = \frac{1}{2}\lambda\tilde{R}^2\phi^2$. When $\tilde{R}$ undergoes spontaneous symmetry breaking it leads to a phase transition from the state $\langle\tilde{R}\rangle = 0$ to $\langle\tilde{R}\rangle = \pm\sigma$ (σ is the spontaneous symmetry breaking mass scale and $\langle\tilde{R}\rangle$ is the vacuum expectation value of $\tilde{R}$ which is homogeneous). So long as temperature T is above or equal to the critical temperature T_c, $\langle\tilde{R}\rangle$ remains confined to the state $\langle\tilde{R}\rangle = 0$. But as T falls very much below T_c, $\langle\tilde{R}\rangle$ tunnels through the temperature barrier ($T = T_c$) and acquires a non-zero constant value $\langle\tilde{R}\rangle = \pm\sigma$. As a result, other scalar field ϕ is massless in the state $\langle\tilde{R}\rangle = 0$ and acquires non-vanishing mass in the state $\langle\tilde{R}\rangle = \pm\sigma$. It is demonstrated that a large number of particle-antiparticle pairs are created due to exponentially expanding model of the early universe in the state $\langle\tilde{R}\rangle = \pm\sigma$.

The paper is organized as follows. Section 2 deals with spontaneous symmetry breaking using temperature dependent Coleman–Weinberg-like potential for $\tilde{R}$ in place of temperature dependent Higgs-like potential used in [9]. Taking the geometrical aspect of $\tilde{R}$, it is found that the state $\langle\tilde{R}\rangle = -\sigma$ behaves like bumps in the rapidly expanding model of the early universe given by the state $\langle\tilde{R}\rangle = +\sigma$. In this section, it is also discussed that a huge amount of energy will be released as a result of spontaneous symmetry breaking. In § 3, the Klein–Gordon equation for ϕ is derived and normalized solutions of the same have been obtained. Section 4 contains discussions concerning creation of particles. Section 5 is the concluding section where energy of the created particles is calculated. The natural units are used throughout the paper.

2. Spontaneous symmetry breaking

The four-dimensional generalization of Gauss–Bonnet theorem implies that

$$\int \mathrm{d}^4 x \sqrt{-g}\,(R_{\mu\nu\rho\sigma}R^{\mu\nu\rho\sigma} - 4R_{\mu\nu}R^{\mu\nu} + R^2) = \chi,$$

where χ is the Euler number. Using it in (1.2), one obtains

$$S_g = \chi + \int \mathrm{d}^4 x \sqrt{-g}\left(\frac{R}{16\pi G} + \alpha R_{\mu\nu}R^{\mu\nu} + \beta R^2\right), \tag{2.1}$$

where α and β are dimensionless coupling constants.

Invariance of S_g, under transformation $g_{\mu\nu} \to g_{\mu\nu} + \delta g_{\mu\nu}$ yields field equations [5, 9, 10]. Taking trace of these field equations, one obtains

$$(\Box + m^2)\tilde{R} = 0 \tag{2.2}$$

where

$$\Box = \frac{1}{\sqrt{-g}}\frac{\partial}{\partial x^\mu}\left(\sqrt{-g}\,g^{\mu\nu}\frac{\partial}{\partial x^\nu}\right)$$

and

$$m^2 = [8\pi G(5\alpha + 12\beta)]^{-1}.$$

To avoid ghost problem α and β are required to obey the condition $5\alpha + 12\beta > 0$.

Equation (2.2) indicates that $\tilde{R}$ also behaves like spinless massive field, provided that S_g contains R^2-terms. At this stage, it is better to know the energy mass scale when R^2 terms become unimportant. The determination of exact mass scale is not possible here, but some idea of relative dominance between $R/16\pi G$ and R^2-terms can be obtained as follows. In natural units, in terms of mass scale $R/16\pi G$ corresponds to $M_P^2 M^2 [16\pi(G|G_0)]^{-1}$ (where M_p is Planck mass, M is the energy mass scale and the Newtonian gravitational constant $G_0 \simeq M_\mathrm{p}^{-2}$) and $(\alpha R_{\mu\nu}R^{\mu\nu} + \beta R^2)$ corresponds to $(\alpha + \beta)M^4$. Thus, it is found that R^2-terms will dominate over $R/16\pi G$ when $M > M_\mathrm{p}[16\pi(\alpha + \beta)(G/G_0)]^{-1/2}$ and can be neglected when $M \ll M_\mathrm{p}\,[16\pi(\alpha + \beta)(G/G_0)]^{-1/2}$. Equation (2.1) can also be derived from the action:

$$S_{\tilde{R}} = \frac{1}{2}\int \mathrm{d}^4 x \sqrt{-g}\,(g^{\mu\nu}\partial_\mu \tilde{R}\partial_\nu \tilde{R} - m^2 \tilde{R}^2) \tag{2.3}$$

on imposing the condition

$$\frac{2}{\sqrt{-g}}\frac{\delta S_{\tilde{R}}}{\partial \tilde{R}} = 0 \tag{2.4}$$

on it. Here $\tilde{R} = \eta R$, as mentioned above. In natural units, the theory requires $S_{\tilde{R}}$ to be dimensionless, which is possible only when $\tilde{R}$ has mass dimension. As discussed above R has (mass)^2 dimension, that is why η (a quantity of unit magnitude and (mass)$^{-1}$ dimension) has been associated with R to get the correct dimension of $\tilde{R}$, $\frac{1}{2}m^2\tilde{R}^2$ is the potential term, which can be replaced by another suitable potential after accepting $\tilde{R}$ as a spinless matter field. In [9], $\frac{1}{2}m^2\tilde{R}^2$ has been replaced by temperature-dependent Higgs-like potential. But in the context of $SU(5)$ grand unified theory (which is very important in the early universe), the Coleman–Weinberg type potential is more suitable. So, in this paper, we replace $\frac{1}{2}m^2\tilde{R}^2$ by temperature- dependent Coleman–Weinberg potential for $\tilde{R}$ [13, 14] as

$$V^T(\tilde{R}) = A\left[\tilde{R}^4 \ln\frac{\tilde{R}^2}{\sigma^2} - \frac{1}{2}\tilde{R}^4 + \frac{1}{2}\sigma^4\right] + CT^2\tilde{R}^2, \tag{2.5}$$

where A and C are dimensionless coupling constants.

The vacuum states are given by

$$\left(\frac{\partial V^T}{\partial \tilde{R}}\right)_{\tilde{R}=\langle\tilde{R}\rangle} = 0 \quad \text{or} \quad 4A\langle\tilde{R}\rangle^3 \ln\frac{\langle\tilde{R}\rangle}{\sigma^2} + 2CT^2\langle\tilde{R}\rangle = 0. \tag{2.6}$$

Equation (2.5) yields

$$\langle\tilde{R}\rangle = \begin{cases} 0, & \text{when } T \geqslant T_c \\ \pm\left[\dfrac{C}{2A}(T_c^2 - T^2)\right]^{1/2}, & \text{when } T \leqslant T_c \end{cases} \tag{2.7}$$

where

$$T_c^2 = \frac{2A}{C}\sigma^2. \tag{2.8}$$

So, when $T \ll T_c$

$$\langle\tilde{R}\rangle = \pm\sigma. \tag{2.9}$$

A spatially homogeneous, flat and isotropic cosmological model of the early universe is given by the Robertson–Walker line-element

$$ds^2 = dt^2 - a^2(t)[(dx)^2 + (dy)^2 + (dz)^2]. \tag{2.10}$$

The geometrical definition of $\tilde{R}$ in the model, given by the line-element (2.10), yields

$$\tilde{R} = 6\eta\left[\frac{\ddot{a}}{a} + \left(\frac{\dot{a}}{a}\right)^2\right], \tag{2.11}$$

where dot denotes derivative with respect to cosmic time t. $\tilde{R}$ given by (2.11), is independent of spatial coordinates, so $R = \langle\tilde{R}\rangle$. Now, the ordinary differential equation, in the state $\langle\tilde{R}\rangle = 0$, is given as

$$\frac{\ddot{a}}{a} + \left(\frac{\dot{a}}{a}\right)^2 = 0 \tag{2.12}$$

which integrates to

$$a^2 = \tilde{\alpha} + \frac{t}{t_{\text{pl}}} \tag{2.13}$$

where $\tilde{\alpha}$ is an integration constant and t_{pl} is the Planck time. Like ref. [9] on taking $V^T(\tilde{R})$ as temperature-dependent Coleman–Weinberg potential, the energy condition is not violated but R^2-terms modify Einstein field equations. For the modified situation, Hawking–Penrose theorem is not applicable. Hence singularity can be avoided. This modification seems at and above the energy scale where R^2 terms in S_g are important.

The expansion, obeying the rule given by (2.13), is adiabatic. Hence, temperature will fall as

$$T = \frac{\text{constant}}{[\tilde{\alpha} + (t/t_{\text{pl}})]^{1/2}}. \tag{2.14}$$

Thus, one finds that temperature falls according to (2.14) in the symmetric state $\langle\tilde{R}\rangle = 0$. As phase transition is expected below Planck scale, the critical temperature T_c will be less than T_{Planck} which is possible at time $t_c > t_{\text{pl}}$, according to rule given by (2.14). When temperature falls very much below T_c i.e. $T \ll T_c$, $\langle \tilde{R} \rangle$ acquires a non-zero constant value σ and spontaneous symmetry breaking takes place at time $t_0 > t_c$.

Again taking the geometrical definition of $\tilde{R}$ given by (2.10), one gets the ordinary differential equation

$$\frac{\ddot{a}}{a} + \left(\frac{\dot{a}}{a}\right)^2 = \frac{\sigma}{6\eta} \tag{2.15}$$

yielding the solution

$$a^2 = a_0^2 \sinh\left[\frac{2}{\eta a_0^2}(t - t_0) + 0{\cdot}89\right] \tag{2.16}$$

where $a_0^2 = (12/\sigma\eta)^{1/2}$. Thus, one finds non-adiabatic expansion in the state $\langle \tilde{R} \rangle = \sigma$. In the case $\langle \tilde{R} \rangle = -\sigma$, the ordinary differential equation will be

$$\frac{\ddot{a}}{a} + \left(\frac{\dot{a}}{a}\right)^2 = -\frac{\sigma}{6\eta} \tag{2.17}$$

yielding the solution

$$a^2 = a_0^2 \sin\left[\frac{2}{\eta a_0^2}(t - t_0) + \frac{\pi}{2}\right] \tag{2.18}$$

which implies that $0 < a(t) \leqslant a_0$ (as discussed above $a(t) \neq 0$ and $a(t)$, being scale factor, cannot be negative or complex number). Thus, the state $\langle \tilde{R} \rangle = -\sigma$ may behave like a small bubble of size $a(t)$ such that $r \leqslant a(t) \leqslant a_0$ (here r is a very small non-zero number). It is interesting to see (from (2.18)) that at $t = t_0$, $a = a_0$. As t increases, $a(t)$ decreases to the smallest non-zero number r at $t = t_0 + (\eta a_0^2 \pi/4)$ and it remains equal to r till $t = t_0 + (3\eta a_0^2 \pi/4)$. When $t > t_0 + (2\eta a_0^2 \pi/4)$, $a(t)$ increases to a_0 at time $t = t_0 + \eta a_0^2 \pi$. This cycle keeps on repeating, so long as R^2-terms are significant in gravitational dynamics. Thus it is interesting to see that the state $\langle \tilde{R} \rangle = -\sigma$ behaves like bumps in the cosmological model of the early universe, given by the state $\langle \tilde{R} \rangle = \sigma$, which expands rapidly with scale factor $a(t)$ obeying (2.16).

Another interesting point (which is important to mention here) is that at $t = t_0$, when $T \ll T_c$, a huge amount of energy will get released with density

$$\begin{aligned} V^T(0) - V^T(\sigma) &= \frac{1}{2}A\sigma^4 - CT^2\sigma^2 \\ &= C\sigma^2\left(\frac{T_c^2}{4} - T^2\right) \simeq \frac{1}{2}A\sigma^4. \end{aligned} \tag{2.19}$$

The gravitational energy so released will be converted into particles and radiation increasing entropy of the universe.

3. $\tilde{R}$ and ϕ interaction and solution of Klein–Gordon equation for ϕ

Manifestation of material aspect of Ricci scalar, at high energy, encourages one to study a theory involving interaction of $\tilde{R}$ and ϕ. The action for such a theory, in curved space-time is given as

$$S = \int d^4x\sqrt{-g}\left[\frac{1}{2}g^{\mu\nu}\partial_\mu\tilde{R}\partial_\nu\tilde{R} - V^T(\tilde{R}) + \frac{1}{2}g^{\mu\nu}\partial_\mu\phi\partial_\nu\phi - \frac{1}{2}(\xi\eta^{-1}\tilde{R} + \lambda\tilde{R}^2)\phi^2\right], \tag{3.1}$$

where $\xi\eta^{-1}\tilde{R}\phi^2 = \xi R\phi^2$ is the non-minimal coupling term of ϕ with gravity alongwith non-minimal coupling constant ξ (which is dimensionless) and $\lambda\tilde{R}^2\phi^2$ is the $\tilde{R}-\phi$ interaction term with dimensionless coupling constant λ. Here, $(\xi\eta^{-1}\tilde{R} + \lambda\tilde{R}^2)\phi^2$ is the mass term which vanishes in the state $\langle\tilde{R}\rangle = 0$ and is equal to $(\pm\xi\eta^{-1}\sigma + \lambda\sigma^2)\phi^2$ in the state $\langle\tilde{R}\rangle = \pm\sigma$. As discussed in the earlier section, the state $\langle\tilde{R}\rangle = -\sigma$ behaves like bumps only in the exponentially expanding cosmological model, so this will not be discussed hereafter.

Imposing the condition

$$\frac{2}{\sqrt{-g}}\frac{\delta S}{\delta\phi} = 0 \tag{3.2}$$

on S, given by (3.1), one gets the Klein–Gordon equation for ϕ as

$$(\Box + \xi\eta^{-1}\tilde{R} + \lambda\tilde{R}^2)\phi = 0 \tag{3.3}$$

in the curved space-time.

For the purpose of second quantization, the general wave solution of Klein–Gordon equation (3.3) can be written, for discrete modes k, as

$$\phi = \sum_k [a'_k f_k(t)\exp(-(ik_a x^a)) + a_k^\dagger f_k^*(t)\exp(+ik_a x^a)] \tag{3.4}$$

Substituting this solution in (3.3), one gets ordinary differential equation for mode k as,

$$\frac{1}{a^3(t)}\frac{d}{dt}\left(a^3(t)\frac{d}{dt}\right)f_k + \left(\frac{k^2}{a^2(t)} + \xi\eta^{-1}\tilde{R} + \lambda\tilde{R}^2\right)f_k = 0 \tag{3.5}$$

in the geometry, given by the line-element (2.10). In the state $\langle\tilde{R}\rangle = \sigma$, $a(t)$ is given by (2.18). So, (3.5) reduces to

$$\ddot{f}_k + \frac{3}{\eta a_0^2}\coth\left[\frac{2}{\eta a_0^2}(t-t_0) + 0{\cdot}89\right]\dot{f}_k + \left[\frac{k^2}{a_0^2\sinh^2\left\{\frac{2}{\eta a_0^2}(t-t_0) + 0{\cdot}89\right\}} + \xi\eta^{-1}\sigma + \lambda\sigma^2\right] f_k = 0. \tag{3.6}$$

Now, defining

$$\tau = \frac{2}{\eta a_0^2}(t-t_0) + 0{\cdot}89 \tag{3.7a}$$

(3.6) is written as

$$\frac{\mathrm{d}^2 f_k}{\mathrm{d}\tau^2} + \frac{3}{2}\coth\xi\frac{\mathrm{d}f_k}{\mathrm{d}\tau} + \left[\left(\frac{3\eta^3}{4\sigma}\right)^{1/2}\frac{k^2}{\sinh^2\tau} + 3\xi + 3\lambda\eta\sigma\right]f_k = 0. \tag{3.7b}$$

On substituting

$$f_k = v_k \sinh^{-3/4}\tau \tag{3.8}$$

in the differential equation (3.7b), one gets the ordinary differential equation

$$\frac{\mathrm{d}^2 v_k}{\mathrm{d}\tau^2} + \left[\left(\frac{3\eta^3}{4\sigma}\right)^{1/2}\frac{k^2}{\sinh^2\tau} + 3\xi + 3\lambda\eta\sigma - \frac{9}{4}\coth^2\tau + \frac{3}{2}\mathrm{cosech}^2\tau\right]v_k = 0. \tag{3.9}$$

With the definition of τ, given by (3.7a), one finds that $e^{-\tau} \leqslant 0{\cdot}41066$ and $e^{\tau} \geqslant 2{\cdot}4351$. So, $\sinh\tau$ and $\coth\tau$ can be approximated as

$$\sinh\tau \approx e^{\tau}/2 \tag{3.10a}$$

and

$$\coth\tau \approx 1 \tag{3.10b}$$

without any harm. As a result, the ordinary differential equation (3.9) can be written in a more convenient form

$$\frac{d^2 v_k}{d\tau^2} + \left[\left\{4\left(\frac{3\eta^3}{4\sigma}\right)^{1/2}k^2 + 3\right\}e^{-2\tau} + 3\xi + 3\lambda\eta\sigma - \frac{9}{16}\right]v_k = 0. \tag{3.11}$$

For large τ (3.11) can be approximated as

$$\frac{\mathrm{d}^2 v_k}{\mathrm{d}\tau^2} + \left(3\xi + 3\lambda\eta\sigma - \frac{9}{4}\right)v_k = 0 \tag{3.12}$$

which yields positive and negative energy solutions $e^{-i\nu\tau}/\sqrt{2\nu}$ and $e^{i\nu\tau}/\sqrt{2\nu}$ respectively, where

$$\nu = \pm[3\xi + \lambda\eta\sigma - 0{\cdot}19)]^{1/2}. \tag{3.13}$$

Equation (3.11) is integrated to

$$v_k = AJ_{i\nu}(Ke^{-\tau}) + BJ_{-i\nu}(Ke^{-\tau}), \tag{3.14a}$$

where

$$K = \pm[(12\eta^3/\sigma)^{1/2}k^2 + 3]^{1/2}, \tag{3.14b}$$

$$A = (2|\nu|)^{-1/2}2^{i\nu}K^{-i\nu}\Gamma(1 + i\nu), \tag{3.14c}$$

$$B = (2|\nu|)^{-1/2}2^{-i\nu}K^{i\nu}\Gamma(1 - i\nu), \tag{3.14d}$$

and $J_l(x)$ is Bessel's function of first kind. In (3.14), A and B have been evaluated using the approximation of Bessel's function for small arguments, given as,

$$J_l(x)x \overset{\simeq}{\rightarrow} 0\frac{(x/2)^l}{\Gamma(1+l)}. \tag{3.15}$$

and

$$AJ_{i\nu}(Ke^{-\tau})\tau \overset{\approx}{\underset{\tau}{\to}} \infty \frac{A(Ke^{-\tau}/2)^{i\nu}}{\Gamma(1+i\nu)} \tag{3.16}$$

which should match with $e^{-i\nu\tau}/\sqrt{2\nu}$. On this kind of matching, one gets A, as given by (3.14c). Similarly, B is also evaluated. But the solution given by (3.14) is not normalized, which is very much important to have a physically reasonable solution with correct dimensions. For the purpose of normalization, the following conditions are used

$$(v_1, v_1) = -(v_2, v_2) = 1 \text{ and } (v_1, v_2) = 0 \tag{3.17}$$

where $v_1 = AJ_{i\nu}(Ke^{-\tau})$ and $v_2 = BJ_{-i\nu}(Ke^{-\tau})$. The orthonormal product of two functions ψ_1 and ψ_2 is defined as

$$(\psi_1, \psi_2) = -i \int_{t=\text{constant}} \mathrm{d}^3 x\, a^3(t)\, [\psi_1(x,t)\partial_t \psi_2^*(x,t) - (\partial_t \psi_1(x,t))\psi_2^*(x,t)].$$

After normalization at $t = t_0$, one gets

$$v_k = a_0^{-3/2}\, V^{-1/2} (3\eta/\sigma)^{1/4} [AJ_{i\nu}(Ke^{-\tau}) + BJ_{-i\nu}(Ke^{-\tau})] \tag{3.18}$$

where V is the volume of 3-dimensional space. Using (3.8) and (3.18), one gets

$$f_k(t) = a_0^{-3/2}\, V^{-1/2} (3\eta/\sigma)^{1/4} \sinh^{-3/4}\tau [AJ_{i\nu}(Ke^{-\tau}) + BJ_{-i\nu}(Ke^{-\tau})], \tag{3.19}$$

where A, B and K are given by (3.14).

4. Production of scalar particles

To study the spectrum of created scalar particles, in-vacuum state ($t \ll t_0$) denoted as $|0\rangle_{\text{in}}$ is defined as

$$a_k^{\text{in}} |0\rangle_{\text{in}} = 0 \text{ and } {}_{\text{in}}\langle 0|0\rangle_{\text{in}} = 1. \tag{4.1}$$

The out-vacuum state ($t \gg t_0$), denoted as $|0\rangle_{\text{out}}$ is defined as

$$a_k^{\text{out}} |0\rangle_{\text{out}} \text{ and } {}_{\text{out}}\langle 0|0\rangle_{\text{out}} = 1. \tag{4.2}$$

The scalar field $\phi(x,t)$ can be expanded in terms of a complete set of orthonormal functions $\phi_k^{\text{in}}(x,t)$ as

$$\phi = \sum_k [a_k^{\text{in}} \phi_k^{\text{in}}(x,t) + a_k^{\text{in}\dagger} \phi_k^{\text{in}*}(x,t)] \tag{4.3}$$

where $\phi_k^{\text{in}}(x,t) = f_k^{\text{in}}(t)\exp(-ik_a x^a)$ with its complex conjugate $\phi_k^{\text{in}*}$ and $a_k^{\text{in}}(a_k^{\text{in}\dagger})$ are annihilation (creation) operators in the in-state $|0\rangle_{\text{in}}$. ϕ can also be expanded, in the second complete set of orthonormal functions $\phi_k^{\text{out}}(x,t)$ as

$$\phi = \sum_k [a_k^{\text{out}} \phi_k^{\text{out}}(x,t) + a_k^{\text{out}\dagger} \phi_k^{\text{out}*}(x,t)] \tag{4.4}$$

where $\phi_k^{\rm out}(x,t) = f_k^{\rm out}(t)\exp(-ik_A x^\alpha)$ with its complex conjugate $\phi_k^{\rm out *}(x,t)$ and $a_k^{\rm out}(a_k^{\rm out\dagger})$ are annihilation (creation) operators in the out-state. Since, both sets are complete, $\phi_k^{\rm out}$ can be expanded in terms of $\phi_k^{\rm in}$ and $\phi_k^{\rm in *}$ as [15]–[17]

$$\phi_k^{\rm out} = \alpha_k \phi_k^{\rm in} + \beta_k \phi_k^{\rm in *}. \tag{4.5}$$

The relations, given by (4.5), are known as Bogoliubov transformations. Here, α_k and β_k are Bogoliubov coefficients, given as

$$\alpha_k = (\phi_k^{\rm out}, \phi_k^{\rm in}) = -i\int_{t=t0} {\rm d}^3 x\, a^3(t)[\phi_k^{\rm out}\partial_0 \phi_k^{\rm in *} - (\partial_0 \phi_k^{\rm out})\phi_k^{\rm in *}] \tag{4.6a}$$

and

$$\beta_k = (\phi_k^{\rm out}, \phi_k^{\rm in *}) = i\int_{t=t0} a^3 x\, a^3(t)[\phi_k^{\rm out}\partial_0 \phi_k^{\rm in} - (\partial_0 \phi_k^{\rm out})\phi_k^{\rm in}]. \tag{4.6b}$$

The Bogoliubov coefficients α_k and β_k obey the condition

$$|\alpha_k|^2 - |\beta_k|^2 = 1. \tag{4.6c}$$

The set of solutions (as $t \ll t_0$) are

$$\phi_k^{\rm in}(x,t) = a_0^{-3/2} A V^{-1/2}\left[-\frac{3\eta}{\sigma}\right]^{1/4} e^{+3\tau/4} J_{i\nu}(Ke^{-\tau}) e^{-ik_a x^a} \tag{4.7a}$$

$$\phi_k^{\rm in *}(x,t) = a_0^{-3/2} B V^{-1/2}\left[-\frac{3\eta}{\sigma}\right]^{1/4} e^{3\tau/4} J_{-i\nu}(Ke^{-\tau}) e^{-ik_a x^a}. \tag{4.7b}$$

The set of solutions (as $t \gg t_0$) are

$$\phi_k^{\rm out}(x,t) = a_0^{-3/2} A V^{-1/2}(3\eta/\sigma)^{1/4} e^{-3\tau/4} J_{i\nu}(Ke^{-\tau}) e^{-ik_a x^a} \tag{4.8a}$$

$$\phi_k^{\rm out *}(x,t) = a_0^{-3/2} B V^{-1/2}(3\eta/\sigma)^{1/4} e^{3\tau/4} J_{-i\nu}(Ke^{-\tau}) e^{ik_a x^a}. \tag{4.8b}$$

Now, for discussion of creation of spinless particles, two cases arise. The first case is possible, when modes k and cosmic time t obey the inequality

$$|k| < \left(\frac{\sigma}{12\eta^3}\right)^{1/4}\left[5{\cdot}93\exp\left\{(t-t_0)\sqrt{\frac{4\sigma}{3\eta}}\right\} - 3\right]. \tag{4.9}$$

In this case, Bessel's function can be approximated, according to (3.15). Now, using (4.7) and (4.8) in (4.6), one can easily compute

$$\alpha_k = -\frac{(3+4i\nu)}{4|\nu|} i^{3/2} \tag{4.10a}$$

and

$$\beta_k = \frac{3i^{3/2}}{4|\nu|} e^{-2i\nu\tau}. \tag{4.10b}$$

Here, it is helpful to elaborate implications of the inequality (4.9). This inequality means that as cosmic time t increases beyond t_0, the approximation of Bessel's function can be valid for higher and higher modes. It implies that if at $t = t_1 > t_0$, $|k| = 0, 1, 2, \ldots |k_1|$, then at $t = t_2 > t_1$, $|k| = 0, 1, 2, \ldots |k_2|$ where $|k_2|| > |k_1|$.

The relative probability of creating a pair of particle-antiparticle in mode k isgiven by

$$\omega_k = |\beta_k/\alpha_k|^2 = \frac{9}{9+16\nu^2}. \tag{4.11}$$

As ω_k, given by (4.11), is independent of k, so it is true for all k satisfying the constraint (4.9). The absolute probability of creation of $0, 1, 2, \ldots$ particle-antiparticle pairs is given by

$$\sum_{n=0}^{\infty} |{}_{\text{out}}\langle 0|n|0\rangle_{\text{in}}|^2 = \sum_{n=0}^{\infty} \prod_k \omega_k^n |\alpha_k|^{-2}. \tag{4.12}$$

Using (4.11), one gets

$$\sum_{n=0}^{\infty} \omega_k^n = \frac{1}{1-\omega_k} = \frac{9+16\nu^2}{16\nu^2}. \tag{4.13}$$

From (4.10a), (4.12) and (4.13)

$$\sum_{n=0}^{\infty} |{}_{\text{out}}\langle 0|\eta|0\rangle_{\text{in}}|^2 = \prod_k \frac{9+16\nu^2}{16\nu^2} \cdot \frac{16\nu^2}{9+16\nu^2} = 1. \tag{4.14}$$

Equation (4.14) implies that the probability of creation of infinitely many pairs of particle–anti-particle in all modes k (satisfying the constraint (4.9)) is 1. Physically, it means that infinitely many pairs of particles will be definitely created by the rapidly expanding geometry given by the line element (2.10) with

$$a(t) = a_0 \sinh^{1/2}\left[\frac{2}{\eta a_0^2}(t - t_0) + 0{\cdot}89\right].$$

The absolute probability that the vacuum remains vacuum i.e., no particle is created in any mode is given by

$$|{}_{\text{out}}\langle 0|0\rangle_{\text{in}}|^2 = \prod_k |\alpha_k|^{-2} = \left(\frac{16\nu^2}{9+16\nu^2}\right)^{1-2|k|} \tag{4.15}$$

which is obtained using (4.10a).

The four-volume is calculated as

$$\begin{aligned} V_4 &= \int_{t_0}^{t} a_0^3 \sinh^{3/2}\tau \mathrm{d}t \int \mathrm{d}^3x \\ &\sim 10{\cdot}72(\eta^{-1}\sigma^{-5})^{1/4}\left[e^{(t-t_0)}\sqrt{\frac{3\sigma}{4\eta}} - 1\right]. \end{aligned} \tag{4.16}$$

The decay rate of the $|0\rangle_{\text{in}}$ state per unit time per unit volume is given as

$$\begin{aligned} \Gamma &= -\frac{1}{V^4} \ln |{}_{\text{out}}\langle 0|0\rangle_{\text{in}}|^2 \\ &= \frac{0{\cdot}093\eta^{1/4}\sigma^{5/4}(1+2|k|)\ln\left(\frac{9+4\nu^2}{4\nu^2}\right)}{\left[\exp\left\{(t-t_0)\sqrt{\frac{3\sigma}{4\eta}}\right\} - 1\right]} \end{aligned} \tag{4.17}$$

which is obtained using the inequality (4.9) and (4.15) and (4.16). Decay of the $|0\rangle_{\text{in}}$ state means creation of particles. So decay rate of the $|0\rangle_{\text{in}}$ state per unit time per unit volume implies creation rate of particle-antiparticle pairs per unit time volume. Equation (4.17) implies that in a particular mode k, satisfying the condition (4.9), creation rate of particle-antiparticle pairs per unit time per unit volume increases till

$$t = t_1 = t_0 + 0{\cdot}797\sqrt{\eta/\sigma}, \tag{4.18}$$

attains maximum and starts decreasing when $t > t_1$. At time t_1, given by (4.19)

$$|k| < 8{\cdot}9436(\sigma/12\eta^3)^{1/4} \tag{4.19}$$

according to inequality (4.9). It shows that particle production is possible in very high modes at $t = t_1$. It is also clear from the inequality (4.9), that as time increases the phenomenon of particle creation can be discussed in higher and higher modes. But, as discussed above, particle creation rate Γ gets suppressed when $t > t_1$ and at $t = t_1$ modes k have upper bound given by the inequality (4.20). When $t > t_1$, it is possible to have k such that $|k| > 8{\cdot}9436(\sigma/12eta^3)^{1/4}$, but particle creation rate will be suppressed.

In the case

$$|k| \gg (\sigma/12\eta^3)^{1/4}\left[5{\cdot}93\exp\left\{(t - t_0)\sqrt{\frac{4\sigma}{3\eta}}\right\} - 6\right] \tag{4.20}$$

using (4.6), (4.7), (4.8) and asymptotic expansion of $J_l(x)$ for large x, as

$$J_l(x) \simeq \left(\frac{\pi x}{2}\right)^{-1/2}\cos\left(x - \frac{\pi}{4} - \frac{l\pi}{2}\right) \tag{4.21}$$

it is found that

$$|\alpha_k|^2 = |\beta_k|^2$$

which does not satisfy the condition (4.6c). It means that particle creation is not possible in extremely high modes.

5. Energy of created spinless particles other than Riccions

The components of energy-momentum of created particles can be defined as [15, 18]

$$\bar{T}^{\mu\nu} = {}_{\text{in}}\langle 0|T^{\mu\nu}|0\rangle_{\text{in}} - {}_{\text{out}}\langle 0|T^{\mu\nu}|0\rangle_{\text{out}}, \tag{5.1a}$$

where

$$T_{\mu\nu} = \partial_\mu\phi^*\partial_\nu\phi - \frac{1}{2}g_{\mu\nu}[\partial^\sigma\phi^*\partial_\sigma\phi - (\xi\eta^{-1}\sigma + \lambda\sigma^2)\phi^*\phi] \tag{5.1b}$$

with

$$\bar{T}^0_0 = {}_{\text{in}}\langle 0|T^0_0|0\rangle_{\text{in}} - {}_{\text{out}}\langle 0|T^0_0|0\rangle_{\text{out}}. \tag{5.1c}$$

In (5.1), divergences are cancelled by taking the difference. The total energy of created particles can be calculated as

$$E = \int d^3x a^3(t)\,\bar{T}^0_0. \tag{5.2}$$

Using (4.7) and (4.8) in (5.1)

$$
{}_{\rm in}\langle 0|\,T^0_0|0\rangle_{\rm in} = \frac{1}{2}\sum_k\Big[\Big(|\alpha_k|^2+|\beta_k|^2\Big)\Big]\Big\{\sqrt{\frac{\sigma}{3\eta}}a_0^{-3}ABV^{-1}\times
$$

$$
\frac{\left(\frac{9}{16}+\nu^2\right)}{\Gamma(1+i\nu)\Gamma(1-i\nu)}e^{-3\tau/2}\exp[ik_a(x^a-x'^a]+
$$

$$
\frac{(\xi\eta^{-1}\sigma+\lambda\sigma^2+k^2)a_0^{-3}ABV^{-1}}{\Gamma(1+i\nu)\Gamma(1-i\nu)}\sqrt{\frac{3\eta}{\sigma}}e^{-3\tau/2}\exp(ik_a(x^a-x'^a)
$$

$$
+\beta_k^*\alpha_k^*a_0^{-3}B^2\,V^{-1}\frac{e^{-3\tau/2}\left(\frac{Ke^{-\tau}}{2}\right)^{-2i\nu}}{(\Gamma(1-i\nu))^2}
$$

$$
\left\{\sqrt{\frac{3\eta}{\sigma}}(\xi\eta^{-1}\sigma+\lambda\sigma^2+k^2)-\sqrt{\frac{\sigma}{3\eta}}\left(\frac{3}{4}-i\nu\right)^2\right\}
$$

$$
\exp(ik_a(x^a+x'^a))
$$

$$
+\alpha_k\beta_k a_0^{-3}A^2\,V^{-1}\frac{e^{-3\tau/2}\left(\frac{Ke^{-\tau}}{2}\right)^{2i\nu}}{(\Gamma(1+i\nu))^2}\exp(-ik_a(x^a+x'^a))\times
$$

$$
\left\{\sqrt{\frac{2\eta}{\sigma}}(\xi\eta^{-1}\sigma+\lambda\sigma^2+k^2)-\sqrt{\frac{\sigma}{3\eta}}\left(\frac{3}{4}+i\nu\right)^2\right\}\Big] \tag{5.3a}
$$

and

$$
{}_{\rm out}\langle 0|\,T^0_0|0\rangle_{\rm out} = \frac{1}{2}\sum_k\frac{AB\exp(ik_a(x^a-x'^a))}{\Gamma(1+i\nu)\Gamma(1-i\nu)}
$$

$$
\left[\sqrt{\frac{\sigma}{3\eta}}\left(\frac{9}{16}+\nu^2\right)+\left(\xi\eta^{-1}\sigma+\lambda\sigma^2+k^2\right)\sqrt{\frac{3\eta}{\sigma}}\right]. \tag{5.3b}
$$

Now

$$
\int \mathrm{d}^3x a_0^3\sinh^{3/2}\tau_{\rm in}\langle 0|\,T^0_0|0\rangle_{\rm in}
$$

$$
\simeq\frac{1}{2}\sqrt{\frac{\sigma}{3\eta}}\left[\frac{(9+16\nu^2)}{|6|\nu|^3}\left(\frac{9}{8}+2\nu^2\right)-\frac{27}{|6|\nu|^3}\sin 4\nu\tau\right.
$$

$$
\left.+\frac{3}{2}\sin 4\nu\tau-\frac{9}{4|\nu|}\cos 4\nu\tau\right] \tag{5.4a}
$$

and

$$
\int \mathrm{d}^3x a_0^3\sinh^{3/2}\tau_{\rm out}\langle 0|\,T^0_0\eta 0\rangle_{\rm out}
$$

$$
\simeq\frac{1}{4|\nu|}\sqrt{\frac{\sigma}{3\eta}}\left(\frac{9}{8}+2\nu^2\right). \tag{5.4b}
$$

Using (5.4) in (5.2)

$$E=\frac{1}{2}\sqrt{\frac{\sigma}{3\eta}}\left[\frac{1}{|6|\nu|^3}(9+8\nu^2)\times\left(\frac{9}{8}+2\nu^2\right)-\frac{27}{|6|\nu|^3}\sin 4\nu\tau+\frac{3}{2}\sin 4\nu\tau-\frac{9}{4|\nu|}\cos 4\nu\tau\right]$$

$$\simeq 3\sigma\sqrt{\lambda}. \tag{5.5}$$

Thus, it is found that an amount of energy equal to E will flow from the $|0\rangle_{\text{in}}$ to $|0\rangle_{\text{out}}$ state produced due to rapidly expanding geometry lying between the two regions, which will contribute to the entropy of the universe.

Acknowledgements

Authors are thankful to Prof. S Odintsov for suggesting to use temperature dependent Coleman–Weinberg like potential for $\tilde{R}$-fields. One of the authors (KPS) is grateful to Council of Scientific and Industrial Research, New Delhi for financial support and the other (SKS) would like to thank the hospitality of the Centre for Theoretical Studies, Indian Institute of Science, Bangalore during the final phase of the work.

References

[1] S W Hawking and R Penrose, *Proc. R. Soc.* (*London*) **A314**, 529 (1970)
[2] R Utiyama and B S DeWitt, *J. Math. Phys.* **3**, 608 (1962)
[3] K S Stelle, *Phys. Rev.* **D16**, 953 (1977)
[4] E S Fradkin and A A Tseylin, *Nucl. Phys.* **B201**, 469 (1982)
[5] I G Avramidy and A O Barvinsky, *Phys. Lett.* **B159**, 269 (1985)
[6] L Parker and D J Toms, *Phys. Rev.* **D29**, 1584 (1984)
[7] I L Buchbinder, S D Odintsov and I L Shapiro, *Effective action in quantum gravity* (IOP Publishing Ltd., 1992)
[8] B Whitt, *Phys. Lett.* **B145**, 176 (1984)
[9] S K Srivastava and K P Sinha, *Phys. Lett.* **B307**, 40 (1993)
[10] S K Srivastava and K P Sinha, *Quantization of Ricci scalar* (submitted)
[11] M B Green, J H Schwarz and E Witten, *Superstring theory* (Cambridge University Press, Cambridge, 1987) vol. 1
[12] J D Barrow and S Cotsakis, *Phys. Lett.* **B214**, 515 (1988); *Phys. Lett.* **B258**, 299 (1991)
[13] R D Tenreiro and M Quiros, *An introduction to cosmology and particle physics* (World Scientific, Singapore, 1988) p. 239
[14] S Coleman and E Weinberg, *Phys. Rev.* **D7**, 883 (1973)
[15] B S DeWitt, *Phys. Rep.* **19**, 295 (1975)
[16] L Parker, *Asymptotic structure of space-time* edited by F P Esposito and L Witten, (Plenum Press, New York 1977)
[17] N D Birrell and P C W Davies, *Quantum fields in curved spaces* (Cambridge University Press, Cambridge, 1982) p. 46
[18] E Mottola, *Phys. Rev.* **D31**, 754 (1985)

[redacted]

PRAMANA
— journal of
physics

© Printed in India

Vol. 44, No. 4,
April 1995
pp. 347–356

Two-loop Majorana neutrino mass and magnetic moment in a gauge model

JYOTI DHAR, UMESH PANDEY and S DEV
Department of Physics, Himachal Pradesh University, Summerhill, Shimla 171 005, India

MS received 2 March 1994; revised 7 July 1994

Abstract. Two-loop contributions to Majorana mass and transition magnetic moment in a gauge model not in conflict with decaying neutrino dark matter (DDM) hypothesis have been studied. Another variant of an earlier model [J Dhar and S Dev, *Pramana – J. Phys.* **39** 541 (1992)] consistent with the DDM hypothesis is proposed and is shown to lead to large enough neutrino magnetic moment and consistent with the phenomenological constraints on neutrino mass.

Keywords. Majorana transition magnetic moment; horizontal symmetry; VVO mechanism; LMA mechanism; BFZ mechanism; decaying dark matter; pseudo Dirac neutrino.

PACS Nos 14·60; 96·60; 97·60

1. Introduction

The neutrino electromagnetic properties were first mooted by Bethe [1]. Cisneros [2] sought to explain the solar neutrino deficit by attributing a sizeable magnetic moment to the electronic neutrino. However, the idea was abandoned after the realization that the neutrino magnetic moment predicted by the theories in vogue at that time was not large enough for this to work in the solar interior. Neutrino magnetic moment hypothesis was again revived in view of the apparent anticorrelation of the solar neutrino flux with the solar magnetic activity suggested by Homestake experiment [3]. Although, Kamiokande [4] and SAGE [5] experiments have not detected any anticorrelation, the statistics is not reliable enough to conclusively rule it out either. However, if further experiments confirm the anticorrelation, magnetic moment solution would be overwhelmingly favoured since no other proposed solution can explain the anticorrelation.

In the minimal standard model, the absence of the right-handed neutrinos in the fermionic spectrum coupled with the conservation of lepton number imply that the neutrino has no mass and no magnetic moment. The addition of one right-handed neutrino for each generation generates a magnetic moment for the neutrino via W-loops. However, since ν_R has no gauge interactions the chirality flip occurs on the external leg and, consequently, the neutrino magnetic moment is proportional to the neutrino mass. In view of the experimental constraint on neutrino mass from triton decay [6]: $m_{\nu_e} < 9{\cdot}5\,\mathrm{eV}$, the resulting magnetic moment is many orders of magnitude smaller than required. In fact, one always encounters a problem with small neutrino mass and a large neutrino magnetic moment when both are loop induced effects [7]. Since both the mass and the magnetic moment operators flip chirality, any mechanism for a large neutrino magnetic moment tends to induce large neutrino mass. The neutrino magnetic moment μ_ν arises only at one-loop level from the diagrams of the generic type (figure 1) with charged fermions l and charged scalars Φ with mass M. Since Majorana neutrinos cannot possess a static magnetic moment, μ_ν is necessarily a transition magnetic moment $\mu_{\nu_e\nu_\mu}$ or $\mu_{\nu_e\nu_\tau}$. More precisely, the transition is of the form $\nu_{eL} \rightarrow (\nu_{\mu L}, \nu_{\tau L})^C$ to account for a change of chirality. Since dipole moments have dimensions $[\text{mass}]^{-1}$ one expects the dipole moments generated by the loop diagram to be of the order eG/M, where G is a combination of dimensionless parameters appearing in the graph such as coupling constants, mixing angles, mass ratios and the loop factors. The photonless counterpart of the same diagram is a higher order correction to the neutrino propagator and represents a contribution to neutrino mass. One expects the mass diagram to involve the same combination G of the dimensionless parameters as in the diagram with an electromagnetic vertex. Thus, one estimated $m_\nu \sim GM$. One expects the neutrino mass m_ν and magnetic moment μ_ν to be related as $em_\nu/M^2 \sim \mu_\nu$ where the scalar mass M is expected to be of the order of vector boson masses or even larger. Therefore, the existing strong constraint on neutrino mass translates into a stringent upper bound on the magnetic moment. If $\mu_\nu \sim 10^{-11}\mu_B$ then the neutrino mass constraint $m_{\nu_e} < 10\,\text{eV}$ implies $M < 1\,\text{GeV}$. Some of the scalars in the graph must be charged and enough is known about charged particles of mass less than 1 GeV and their interactions to rule out the possibility of such a large neutrino magnetic moment arising from that quarter.

Two different scenarios have been invoked to avoid this serious conflict. In the first [8], a symmetry larger than the standard $SU(2) \times U(1)$ group is imposed on such models of large magnetic moment for light neutrinos. As a result, contributions to both the mass and magnetic moment come from pairs of diagrams related by this additional symmetry and the two contributions add for the magnetic moment whereas they cancel in the case of the induced mass. In the second scenario advocated by Georgi and collaborators [9], one can find diagrams which contribute only to the mass but not to the magnetic moment since all the intermediate particles are neutral. The mass contribution from these more exotic diagrams can be arranged to be cancelled by the mass contribution from the usual diagrams. However, this scenario sets too low an intermediate mass scale to be acceptable.

Recently, Barr *et al* (BFZ) [10] have discovered a very elegant mechanism, based on Lorentz symmetry, to suppress the contribution to the mass which at the same time allows a sizeable magnetic moment large enough to explain the solar neutrino deficit and, in particular, the anticorrelation of solar neutrino flux with solar activity. Here, the magnetic transition moment and the transition mass are induced at the two-loop level but the contribution to the transition magnetic moment does not involve a chirality flip in the internal lepton line. Due to spin considerations, the mass contribution has a strong-suppression proportional to the charged lepton mass squared in comparison with the dimensional estimate $m_\nu \sim M^2/e\,\mu_\nu$. It is interesting to note that this kind of scenario is especially useful for decaying dark matter (DDM)

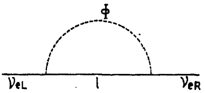

Figure 1. A generic one loop diagram for induced mass in the standard model.

hypothesis [11] where dark matter (DM) could consist of a massive neutrino which decays into hydrogen ionizing photons with a life time 10^{23} s. The DDM hypothesis could solve, besides the DM problem, several ionization problems in astrophysics and cosmology if the heavy neutrino mass lies between 27·8 eV and 29 eV and the residual light neutrino in the decay has a mass less than 3 eV. In the DDM scenario, the magnetic moment interactions are responsible for the decay of the heavy neutrino which, however, generate large neutrino oscillations whenever the induced transition mass and the transition magnetic moment are generated at the same loop level and the necessary chirality flip is realized on the internal fermion line. However, this is precisely the situation in the most viable models for large neutrino magnetic moment proposed so far and this would invalidate the DDM scenario from the viewpoint of particle physics in spite of its tremendous potential in astrophysics and cosmology. Thus DDM hypothesis would especially favour models for large neutrino magnetic moment based on BFZ mechanism. The implementation of this mechanism allows to realize naturally the DDM scenario without dangerous neutrino oscillations since the mixing angle becomes suppressed by a factor $(m_l/M_{\mathrm{loop}})^2$.

In fact, BFZ examined two-loop contributions to neutrino mass and magnetic moment in a Zee-type model containing an additional scalar doublet. However, BFZ realized that the 'spin polarization mechanism' operating in their model is quiet general and could be implemented in a general class of models with or without lepton flavor symmetry. BFZ also emphasized the need to examine the two-loop moments in the original Zee model with just two Higgs doublets. The realization that the two-loop neutrino magnetic moment could be large enough to solve the solar neutrino puzzle actually motivated us to undertake an investigation of two loop contribution to mass and magnetic moment of Majorana neutrinos in a variant of a model proposed recently [12] with an explicit lepton flavor symmetry.

2. Laboratory, astrophysical and cosmological constraints on neutrino magnetic moment

Two different types of magnetic moments are possible for the neutrino: a static Dirac-type moment would transform the neutrino into a sterile right-handed neutrino whereas the Majorana moment would be essentially a transition moment that would connect a left-handed neutrino of one generation to an active right-handed antineutrino of another generation via magnetic moment interactions of the type $\bar{\nu}_c\sigma_{\mu\nu}\nu^c_\mu F^{\mu\nu}$. However, both types of electromagnetic moments are severely constrained by reactor experiments as well as from astrophysics and cosmology. Neutrino magnetic moments of both types would contribute to the scattering of reactor neutrinos on electrons via photon exchange and the resulting amplitude does not interfere with the standard weak amplitude as a result of the difference in the final state helicities so that the consistency with the standard model [13] implies a constraint $\mu_\nu < 4 \times 10^{-10}\mu_B$ which is still large enough for a solution of the solar neutrino puzzle. A large neutrino magnetic moment either or Dirac of Majorana type would lead to plasmon decay $\gamma \to \bar{\nu}\nu$ inside a star which would drastically alter stellar evolution which severely constrains neutrino magnetic moment [14]. This implies a bound $\mu_\nu \leqslant 1{\cdot}3 \times 10^{-10}\mu_B$ from the sun: $\mu_\nu \leqslant 0{\cdot}4 \times 10^{-10}\mu_B$ from white dwarf cooling and a little more stringent bound $\mu_\nu \leqslant 0{\cdot}14 \times 10^{-10}\mu_B$ from red giants. Also Dirac magnetic moments for the neutrinos are severely constrained from big bang nucleosynthesis scenario which puts an upper limit of 3·3 on the number of neutrino species in equilibrium with the plasma during the nucleosynthesis epoch. If the Dirac magnetic moment is larger than $2 \times 10^{-11}\mu_B$, then the right-handed neutrinos would achieve equilibrium via their magnetic moment interactions with electrons which would add another neutrino species in conflict with the nucleosynthesis bound [15]. The observed neutrino pulse from the supernova SN 1987A severely constrains Dirac moment since the magnetic moment interactions of the photon could mediate the reaction $\nu_L e \rightarrow \nu_R e$ in the supernova core and ν_Rs thus produced would escape freely thus draining energy. The magnetic moment interactions themselves could trap the right-handed neutrinos provided $\mu_\nu \geqslant 10^{-9}\mu_B$ which, however, violates the laboratory bound. The requirement that the energy drained by right-handed neutrinos be smaller than the total energy released in the supernova collapse imposes a very stringent bound $\mu_\nu \leqslant 10^{-12}\mu_B$ on the Dirac type moments [16]. One could postulate new interactions for ν_R which would trap ν_Rs inside the supernova core but these very interactions would also keep ν_Rs in equilibrium during nucleosynthesis epoch thus contributing an extra neutrino species and violating the nucleosynthesis bound. This would rule out the relevance of Dirac-type magnetic moment for the solar neutrinos. However, the supernova and the nucleosynthesis bounds do not apply to Majorana transition moment as the right-handed component is active and would not drain energy away. We propose to enlarge this list of already known constraints by including the DDM constraint discussed in detail in § 1.

3. Model building for large neutrino magnetic moment

In the standard model based on the gauge group $SU(3)_C \times SU(2)_L \times U(1)_y$, the fermions are assigned to the following representation of the gauge group:

$$q_L(3,2,1/6) = \begin{bmatrix} u \\ d \end{bmatrix}_L, \quad \begin{bmatrix} c \\ s \end{bmatrix}_L, \quad \begin{bmatrix} t \\ b \end{bmatrix}_L; \quad u_R(3,1,2/3) \text{ etc},$$

$$\psi_L(1,2,-1/2) = \begin{bmatrix} \nu_e \\ e \end{bmatrix}_L, \quad \begin{bmatrix} \nu_\mu \\ \mu \end{bmatrix}_L, \quad \begin{bmatrix} \nu_\tau \\ \tau \end{bmatrix}_L \quad e_R(1,1,-1) \quad \mu_R, \tau_R \text{ etc.}$$

The model assumes the existence of a single doublet of Higgs bosons

$$\Phi(1,2,\tfrac{1}{2}) = \begin{bmatrix} \Phi^+ \\ \Phi^0 \end{bmatrix}.$$

There are no right-handed neutrinos in the minimal standard model and hence Dirac masses for neutrinos are not allowed. In the minimal version, lepton number is an exact global symmetry of the standard model lagrangian and therefore Majorana masses for neutrinos are also forbidden and also the neutrinos cannot have a magnetic moment.

A simple extension of the standard model is obtained if we add right-handed neutrinos into the leptonic sector which will not spoil any of the successes of the standard model. This will lead to non-zero Dirac as well as Majorana masses and the well-known see-saw mechanism [17]. However, it is not essential to introduce right-handed neutrinos into the fermionic spectrum of the standard model to generate non-zero neutrino masses. With a little more cumbersome scalar sector lepton number violation can occur which would lead to Majorana masses for left-handed neutrinos. In fact, the symmetries of the standard model allow the following scalars to couple to the leptons:

$$\Delta(1,3,1), h^{+}(1,1,1); k^{++}(1,1,2)$$

Introducing one or more of these scalar fields leads to different models of neutrino masses [18].

Here we choose to introduce a singly charged scalar field $h^{+}(1,1,1)$ in addition to the usual Higgs doublet following Zee [19]. This leads to trilinear coupling of the type $M_{\alpha\beta}\epsilon_{ij}\Phi^{i}_{\alpha}\Phi^{j}_{\beta}h$ where α,β distinguish between different scalar doublets. The gauge assignments of h allow gauge invariant Yukawa couplings of the type.

$$f_{ab}(\psi^{i}_{aL}C\psi^{j}_{bL})\varepsilon_{ij}h$$

where (a,b) denote the family indices, (i,j) the isospin indices and ε_{ij} the antisymmetric unit symbol. Fermi statistics requires $f_{ab}=-f_{ba}$, here C is the charge conjugation matrix. The couplings $M_{\alpha\beta}\varepsilon_{ij}\Phi^{i}_{\alpha}\Phi^{j}_{\beta}h$ violate lepton number by two units and could generate Majorana masses for the neutrinos. In case $\Phi_{\alpha}=\Phi_{\beta}$, Bose symmetry would force these couplings to be zero. Thus, it is necessary to have at least two scalar doublets in this model. The trilinear scalar couplings would result in a mixing of the h field with the two fields and result in a finite neutrino mass via diagrams of the type shown in figure 2. The same Yukawa couplings also generate neutrino magnetic moment via charged Higgs exchange where the photon can couple to the internal charged lepton or the charged Higgs line. However, the diagram generating the magnetic moment will also generate neutrino mass after the removal of the external photon line so that it is difficult to reconcile a small neutrino mass and a large neutrino magnetic moment when the two are loop induced effects. Of course, neutrino mass being a dimension 3 operator undergoes an infinite renormalization and one can always bring it down to the observed value by adding a mass counter-term whereas the magnetic moment being a dimension 5 operator it is always finite. This, however, does not provide any insight into the lightness of the neutrino. It was pointed out by a number of authors [20] that the Zee model at one-loop level cannot induce a large enough magnetic moment for a naturally light electronic neutrino in spite of an erroneous claim made by Pal [21]. Moreover, the spin precession mechanism in Voloshin *et al* (VVO) [22] or Lim *et al* (LMA) [23] scenarios is not efficient enough in the Zee model because there is nothing to guarantee the requisite high degree of mass degeneracy between the two different Majorana neutrino states.

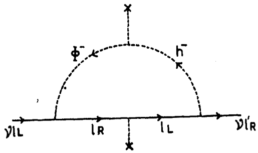

Figure 2. A generic one loop diagram for induced mass in the Zee model.

4. A model with an approximate horizontal symmetry

One possible way to achieve the required suppression of neutrino mass in comparison with the neutrino magnetic moment is to introduce an additional symmetry which forbids neutrino masses but allows electromagnetic dipole moments. Voloshin [24] noted the different transformation properties of mass and magnetic moment operators under a $SU(2)_\nu$ symmetry under which $(\nu\nu^c)$ form a doublet. The antisymmetric combination being a singlet under $SU(2)_\nu$ would be allowed but the symmetric mass terms belonging to a triplet of $SU(2)_\nu$ would be forbidden. As a consequence, Voloshin's symmetry would decouple neutrino mass from its magnetic moment. However, there is no evidence for ν transforming into ν^c in nature. Rather, ν transforms as a doublet of weak isospin $SU(2)_L$ whereas ν_C transforms as a singlet so that Voloshin's $SU(2)_\nu$ does not even commute with the standard model gauge group. Difficulties encountered in the implementation of Voloshin's symmetry in realistic models have been discussed by Barbieri and Mohapatra [25].

In this context, it is important to note that within the framework of the standard model certain parameters are magically small numbers. Electron and muon masses are a case in point. There is no satisfactory theory to explain their small values even though some models are successful in generating small values for them. In the standard model, when the Yukawa couplings associated with electron and muon masses are set to zero, the theory possesses a leptonic chiral $SU(2) \times SU(2)$ symmetry. In this limit, a custodial horizontal symmetry automatically emerges under which neutrino masses are zero but magnetic moments are non-zero. In this class of models, the smallness of neutrino masses relative to the magnetic moments is linked to the smallness of charged lepton masses relative to the gauge boson masses. Thus neutrino mass can be decoupled from its magnetic moment by embedding the standard model gauge group in a larger group. The bigger group is endowed with additional Higgs particles. To each diagram generating neutrino mass, there exists an analogous diagram involving just an additional external photon which contributes to the neutrino magnetic moment. However, each element of the mass and magnetic moment matrices is generated by the two one-loop diagrams. The extended symmetry guarantees that the two diagrams add in the case of the magnetic moment leading to a larger μ_ν/m_ν. One of the first models of this type proposed by Barbieri and Mahapatra [25] is based on the extended symmetry $SU(3)_L \times U(1)$. The scalars belong to a $SU(3)_L$ triplet $(\eta_1^+, \eta_2^+, \eta^o)$. The resulting Dirac neutrinos can have $m_{\nu_e} = 0$ and $\mu_\nu = 10^{-11}\mu_B$ provided $m_{\eta_1} = m_{\eta_2}$ which is possible for a reasonable choice of parameters. However, this can only be ensured by fine tuning after symmetry breaking [26]. Moreover, there is nothing in the model to guarantee the high degree of mass degeneracy required for spin precession mechanism to be effective. Another, model of this class proposed by Babu and Mahapatra [8] is based on the extended gauge group $SU(2)_H \times SU(2)_L \times U(1)_Y$ and contains among others a $SU(2)_H$ scalar doublet (η_1^+, η_2^+) which contributes to both the neutrino mass and magnetic moment yielding a large enough μ_ν/m_ν. This model exhibits advantages and disadvantages similar to the one proposed by Barbieri and Mahapatra [25]. The $SU(2)_H$ in this model is gauged. The model utilizes two additional real triplets for spontaneous symmetry breaking at very high energies thus reintroducing the fine tuning. In addition $SU(2)_H$ in this model has global anomalies since there is an odd number of Weyl doublets.

A $SU(2)_H$ symmetric model with Zee model type scalar spectrum was proposed by Dhar and Dev [12] and 1-loop induced transition magnetic moments and masses for

Majorana neutrinos were studied in this model. The model utilizes the lepton flavour symmetry $SU(2)_H$ acting between the first two leptonic generations which is explicitly broken only by the weak gauge interaction leaving a subgroup $U(1)_N$ of $SU(2)_H$ unbroken to ensure $\Delta m^2_{\nu_e\nu_\mu}$ to be sufficiently small for the spin precession mechanism to be effective in the convective zone of the sun. In this model ν_e and ν^C_μ pair up to form a ZKM [27] type pseudo Dirac neutrino.

In the exact $SU(2)_H$ limit, the leptons and the scalar particles have the following assignments:

$$\psi^{a\in SU(2)_H}_{Li\in SU(2)_L} = \begin{pmatrix} \nu_e & \nu_\mu \\ e & \mu \end{pmatrix}; \quad T = \begin{pmatrix} \nu_\tau \\ \tau \end{pmatrix},$$

$$\psi^a_R = (e, \mu)_R, \quad \tau_R.$$

The scalar sector is enlarged which now comprises of two additional $SU(2)_H$ doublets D and S apart from the standard Higgs which is a singlet under $SU(2)_H$:

$$D^a_i = \begin{pmatrix} d^0_e & d^0_\mu \\ D^-_e & D^-_\mu \end{pmatrix}; \quad S^a_i = (S^-_e \; S^-_\mu); \quad H = \begin{bmatrix} H^+ \\ H^0 \end{bmatrix}.$$

The most general $SU(2)_H$ invariant Higgs potential for the model can be written as

$$\begin{aligned}
\mathscr{L}_{\text{Higgs}} = {} & \lambda_1(H^\dagger H - \vartheta^2)^2 + \lambda_2(\mathrm{Tr}(D^\dagger D))^2 + M^2_D \mathrm{Tr}(DD^\dagger) \\
& + \lambda_3(SS^\dagger)^2 + M^2_S SS^\dagger + \lambda_4(H^\dagger H - \vartheta^2)\mathrm{Tr}(DD^\dagger) \\
& + \lambda_5(H^\dagger H - \vartheta^2)SS^\dagger + \lambda_6 \mathrm{Tr}(DD^\dagger)SS^\dagger + \lambda_7 \mathrm{Tr}(DD^\dagger DD^\dagger) \\
& + \lambda_8 H^\dagger DD^\dagger H + \lambda_9 SD^\dagger DS^\dagger + \lambda_{10}(\vartheta S + H^\dagger i\tau_2 D)(\vartheta S^\dagger - D^\dagger i\tau_2 H^*) \\
& + \mu^2_D \mathrm{Tr}(D\sigma_3 D^\dagger) + \mu^2_S S\sigma_3 S^\dagger + \lambda_{11}[\mathrm{Tr}(D\sigma_3 D^\dagger)]^2 \\
& + \lambda_{12}(S\sigma_3 S^\dagger)^2 + \lambda_{13}(H^\dagger H - \vartheta^2)\mathrm{Tr}(D\sigma_3 D^\dagger) \\
& + \lambda_{14}(H^\dagger H - \vartheta^2)S\sigma_3 S^\dagger + \lambda_{15}\mathrm{Tr}(DD^\dagger)\mathrm{Tr}(D\sigma_3 D^\dagger) \\
& + \lambda_{16}\mathrm{Tr}(DD^\dagger)S\sigma_3 S^\dagger + \lambda_{17}SS^\dagger \mathrm{Tr}(D\sigma_3 D^\dagger) \\
& + \lambda_{18}SS^\dagger S\sigma_3 S^\dagger + \lambda_{19}\mathrm{Tr}(D\sigma_3 D^\dagger)S\sigma_3 D^\dagger \\
& + \lambda_{20}H^\dagger D\sigma_3 D^\dagger H + \lambda_{21}S(1 - i\sigma_3)D^\dagger D(1 + i\sigma_3)S^\dagger \\
& + \lambda_{22}(\vartheta S + H^t i\tau_2 D)\sigma_3(\vartheta S^\dagger - D^\dagger i\tau_2 H^*) \\
& + \delta(H^\dagger D + e^{i\alpha}H^t D^* i\sigma_2)\sigma_3(D^\dagger H - e^{-i\alpha} i\sigma_2 D^t H^*).
\end{aligned}$$

In these terms, the σ_i's are Pauli matrices acting in the $SU(2)_H$ space, while $i\tau_2$ acts in the weak isospin space. δ is a measure of weak isospin symmetry breaking and can be fine tuned to be as small as one desires. The scalar potential contains the following invariant term $SD^\dagger i\tau_2 H^* + H.C$ apart from others. In the exact $SU(2)_H$ limit and broken $SU(2)_{WS} \times U(1)_y$ via $\langle H^0 \rangle = \vartheta$, the fields D and S will mix but (S^-_e, S^-_μ) as well as (D^-_e, D^-_μ) will remain degenerate to give the following physical scalars:

$$\begin{bmatrix} K \\ K' \end{bmatrix} = \begin{pmatrix} \cos\beta & \sin\beta \\ -\sin\beta & \cos\beta \end{pmatrix} \begin{bmatrix} D^a_i \\ S^a_i \end{bmatrix}$$

where β is the mixing angle and the mass eigenstates are K and K'. The charged physical scalars K and K' are mixtures of doublet and singlet under weak isospin.

The most general leptonic Yukawa couplings of the model are

$$= h_1 \operatorname{Tr}(\bar{\psi}_L H \psi_R) + h_2 \bar{T} \mathscr{H} \tau_R + h_3 \bar{T} D i \tau_2 \psi'_R$$
$$+ f S \tau_2 \psi_L^T \tau_2 C^{-1} T + f' \operatorname{Tr}(\bar{\psi}_L D) \tau_R + \text{h.c.}$$

The last two terms are crucial for generating neutrino magnetic moment. Neutrino masses and magnetic moments are generated via the pairs of graphs given in figure 3. Contributions to induced mass and magnetic moment come from pairs of graphs through (S_e, D_e) and (S_μ, D_μ) exchange. In the exact $SU(2)_H$ limit, the masses of the scalar particles circulating inside the loop are the same, so the two graphs contribute equally. But because of the relative minus sign at one of the vertices, their contribution to induced Majorana mass cancels out but attaching a photon line on the internal loop brings in another relative minus sign (because of the difference in the direction of charged flow in the two graphs) so that the contributions of the two graphs add for the magnetic moment. However, the $SU(2)_H$ is only an approximate symmetry of the standard model and is broken explicitly by the difference in the Yukawa couplings of the first two leptonic generations characterized by the parameter

$$\frac{f_\mu - f_e}{2} = \frac{m_\mu - m_e}{2\langle H_0 \rangle} \approx 3 \times 10^{-4}$$

where f_e and f_μ are the leptonic Yukawa couplings of the first two generations. The $SU(2)_H$ breaking manifests itself in a finite mass difference $m_\mu \neq m_e$. Now we choose to break $SU(2)_H$ only in the Yukawa coupling of e and μ with the Higgs doublet (so as to yield a finite mass difference for the electron and the muon while leaving the subgroup $U(1)_N$ intact to ensure conservation of $N\mu - N_e$) and require all other interactions involving new scalars to be $SU(2)_H$ symmetric. This is significantly different from the pattern of horizontal symmetry breaking chosen earlier [12]. One loop contribution to neutrino mass involves only the τ-lepton and the new scalars but not e and μ and hence vanishes. The neutrino mass only arises at the two-loop level from one-loop corrections involving e and μ to new scalar propagators. A typical 2-loop diagram contributing to neutrino mass is given in figure 4. The contribution of the fermionic subloop on the scalar propagator to neutrino mass can be estimated to be of the following order

$$m_\nu^{2\text{-loop}} \sim \frac{f^2}{16} m_\mu^2.$$

The relevant diagrams for magnetic moment are obtained by attaching an external photon line to any of the charged scalars or the internal lepton in figure 4. But the

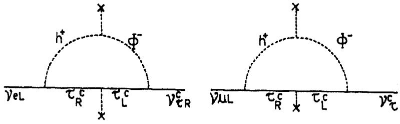

Figure 3. Dominant contribution to one loop induced Majorana neutrino mass in the Zee model.

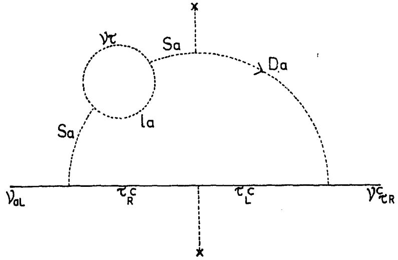

Figure 4. A typical two loop diagram contributing to Majorana neutrino mass.

one-loop contribution to μ_ν estimated in [12] will be the dominant contribution:

$$\mu_\nu \sim \frac{e}{16\pi^2}\frac{f_{e\tau}f_{\mu\tau}}{M^2}m_\tau \ln(M^2/m_\tau^2)$$

One, thus, expects

$$m_\nu \sim \frac{\mu_\nu}{e}\frac{f^2}{16\pi^2}m_\mu^2 \sim 10^{-3}f^2\,\mathrm{eV}$$

yielding a neutrino mass which is experimentally unobservable. New scalar masses could now be as large as 1 TeV. Thus the model parameters are now more flexible than in [12]. The prediction of new scalars with mass of the order of 50 GeV in [12] cannot thus be taken as firm as the lightest charged scalars in this scenario could have masses of the order of 1 TeV while the resulting ZKM pseudo Dirac neutrino could be as light as 10^{-3} eV. Moreover, DDM constraint is naturally satisfied since the mass and magnetic moment are not induced at the same loop level now.

5. Conclusions

Decaying neutrino dark matter hypothesis would solve several ionization problems in cosmology and astrophysics provided the heavy neutrino decays into a light neutrino and hydrogen ionizing photons via magnetic moment interactions. The requisite lifetime of the order of 10^{23} s is obtained with a transition magnetic moment $\mu_{\nu_h\nu_e} \sim 10^{-14}\mu_B$. However, the same magnetic moment interactions would generate dangerously large neutrino oscillations whenever the transition mass and transition magnetic moment are induced at the same loop level and the necessary chirality flip is realized on an internal fermion line. It is noted that this is precisely the situation with the most viable models for large neutrino magnetic moment proposed so far. This would render the DDM scenario rather unattractive from the viewpoint of particle physics in spite of its tremendous success in astrophysics and cosmology. The need to construct gauge models for large neutrino magnetic moment not in conflict with DDM hypothesis has been emphasized. A model for large neutrino magnetic moment consistent with DDM hypothesis has been presented. Two loop contributions to induced Majorana mass and transition magnetic moment have been estimated. The induced neutrino mass in this model only arises at the two loop level from one loop corrections involving the electron and the muon to the new scalar propagators and is too small to be experimentally observable. The one loop induced neutrino magnetic moment, on the other hand, is the dominant contribution in this model and is large enough for the solution of the solar neutrino puzzle. The masses of the new charged scalars are pushed to the TeV range as an additional advantage.

References

[1] H A Bethe, *Proc. Camb. Philos. Soc.* **31**, 108 (1935)
[2] A Cisneros, *Astrophys. Space Sci.* **10**, 87 (1971)
[3] R Davis, *Proc. Workshop on Neutrino telescopes* edited by M Baldo-Ceolin (Palazzo Loredan, Venice, 1990), p. 1
[4] M Mori, *Proc. Workshop on neutrino telescopes* edited by M Baldo-Ceolin (Palazzo Loredan, Venice, 1991) p. 61
[5] V N Gavrin, *Int. Conf. On High Energy Phys.* Singpore (Aug. 1990); *Proc. Workshop on neutrino telescopes* edited by M Baldo-Ceolin (Palazzo Loredan, Venice, 1991) p. 1
[6] T Bowles *et al*, LAMPF preprint LA-89-2010
[7] R Barbieri and G Fiorentini, *Nucl. Phys.* **B304**, 909 (1988)
[8] R Barbieri and R N Mohapatra, *Phys. Lett.* **B218**, 225 (1989)
K S Babu and R N Mohapatra, *Phys. Rev. Lett.* **63**, 228 (1989)
[9] H Georgi and M Luke, Harvard preprint HUTP-90/A0003/90
H Georgi and L Randall, Harvard preprint HUTU-90/A 0 12 4/90
[10] S M Barr, E M Freire and A Zee, *Phys. Rev. Lett.* **65**, 2626 (1990)
[11] D W Sciama, *Nucl. Phys.* (Proc. Suppl) **B19**, 138 (1991) and references therein
[12] Jyoti Dhar and S Dev. *Pramana – J. Phys.* **39**, 541 (1992)
[13] F Reines, H S Gurr and H W Sobel, *Phys. Rev. Lett.* **37**, 315 (1977)
[14] M Fukugita and S Yazaki, *Phys. Rev.* **D36**, 3817 (1987)
G Raffelt, *Phys. Rev. Lett.* **64**, 2856 (1990)
[15] G Raffelt, *Phys. Rcv. Lett.* **64**, 2856 (1990)
K Olive, D Schramm, G Steigman and T P Walker, *Phys. Lett.* **B236**, 454 (1990)
[16] R Barbieri and R N Mohapatra, *Phys. Rev. Lett.* **61**, 21 (1988)
J Lattimer and J Cooperstein, *Phys. Rev. Lett.* **61**, 23 (1988)
D Notzold, *Phys. Rev.* **D38**, 1658 (1988)
I Goldman, G Alexander, Y Aharonov and S Nussinov, *Phys. Rev. Lett.* **60**, 1789 (1988)
[17] M Gell Mann, P Ramond and R Slansky, *in Supergravity* edited by D Z Freedman (North Holland, Amsterdam, 1979)
T Yanagida, *in Proc. of Workshop on unified theory and baryon number in the universe* edited by O Sawada and A Sugamoto (KEK, 1979)
[18] T P Cheng and L F Li, *Phys. Rev.* **D22**, 2860 (1980)
[19] A Zee, *Phys. Lett.* **B93**, 839 (1980); *Phys. Lett.* **B161**, 141 (1985)
[20] J Liu, *Phys. Lett.* **B216**, 367 (1989)
J Pulido, *Phys. Lett.* **B216**, 419 (1989)
J Dhar and S Dev [Submitted to *Phys. Rev.* D.]
[21] B K Pal, *Phys. Rev.* **D44**, 2261 (1991)
[22] M B Voloshin, M I Vysotsky and L B Okun, *Sov. J. Nucl. Phys.* **44**, 440 (1986)
[23] C S Lim and W J Marciano, *Phys. Rev.* **D37**, 1368 (1988)E Akhmedov, *Phys. Lett.* **B213**, 64 (1988)
[24] M B Voloshin, *Sov. J. Nucl. Phys.* **48**, 512 (1988)
[25] R Barbieri and R N Mohapatra, *Phys. Lett.* **B218**, 225 (1988)
[26] J Liu, *Phys. Lett.* **B225**, 148 (1989)
[27] Ya B Zeldovich, *Dokl. Akad. Nauk USSR*, **86**, 505 (1952)
E S Konopinsky and M Mahmoud, *Phys. Rev.* **92**, 1045 (1953)

PRAMANA
— journal of
physics

© Printed in India

Vol. 44, No. 4,
April 1995
pp. 357–374

S-wave baryons in an equally mixed scalar-vector square root potential model of independent quarks

S N JENA and M R BEHERA
Department of Physics, Berhampur University, Berhampur 760 007, India

MS received 18 January 1994; revised 28 November 1994

Abstract. A relativistic model of independent quarks based on Dirac equation with an equally mixed scalar-vector square root confining potential is used to compute the quark core contributions to the static properties like magnetic moments, charge radii and axial vector coupling constant ratios of the baryon octet. The results obtained with appropriate corrections due to centre-of-mass motion agree fairly well with experimental values. The model is also extended to the study of magnetic moments of the quark core of baryons in the charmed and *b*-flavoured sectors and the overall predictions so obtained compare well with other model predictions.

Keywords. Dirac equation; linear potential; baryon octet; magnetic moments; charge radii; axial vector coupling constant; charmed and *b*-flavoured baryons; centre-of-mass correction; Qq mesons.

PACS No. 13·40

1. Introduction

Most of the theoretical and phenomenological models constructed in connection with the study of the heavy mesons of Ψ and Υ-families are based on the assumption of the non-relativistic motion of quarks inside hadrons. The two body interquark force believed to be flavour independent is generally described by the traditional coulomb plus linear potential [1–3] obtained by a simple superposition of both the asymptotic limits. Although one expects QCD to be the theory underlying this description, one cannot as yet derive such a potential completely from first principles. Therefore, various kinds of phenomenological potentials [1] have been suggested in the process, each having its own theoretical or phenomenological motivations and all of them have been found to be more or less successful in describing the mass spectra and decay widths etc. of the heavy mesons. These non-relativistic quark models when extended to ordinary light hadrons have also shown remarkable qualitative success.

However, tackling baryons, unlike mesons, in these non-relativistic quark models, have not been always quite straight forward and simple due to their three body (qqq) bound state character for which they have not been so extensively investigated. Nevertheless, well within the limitations involved in the process, some aspects of the ground and excited states of hadrons have been studied [4–7] in such models with reasonable success. But Stanley and Robson [8] and Bhaduri *et al* [9] have pointed out some drawbacks in non-relativistic quark-model studies of the hadronic hyperfine levels in the usual perturbative approach. They have shown that the conventional coulomb potential as expected from QCD and the resulting spin–spin hyperfine interaction term taken to have the usual contact form proportional to $S_1 \cdot S_2 \delta(r)/$

$m_{q_1} \cdot m_{q_2}$ invalidates the non-relativistic approximation in addition to making inaccurate the perturbation estimates of the mass splittings for lighter hadrons. The required remedy suggested by Bhaduri *et al* [9] is to take an effective potential with a noncoulombic part instead of coulomb one in addition to replacing $\delta(r)$ in the spin–spin hyperfine interaction by some suitable form factor $f(r, r_0)$. With harmonic or linear potential, in place of coulomb one, they have tried various forms of $f(r, r_0)$ in order to validate the use of the non-relativistic approach for study of light hadrons.

However, instead of such hand-waving techniques it would be more justified, in principle, to treat the motion of the quarks inside light hadrons relativistically. Moreover, besides the spectroscopic implications, many physical quantities such as the magnetic moments, the axial vector coupling constants and the electromagnetic form factors in baryonic sector are closely related to the relativistic motion of the quarks.

The relativistic bound states of quarks composing hadrons have been studied by various quark models [10–12]. Still no unique relativistic quark model for all ranges has emerged so far either from the first principle theoretical derivations or from simple phenomenological studies. In the common areas of investigation belonging to mesonic and baryonic sectors the existing data do not seem to prefer uniquely any one of the various potential models available so far in the literature. Only a wider range of more accurate data involving certain aspects, more sensitive to the specific features of the models, may enable one to select out some in preference over the others. The bag model [13–15] with its different versions is essentially the only phenomenological model which has been found very extensive in its applications and reasonably successful in predictions. Yet this model is believed to be neither unique nor totally free from difficulties and objections. Therefore, there have been, in recent past, several attempts to formulate alternative schemes with confining potentials of appropriate Lorentz structures. For example, a scalar potential in linear form was used by Critchfield [16] to confine the relativistic individual quarks in nucleons. Potentials of a different type of Lorentz structure with equally mixed scalar-vector parts in linear [17–19], harmonic [20–23], logarithmic [24–27], as well as non-coulombic power law [28–31] form have also been investigated in this context.

The effective potential of individual quarks in such models which is basically due to the interaction of quarks with the gluon field, may be thought of as being mediated in a self-consistent manner through Nambu-Jona-Lasino (NJL) type models [32–33] by some kind of instanton induced effective quark–quark contact interaction with position dependent coupling strength. The position dependent coupling strength supposed to be determined by the multigluon mechanism cannot be calculated theoretically from first principles, although it is believed to be small at the origin and increases rapidly towards the hadronic surface. Therefore, one needs to introduce the effective potential for individual quarks in a phenomenological manner to seek a posteriori justification in finding its conformity with the supposed qualitative behaviour of the position dependent coupling strength in the contact interaction. With such arguments Tegen-Brockmann and Weise group [34–36] have introduced the phenomenological scalar harmonic and cubic potentials for the study of electromagnetic properties of baryons. All these potential models, used in a limited baryonic sector, only meet with a success more or less identical to the bag model. However, this does not establish the non-uniqueness of bag-like models, unless the potential models of such kind are pursued extensively over a much wider range of mesonic and baryonic phenomena. The present work is only a step in that direction where a phenomenological model with an independent quark square-root potential taken as a combination of a scalar and the fourth component of a vector in equal parts in the form

$$U_q(r) = \tfrac{1}{2}(1 + \gamma^0)(ar^{1/2} + V_0), \quad a > 0, \tag{1}$$

has been used in Dirac equation to study various aspects of the mesonic and baryonic phenomena. This potential is assumed to represent the average non-perturbative multigluon interaction responsible for the confinement of individual constituent quarks.

The important feature of the scalar plus vector potential taken here is that it provides a consistent picture for both mesons and baryons. On the other hand if one takes a pure vector potential it would produce only $q\bar{q}$ bound states where as the choice of a pure scalar potential provides an attractive force for both the $q\bar{q}$ and qq states [37]. Since there are no diquark states, the q–q interaction must be weaker, which can possibly be provided by the repulsive nature of the vector potential. Thus for the confinement of quarks a mixed scalar and vector potential is a more appropriate choice. In fact, the choice of such a potential has been immensely successful in the predictions of the hadronic properties. Additionally, the Lorentz scalar plus vector potential does not have the Klein-paradox. Moreover, if one chooses an effective potential with an equal mixture of scalar and vector parts as taken in (1), then both the scalar and vector parts in equal proportion at every point would render the solvability of Dirac equation for independent quarks by reducing it to the form of Schrödinger-like equation. This has also an additional advantage of generating no spin-orbit splitting, as observed in the experimental baryon spectrum. The implications of such potential forms in the Dirac framework of independent quarks have been discussed by Smith and Tassie [38]. Bell and Ruegg [39] have also shown that the spin-orbit interaction is absent in such a scheme due to exact cancellation of such terms coming from vector and scalar parts of the potential if taken in equal proportion. This is clearly a welcome aspect of the model in case of baryons since the contribution of the spin-orbit interaction term to the baryon mass splittings is already known [40] to be negligible. Eichten and Feinberg [41] provide further support to the above Lorentz structure from a gauge invariant formalism where confinement mechanism is assumed to be purely colour electric in character. Furthermore, such a Lorentz structure of the two body confining potential have been observed [21, 42, 43] phenomenologically in the study of fine hyperfine splittings of heavy meson spectra.

The choice of the effective square root confining potential in the present study is motivated by the fact that qualitatively the confining potential would be strongly weakened by the screening effects due to the quark pair creation above threshold. On the other hand evidences for a confinement potential weaker than the linear one also exist [44, 45] because the linear potential has discrepancies with the experimental data only in the domains where either spin-dependent effects cannot be explained (such as the hyperfine splittings of p-wave heavy quarkonia) or decay processes (such as leptonic decays) where the derivative of confining potential are involved. In fact, the increasing of linear potential with r seems too fast so that the calculated leptonicwidths of higher $c\bar{c}$ and $b\bar{b}$ excited states exceed the experimental data. Olsson and Suchyta III [46] discussed the spin orbit contribution of the confining interaction and found that the confining potential must fall below the linear potential. More recently, the calculation of lattice QCD for baryon spectrum leads to an effective potential [47] $V(r) = Ar^{\varepsilon}$ ($A = 0{\cdot}508$, $\varepsilon = 0{\cdot}671$) which also shows a potential weaker than linear might be more suitable for describing effective quark confinement in hadrons. Therefore, a phenomenological square-root potential of the form $(ar^{1/2} + V_0)$ which is inspired by the fact that it is weaker than the linear potential has been chosen in this work for an unified study of mesons and baryons. In fact, recently a square-root potential of the form $ar^{1/2}$ has been used by Xiatong Song [48] as a Lorentz scalar part along with a Lorentz vector part of the form $br^{-1/2}$ for the study of heavy quarkonium. However in the present work the potential $ar^{1/2}$ has been used with equally mixed scalar and vector parts in the form $\frac{1}{2}(1+\gamma^0)(ar^{1/2} + V_0)$ because of its simplifying feature in converting the single quark Dirac equation into an effective Schrödinger equation for the upper component of the Dirac spinor which can be solved easily.

In the baryonic dimensions, the long range behaviour of the quark–quark interaction which arises out of non-perturbative multi-gluon mechanism including gluon self-couplings, is believed to be dominant enough in comparison to its short-range coulomb like behaviour arising out of one-gluon exchange. In absence of any detailed knowledge about this long-range confining part of the quark–quark interaction from QCD, one usually relies on phenomenological approaches providing confinement of individual constituent quarks through some average potential, to determine the zeroth order quark dynamics inside the baryon core. With this motivation we have introduced here a phenomenological square-root potential with equally mixed scalar-vector Lorentz structure to study the quark-core contributions to the static properties of baryons. The residual interactions like the one arising out of short distance one gluon exchange and also that due to possible quark-pion coupling which are believed to be weak are left out here to be treated in our subsequent work as low order perturbations. It must be pointed out here that in such a perturbative study solvability of the zeroth order equation in a straight forward and simple manner can render sufficient tractability and enough insight into the whole mechanism involved in the process of the investigation. With the present choice of $V(r)$ in non-coulombic square-root form, analytic solutions to the zeroth order equation exists in the WKB limit. On the other hand for exactness, the model predictions of the physical quantities to be investigated in baryon sector can be expressed in closed form in terms of some appropriate expectation values which can be evaluated numerically in a straight forward manner. In the present work we intend to understand the static baryon properties in the framework of a relativistic independent quark-model based on the Dirac equation with the confining square-root potential taken in the form (1). Here we study the quark core contributions to the static properties like magnetic moments μ_B, r.m.s. charge radii $\langle r^2 \rangle_B^{1/2}$ and axial vector coupling constant ratio (g_A/g_V) of octet baryons taking into account the possible centre-of-mass corrections; but for the moment we leave aside the correction due to pion cloud effects on the static baryon properties. This model is also extended to study the magnetic moments of charmed and b-flavoured baryons. Finally, in order to justify the further applicability of the model in the mesonic sector the mass levels of atom-like light quark systems $Q\bar{q}$ have been investigated.

Keeping the Lagrangian mass parameters of the quarks as current quark masses within the limits of broken $SU(3)$ $(m_u = m_d \neq m_s)$, we present in § 2 a brief outline of the potential model and its solution leading to a complete description of the relativistic bound states of the individual confined quarks of the hadron core. Then with the

Dirac wave-function for the ground state in hand, the core contribution to the static properties of the baryon $(1/2)^+$ octet in terms of magnetic moments μ_B, charge radii $\langle r^2\rangle_B^{1/2}$ and axial vector constant ratio (g_A/g_V) for β-decay processes are calculated in the usual manner. We also present here the modified expressions for the static properties due to center-of-mass correction. In § 3, we estimate the potential parameters and the quark masses suitably in order to yield an appropriate ground state energy for the non-strange quarks which gives the average nuclear and Δ (1232) mass approximately, keeping in mind the correction due to center-of-mass motion and the pionic cloud. The static properties of octet baryons calculated after c.m. corrections turn out to be in reasonable agreement with experimental results. The quark core contributions to the magnetic moments of charmed and b-flavoured baryons are also predicted in § 3. Using the same set of parameters we also compute the mass spectra of atom-like $Q\bar{q}$ mesons. Lastly, § 4 is devoted to brief discussion of the results and the conclusions.

2. Basic theory

In this section we briefly outline the framework of the model adopted here to study the quark-core contribution to the static properties of baryons and the corrections due to the centre-of-mass motion.

2.1 *The relativistic potential model*

We start with the assumption that the quarks in a hadron core move independently in an average flavour-independent potential taken in the form

$$U_q(r) = \tfrac{1}{2}(1+\gamma^0)\, V(r) \tag{2.1}$$

where $V(r) = ar^{1/2} + V_0$, with $a > 0$, and the quarks obey the Dirac equation derivable from a Lagrangian density

$$\mathscr{L}_q(x) = \bar{\Psi}_q(x)\left[\frac{i}{2}\gamma^\mu \overleftrightarrow{\partial}_\mu - m_q - U_q(r)\right]\Psi_q(x). \tag{2.2}$$

Hence the Lagrangian mass parameter m_q for the quarks must be regarded as the current quark mass. Then the independent quark wave function $\Psi_q(\mathbf{r})$ satisfies the Dirac equation ($\hbar = c = 1$)

$$[\gamma^0 E_q - \boldsymbol{\gamma}\cdot\mathbf{p} - m_q - U_q(r)]\Psi_q(\mathbf{r}) = 0 \tag{2.3}$$

The solution to the independent-quark wave function $\Psi_q(\mathbf{r})$ can be obtained in the two-component form as

$$\Psi_q(\mathbf{r}) = N_q \begin{pmatrix} ig_q(r)/r \\ \boldsymbol{\sigma}\cdot\hat{r}\, f(r)/r \end{pmatrix} y_{ljm}(\hat{r}) \tag{2.4}$$

where the normalized spin angular part

$$y_{ljm}(\hat{r}) = \sum_{m_l, m_s} \langle l, m_l, \tfrac{1}{2}, m_s | j, m_j\rangle\, Y_l^{m_l}(r)\chi_{1/2}^{m_s} \tag{2.5}$$

and the reduced radial part of the upper component of the Dirac spinor $\Psi_q(\mathbf{r})$ satisfies the equation

$$\frac{d^2 g_q(r)}{dr^2} + \left[\lambda_q(E_q - m_q - V(r)) - \frac{l(l+1)}{r^2}\right] g_q(r) = 0 \tag{2.6}$$

which can be transformed into a convenient dimensionless form

$$\frac{d^2 g_q(\rho)}{d\rho^2} + \left[\varepsilon_q - \rho^{1/2} - \frac{l(l+1)}{\rho^2}\right] g_q(\rho) = 0 \tag{2.7}$$

where $\rho = (r/r_{0q})$ is a dimensionless variable with

$$r_{0q} = [a(E_q + m_q)]^{-2/5} \tag{2.8}$$

and

$$\varepsilon_q = (E_q - m_q - V_0)[(E_q + m_q)/a^4]^{1/5}. \tag{2.9}$$

The solution of basic eigen-value equation either by a standard numerical method or by WKB method [49–50] would yield a positive definite value of $\varepsilon_q = \varepsilon_{nl}$ corresponding to binding energy $E_q = E_{nl}$ for the independent-quarks. Taking

$$(E_{nl} - m_q - V_0) = a x_{nl} \tag{2.10}$$

and

$$2m_q + V_0 = ab \tag{2.11}$$

the eqn. (2.9) can be converted to the form

$$a^2 x_{nl}^5 (x_{nl} + b) = \varepsilon_{nl}^5 \tag{2.12}$$

Then using ε_{nl} values from the solution of (2.7) and b from (2.11) with the known potential parameters V_0, a and m_q, eqn. (2.12) can be solved for a unique positive root x_{nl} which would yield the independent-quark binding energy E_{nl} as

$$E_{nl} = m_q + V_0 + a x_{nl} \tag{2.13}$$

The independent-quark wave-function $\Psi_q(\mathbf{r})$ given by (2.4) and the corresponding binding energy E_{nl} leads to a complete description of the relativistic bound states of the confined constituent quarks inside the hadron core.

Following the usual bag model approach we further assume that all the three quarks in the baryon core are in their ground states with $J^P = \frac{1}{2}^+$ and $J_z = \frac{1}{2}$. Therefore, for baryons the independent-quark wave-function can be written as

$$\Psi_q(\mathbf{r}) = N_q \begin{bmatrix} \Phi_q(\mathbf{r}) \\ \dfrac{\boldsymbol{\sigma}\cdot\mathbf{p}}{\lambda_q} \Phi_q(\mathbf{r}) \end{bmatrix} \quad \chi\uparrow \tag{2.14}$$

where

$$\lambda_q = E_q + m_q$$

and

$$\phi_q(\mathbf{r}) = A_q \frac{g_q(r)}{r} \gamma_0^0(\theta, \phi) \tag{2.15}$$

is the normalised radial angular part of $\Psi_q(\mathbf{r})$ with normalization constant A_q. The overall normalization constant N_q of $\Psi_q(\mathbf{r})$ can be easily obtained as

$$N_q^2 = [1 + (E_q - m_q - V_0 - a\langle r^{1/2}\rangle_q)/\lambda_q]^{-1}. \tag{2.16}$$

The value of $\langle r^{1/2}\rangle_q$ in (2.16) can be easily obtained through WKB method [49, 50] as

$$\langle r^{1/2}\rangle_q = 4(E_q - m_q - V_0)/5a \tag{2.17}$$

with which the expression (2.16) simplifies to

$$N_q^2 = 5(E_q + m_q)/(6E_q + 4m_q - V_0). \tag{2.18}$$

For the ground state, the eqn. (2.12) can be solved for a unique positive root x_{1S} which would yield from (2.13) the individual quark binding energy $E_q = E_{1S}$ for quarks in the baryon.

Now with the ground state wavefunction $\Psi_q(\mathbf{r})$ as given in equation (2.14) it is straight forward to derive the expressions for the quark-core contributions to certain measurable quantities of the S-wave baryons which are obtained simply by appropriately adding the contributions of each individual quark.

2.2 *Static properties of the S-wave baryon core*

(i) *Magnetic moments of baryon core*: The magnetic moment of a $\frac{1}{2}^+$ baryon primarily consists of contributions from its quark-core in terms of the corresponding constituent quark moments which are defined as

$$\mu_q = \frac{1}{2}\int d^3r[\mathbf{r} \times \mathbf{J}(\mathbf{r})]_z, \tag{2.19}$$

where

$$\mathbf{J}(\mathbf{r}) = e_q\bar{\Psi}_q(r)\gamma\Psi_q(\mathbf{r}).$$

Here e_q is the charge of the quark in units of proton charge. Using (2.14) for $\Psi_q(\mathbf{r})$, (2.19) simplifies to

$$\mu_q = (2M_pN_q^2/\lambda_q)e_q\text{n.m}, \tag{2.20}$$

where M_p is the mass of the proton and n.m stands for nuclear magneton. The quark-core contribution to the magnetic moment of a baryon B is given by

$$\mu_B = \text{£}B\uparrow\left|\sum_q \mu_q\sigma_z^q\right|B\uparrow^\circ \tag{2.21}$$

where $|B\uparrow\rangle$ represents the state vectors of the baryons. In the case of octet baryons $|B\uparrow\rangle$ represents the regular $SU(6)$ state vectors. For the charmed and b-flavoured baryons the corresponding state vectors are obtained by the straightforward extensions as given by Singh [51]. The relations for the magnetic moments, ordinary, charmed and b-flavoured baryons in terms of constituent-quark moments are well-known [52–57] and can be used to compute the quark-core contributions to the magnetic moments of baryons with the present model.

(ii) *Mean squared charge radii of the baryon core*: The distribution of electric charge within a baryon core is determined by a convenient parameter called the mean square charge radius $\langle r^2\rangle_B$ which is usually defined as

$$\langle r^2\rangle_B = \sum_q e_q \int \Psi_q^+(\mathbf{r}) r^2 \Psi_q(\mathbf{r}) \mathrm{d}^3 r \tag{2.22}$$

where e_q is the quark electric charge.

Using the expression for $\Psi_q(\mathbf{r})$ from (2.13), eqn. (2.21) can be easily simplified to

$$\langle r^2\rangle_B = \sum_q e_q \frac{N_q^2}{\lambda_q}\left[(2E_q - V_0)\langle\langle r^2\rangle\rangle_q - a\langle\langle r^{5/2}\rangle\rangle_q + \frac{3}{\lambda_q}\right] \tag{2.23}$$

The double angular brackets appearing in (2.23) are the expectation values with respect to $\phi_q(r)$ which can be evaluated numerically or by the WKB method [49, 50] through the general expression

$$\langle\langle r^\alpha\rangle\rangle = 2\alpha(2\alpha+1) r_{0q}^\alpha \varepsilon_q^{2\alpha} \beta(2\alpha, 5/2) \tag{2.24}$$

(iii) *Center-of-mass corrections*: In this model there would be a sizeable spurious contribution to the energy E_q from the motion of the centre-of-mass of the three quark system. Unless this aspect is duly accounted for, the concept of the independent motion of quarks inside the core will not lead to a physical baryon state of definite momentum, since our shell type relativistic quark model is not translationally invariant. The problem appears in the same way in nuclear physics in case of He and also in the MIT bag model [58] and has to be resolved accordingly [59–61].

Here following the technique adopted by Bartelski and Eich [61, 62], the expressions for static core quantities μ_B, $\langle r^2\rangle_B$ and (g_A/g_V) as obtained above can be modified taking the c.m. motion

$$\mu_B' = [3\mu_B + Q_B(M_P/M_B)(1-\delta_B)]/(1+\delta_B+\delta_B^2), \tag{2.25}$$

$$\langle r^2\rangle_B' = \left[.3\langle r^2\rangle_B - 3\sum_q \left\{2e_q\left(\frac{E_q}{E_B}\right) - Q_B\left(\frac{E_q}{E_B}\right)^2\right\}\langle r^2\rangle_q\right]\Big/(2+\delta_B^2) \tag{2.26}$$

and

$$(g_A/g_V)' = 3(g_A/g_V)/(1+2\delta_B), \tag{2.27}$$

where

$$\delta_B = (M_B/E_B) \simeq (1+\delta_B^2)/2, \tag{2.28}$$

$$\delta_B^2 = (M_B^2/E_B^2) = 1 - \langle \mathbf{p}_B^2\rangle/E_B^2. \tag{2.29}$$

Here $E_B = \sum_q E_q$ is the relativistic energy of the quark core and Q_B is the charge of the baryon. The physical mass of the bare baryon core is $M_B = (E_B^2 - \langle \mathbf{P}_B^2\rangle)^{1/2}$ and P_B is the centre of mass momentum and $\langle \mathbf{P}_B^2\rangle$ is evaluated with the usual approximation as

$$\langle \mathbf{P}_B^2\rangle = \sum_q \langle \mathbf{P}^2\rangle_q,$$

where $\langle \mathbf{P}^2\rangle_q$ are the mean-square individual quark momenta with respect to $\Psi_q(r)$. In the present model we find that

$$\begin{aligned}\langle \mathbf{P}^2\rangle_q = N_q^2[&2E_q(E_q - m_q) - (3E_q - m_q - V_0)V_0 \\ &- (3E_q - m_q - 2V_0)a\langle\langle r^{1/2}\rangle\rangle + a^2\langle\langle r\rangle\rangle]\end{aligned} \tag{2.30}$$

The double angular brackets appearing in (2.30) are the expectation values with respect to $\Phi_q(r)$ and the evaluation of $\langle \mathbf{P}^2 \rangle_u$ and $\langle \mathbf{P}^2 \rangle_s$ would lead to a correct estimate of the static properties of the octet baryons.

(iv) *Axial vector coupling constant ratio* (g_A/g_V): Interpreting the weak β-decays of the baryons $B \rightarrow B' + e^- + \bar{\nu}_e$ as quark β-decays like $q_j - u + e^- + \bar{\nu}_e$ occurring inside the baryon core (where q_j could be a d or s quark), one can obtain in lines of bag model calculations [63, 58] the axial vector coupling constant ratio g_A/g_V as

$$(g_A/g_V) = (g_A/g_V)^{\mathrm{NR}}(1 - 2\Delta_{ju}) \tag{2.31}$$

where g_A and g_V are the axial-vector and vector coupling constants for the baryons. $(g_A/g_V)^{\mathrm{NR}}$ is the non-relativistic $SU(6)$ value [64] which for various β-decays can be computed by using $SU(6)$ wave function for $|B\uparrow\rangle$ states [50]. Δ_{ju} is the relativistic correction in the axial coupling for the β-decay of quarks 'j' into the quark 'u' and is given by

$$\Delta_{ju} = \int \psi_u^+ L_z \psi_j \mathrm{d}^3 r \tag{2.32}$$

which on putting the expression for $\psi_q(r)$ from (2.14) for quarks in the $1S_{1/2}$ state becomes

$$\Delta_{ju} = \left(\frac{2N_u N_j}{3\lambda_u \lambda_j} \right) I_{uj} \tag{2.33}$$

with

$$I_{uj} = \int_0^\infty r^2 \mathrm{d}r\, f_u'(r) f_j'(r). \tag{2.34}$$

Integrating by parts and using (2.6) with $\dfrac{g_q(r)}{r} = f_q(r)$, we get

$$I_{uj} = \frac{1}{r_{0j}^2} \int_0^\infty \mathrm{d}r [\varepsilon_q - (r/r_{0j})^{1/2}] g_j(r) g_u(r) \tag{2.35}$$

Here we use for simplicity the WKB solution for $g_q(r)$ [49] to obtain I_{uj}

$$I_{uj} = \frac{36}{231} \frac{\varepsilon_q}{r_{0j}^2} \left(\frac{r_{0j}}{r_{0u}} \right)^{1/2} \quad F\left(\frac{1}{4}, 2, \frac{15}{4}; k^2 \right) \tag{2.36}$$

where $k^2 = \left(\dfrac{r_{0j}}{r_{0u}} \right)^{1/2}$ and $F\left(\dfrac{1}{4}, 2, \dfrac{15}{4}; k^2 \right)$ is the hypergeometric function. Thus g_A/g_V values for various β-decays can be computed using (2.31), (2.33), and (2.36). For neutron beta-decay

$n \rightarrow pe\bar{\nu}$(or $d - u + e + \nu_e^-$) eq. (2.26) reduces to

$$(g_A/g_V)_{n\text{-}pe\bar{\nu}_e} = \frac{5}{3} \left[1 - \frac{4}{3} \frac{N_u^2}{\lambda_u^2} \frac{\varepsilon_q}{r_{0u}^2} (1/5) \right], \tag{2.37}$$

which alternately simplifies to

$$(g_A/g_V)_{n\text{-}pe\bar{\nu}_e} = \frac{5}{9}(4N_u^2 - 1). \tag{2.38}$$

3. Model parameters and results

The computation of the static properties of octet baryons in the present model depends on the choice of the Lagrangian mass parameters (m_u, m_d, m_s) and the potential parameters (a, V_0) which would lead to the individual quark binding energies (E_u, E_d, E_s) and the corresponding quark wave function through the eigen value equations (2.4) to (2.13).

In the Lagrangian formulation adopted here we first of all choose to fix the quark mass parameters

$$(m_u = m_d, m_s) = (5, 210)\,\text{MeV} \tag{3.1a}$$

in the current quark limit. To estimate the potential parameters a and V_0, we prefer to take $N-\Delta$ spin-isospin average mass $\bar{M}_N = 1173\,\text{MeV}$ and the Ω^- mass $M_{\Omega^-} = 1670\,\text{MeV}$ as the guiding inputs to suggest the individual quark binding energies $E_u = E_d \simeq \frac{1}{3}\bar{M}_N$ and $E_s \simeq \frac{1}{3}M_{\Omega^-}$. However keeping in view the possible corrections like those due to centre-of-mass motion and the pion-cloud effect etc to be accounted for in subsequent work, to yield the correct N, Δ and Ω^- masses, we prefer these binding energies to be somewhat greater than the above suggested values and we find that with binding energies as $E_u = E_d = 560\,\text{MeV}$ and $E_s = 700\,\text{MeV}$ and with $\varepsilon_q = 1{\cdot}8418$ which is provided by the numerical solution of the dimensionless eq. (2.7), the eqs (2.9) to (2.12) for the non-strange and the strange quarks separately yield the parameters

$$(a, V_0) = (0{\cdot}2698\,\text{GeV}^{1{\cdot}5}, -0{\cdot}1679\,\text{GeV}) \tag{3.1b}$$

which subsequently generate the contributions of the quark cores to the static baryon properties as

$$(\mu_P, \mu_A) = (2{\cdot}62, -0{\cdot}5956)\text{nm}, \tag{3.2}$$

$$\langle r^2 \rangle_p^{1/2} = 1{\cdot}1255\,\text{fm} \tag{3.3}$$

and

$$(g_A/g_V)_{n\to pe\bar{\nu}} = 1{\cdot}2142 \tag{3.4}$$

These results seem to be quite reasonable in view of the possible c.m motion corrections involved.

With the parameters a, V_0 and m_q along with the corresponding binding energy E_q being known, all the relevant quantities leading to the predictions of the magnetic moments of the octet baryons can be calculated. First of all we obtain the quark wave function normalizations from (2.18) as

$$(N_u^2 = N_d^2, N_s^2) = (0{\cdot}7963, 0{\cdot}8736) \tag{3.5}$$

which in turn yield from eq. (2.20) the constituent quark magnetic moments

$$\mu_u = -2\mu_d = 1{\cdot}7466\,\text{nm} \tag{3.6}$$

and

$$\mu_s = -0{\cdot}5956\,\text{nm}$$

With these values it is straightforward to compute the uncorrected magnetic moments of baryon cores in the nucleon octet using expression (2.21). The results so obtained are presented in table 1.

In the framework of the present model we calculate the expression (2.24) for u and s quark as

$$\begin{aligned} &\langle\langle r^2\rangle\rangle_u = 1{\cdot}1164\,\text{fm}^2, \quad \langle\langle r^2\rangle\rangle_s = 0{\cdot}7632\,\text{fm}^2 \\ &\langle\langle r^{5/2}\rangle\rangle_u = 1{\cdot}2277\,\text{fm}^{5/2}, \quad \langle\langle r^{5/2}\rangle\rangle_s = 0{\cdot}7633\,\text{fm}^{5/2} \end{aligned} \tag{3.7}$$

which lead to the evaluation of r.m.s charge radii $\langle r^2\rangle_B^{1/2}$ for the octet baryons from (2.23). The results thus calculated without c.m correction are given in table 2. Then computing the expression I_{uj} in eq. (2.36) to obtain the values as

$$(I_{uu}, I_{us}) = (0{\cdot}0818, 0{\cdot}1034)\,\text{GeV}^2. \tag{3.8}$$

We can obtain the axial-vector coupling constant g_A for the β-decay processes corresponding to the members of the nucleon octet with appropriate values [64] of $(g_A/g_V)^{\text{NR}}$. The results obtained here without c.m. corrections are presented in table 3.

For introducing centre-of-mass corrections, we estimate the factor δ_B from expressions (2.28) and (2.29), which certainly depends on the flavour combinations of the quark core in baryons. Accordingly we find $\delta_B = 0{\cdot}9449$, $0{\cdot}9475$ and $0{\cdot}9499$ respectively for the baryon cores with three nonstrange quarks, two nonstrange

Table 1. Magnetic moments of the nucleon octet calculated by the present model with and without c.m correction as compared with the results of cloudy-bag-model (CBM) and the experimental data (all numbers in nuclear magnetons).

	Present calculation			
Baryon	Uncorrected	After cm correction	CBM calculation [13, 71]	Experimental (Particle data group [69])
p	2·6200	2·7809	2·60	2·7928444 ± 0·0000011
n	− 1·7466	− 1·8463	− 2·01	− 1·91304308 ± 0·00000054
Λ^0	− 0·5956	− 0·6280	− 0·58	− 0·613 ± 0·004
Σ^+	2·5274	2·6747	2·34	2·379 ± 0·020
Σ^0	0·7807	0·8232	—	0·61 ± 0·08*
Σ^-	− 0·9658	− 1·0282	− 1·08	− 1·14 ± 0·05
Ξ^0	− 1·3764	− 1·4476	− 1·27	− 1·250 ± 0·014
Ξ^-	− 0·5031	− 0·5379	− 0·51	− 0·69 ± 0·04
(Λ, Σ^0)	− 1·5126	− 1·5990	—	− 1·82 + 0·18** − 0·25

*Values computed according to the definition $\mu_0 = \frac{1}{2}(\mu_{\Sigma^+} + \mu_{\Sigma^-})_{\text{exp}}$ which is quite often referred to as the measured value.

**Dydak *et al* [70].

Table 2. $\langle r^2\rangle_B^{1/2}$ rms charge radii of octet baryons calculated in the present model with and without cm corrections as compared to the experiment and Ferreira–Helayel–Zagury (FHZ) model values (all numbers in fm).

Baryon	$\langle r^2\rangle_B^{1/2}$ uncorrected	$\langle r^2\rangle_B^{1/2}$ with cm correction	Experiment	FHZ model [21]
p	1·1255	0·9632	$0{\cdot}87 \pm 0{\cdot}02$	0·932
n	0	0	$-0{\cdot}341$	0
Λ^0	0·3828	0·3421		0·346
Σ^+	1·1889	1·0260		0·994
Σ^0	0·3828	0·3421		0·346
Σ^-	1·0584	0·9048		0·86
Ξ^0	0·5414	0·4884		0·48
Ξ^-	0·9867	0·9097		0·79

Table 3. Axial vector coupling constant ratio (g_A/g_V) calculated in the present model with and without cm correction as compared to the experiment.

Decay mode	Axial vector coupling constant ratio		(g_A/g_V) Experiment Ref. [69] (Particle data group [69])
	Uncorrected (g_A/g_V)	With cm corrected (g_A/g_V)	
$n \to pe\bar{\nu}$	1·2142	1·2604	$1{\cdot}254 \pm 0{\cdot}006$
$\Lambda \to pe\bar{\nu}$	0·7766	0·8048	$0{\cdot}694 \pm 0{\cdot}025$
$\Sigma^- \to ne\bar{\nu}$	$-0{\cdot}2588$	$-0{\cdot}2682$	$-0{\cdot}362 \pm 0{\cdot}043$
$\Xi^- \to \Lambda e\bar{\nu}$	0·1725	0·1785	$0{\cdot}25 \pm 0{\cdot}05$
$\Xi^- \to \Sigma^0 e\bar{\nu}$	1·2944	1·3391	—
$\Xi^0 \to \Sigma^+ e\bar{\nu}$	1·2944	1·3391	—

quarks with one strange quark and one nonstrange quark with two strange quarks respectively. Then it is straightforward to obtain the corrected values of the magnetic moments, the proton rms charge radius and vector coupling constant from expressions (2.25), (2.26) and (2.27). These quantities so obtained after the centre-of-mass corrections, are presented in the appropriate tables (1, 2 and 3) in comparison with the corresponding uncorrected values as well as the experimental ones.

Now with the assumed flavour-independence of the potential we use the same set of potential parameters a and V_0 as obtained in (3.1) along with the quark masses

$$(m_c, m_b) = (1.449, 4{\cdot}764)\,\mathrm{GeV} \tag{3.9}$$

taken-well within the limits of current algebra predictions, to obtain the energy eigen values from (2.13) as

$$(E_c, E_b) = (1{\cdot}7917, 5{\cdot}0056)\,\mathrm{GeV} \tag{3.10}$$

Now with the help of these parameters we obtain from (2.18) the quark-wave function normalizations

$$(N_c^2, N_b^2) = (0{\cdot}9694, 0{\cdot}9916) \tag{3.11}$$

which are then used in (2.20) to compute the constituent quark magnetic moments as

$$(\mu_c, \mu_b) = (0{\cdot}3713, -0{\cdot}0630)\,\text{n.m} \tag{3.12}$$

The magnetic moments of the baryons in charmed and b-flavoured sectors are calculated in a straightforward way by using the constituent quark magnetic moments obtained in (3.6) and (3.12). Since no experimental data are available for the magnetic moments of charmed and b-flavoured baryons we do not incorporate the c.m corrections in these cases and the uncorrected results are displayed in tables 4 and 5 in comparison with the predictions of some other models [53, 65, 66]. The symbols used in these tables are according to Pandita *et al* [53].

To test the further applicability of the present model in understanding the atom-like $Q\bar{q}$ systems we calculate the mass spectra for $D(c\bar{u})$, $F(c\bar{s})$, $B(b\bar{u})$ and $G(b\bar{s})$ mesons. Using same set of parameters as chosen in (3.1b) and the quark masses given in (3.1a) and (3.9), we obtain the ground state mass values for $D(c\bar{u})$, $F(c\bar{s})$ and $B(b\bar{u})$ mesons from (3.13) as

$$\begin{aligned} M_{1S}(c\bar{u}) &= 2{\cdot}010(2{\cdot}01 \pm 0{\cdot}0007)\,\text{GeV} \\ M_{1S}(c\bar{s}) &= 2{\cdot}1493(2{\cdot}14 \pm 0{\cdot}06)\,\text{GeV} \\ M_{1S}(b\bar{u}) &= 5{\cdot}325(5{\cdot}325)\,\text{GeV} \end{aligned} \tag{3.13}$$

Table 4. Magnetic moment of charmed baryons computed in the present model as compared to the values obtained in the bag model and de Rujula–Georgi–Glashow (DGG) model (all numbers in nuclear magneton).

Symbol	Quark content	Present calculation	Bag model [65, 66]	DGG model [53]
Σ_c^{++}	*cuu*	2·2051	1·955	2·36
Σ_c^{+}	*cud*	0·4584	0·363	0·43
Σ_c^{0}	*cdd*	− 1·2882	− 1·23	− 1·43
Ω_c^{0}	*css*	− 0·9180	− 0·98	− 0·89
Ξ_c^{+}	*csu*	0·6435	0·475	0·73
Ξ_c^{0}	*csd*	− 1·1031	− 1·09	− 1·16
Ξ_{cc}^{++}	*ccu*	− 0·0871	− 0·167	− 0·12
Ξ_{cc}^{+}	*ccd*	0·7862	0·865	0·82
Ω_{cc}^{+}	*ccs*	0·6936	0·838	0·69
Λ_c^{+}	*c*(*ud*)*a*	0·3713	0·503	0·37
$\Xi_c'^{+}$	*c*(*us*)*a*	0·3713	0·503	0·37
$\Xi_c'^{0}$	*c*(*ds*)*a*	0·3713	0·503	0·37

Table 5. Magnetic moments of *b*-flavoured baryons computed in the present model as compared to the values obtained in the bag model and DGG model (all numbers in nuclear magneton).

Symbol	Quark content	Present calculation	Bag model [65, 66]	DGG model [53]
Σ_b^+	*buu*	2·3498	2·318	2·5
Σ_b^0	*bud*	0·6032	0·587	0·61
Σ_b^-	*bdd*	− 1·1434	− 1·117	− 1·28
Ω_b^-	*bss*	− 0·7732	− 0·838	− 0·55
Ξ_{cb}^0	*bcd*	− 0·3136	− 0·39	− 0·38
Ξ_{cb}^+	*bcu*	1·4329	2·04	1·5
Ω_{ccb}^+	*bcc*	0·5161	0·894	0·51
Ξ_{bb}^0	*bbu*	− 0·6662	− 0·614	− 0·7
Ξ_{bb}^-	*bbd*	0·2071	0·14	0·23
Ω_{bb}^-	*bbs*	0·1145	0·084	0·105
Ω_{cbb}^0	*bbc*	0·2077	− 0·31	− 0·21
Ξ_b^0	*bsu*	0·7883	0·73	0·87
Ξ_b^-	*bsd*	− 0·9583	− 0·977	− 1·05
Ω_{cb}^0	*bcs*	− 0·1285	− 0·223	− 0·11

which closely agree with the experimental values given in the parentheses. For this calculation we use the numerically calculated eigen values $\varepsilon_q = \varepsilon_{nl}$ corresponding to different bound states of these mesons. The results thus calculated from (3.13) for the mass spectra of $D(c\bar{u})$, $F(c\bar{s})$, $B(b\bar{u})$, $G(b\bar{s})$ mesons are displayed in table 6. All these predictions of our model may hopefully be tested in future experiments of CERN and Fermilab.

4. Discussion and conclusion

We observe that our results for the magnetic moments, rms charge radii and axial vector coupling constant ratios compare reasonably well with the existing experimental data. However, the proton charge radius $\langle r^2\rangle_p^{1/2}$ which was 1·1255 fm before the centre-of-mass correction, becomes 0·9632 fm, as against the experimental value of 0·87 ± 0·02 fm. Furthermore we find $\langle r^2\rangle_n^{1/2} = 0$ contrary to the experimental value of − 0·341 fm. This is of course the case with most of the models of this kind including the bag model. In the absence of experimental data of $\langle r^2\rangle_B^{1/2}$ for other members of the octet baryons we compare our results with those obtained by Ferreira *et al* [21].

The minor discrepancies of our results are common to most of the phenomenological models and can be partly accounted for by the suitable pionic corrections, as investigated in the cloudy bag model. However, these results might be improved by incorporating chiral symmetry so as to bring in the pionic effects which is being taken in our subsequent work. Nevertheless, in view of testing the applicability of the model in these areas of study, the present model has been found to be meaningful with its simple and straightforward approach yielding qualitatively encouraging and reasonable results.

Table 6. Mass spectrum for the atom-like mesons of $D(c\bar{u})$, $B(b\bar{u})$, $F(c\bar{s})$ and $G(b\bar{s})$ families calculated in the present model as compared with the experimental data.

n	l	ε_{nl}	$M_{nl}(D)$ GeV	Experimental value	$M_{nl}(B)$ GeV	Experimental value	$M_{nl}(F)$ GeV	Experimental value	$M_{nl}(G)$ GeV	Experimental value
1	*S*	1·8418	2·010	2·010 ± 0·007	5·325	5·325	2·1493	2·140 ± 0·60	5·4643	—
2	*S*	3·5686	2·2311		5·5461		2·3700		5·6850	
3	*S*	3·0743	2·3789		5·6939		2·5176		5·8326	
4	*S*	3·4726	2·4925		5·8075		2·6310		5·9460	
1	*P*	2·3069	2·1527		5·4677		2·2918		5·6068	
2	*P*	2·8691	2·3195		5·6345		2·4582		5·7732	
1	*D*	2·6629	2·2590		5·5740		2·3979		5·7129	
2	*D*	3·1336	2·3960		5·7110		2·5346		5·8496	

In our present investigation, we have not looked into the baryon mass spectrum which could strictly require taking into account the corrections due to (i) energy associated with centre-of-mass motion (ii) color-electric and magnetic energy arising out of the residual one gluon exchange interaction at short distance and (iii) the pionic self energy of the baryons arising out of the baryon-pion couplig at the vertex. The masses of baryons would therefore have contributions from the baryon core corrected by these contributions. Investigations along this line in similar schemes with different confinement potentials have been done [17–31, 67, 68] with success. Therefore, we believe that for the present model similar analysis can be done which would be taken up in our subsequent work. The present model can also be extended to study the phenomena like hyperfine splitting of P-wave quarkonia and the leptonic decays of mesons which would directly depend on the square-root nature of the confining potential, the investigations in this line which would certainly give new insight about the nature of a confining potential are being taken up with the present model and will be reported shortly in a separate communication.

In this work we find that a simple independent-quark model based on the Dirac equation with an equally mixed scalar-vector square-root confining potential of the form given by (1.1) provides an excellent fit to the static properties of baryon octet and mass spectra of $Q\bar{q}$ mesons in a flavour-indpendent manner. In view of the simplicity of the model in treating baryons and mesons in the same footing the results obtained are quite encouraging. This effective individual quark potential, phenomenologically representing the confining interaction due to a non-perturbative multigluon mechanism seems as an alternative scheme to the CBM in studying baryons and mesons. We find that our potential unlike the QCD based one is non-singular at the origin and it doe not possess the short distance coulombic part of the potential as given by QCD (i.e. r^{-1} or $r^{-1}|\ln(r/r_0)|)^{-1}$. Therefore, even if the non-singular behaviour of this potential does not conform to the expectations of QCD, we can successfully describe the static baryon properties as well as the mass spectra of the light $Q\bar{q}$ mesons in a flavour independent manner.

The purpose of this work is not so much as to claim that nature prefers such a square-root confinement scheme over other schemes advanced earlier in this correction but to present an analysis that complements studies based upon various potential models. Such studies with various quark models when extended to describe the hadronic properties in a much wider sector may provide an opportunity to resolve the question regarding the true nature of quark confinement which is not straightforward to conclude on purely theoretical grounds based on QCD.

Acknowledgement

The authors are thankful to Dr N Barik, Utkal University, India for his valuable suggestions.

References

[1] E Eichten, K Gottfried, T Kinoshita, K D Lane and T M Yan, *Phys. Rev.* **D21**, 203 (1980); **D11**, 3090 (1978)
[2] T Appelquist, R M Barnett and K D Lane, *Ann. Rev. Nucl. Sci. Part* **28**, 387 (1978)
[3] J D Jackson, C Quigg and J L Rosner, *Proc. of the Int. Conf. on high energy physics*, Tokyo (1978) p 391

[4] N See Isgur, Editions Frontiers France 'New Flavours and Hadron Spectroscopy' *Proc. XVI, Recontre de Moriond*, edited by J Tran Thanh Van (1981)
[5] J M Richard and P Taxil, *Ann. Phys.* (*NY*) **150**, 267 (1983); *Phys. Lett.* **B123**, 4531 (1983)
[6] N Isgur and G Karl, *Phys. Rev.* **D18**, 4187 (1978); **D20**, 1191 (1979)
[7] Y Nogami and N Ohtsuka, *Phys. Rev.* **26**, 261 (1982)
[8] D P Stanley and R Robson, *Phys. Rev.* **D21**, 3180 (1980)
[9] R K Bhaduri, L E Cohler and Y Nogami *Phys. Rev. Lett.* **44**, 1369 (1980)
[10] A N Mitra, *Phys. Lett.* **B89**, 54 (1979)
[11] M Bando, T Kugo and S Tanaka, *Prog. Theor. Phys.* **53**, 544 (1975)
[12] H Bando and M Bando, *Phys. Lett.* **B100**, 228 (1981)
[13] A W Thomas, S Theberge and G A Miller, *Phys. Rev.* **D24**, 216 (1981)
[14] A W Thomas, *Adv. Nucl. Phys.* **13**, 1 (1983)
[15] G A Miller, *Int. Rev. Nucl. Phys.* edited by W Weiss (Singapore, World Scientific, 1984) Vol 1
[16] C L Critchfield, *Phys. Rev.* **D12**, 923 (1975)
[17] P Leal Ferreira, *Lett. Nuovo Cimento* **20**, 157 (1977)
[18] S N Jena and S Panda, *Pramana – J. Phys.* **35**, 21 (1990)
[19] S N Jena and S Panda, *Int. J. Mod. Phys.* **A7**, 2841 (1992a); *J. Phys.* **G18**, 273 (1992b)
[20] P L Ferreira, and N Zagury, *Lett. Nuovo Cimento* **20**, 511 (1977)
[21] P L Ferreira, J A Halayal and N Zagury, *Nuovo Cimento* **A55**, 215 (1980)
[22] N Barik, B K Dash and M Das, *Phys. Rev.* **D31**, 1952 (1985); **D31**, 1652 (1985a), **D32**, 1725 (1985b)
[23] N Barik and B K Dash, *Phys. Rev.* **D33**, 1925 (1986)
[24] E Magyari, *Phys. Lett.* **B95**, 295 (1980)
[25] C Quigg and J L Rosner, *Phys. Lett.* **B71**, 153 (1977)
[26] S N Jena and D P Rath, *Pramana – J. Phys.* **27**, 775 (1986b)
[27] N Barik, S N Jena and D P Rath, *Phys. Rev.* **D41**, 1568 (1990); *Int. J. Mod. Phys.* **47**, 6813 (1992)
[28] A Martin, *Phys. Lett.* **B93**, 338 (1980)
[29] N Barik and S N Jena, *Phys. Lett.* **B97**, 761 (1980b); **B97**, 265 (1980a)
[30] N Barik and S N Jena, *Phys. Rev.* **D26**, 618 (1982)
[31] N Barik and M Das, *Phys. Lett.* **B120**, 403 (1983a); *Phys. Rev.* **D28**, 2823 (1983b); **D33**, 176 (1986a); *Pramana – J. Phys.* **D27**, 783 (1986b)
[32] Y Nambu and G Jona Lasino, *Phys. Rev.* **112**, 345 (1961); **124**, 246 (1961)
[33] R Brockmann, W Weise and E Werner, *Phys. Lett.* **B122**, 201 (1983)
[34] R Tegen, R Brockmann and W Weise, *Z. Phys.* **A307**, 339 (1982)[35] R Tegen, M Schedle and W Weise, *Phys. Lett.* **B125**, 9 (1983)
[36] R Tegen and W Weise, *Z. Phys.* **A314**, 357 (1985)
[37] P C Vinod Kumar, K B Vijaya Kumar and S B Khadkikar, *Pramana – J. Phys.* **39**, 47 (1992)
[38] G B Smith and J J Tassie, *Ann. Phys.* **65**, 352 (1971)
[39] J S Bell and H Ruegg, *Nucl. Phys.* **B98**, 151 (1975); **B104**, 546 (1976)
[40] Feynmann *et al*, *Phys. Rev.* **D3**, 2706 (1971)
[41] E Eichten and E L Feinberg, *Phys. Rev. Lett.* **43**, 1205 (1979)
[42] N Barik and S N Jena, *Phys. Lett.* **B97**, 265; **101**, 282 (1981)
[43] D Beavis, B R Desai and P Kaus, *Phys. Rev.* **D20**, 2345 (1979)
[44] B Bambah, K Dharamvir, R Kaur and A Sharma, *Phys. Rev.* **D45**, 1769 (1992)
[45] R Kaur and B Bambah, *Phys. Rev.* **D47**, 5079 (1993)
[46] M G Ollsson and C J Suchyta III, *Phys. Rev.* **D36**, 1459 (1987)
[47] H B Thacker, E Eichen and J G Sexton, *Fermilab Conf.* 87/204–4
[48] Xiaotong Song, ICTP Preprint, IC/88/223 (1988)
[49] C Quigg and J L Rosner, *Phys. Rev.* **C56**, 167 (1979)
[50] C Quigg, *Fermilab Conf.* Report No 81/78-TH (1981)
[51] L P Singh, *Phys. Rev.* **D16**, 158 (1977)
[52] L P Singh, *Phys. Rev.* **D19**, 2812 (1979)

[53] P N Pandita *et al*, *Acta Phys. Austriaca* **53**, 211 (1981)
[54] A L Choudhury and V Joshi, *Phys. Rev.* **D13**, 3115 (1976)
[55] D L Lichtenberg, *Phys. Rev.* **D15**, 345 (1977)
[56] R J Johnson and M Shah Jahan, *Phys. Rev.* **D15**, 1400 (1977)
[57] J Franklin, *Phys. Rev.* **172**, 1807 (1968)
[58] J F Donoghus and K Johnson, *Phys. Rev.* **D21**, 1975 (1980)
[59] D L Hill and J A Wheeler, *Phys. Rev.* **89**, 1102 (1953)
[60] C W Wong, *Phys. Rev.* **C15**, 283 (1975)
[61] J A Bartelski, A Szymacha, L Mankcewicz and S Tatur, *Phys. Rev.* **D29**, 1035 (1984)
[62] E Eich, D Rein and R Rodenberg, PITHA Report No 83/21 (1983)
[63] A Chodes, R L Jaffe, K John, C B Thorn, V F Weiss Koff, *Phys. Rev.* **D9**, 3479 (1974a)
A Chodes, R L Jaffe, K Johnson and C B Thorn, *Phys. Rev.* **D10**, 2599 (1974b)
[64] J J J Kokkedee, *The quark model* (New York, Benjamin) p. 53 (1969)
[65] S K Bose and L P Singh, *Phys. Rev.* **D22**, 773 (1980)
[66] E Eich, D Rein and R Rodenberg, *Z Phys.* **C28**, 225 (1985)
[67] A P Kobuskin, Report No 11 p-58E, Kiev (1976)
[68] S N Jena and D P Rath, *Phys. Rev.* **D34**, 196 (1986a)
[69] Particle Data Group, *Phys. Lett.* **1708**, 11 (1986)
[70] F Dydak *et al*, *Nucl. Phys.* **B118**, 1 (1977)
[71] S Theberge and A W Thomas, *Phys. Rev.* **D25**, 284 (1982)

PRAMANA
— journal of
physics

© Printed in India

Vol. 44, No. 4,
April 1995
pp. 375–391

Shape transitions in even Mo and Sm isotopes: Study in a new microscopic interacting boson model scheme

SUBRATA SARANGI and JITENDRA C PARIKH
Physical Research Laboratory, Navrangpura, Ahmedabad 380 009, India

MS received 21 February 1995

Abstract. A simple dynamic procedure, based on the deformed Hartree-Fock solution of a nucleus, is presented to construct the IBM operators in microscopic basis. The parameters of these operators are evaluated by establishing a Marumori mapping from the truncated shell model space onto the boson space. The transitions from spherical to axial-rotor shape observed in the low-lying levels of *even* $^{96-108}$Mo and $^{146-154}$Sm isotopes are reproduced qualitatively by applying this procedure with a fixed set of fermion input parameters to each chain. Variation of a few parameters in fermion space leads to quantitative agreement.

Keywords. Shape transitions; Mo and Sm isotopes; interacting boson model.

PACS Nos 21·60; 27·60

1. Introduction

The phenomenological interacting boson model (IBM) [1] has provided a unifying symmetry based scheme to study the low-energy collective behaviour of even-even medium and heavy mass nuclei and has been able to explain the observed collectivity very well [2, 3]. This success has quite naturally stimulated a great deal of endeavour to unravel the microscopic foundations of the model [4, 5]. Such calculations have been referred to as microscopic basis IBM calculations. It ought to be stressed that there is as yet no consensus among the scientists about the correct way to establish this connection. In this paper, we propose a different method and illustrate it with calculations of Mo and Sm isotopes.

In microscopic basis IBM calculations the construction of IBM operators is achieved in two stages: (i) An appropriate truncation of the large shell model space into a smaller space physically relevant to the low-lying spectra of interest; and (ii) Definition of the boson space and operators by establishing a correspondence with the truncated fermion space and operators defined therein.

Broadly speaking, two different procedures have emerged to carry out these operations. In the widely followed Otsuka–Arima–Iachello (OAI) mapping procedure [6–12] first a truncation of the many particle shell model space to the S-D or S-D-G subspace is carried out. The S-D-G subspace is composed of S, D and G pairs of identical particles corresponding to the pairing, quadrupole and hexadecapole collective degrees of freedom of the nucleus respectively. A Marumori mapping is then constructed from the S-D-G subspace onto the corresonding s-d-g boson space. The parameters of the n-body boson operators defined in th s-d-g space are then evaluated by equating them to the matrix elements of the corresponding n-body operators in the fermionic space. The recently suggested "democratic" mapping procedure [13, 14] also follows a similar path. The procedures [15, 16] following the alternative Belyaev–Zelevinsky method first construct the boson operators and then carry out the truncation in the boson space.

In this paper, we describe a simple dynamic procedure [17] to construct the IBM operators from fermion basis and apply it to examine the collective shape transitions in even-A Mo and Sm isotopes. Taking into account the considerable amount of evidence that the G-pairs (or equivalently the g-bosons) play a necessary and sufficient role [10, 13, 16–23] in describing the low-lying spectra of interest, we assume that the relevant truncated fermion space is composed of only the "correlated" identical nucleon S, D and G pairs. Correspondingly we have the s-d-g IBM-2 boson space. We construct the correlated pairs by projecting good angular momentum states from mean field Hartree-Fock (HF) solutions. We then establish a Marumori mapping from the fermion single-pair and two-pair spaces to the corresponding one- and two- boson spaces. The boson matrix elements are then determined by equating them to the corresponding fermion matrix elements. Since a one-to-one correspondence from the identical two-pair space to the corres- ponding two boson space cannot be established, we ignore the identical boson interaction terms in the Hamiltonian. Actually, it has earlier been argued [4] that these terms do not play a significant role in the low-lying regions. The distinguishing aspect of our procedure from the OAI mapping is that in the latter N-pair states are mapped onto N-boson states and the fermion matrix elements are calculated in the N-pair space. Finally, due to lack of a suitable IBM-2 code incorporating g-bosons, the boson spectroscopic calculations are carried out in the IBM-1 domain by projecting from IBM-2 operators [24] and using the SDGIBM1 code of Devi and Kota [25].

The structure of the correlated identical nucleon pairs, which reflect the number of valence nucleons distributed over a set of single particle levels, the Pauli blocking effects etc., incorporates the dynamics and quite obviously plays a crucial role in evaluating the boson parameters. There have been several studies with varied approaches and approximations to study these aspects. The calculations [8, 9, 11] based on the broken pair approximation [26] evaluate the structure coefficients variationally with the assumption that the ground state of the nucleus consists of only S-pairs. These are clearly well-suited for spherical nuclei with a few valence nucleons. In the iterative scheme of Scholten [10] these coefficients are evaluated by minimising the N-pair ground state energy in the S-D-G space. This scheme has been applied to study the spherical to axially-deformed shape transition in the even-A Sm nuclei. There have also been procedures in the deformed basis where the coefficients are evaluated by projecting out good angular momentum states from deformed Cooper pairs obtained by number projection from BCS-Nilsson states [21, 22] or HFB solutions [20 27]. The correlated pairs constructed in our procedure from mean-field HF solutions do not include the pairing correlations, unlike those from the HFB solutions, but would include other deformation producing correlations, However, in the present study, we go beyond the work reported in [20, 27] in the sense that we actually construct the IBM Hamiltonian and other operators and carry out the spectroscopic calculations. Navrátil and Dobeš also evaluate these coefficients in the boson picture by establishing a canonical trans- formation from the non-collective boson space to the collective boson space and then choose the most collective state by looking at the lowest energy states of the Hamiltonian [16].

As mentioned earlier, we have applied our scheme to study the spherical to axial-rotor shape transition observed in the low-lying spectra of even $^{96-108}$Mo [28–30] and $^{146-154}$Sm [31, 32] isotopes. The microscopic IBM calculations for the

Mo isotopes are the first to be reported here. We compare our results for the Sm isotopes with those of Scholten [10] and Navrátil and Dobeš [16] who have also explicitly carried out the spectroscopic calculations using their respective procedures. From our results we observe the necessity to vary the strength parameters of the fermion two-body interaction (Surface delta interaction) in order to quantitatively reproduce the observed spectra and $B(E2)\uparrow$ values. Such variation in seen to be necessary in the transition region. Navrátil and Dobeš [16] have also observed the necessity to vary the fermion input parameters and have explicitly employed a thumb-rule (eq. (13) in ref. [16]) to vary them. Although no such variations were carried out by Scholten [10], the scaled-up spectra (with respect to the experimental ones) for the heavier Sm-chain probably indicate necessity of such a variation. We also observe similar effects in our results for Sm isotopic chain.

Our scheme of constructing the IBM operators is presented in § 2. The studies of shape transition in the Mo and Sm isotopic chains applying this scheme are presented in § 3. We summarize and conclude with a few remarks in § 4.

2. Our scheme

The scheme consists of four broad steps which are described in the following subsections. In the first step, we present a prescription to construct the correlated identical nucleon pairs from the occupied HF orbits of the nucleus. In § 2·2, we discuss the Marumori mapping from the correlated pair space onto the boson space. In § 2·3, we evaluate the IBM-2 parameters in terms of appropriate matrix elements in the fermion space. The IBM-1 parameters obtained from those of the IBM-2 operators by means of a projection scheme [24] are presented in § 2·4.

2.1 *Construction of correlated pairs*

We present here a simple prescription by which we construct the correlated pair states of identical nucleons for each nucleus. Clearly the structure of these pairs ought to effectively represent the distribution of all the valence nucleons ($\rho = \nu$(neutrons); π(protons)) over the chosen spherical model space $\{j_i^\rho\}$. A natural choice to carry out such a construction is to consider the occupancies of the spherical j_i^ρ orbits in a given state of the nucleus. However, a complete shell model calculation is almost impossible for the nuclei under our consideration. Hence we choose a practical, though approximate way out, i.e., to calculate the occupancies from the self-consistently generated set of deformed HF orbits. With the knowledge of the occupancies, we construct an effective single particle (s.p.) deformed orbit $|\rho; K\rangle_{\text{eff}}$ incorporating the relative distribution of the valence nucleons (ρ) over the model space. The correlated S, D, G pairs are then obtained by projecting out good angular momentum ($J = 0, 2, 4$ respectively) positive parity pairs from the two particle determinant defined by the states $|\rho; K\rangle_{\text{eff}}$.

We now describe the scheme in detail. We consider an even-even nucleus with n_ρ number of valence nucleons occupying a major oscillator shell $\{j_i^\rho\}$. The axially-deformed good-parity HF s.p. orbits $|\rho; \pm K\Pi\rangle$ for this system are then given by

$$|\rho; K\Pi\rangle = \sum_{j_i^\rho} C_{j_i^\rho K\Pi} |j_i^\rho K\Pi\rangle \quad \text{[time-like]} \tag{1}$$

$$|\rho; -K\Pi\rangle = \sum_{j_i^\rho} (-1)^{j_i^\rho - K} C_{j_i^\rho K\Pi} |j_i^\rho - K\Pi\rangle \quad \text{[time-reversed]} \tag{2}$$

where K and π are respectively, the s.p. projection (along the symmetry axis of the nucleus) and the parity associated with the orbit j_i^ρ. From the set of occupied HF we evaluate the occupancy of j_i^ρ

$$X_{j_i^\rho} = 2 \sum_{i=1}^{n_\rho/2} |C^{(l)}{}_{j_i^\rho}|^2 \tag{3}$$

where l is the index for the occupied orbits and the factor 2 accounts for the pair of time-like and time-reversed occupied orbits for each K and Π.

We then construct the effective s.p. deformed orbit

$$|\rho; K = \tfrac{1}{2}\rangle_{\text{eff}} = \sum_{j_i^\rho} p_{j_i^\rho} \bar{C}_{j_i^\rho} |j_i^\rho \tfrac{1}{2} \Pi\rangle. \tag{4}$$

Here the coefficients of expansion $\bar{C}_{j_i^\rho}$ are given by $\bar{C}_{j_i^\rho} = +\sqrt{X_{j_i^\rho}/n_\rho}$. The relative phase factors $p_{j_i^\rho}$ are fixed to be $p_{j_i^\rho} = C^{(1)}_{j_i^\rho} | C^{(1)}_{j_i^\rho}|$ where $C^{(1)}_{j_i^\rho}$ are the coefficients of expansion of the first (energetically lowest) HF orbit. Note from the definition of $\bar{C}_{j_i^\rho}$ that this orbit is normalized.

A few points are to be noted at this step. The HF solutions for all the nuclei studied by us are prolate in nature. We therefore choose the projection quantum number $K = \frac{1}{2}$ for the effective orbit. This also allows all the spherical shells in the model space starting from $j^\rho = \frac{1}{2}$ to contribute to this orbit. Its constituent $\bar{C}_{j_i^\rho}$ coefficients retain the relative distribution of valence nucleons over the model space and the effects of Pauli blocking etc. The motivation behind the above choice of phases $p_{j_i^\rho}$ is the fact that the prolate orbit with this phase choice is invariably the most deformed orbit with maximum intrinsic quadrupole moment. One would therefore expect that the pair wave function constructed from such an effective orbit would describe the low-lying collective states of the nucleus. Moreover, as this orbit is defined over a major oscillator shell including the intruder shell, it does not have good parity. In case of an occupied intruder shell, there is also the question of defining the corresponding phase factor $p_{j_i^\rho}$ in (4). Since we finally consider only positive parity pair states projected out of the product of a pair of effective orbits, the phase of the intruder orbit here is irrelevant.

From the two particle determinant constructed by $|\rho; K = \pm 1/2\rangle_{\text{eff}}$, we project out the good angular momentum positive parity pairs $|B^\rho_{JM=0}\rangle$ or in short $|B^P_J\rangle$

$$|B^\rho_J\rangle = \sum_{kl} \mathscr{C}^\rho_{(kl)J} |(\rho; kl)J\rangle \tag{5}$$

where the expansion coefficients $\mathscr{C}^\rho_{(kl)J}$ is given by

$$\mathscr{C}^\rho_{(kl)J} = \mathscr{N}^\rho_J (-1)^{j_l^\rho - \frac{1}{2}} \sqrt{1 + \delta_{kl}} (2 - \delta_{kl}) \langle j_k^\rho \tfrac{1}{2} j_l^\rho - \tfrac{1}{2} | j_k^\rho j_l^\rho : J0\rangle p_{j_k^\rho} p_{j_l^\rho} \bar{C}_{j_k^\rho} \bar{C}_{j_l^\rho}. \tag{6}$$

The quantity $\langle j_k^\rho \frac{1}{2} j_l^\rho - \frac{1}{2} | j_k^\rho j_l^\rho : J0\rangle$ in the above equation is the Clebsch–Gordan coefficient and $\mathscr{N}^\rho_J$ is the normalization factor. In (5) $|(\rho; kl)J\rangle = |(j_k^\rho j_l^\rho)J0\rangle$ is the two particle state coupled to angular momentum J. These correlated pairs are dynamic in nature, although in an average sense, as they are based on the occupancies of the model orbits calculated for each nucleus from the respective HF solutions. This prescription, like those of [20, 21, 22, 27], is applicable to all even-even nuclei—

spherical, transitional or rotational—away from closed-shell and whose lowest energy HF solution is prolate.

2.2 *Construction of the Boson operators*

Following usual tensor coupling notations, we may write the IBM-2 Hamiltonian

$$\mathscr{H}_{\mathrm{IBM}-2} = \sum_J (-1)^J \varepsilon_J^{\nu} (b_J^{\nu\dagger} \cdot \tilde{b}_J^{\nu}) + \sum_J (-1)^J \varepsilon_J^{\pi} (b_J^{\pi\dagger} \cdot \tilde{b}_J^{\pi}) + \sum_{J_1 J_2 J_3 J_4; J'} (-1)^{J'} W^{J'}_{J_1 J_2 J_3 J_4} ((b_{J_1}^{\nu\dagger} \times b_{J_2}^{\pi\dagger})^{J'} \cdot (\tilde{b}_{J_3}^{\nu} \times \tilde{b}_{J_4}^{\pi})^{J'}) \tag{7}$$

where $b_J^{\rho\dagger}$ and $\tilde{b}_J^{\rho}$ are respectively the boson creation and annihilation spherical tensor operators with $J = 0, 2$ and 4 for the s, d and g bosons. We also have the $E2$-transition operator

$$\mathscr{T}^{(\mathrm{E2})}_{\mathrm{IBM}-2} = \sum_{\rho=\nu,\pi} \sum_{JJ'} e^{\rho}_{JJ'} (b_J^{\rho\dagger} \tilde{b}_{J'}^{\rho})^2_0. \tag{8}$$

Our objective is to evaluate the single boson energy ε_J^{ρ}, the $\nu - \pi$ boson two-body matrix element (tbme) $W^{J'}_{J_1 J_2 J_3 J_4}$ in eq. (7) and the effective boson charge $e^{\rho}_{JJ'}$ in eq. (8) microscopically. To this end, we first establish the following Marumori mapping from the identical nucleon pair space onto the boson space

nucleon pairs bosons

$$|B_J^{\rho}\rangle \to |b_J^{\rho}\rangle;\ J = 0, 2, 4 \tag{9}$$

$$|(B^{\nu}_{J_1} B^{\pi}_{J_2}) J\rangle \to |(b^{\nu}_{J_1} b^{\pi}_{J_2}) J\rangle;\ J_1, J_2 = 0, 2, 4. \tag{10}$$

It is to be noted in (10) that the nucleon pairs and the bosons being distinguishable, there is no (anti) symmetry requirement and the one-to-one correspondence is straightforward.

The above mappings (9–10) lead to evaluation of the parameters of the boson operators in eqs (7–8) in the following manner

boson matrix elements nucleon pair matrix elements

$$\varepsilon_J^{\rho} \equiv \langle b_J^{\rho} | \mathscr{H}_{\mathrm{IBM}-2} | b_J^{\rho} \rangle = \langle B_J^{\rho} | \mathscr{H}_{\rho} | B_J^{\rho} \rangle \tag{11}$$

$$W^{J}_{J_1 J_2 J_3 J_4} \equiv \langle (b^{\nu}_{J_1} b^{\pi}_{J_2}) J | \mathscr{H}_{\mathrm{IBM}-2} | (b^{\nu}_{J_3} b^{\pi}_{J_4}) J \rangle = \langle (B^{\nu}_{J_1} B^{\pi}_{J_2}) J | \mathscr{V}^{F}_{\nu\pi} | (B^{\nu}_{J_3} B^{\pi}_{J_4}) J \rangle \tag{12}$$

$$e^{\rho}_{JJ'} \equiv \langle b_J^{\rho} | \mathscr{T}^{(\mathrm{E2})}_{\mathrm{IBM}-2} | b_{J'}^{\rho} \rangle = \langle B_J^{\rho} | \mathscr{T}^{(\mathrm{E2})} | B_J^{\rho} \rangle. \tag{13}$$

On the r.h.s. of eqs (11–13), we have respectively the one-plus-two-body identical nucleon Hamiltonian $\mathscr{H}_{\rho}$, the two-body neutron-proton interaction operator $\mathscr{V}_{\nu\pi}$ and the fermion $E2$-transition operator $\mathscr{T}^{(\mathrm{E2})}$ discussed in the next subsection.

As pointed out earlier, a one-to-one correspondence between the states $|(B^{\rho}_{J_1} B^{\rho}_{J_2}) J\rangle$ and $|(b^{\rho}_{J_1} b^{\rho}_{J_2}) J\rangle$ cannot be established. We have, therefore, dropped the terms involving these boson states in the Hamiltonian $\mathscr{H}_{\mathrm{IBM}-2}$ (eq. (7)). However, this approximation is not a severe handicap as it has been shown [4] that in the low-lying spectra these matrix elements play a negligible role.

Further, the Marumori mapping constructed in (9–10) are not of OAI type where N-pair ($N = N_\nu + N_\pi$) states are mapped onto N-boson states [6–12] and the boson parameters are evaluated by calculating a few fermion matrix elements in the N-pair space using the generalised seniority scheme.

2.3 *Evaluation of the boson parameters*

2.3.1 *The single boson energy*: The single boson energy $e^\rho_J = \langle B^\rho_J | \mathscr{H}_\rho | B^\rho_J \rangle$ of (11) alongwith (5) for $|B^\rho_J\rangle$ is given by

$$\varepsilon^\rho_J = \sum_{k_1 l_2} \sum_{k_2 l_2} \mathscr{C}'^{\rho}_{(k_1 l_1)J} \mathscr{C}^{\rho}_{(k_2 l_2)J} \langle (\rho; k_1 l_1)J | \mathscr{H}_\rho | (\rho; k_2 l_2)J \rangle. \tag{14}$$

The matrix elements (m.e.) on the r.h.s. of (14) is easily evaluated

$$\langle (\rho; k_1 l_1)J | \mathscr{H}_\rho | (\rho; k_2 l_2)J \rangle = (\varepsilon_{j^\rho_{k_1}} + \varepsilon_{j^\rho_{l_1}}) \delta_{j^\rho_{k_1} j^\rho_{k_2}} \delta_{j^\rho_{l_1} j^\rho_{l_2}} + V^{J}_{j^\rho_{k_1} j^\rho_{l_1} j^\rho_{k_2} j^\rho_{l_2}} \tag{15}$$

where $\varepsilon_{j^\rho_k}$ is the single particle energy (spe) of the valence SM orbits j^ρ_k and $V^{J}_{j^\rho_{k_1} j^\rho_{l_1} j^\rho_{k_2} j^\rho_{l_2}}$ is the identical particle nucleonic two-body matrix element (tbme)

2.3.2 *The neutron-proton boson interaction matrix element*: The ν–π boson two-body matrix element $W^J_{J_1 J_2 J_3 J_4} = \langle (B^\nu_{J_1} B^\pi_{J_2})\, J | \mathscr{V}_{\nu\pi} | (B^\nu_{J_3} B^\pi_{J_4}) J \rangle$ of (12) alongwith (5) is given by

$$W^J_{J_1 J_2 J_3 J_4} = \sum_{k_1 l_1} \sum_{k_2 l_2} \sum_{k_3 l_3} \sum_{k_4 l_4} \mathscr{C}^{\nu}_{(k_1 l_1) J_1} \mathscr{C}^{\pi}_{(k_2 l_2) J_2} \mathscr{C}^{\nu}_{(k_3 l_3) J_3} \mathscr{C}^{\pi}_{(k_4 l_4) J_4}$$
$$\langle ((\nu; k_1 l_1) J_1, (\pi; k_2 l_2) J_2) J | \mathscr{V}_{\nu\pi} | ((\nu; k_3 l_3) J_3, (\pi; k_4 l_4) J_4) J \rangle. \tag{16}$$

The matrix element on the rhs of (16) is the basic matrix element with the two-body ν–π-interaction operator

$$V_{\nu\pi} = \sum_{j^\nu j^\pi j'^\nu j'^\pi;\, J'} [J']^{1/2}\, V^{J'}{}_{j^\nu j^\pi j'^\nu j'^\pi} ((a^\dagger_{j^\nu} \times a^\dagger_{j^\pi})^{J'} \times (\grave{a}_{j'^\nu} \times \grave{a}_{j'^\pi})^{J'})^0 \tag{17}$$

with $a^\dagger_{j^\rho}, \tilde{a}_{j^\rho}$ etc. as the nucleon creation and annihilation tensor operators and the matrix elements $V^{J'}{}_{j^\nu j^\pi j'^\nu j'^\pi}$ in ν–π formalism.

Rewriting the operator $\mathscr{V}_{\nu\pi}$ in the multipole form and applying the Wigner–Eckart theorem, the basic matrix element can be factorised [33]

$$\langle ((\nu; k_1 l_1) J_1, (\pi; k_2 l_2) J_2) J | \mathscr{V}_{\nu\pi} | ((\nu; k_3 l_3) J_3), (\pi; k_4 l_4) J_4) J \rangle$$
$$= (-1)^{J_2 + J_3 + J} \sum_{j^\nu j^\pi j'^\nu j'^\pi;\, J'} (-1)^{j^\pi + j'^\nu + J'} [J']\, V^{J'}{}_{j^\nu j^\pi j'^\nu j'^\pi}$$
$$\sum_{J''} \begin{Bmatrix} J_1 & J_2 & J \\ J_4 & J_3 & J'' \end{Bmatrix} \begin{Bmatrix} j^\nu & j^\pi & J' \\ j'^\pi & j'^\nu & J'' \end{Bmatrix} \langle (\nu; k_1 l_1) J_1 \| (a^\dagger_{j^\pi} \times \tilde{a}_{j'^\nu})^{J''} \| (\nu; k_3 l_3) J_3 \rangle$$
$$\langle (\pi; k_2 l_2) J_2 \| (a^\dagger_{j^\pi} \times \tilde{a}_{j'^\pi})^{J''} \| (\pi; k_4 l_4) J_4 \rangle. \tag{18}$$

The m.e.'s on the rhs of (18) are evaluated by employing standard techniques of shell model spectroscopy, namely, intermediate state expansion, recoupling of spherical tensors and application of the fermion anti-commutation relations. We obtain

$$\begin{aligned}
&\langle((\nu;k_1l_1)J_1,(\pi;k_2l_2)J_2)J|\mathscr{V}_{\nu\pi}|((\nu;k_3l_3)J_3,(\pi;k_4l_4)J_4)J\rangle\\
&\quad=(-1)^{J_1+J_4+J+1}\prod_{i=1}^{4}\zeta_{k_il_i}[J_i]^{1/2}\varepsilon_{k_il_iJ_i}\\
&\qquad\sum_{J'J''}(-1)^{j^\nu_{k_1}+j^\nu_{k_3}+j^\nu_{l_1}+j^\pi_{l_2}+J'}[J'J'']\,V^{J'}{}_{j^\nu_{k_1}j^\pi_{k_2}j^\nu_{k_3}j^\pi_{k_4}}\begin{Bmatrix}J_1 & J_2 & J\\ J_4 & J_3 & J''\end{Bmatrix}\\
&\qquad\begin{Bmatrix}j^\nu_{k_1} & j^\pi_{k_2} & J'\\ j^\pi_{k_4} & j^\nu_{k_3} & J''\end{Bmatrix}\begin{Bmatrix}J_1 & j^\nu_{k_1} & j^\nu_{l_1}\\ j^\nu_{k_3} & J_3 & J''\end{Bmatrix}\begin{Bmatrix}J_2 & j^\pi_{k_2} & j^\pi_{l_2}\\ j^\pi_{k_4} & J_4 & J''\end{Bmatrix}\delta_{j^\nu_{l_1}j^\nu_{l_3}}\delta_{j^\pi_{l_2}j^\pi_{l_4}}
\end{aligned}\tag{19}$$

where $\zeta_{k_il_i}=(1/(1+\delta_{k_il_i})^{1/2})$, $[J]=2J+1$ and the exchange operator ε_{klJ} defined as

$$\varepsilon_{klJ}f(k,l,J)=f(k,l,J)-(-1)^{j_k+j_l-J}f(l,k,J).\tag{20}$$

2.3.3 *The E2-transition effective boson charge*: The effective boson charge $e^\rho_{JJ'}$ for $E2$-transition in (8) is evaluated from (13). By applying Wigner–Eckart theorem and carrying out the contraction on the double-barred matrix element through boson commutation relations, the boson matrix element on the lhs of (13) can be reduced to

$$\langle b^\rho_{J_1}|\mathscr{T}^{(\mathrm{E2})}_{\mathrm{IBM}-2}|b^\rho_{J_2}\rangle=\frac{[2]^{1/2}}{[J_1]^{1/2}}\langle J_2020|J_10\rangle e^\rho_{J_1J_2}\tag{21}$$

where the quantity $\langle J_2020|J_10\rangle$ is the Clebsch–Gordan coefficient. The effective charge parameter of the bosons is thus given by

$$e^\rho_{J_1J_2}=\frac{[J_1]^{1/2}\langle B^\rho_{J_1}|\mathscr{T}^{(\mathrm{E2})}|B^\rho_{J_2}\rangle}{[2]^{1/2}\langle J_2020|J_10\rangle}.\tag{22}$$

The $E2$-transition operator $\mathscr{T}^{(\mathrm{E2})}$ in the nucleonic space is given by

$$\mathscr{T}^{(\mathrm{E2})}=-\frac{1}{\sqrt{5}}\sum_\rho e_\rho\sum_{j^\rho j'^\rho}q_{j^\rho j'^\rho}(a^\dagger_{j^\rho}\times\tilde{a}_{j'^\rho})^2_0\tag{23}$$

where e_ρ is the effective nucleon charge, $q_{j^\rho j'^\rho}=\langle j^\rho\|r^2\,Y^2\|j'^\rho\rangle$ is the reduced quadrupole matrix element in units of oscillator size parameter $b^2_\rho(=0{\cdot}0102(4N_\rho/A^2)^{-1/3}$ barns) [34] for a nucleus with N_ρ number of ρ-pairs and atomic number A.

Expanding the m.e. on the rhs of (22) by (5) we have

$$\langle B^\rho_{J_1}|\mathscr{T}^{(\mathrm{E2})}|B^\rho_{J_2}\rangle=\sum_{k_1l_1}\sum_{k_2l_2}\mathscr{C}^\rho_{(k_1l_1)J_1}\mathscr{C}^\rho_{(k_2l_2)J_2}\langle(\rho;k_1l_1)J_1|\mathscr{T}^{(\mathrm{E2})}|(\rho;k_2l_2)J_2\rangle.\tag{24}$$

The basic matrix element on the rhs of (24) is evaluated by substituting for $\mathscr{T}^{(\mathrm{E2})}$ (23) and applying the spherical tensor recoupling and commutation relations. We obtain

$$\begin{aligned}
&\langle(\rho;k_1l_1)J_1|\mathscr{T}^{(\mathrm{E2})}|(\rho;k_2l_2)J_2\rangle\\
&\quad=e_\rho[J_2]^{1/2}\langle J_2020|J_10\rangle\varepsilon_{k_1l_1J_1}\varepsilon_{k_2l_2J_2}(-1)^{j^\rho_{k_1}+j^\rho_{l_1}+J_2}q_{j^\rho_{k_1}j^\rho_{k_2}}\\
&\qquad\zeta_{k_1l_1}\zeta_{k_2l_2}\begin{Bmatrix}j^\rho_{k_1} & j^\rho_{l_1} & J_1\\ J_2 & 2 & j^\rho_{k_2}\end{Bmatrix}\delta_{j^\rho_{l_1}j^\rho_{l_2}}
\end{aligned}\tag{25}$$

Combining (22), (24) and (25) we calculate the effective charge parameter $\varepsilon^{\rho}_{J_1J_2}$.

2.3 *Construction of IBM-1 operators*

Due to the lack of an IBM-2 code incorporating g-bosons explicitly, we carry out the spectroscopic calculations in IBM-1 regime. The parameters of the IBM-1 operators are calculated from those of IBM-2 by a projection scheme [24] based on the F-spin symmetry amongst neutron and proton bosons. The IBM-2 to IBM-1 projection is carried out with the assumption that the low-lying IBM-2 levels of our interest have F-spin $F = F_{\max}$ and hence are completely symmetric under interchange of ν–π labels. This symmetry can be realized by either constructing an F-scalar Hamiltonian [35] or, alternatively, by including in a non-F-scalar Hamiltonian a large Majorana force $M_{\nu\pi}$ [36, 37].

The IBM-2 Hamiltonian (eq. (7)) constructed in our microscopic procedure is clearly not F-scalar. However, we assume that the low-lying levels and, in particular, the Yrast levels among them that we are interested in do have $F = F_{\max}$ and project out the IBM-1 Hamiltonian from the IBM-2 Hamiltonian. Those terms in the expansion of the IBM-2 Hamiltonian which contribute to the Majorana operator collapse in IBM-1 because of symmetry requirements of the IBM-1 states. Out of the 82 parameters in the two-body part of $\mathscr{H}_{\text{IBM}-2}$ only 68 contribute to $\mathscr{H}_{\text{IBM}-1}$ m.e. and the rest are mapped to zero. The 3 single boson energies ε_J and 32 two-body matrix elements $V^{J'}_{J_1J_2J_3J_4}$ of the (sdg) IBM-1 Hamiltonian

$$\mathscr{H}_{\text{IBM}-1} = \sum_J (-1)^J \varepsilon_J (b^\dagger_J \cdot \tilde{b}_J) + \sum_{J_1J_2J_3J_4;J'} (-1)^{J'} \zeta_{J_1J_2}\zeta_{J_3J_4} \\ V^{J'}_{J_1J_2J_3J_4} (b^\dagger_{J_1} b^\dagger_{J_2})^{J'} \cdot (\tilde{b}_{J_3} \tilde{b}_{J_4})^{J'} \tag{26}$$

and the 4 effective $E2$-charge parameters $e_{JJ'}$ of the IBM-1 $E2$-transition operator

$$\mathscr{T}^{(\text{E2})}_{\text{IBM}-2} = \sum_{JJ'} e_{JJ'} (b^\dagger_J \tilde{b}'_J)^2_0 \tag{27}$$

are related to the corresponding IBM-2 parameters through the neutron(proton) boson numbers $N_\nu(N_\pi)$ and the total boson number N and are given below

IBM − 1 IBM − 2

$$\varepsilon_J = \frac{1}{N}(N_\nu \varepsilon^\nu_J + N_\pi \varepsilon^\pi_J) \tag{28}$$

$$V^{J'}_{J_1J_2J_3J_4} = \frac{N_\nu N_\pi}{N(N-1)} \bar{W}^{J'}_{J_1J_2J_3J_4} \tag{29}$$

$$e_{JJ'} = \frac{1}{N}(N_\nu e^\nu_{JJ'} + N_\pi e^\pi_{JJ'}). \tag{30}$$

In eq. (29) $\bar{W}^{J'}_{J_1J_2J_3J_4}$ is the sum of all $W^{J'}_{J_1J_2J_3J_4}$ for a given J' in $\mathscr{H}_{\text{IBM}-2}$ including the distinct permutations of (J_1, J_2) and (J_3, J_4) respectively.

The IBM-1 parameters (28–30) are then used in the SDGIBM-1 boson code of Devi and Kota [25] to produce the spectra and $B(E2)$ values for the even-even Mo and Sm isotopes. Due to computational difficulties we have truncated the boson space to configurations with number of g-bosons $N_g \leqslant 2$ for all calculations reported here. In case of the Sm isotopes, the basis space has been further truncated by imposing the condition on number of s-bosons $N_s \geqslant 2$ on the basis states. Earlier calculations [16, 38] have demonstrated that such approximations produce satisfactory results.

3. Shape transition in Mo and Sm isotopes

We now present the results of the application of this simple procedure to study the spherical to axially-deformed shape transition in even—A^{96-108}Mo and $^{146-154}$Sm isotopes. We have used the surface delta interaction (SDI) $\mathcal{O}_{\rho\rho'}$ as the residual two-body interaction. It can be written in terms of spherical harmonics Y^l_m

$$\mathcal{O}_{\rho\rho'} = -A_{\rho\rho'} \sum_{l=0}^{\infty} (-1)^l (2l+1)^{1/2} (Y^l(\rho) \cdot Y^l(\rho')) \tag{31}$$

with strength parameters $A_{\rho\rho'}$. Qualtitative features of shape transition are observed with a given set of fermion input parameters, namely, spe $\varepsilon_{j\rho}$, SDI strength $A_{\rho\rho'}$ and effective nucleon charge e_ρ, for each set of isotopes. However, in quantitative terms, the same set of parameters while producing results in agreement with experiment for the lighter isotopes, produce scaled-up spectra for the heavier ones. One then needs to vary these parameters in the deformed region to reproduce numbers akin to experimental results. Such scaling-up of spectra has also been reported by other authors [10, 12, 16]. Navrátil and Dobesy carry out the variation of all the input parameters dynamically by a further parametrization [16] involving the boson numbers of the nucleus under consideration. Our attempt, however, has been to minimize the number of free parameters and also to economise on their variation.In order to demonstrate the necessity of varying these parameters, we adopt the following approach. For the Mo chain, we carry out variation of $A_{\rho\rho'}$ with a view to closely reproducing the experimental results. For the Sm chàin, however, we keep the strength parameters fixed and compare the results with the observed spectra as well as with those of Scholten [10] whose calculations are also carried out without variation of the parameters. The effective nucleon charges for the Sm isotopes are varied to compare with the results of Navrátil and Dobesy [16]. We have also carried out detailed calculations for ^{148}Sm and ^{152}Sm with different values of the parameters $A_{\rho\rho'}$ and e_ρ. Results of these calculations are not given here for brevity but they compare well with those of [16, 38, 39] and experiments [31, 32].

3.1 *The Mo isotopes*

The model spaces for the valence protons and neutrons in the even $^{96-108}$Mo isotopes alongwith the spe [40] are given in table 1. It has also been shown [40] that the role of the $2p_{1/2}$ shell protons is negligible in the shape transition; hence we ignore them. The set of SDI strength parameters $A_{\nu\nu} = A_{\pi\pi} = 0{\cdot}35$ MeV and $A_{\nu\pi} = 0{\cdot}6$ MeV, taken by Federman and Pittel [41] to study the shape transitions in this isotopic chain, produce in our calculations results in agreement with experiment for the lighter isotopes but scaled-up spectra for the heavier ones. We, therefore, vary these parameters as shown in table 2. These numbers indicate, as one would expect, that the deformation producing $\nu\pi$ interaction becomes much stronger in the deformed heavy isotopes compared to the identical particle interaction which would include the

Table 1. The model space and the single particle energies for Mo isotopes.

	orbit	energy (MeV)
protons	$1g_{9/2}$	0·0
neutrons	$2d_{5/2}$	0·0
	$3s_{1/2}$	1·0
	$2d_{3/2}$	2·5
	$1g_{7/2}$	3·0
	$1h_{11/2}$	3·6

Table 2. Adopted SDI strength parameters for $^{96-108}$Mo isotopes.

Isotope	$A_{\rho\rho}(\rho = \nu, \pi)$ (in MeV)	$A_{\nu\pi}$ (in MeV)
^{96}Mo	0·37	0·60
^{98}Mo	0·37	0·60
^{100}Mo	0·33	0·60
^{102}Mo	0·10	0·40
^{104}Mo	0·05	0·40
^{106}Mo	0·05	0·40
^{108}Mo	0·05	0·40

sphericity producing pairing interactions even though their absolute values decrease. The effective neutron charges are chosen to be $e_\nu = 0{\cdot}9e$ and $e_\pi = 1{\cdot}9e$.

In the axially-deformed prolate HF solutions we do not observe occupation of the intruder $1h_{11/2}$ orbit. The normalized occupancies $|\bar{C}_{j^\nu}|^2$ calculated from $|\nu; k = 1/2)_{\text{eff}}$ (4) for every valence orbit j_i^ν are plotted for all isotopes in figure 1(a). In the case of ^{98}Mo the $2d_{5/2}$ orbit gets almost filled with very little participation of the rest of the model orbits and we observe a (sub)shell effect here. It has been argued [42] that this effect at $N = 56, 58$ is responsible for the delay in the onset of shape transition in Mo isotopes. With addition of more neutrons, collectivity sets in and for $A = 106, 108$ the $2d_{3/2}$ and $1g_{7/2}$ orbits also take part substantially.

Federman and Pittel [43], in their analysis of the microscopic aspects of nuclear deformation and shape transition, proposed that the onset of nuclear deformation occurs in the region where valence neutrons and protons occupy spherical orbits with good overlap. The neutron and proton orbits $(n_\nu l_\nu j_\nu)$ and $(n_\pi l_\pi j_\pi)$ are shown to have good overlap [44] if $n_\nu = n_\pi$ and $l_\nu = l_\pi$, $l_\pi \pm 1$. Following this, Federman and Pittel [41] showed that it is indeed the occupation of the $(1g_{9/2})^\pi$ and $(1g_{7/2})^\nu$ orbits by the valence nucleons which is responsible for the onset of deformation in the heavier Mo isotopes. In figure 1(a), we observe similar effects with $1g_{7/2}$ being rapidly occupied for $A = 104$–108. Similar effects are also seen in the occupancies of the model orbits for the Sm isotopes.

The IBM-1 d- and g-boson energies $\varepsilon_d, \varepsilon_g$ with respect to the s-boson energies are plotted in figure 1(b). Barring the case of ^{98}Mo, these quantities vary smoothly. It

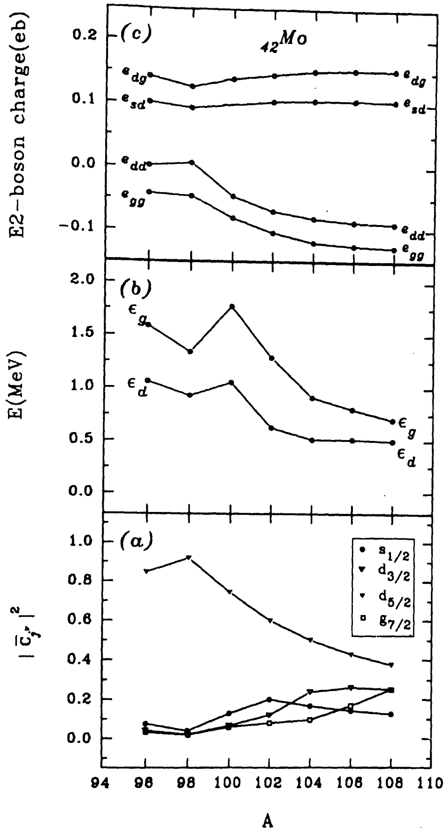

Figure 1. Mo Isotopes: (a) effective occupancies $|\bar{C}_{j^\nu}|^2$ of single particle neutron orbits from $|\nu; k = +\frac{1}{2}\rangle_{eff}$ orbit; (b) the IBM-1 d- and g- boson energies ε_d and ε_g w.r.t ε_s; and (c) IBM-1 effective boson charges for $E2$-transitions are plotted against the atomic number A.

should be noted that for $^{104-108}$Mo, with the SDI strength parameters kept constant table 2, there is a gradual decrease in the ε_d–ε_g gap. This decrease facilitates a stronger mixing of the d- and g-bosons and probably helps the onset and sustenance of the deformation.

The IBM-1 $E2$-charges $e_{JJ'}$ in eb unit are plotted in figure 1(c). It is gratifying to note that for the heavier (deformed) nuclei these microscopically calculated parameters have the same relative phases as the $E2$-transition operator in $SU(3)$ limit [45]

$$\mathscr{T}^{(\mathrm{E2})}_{\mathrm{IBM}-1}(SU(3) = e^{B}\left(4\left(\frac{7}{15}\right)^{1/2}(s^{\dagger}\tilde{d} + d^{\dagger}\tilde{s})^{2}_{0} - 11\left(\frac{2}{27}\right)^{1/2}(d^{\dagger}\tilde{d})^{2}_{0}\right.$$
$$\left. + \frac{36}{\sqrt{105}}(d^{\dagger}\tilde{g} + g^{\dagger}\tilde{d})^{2}_{0} - 2\left(\frac{33}{7}\right)^{1/2}(g^{\dagger}\tilde{g})^{2}_{0}\right) \qquad (32)$$

and with the free parameter $e^{B} = 0{\cdot}04\,\mathrm{eb}$, the two sets of parameters become comparable for the deformed nuclei like $^{106-108}$Mo.

In figure 2(a), the observed [31] and calculated 2_1^+, 4_1^+ and 6_1^+ energies of the isotopes (A) are plotted with respect to the respective ground state energies. The

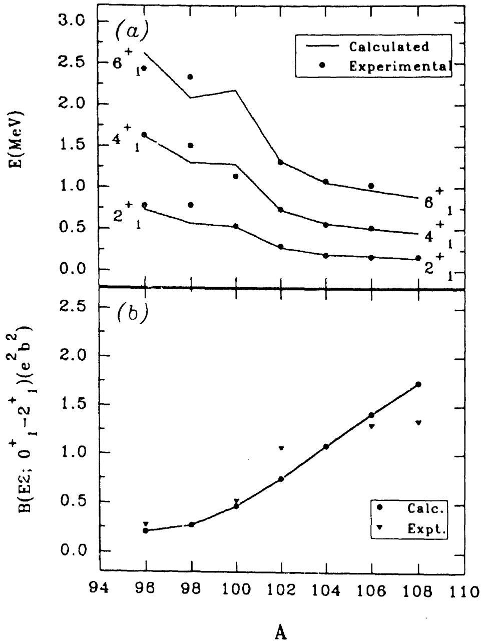

Figure 2. Mo isotopes: the experimental and calculated (**a**) Yrast spectra; and (**b**) the $E2$-transition probabilities ($B(E2; 0_1^+ \to 2_1^+)$).

$B(E2; 0_1^+ \rightarrow 2_1^+)$ (or $B(E2)\uparrow$) are presented alongwith the experimental values [32] in figure 2(b). The spherical to axial-rotor shape transition is clearly borne out with lowering of the 2_1^+ level with A, the transition in the energy spectrum from vibrational to rotational and also the enhancement of $B(E2)\uparrow$ values around $A = 100, 102$. The overproduction of $B(E2)\uparrow$ for $A = 106, 108$ is also observed by other phenomenological studies [30, 36]. It may be noted in table 2 that the necessity to vary the SDI strength parameters occurs near $A \simeq 100, 102$ where the transition evidently occurs.

3.2 *The Sm isotopes*

The single particle spaces and the corresponding energies of the orbits are given in table 3. The beginning-shell single-particle (BSSP) energies [7] have been taken for both neutrons and protons. The strength parameters of SDI are kept fixed at $A_{\nu\nu} = A_{\pi\pi} = 0{\cdot}3$ MeV and $A_{\nu\pi} = 0{\cdot}12$ MeV. The energies of a few low-lying levels with respect to the corresponding ground state energies given by our calculation alongwith the corresponding experimental values [31] are plotted in figure 3(a). The spectra generated in [10] are plotted in figure 3(b) for comparison. The calculated levels for the deformed nuclei, namely, $^{152-154}$Sm are pushed up compared to the observed ones. The same effects are also observed in figure 3(b). The evidence of the shape transition at $A = 150$–152 is clearly seen from the Yrast levels 2_1^+ and 4_1^+ plotted with respect to the ground state. The behavior of the 0_2^+ has been pointed out to be remarkable [47] in the shape transition. Being a member of the two-phonon triplet of a spherical nucleus, it first drops linearly alongwith 2_2^+ and 4_1^+. As the transition to axially-deformed shape occurs, it moves up and becomes the head of the β-band. The 2_2^+ level also goes up as seen in the experimental curve (figure 3(a)). However, the 0_2^+ and 2_2^+ levels for $^{152-154}$Sm in our calculation are produced at higher energies compared to those of [10] in figure 3(b). As already mentioned earlier, the excess of pairing correlation supplied by a higher than realistic value of $A_{\nu\nu}$ and $A_{\pi\pi}$ may be playing a role in this scale-up. It is also likely that the excited boson states such as s′ and d′ play a role even in the low-lying spectra of deformed nuclei. In addition, for our calculated levels the mixing of F-spin mixed-symmetry states with those of F-spin symmetric ones may also be party responsible. As Scholten's calculations are carried out in IBM-2 with a Majorana force which pushes the F-spin mixed-symmetry levels up, the 0_2^+, 2_2^+ levels produced thereby should correspond closer to pure F-spin symmetric levels.

Table 3. The neutron and proton model spaces for $^{146-156}$Sm and the spe.

Neutrons		Protons	
orbits	energies (MeV)	orbits	energies (MeV)
$2f_{7/2}$	1·00	$1g_{7/2}$	0·00
$3p_{3/2}$	1·50	$2d_{5/2}$	0·96
$3p_{1/2}$	2·25	$2d_{3/2}$	2·69
$1h_{9/2}$	2·45	$1h_{11/2}$	2·76
$2f_{5/2}$	2·60	$3s_{1/2}$	2·99
$1i_{13/2}$	2·80	—	—

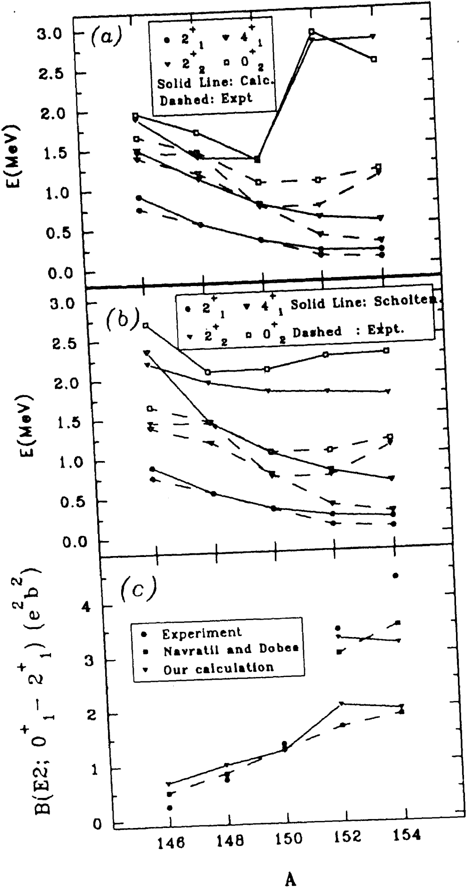

Figure 3. Sm isotopes: (**a**) experimental (expt.) and calculated (calc). spectra; (**b**) spectra produced in Scholten's calculation alongwith the experiment levels; and (**c**) the $B(E2;0_1^+ \rightarrow 2_1^+)$ in e^2b^2 units. A different set of e_ν and e_π produces the $B(E2)$ values closer to the experimental values for $A = 152, 154$.

The $B(E2)\uparrow$ values plotted in figure 2(c) alongwith the experimental values [32] and those of Navrátil and Dobesy [16] also show the enhancement at $A \simeq 152$—a characteristic of the transition. However, we observe that the initial choice of the fermion effective charges $e_\nu = 0{\cdot}5\,e$ and $e_\pi = 1{\cdot}3\,e$ is not able to produce enough enhancement as observed at the transition. In order to reproduce the enhancement closer to observed values we have to adopt a new set of parameters, i.e. $e_\nu = 0{\cdot}7$ e and $e_\pi = 1{\cdot}6$ e. Similar observation has also been made by Navrátil and Dobesy. Such a variation of the parameters is also evidently necessary in the case of the spectra (both ours as well as Scholten's) which while qualitatively showing the transition are scaled up at the point of transition, i.e. at $A = 150$–152.

4. Discussion

A great deal of work probing the microscopic foundations of IBM has been reported in literature. Several schemes and procedures have been developed to construct the bosons and the bosonic operators microscopically from fermion inputs. These studies demonstrate various degrees of success in explaining different aspects of low-lying collectivity in nuclei. However, there have been only very few microscopic IBM calculations to study detailed spectroscopic properties.

The highlight of the procedure presented here is that with a simple prescription it dynamically evaluates the boson structure and matrix elements of the boson operators for each nucleus from its deformed HF solution. Secondly, this procedure is success- fully applied to carry out spectroscopic calculations to study the spherical to axially- deformed shape transition in even-A Mo and Sm isotopes.

This procedure is based on the following assumptions:

(i) The truncation of the full shell model space to S-D-G space is both viable and sufficient;
(ii) The many particle fermion states of the S-D-G space and the matrix elements of the fermionic operators defined in this space are correctly represented by the corresponding boson states in the s-d-g space and the matrix elements of the bosonic operators;
(iii) The lowest energy HF solutions from which the correlated S, D and G pairs are constructed are prolate in character.
(iv) The identical boson interaction terms are negligible compared to the neutron-proton interaction term in the boson Hamiltonian.
(v) The low-lying IBM-2 states of interest are F-spin symmetric.
(vi) For computational limitations, the boson configuration space has been truncated with the condition $N_g \leqslant 2$ of g-bosons. For the Sm isotpoes, we also have a further truncation $N_s \geqslant 2$ of s-bosons.

In our study of shape transitions, we observe a necessity to vary the fermion two-body interaction (SDI) strength parameters is the transition region. Our strategy of variation parameters is somewhat different from that of Navrátil and Dobesy [16] who vary all the fermion parameters through a prescription laying more stress on the variation of single-particle energies.

It is of course desirable that one should be able to reproduce the observed transition from the same set of parameters used throughout the isotopic chain. It is possible that the drastic truncation of the shell model space mapped onto the boson space and further approximations in the boson space does not allow the interaction to take its course and demonstrate the transition. This requires us to adjust the parameters by hand to reproduce the transition. However, it has also been shown in shell model calculations [48] that in order to reproduce the observed spectra for all the nuclei in the s-d shell, the two-body matrix elements have to be multiplied by a factor $\sim A^{1/3}$. Such calculations are prohibitively difficult for the set of nuclei under our consideration. Notwithstanding, we can at the least say that the need to vary fermion parameters may be attributed to the absence of excited bosons (s$'$, d$''$, g$'$, $\cdots$) which may correspond to nearby minima of the variationally minimized energy surface in our HF calculations. Recently it has indeed been shown [14] that inclusion of these bosons does produce better results for lighter nuclei. It is well-known that angular momentum projected HF band-mixing calculations have been eminently successful in studying various spectroscopic properties of nuclei in different regions of the periodic table [49, 50, 51]. We therefore conjecture that if our HF based procedure can be extended to include these excited bosons it may not be necessary to vary the parameters. In summary, we think that the approach proposed in this paper is the simplest, has close connection with the HF band mixing calculations of nuclei and consequently has a natural way of incorporating s$'$ d$'$ g$'$ bosons.

Acknowledgements

We are deeply indebted to our colleagues V K B Kota and Y Durga Devi for allowing us access to the code SDGIBM1 developed and documented by them and for helping us out with the technicalities of running it. Besides, we benefited greatly from discussions with them. We are also grateful to S P Pandya and V K B Kota for a careful reading of the manuscript and for making many useful comments. Thanks are also due to C R Praharaj, B K Agarwal and A K Rath for providing us with the HF code and teaching us how to run it.

References

[1] A Arima and F Iachello, *Phys. Rev. Lett.* **35**, 1069 (1975)
[2] F Iachello and A Arima, *Interacting boson model* (Cambridge University Press, Cambridge, England, 1987)
[3] R F Casten and D D Warner, *Rev. Mod. Phys.* **60**, 389 (1988)
[4] F Iachello and I Talmi *Rev. Mod. Phys.* **59**, 375 (1987)
[5] A Klein and E R Marshalek, *Rev. Mod. Phys.* **63**, 375 (1991)
[6] T Otsuka, A Arima and F Iachello, *Nucl. Phys.* **A309**, 1 (1978b)
[7] S Pittel, P D Duval and B R Barrett, *Ann. Phys.* (*N.Y.*) **144**, 168 (1982)
[8] Y K Gambhir, P Ring and P Schuck, *Phys. Rev.* **C25**, 2858 (1992a)
[9] Y K Gambhir, P Ring and P Schuck, *Nucl. Phys.* **A384**, 37 (1982b)
[10] O Scholten, *Phys. Rev.* **C28**, 1783 (1983)
[11] A Van Egmond and K Allaart, *Nucl, Phys.* **A425**, 275 (1984)
[12] C H Druce, S Pittel, B R Barrett and P D Duval, *Ann. Phys.* **176**, 114 (1987)
[13] L D Skouras, P Van Isacker and M A Nagarajan, *Nucl. Phys.* **A516**, 255 (1990)
[14] D Bonatsos, L D Skouras, P Van Isacker and M A Nagarajan, *J. Phys.* **G17**, 1803 (1991)
[15] P Navrâtil and J Dobesy, *Nucl. Phys.* **A507**, 340 (1990)
[16] P Navrâtil and J Dobesy, *Nucl. Phys.* **A533**, 223 (1991)
[17] S Sarangi and J C Parikh, *Pramana - J. Phys.* **40**, 43 (1993)
[18] A Sethi, F Todd Baker, G T Emery, W P Jones and M A Grimm, *Nucl. Phys.* **A518**, 536 (1990)
[19] A Sethi, N M Hintz, D N Mihailidis, A M Mack, M Gazzaly, K W Jones, G Pauletta, L Santi and D Goutte, *Phys. Rev.* **C44** , 700 (1991)

[20] W Pannert, P Ring and Y K Gambhir, *Nucl. Phys.* **A443**, 189 (1985)
[21] T Otsuka, A Arima, and N Yoshinaga, *Phys. Rev. Lett.* **48**, 387 (1982)
[22] D R Bes, R A Broglia, E Maglione, and A Vitturi, *Phys. Rev. Lett.* **48**, 1001 (1982)
[23] N Yoshinaga, A Arima and T Otsuka, *Phys. Lett.* **B143**, 5 (1984)
[24] W Frank and P O Lipas, *J. Phys.* **G16**, 1653 (1990)
[25] Y D Devi and V K B Kota, FORTRAN *programmes for spectroscopic calculations in (sdg)-boson space: The package SDG-IBM1* (PRL-TN-90-68, 1990)
[26] K Allaart, E Boeker, G Bonsignori, M Savoia and Y K Gambhir, *Phys Rep.* **169**, 209 (1988)
[27] S Pittel and J Dukelsky, *Phys. Lett.* **B128**, 9 (1983)
[28] E Cheifetz, R C Jared, S G Thompson and J B Wilhelmy, *Phys. Rev. Lett.* **25**, 38 (1970)
[29] F K Whon, H Mach, M Moszyński, R L Gill and R F Casten, *Nucl. Phys.* **A507**, 141c (1990)
[30] M Liang, H Ohm, B De Sitter, K Sistemich, B Fazekas and G Molnár, *Z. Phys.* **A340**, 223 (1991)
[31] C M Lederer and V S Shirley, (eds) *Tables of isotopes* (Seventh Ed.) (John Wiley, 1978)
[32] S Raman, C H Malarkey, W T Milner, C W Nestor and P H Stelson, *At. Data Nucl. Data Tables* **36**, 1 (1987)
[33] J B French, *in Multipole and sum rule methods in spectroscopy, Proc. Int. School of Physics.* Enrico Fermi, Course 36, Varenna, 1965, edited by C Bloch (Academic Press, New York, 1966) p. 278
[34] P Ring and P Schuck, in *The nuclear many-body problem* (Springer-Verlag, New York. 1980)
[35] P O Lipas, P Von Brentano and A Gelberg, *Rep. Prog. Phys.* **53**, 1355 (1990)
[36] F Iachello, G Puddu, O Scholten, A Arima and T Otsuka, *Phys, Lett.* **B89**, 1 (1979)
[37] W Frank, P von Brentano, A Gelberg and H Harter, *Phys. Rev.* **C38**, 2358 (1988)
[38] Y D Devi and V K B Kota, *Phys. Rev.* **C45**, 2238 (1992)
[39] K Kumar, *Nucl. Phys.* **A231**, 189 (1974)
[40] S K Khosa, P N Tripathi and S K Sharma, *Phys. Lett.* **B119**, 257 (1982)
[41] P Federman and S Pittel, *Phys. Lett.* **B77**, 29 (1978)
[42] H Mach, F K Wohn, G Molnár, K Sistemich, John C Mill, M Moszyński, R L Gill, W Krips and D S Brenner, Nucl. Phys. **A 523**, 197 (1991)
[43] P Federman and S Pittel, *Phys. Lett.* **B69**, 385 (1977)
[44] A de Shalit and M Goldhaber, *Phys. Rev.* **92**, 1211 (1953)
[45] H C Wu, *Phys. Lett.* **B110**, 1 (1981)
[46] M Sambataro and G Molnár. *Nucl. Phys.* **A376**, 201 (1982)
[47] O Scholten, F Iachello and A Arima, *Ann. Phys. (N. Y.)* **115**, 325 (1978)
[48] B H Wildenthal, *Prog. Part. Nucl. Phys.* **11**, 5 (1984)
[49] C R Praharaj and S B Khadkikar, *Phys. Rev. Lett.* **50**, 1254 (1983)
[50] A K Rath, Ph. D Thesis, (Institute of Physics, Bhubaneswar, 1991), unpublished
[51] R Sahu and S P Pandya, *Nucl. Phys.* **A529**, 20 (1991)

PRAMANA
— journal of
physics

© Printed in India

Vol. 44, No. 4,
April 1995
pp. L393–L396

Giant magnetoresistance in bulk samples of $LaMnO_3$ with varying Mn^{4+} content

R MAHENDIRAN[§], R MAHESH[†], A K RAYCHAUDHURI[§] and C N R RAO[†]*
[§]Department of Physics and [†]Solid State and Structural Chemistry Unit, Indian Institute of Science, Bangalore 560 012, India
*To whom correspondence should be addressed

MS received 8 March 1995

Abstract. Magnetoresistance (MR) in bulk samples of $LaMnO_3$ has been investigated by varying the Mn^{4+} content from 10 to 33 per cent by chemical means, without aliovalent doping. With the increase in Mn^{4+} content, the structure of $LaMnO_3$ changes first from orthorhombic to rhombohedral and then to cubic and the material becomes increasingly ferromagnetic, exhibiting a resistivity maximum akin to an insulator-metal transition at T_{Peak}, just below the ferromagnetic T_c. The magnitude of MR is highest in the cubic sample (with 33% Mn^{4+}) around the T_{Peak}, and negligible in the non-magnetic orthorhombic sample (12% Mn^{4+}).

Keywords. Metal-nonmetal transition; perovskite oxides; mixed valency; giant magnetoresistance.

PACS No. 72·20

The observation of giant magnetoresistance (GMR) in films of the perovskite oxides, $La_{1-x}A_xMnO_3 (A = Ca$ or $Ba)$ has caused considerable sensation in recent months ([1]–[3]). GMR in these oxide films is found in the range 77–300 K where the material is ferromagnetic and nearly metallic. The magnitude of magnetoresistance, as defined by,

$$\mathrm{GMR} = \Delta\rho/\rho(0) = [\rho(\mathrm{H}) - \rho(0)]/\rho(0),$$

where $\rho(H)$ and $\rho(0)$ are respectively the resistivities at magnetic field H and zero field at the same temperature, has been found to be very high in some of the films. The $La_{1-x}A_xMnO_3$ ($A = Ca, Ba$) perovskites are itinerant electron ferromagnets wherein the ferromagnetism is caused by Mn^{3+}-O-Mn^{4+} interaction of the Zener-type ([4]–[6]). Because of fast electron hopping between Mn^{3+} and Mn^{4+}, the material shows metal-like resistivity behaviour as it becomes ferromagnetic, exhibiting a resistivity maximum signifying an insulator-metal (I-M) type transition, just below the ferromagnetic Curie temperature. We have explored the occurrence of GMR in bulk samples of $LaMnO_3$ without substituting La partly by an alkaline earth, but by varying the proportion of Mn^{4+} by chemical means.

$LaMnO_3$ samples were prepared by decomposing a gel, obtained by treating citric acid and ethylene diamine with the nitrate solution of La and Mn ions, at various temperatures [7]. The sample sintered at 1470 K in air for 12 hr was orthorhombic (figure 1) with $\mathbf{a} = 5{\cdot}543$ Å, $\mathbf{b} = 5{\cdot}494$ Å and $\mathbf{c} = 7{\cdot}805$ Å, containing 12% Mn^{4+} as determined by redox titrations and thermogravimetry and was a paramagnetic insulator. Progressive oxidation of the orthorhombic sample in a stream of oxygen around 1200 K transformed it to a rhombohedral ($\mathbf{a} = 5{\cdot}478$ Å, $\alpha = 60{\cdot}55°$) and then to a cubic structure ($\mathbf{a} = 7{\cdot}788$ Å) containing 24% and 33% Mn^{4+} respectively [7] as shown in figure 1. We could also prepare rhombohedral and cubic samples of $LaMnO_3$ by electrochemical oxidation ([8]–[9]). The resistivity of $LaMnO_3$ decreases with increase in Mn^{4+} content. Furthermore, the ferromagnetism as well as the resistivity maxima associated with the I-M type transition manifest themselves in $LaMnO_3$ with increasing percentage of Mn^{4+}, the magnitudes of T_c and T_{Peak} increasing with % Mn^{4+}. Accordingly, the rhombohedral and cubic samples were ferromagnetic ($T_c \sim 180$ and 220 K) and showed the resistivity maxima around 170 and 200 K (T_{Peak}) respectively (figure 2).

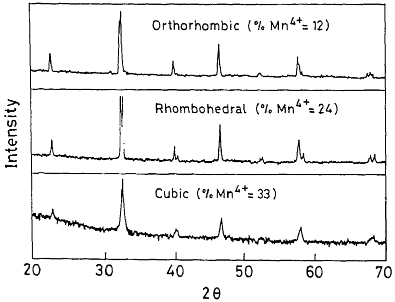

Figure 1. X-ray diffraction patterns of $LaMnO_3$ containing different percentages of Mn^{4+} showing orthorhombic, rhombohedral and cubic structures. The width of the X-ray diffraction profiles is slightly broader, specially in the cubic phase, due to the small particle size.

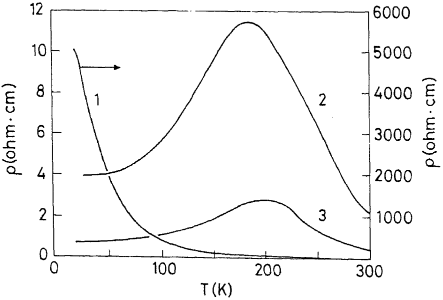

Figure 2. Temperature variation of resistivity of $LaMnO_3$ samples at zero field: 1, orthorhombic; 2, rhombohedral and 3, cubic.

Magnetoresistance in bulk samples

We have determined the extent of oxidation of $LaMnO_3$ in different samples in terms of % Mn^{4+}. This is justified because of the defect structure of this perovskite. Although traditionally considered to be anion excess, detailed investigations by employing high-resolution electron microscopy and other cognate techniques, besides density measurements, has established that the defect structure does not involve oxygen excess to produce Mn^{4+} as there is no room for the excess oxygen in the close-packed structure ([10]–[11]). In fact, all the samples have three oxygens as given by the formula. We do not observe any defect ordering, extended defects or cation displacements. Instead, there is a random distribution of cation vacancies on both the La and Mn sites. Accordingly, $LaMnO_3$ with 12% Mn^{4+} is to be written on $La_{0.98}Mn_{0.98}O_3$ or $La_{0.98}Mn^{3+}_{0.86}Mn^{4+}_{0.12}O_3$. With 24% and 33% Mn^{4+}, the compositions are $La_{0.96}Mn_{0.96}O_3$ and $La_{0.945}Mn_{0.945}O_3$ respectively.

Magnetoresistance measurements on the $LaMnO_3$ samples were carried out with bar-shaped samples (0·5 mm × 1 mm × 10 mm) of $LaMnO_3$ up to an applied field of 6 T using a superconducting solenoid. The field was applied perpendicular to the direction of the current and the resistance was measured by the 4-probe technique by the low-frequency (20 Hz) a.c. method as well as by the d.c. method.

In figure 3 we have shown the temperature variation of the per cent magnetoresistance, $100 \times \Delta\rho/\rho(0)$, for the three samples of $LaMnO_3$ (figure 1) containing different percentages of Mn^{4+}. The orthorhombic sample with ~ 12% Mn^{4+} does not show magnetoresistance above 100 K. The rhombohedral sample with 24% Mn^{4+}, on the other hand, shows 52% MR at $H = 6\,T$ with the MR peaking around 165 K. The cubic sample with 33% Mn^{4+} shows 69% MR at 6 T, the MR peaking around 170 K. In figure 4, we show the variation of $\Delta\rho/\rho(0)$ with the applied magnetic field for the three samples of $LaMnO_3$ at 4·2 K. Cubic and rhombohedral $LaMnO_3$ show MR of 49% and 43% respectively at 6 T whereas the orthorhombic phase shows hardly 17% MR. Figure 4 also suggests that there are two types of contributions to MR.

The present study demonstrates that magnetoresistance in $LaMnO_3$ becomes maximum around a temperature just around the temperature corresponding to the

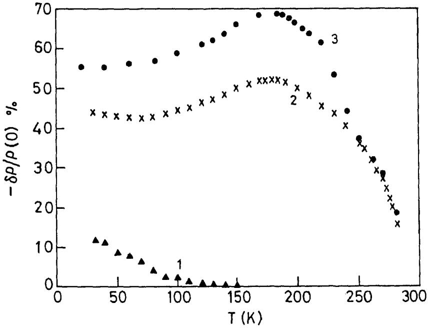

Figure 3. Temperature variation of per cent magnetoresistance, $100 \times \Delta\rho/\rho(0)$, of $LaMnO_3$ samples at $H = 6\,T$: 1, orthorhombic; 2, rhombohedral and 3, cubic.

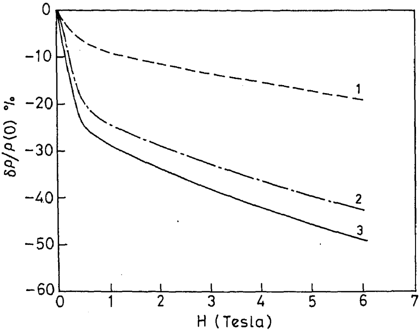

Figure 4. Variation of per cent magnetoresistance of $LaMnO_3$ samples with magnetic field at 4·2 K: 1, orthorhombic; 2, rhombohedral and 3, cubic.

resistivity maximum, T_{peak}, or the ferromagnetic T_c, both of which are related to the Mn^{4+} content. It is noteworthy that in the ferromagnetic regime, when the resistivity decreases with decreasing temperature, the material is really not a metal in the conventional sense. While the electrons become itinerant because of fast hopping between Mn^{3+} and Mn^{4+} ions below T_c, it is likely that scattering of conducting electrons by ferromagnetic clusters is the important factor.

References

[1] K Chanara, T Ohno, M Kasai and Y Kozono, *Appl. Phys. Lett.* **63**, 1990 (1993)
[2] R von Helmolt, J Wecker, B Holzapfel, L Schultz and K Samwer, *Phys. Rev. Lett.* **71**, 2331 (1993)
[3] S Jin, T H Tiefel, M McCormack, R A Fastnacht, R Ramesh and L H Chen, *Science* **264**, 413 (1994)
[4] G H Jonker and J H van Santen, *Physica* **16**, 337 (1950)
[5] E O Wollan and W C Koehler, *Phys. Rev.* **100**, 545 (1955)
[6] J B Goodenough, *Prog. Solid State Chem.* **5**, 149 (1971)
[7] M Verelst, N Rangavittal, C N R Rao and A Rousset, *J. Solid State Chem.* **104**, 74 (1993)
[8] C N R Rao, *Chemical approaches to the synthesis of inorganic materials* (John Wiley, New York and Wiley Eastern, New Delhi, 1994)
[9] R Mahesh, K R Kannan and C N R Rao, *J. Solid State Chem.*, **114**, 294 (1995)
[10] M Hervieu, R Mahesh, N Rangavittal and C N R Rao, *Euro. J. Solid State Inorg. Chem.* (1995) In print
[11] J A M van Roosmalen and E H P Cordfunke, *J. Solid State Chem.* **110**, 106 (1994)

PRAMANA
— journal of
physics

RAMAN
L
BANG

© Printed in India

Vol. 44, No. 5,
May 1995
pp. 397–404

Effect of nonlocal elasticity on internal friction peaks observed during martensite transformation

ALI DOĞAN
Firat Üniversitesi, Fen-Ed. Fak, Fizik Bölümü, 23169, Elaziğ Türkey

MS received 28 September 1994

Abstract. The internal friction associated with martensite is calculated using elastic interaction energy between dislocations and solute atoms in nonlocal elasticity during low temperature aging process. The relaxation strength depends on the lattice parameter of the crystal as well as the temperature and the heating rate. The peak heights increase with increasing lattice parameter. The proposed model can demonstrate more realistically the shape of the change of internal friction versus temperature when nonlocal elasticity is included.

Keywords. Internal friction; dislocation; solute atoms; solid state phase transformation; martensite.

PACS Nos **81·30; 62·20; 62·40**

1. Introduction

In the last thirty years, internal friction associated with the martensite has been of interest to metallurgists to explain the aging and tempering process of martensite with subambient M_s temperature, i.e. martensite starting temperature [1–4]. There are three types of processes viz... relaxation, aging and tempering where the redistribution of solute atoms such as carbon can take place at temperatures as low as 230 K in virgin lenticular martensite having body-centered-tetragonal (b.c.t) lattice [4–16]. The low frequency internal friction evolution of Fe-28 Ni-0·2 C lenticular martensite during low temperature aging has been simulated by four peaks at different temperatures and a model has been proposed to describe the internal friction evolution of the process concerning with the diffusion of carbon atoms to dislocations at low temperature [4, 17]. The classic (local) continuum theory of elasticity was used for computation of the internal friction peaks in the models in question. Therefore, the peak heights and shapes did not exactly fit the experimental results.

This paper determines the effects of nonlocal elasticity on the internal friction peak heights observed during the low temperature aging process considering the elastic interaction energy between a dislocation and a solute atom in nonlocal elasticity.

2. Nonlocal elasticity effect and internal friction model

The basic idea of nonlocal elasticity is that the theory takes into account long-range, i.e. nonlocal interactions in the determination of the elastic stresses originating from a displacement field, eliminating the stress singularities which appear in classic (local) elasticity. The theory is linear in strain, like the classical (local) continuum theory of elasticity. By considering the interaction due to the size effect of a solute atom as being due to the effect of a dilatation centre, in a linear, isotropic, nonlocal elastic medium, the elastic interaction energy between an edge dislocation and a solute atom in nonlocal elasticity is obtained as [18, 19]

$$V_{nc}(r) = -\frac{\mu b(1+\nu)}{3\pi(1-\nu)}\Delta V\frac{\sin\theta}{r}\left[1-\exp(-k_0^2r^2/a^2)\right], \tag{1}$$

where a is the lattice constant, k_0 is the attenuation factor, b is Burger's vector of dislocation and r, θ represents the plane polar coordinates, $\Delta V = V - V_0$ is the volume change due to an impurity defect which can be obtained from experimental data or atomistic theories of the region surrounding the defect [20]. The shear moduli and Poisson's ratio of the slip system $\{111\}$, $\langle 110\rangle$ are determined by [21]

$$\mu = 3C_{44}(C_{11}-C_{12})/[4C_{44}+C_{11}-C_{12}],$$

and

$$\nu = C_{12}/2(C_{12}+C_{44}). \tag{2}$$

If a goes to zero, (1) reverts to the result of classical elastic theory [4, 22]

$$V_c(r) = -\frac{\mu b(1+\nu)}{3\pi(1-\nu)}\Delta V\frac{\sin\theta}{r}. \tag{3}$$

Under a force F an atom migrating by thermal agitation acquires a steady drift velocity v (in addition to its random diffusion movement) in the direction of F, where D is coefficient of diffusion. This velocity may be described by the equation which is called Einstein's formula

$$v = DF/kT, \tag{4}$$

where k is Boltzmann's constant and F is given by

$$F = -\mathrm{d}V_{nc}(r)/\mathrm{d}r. \tag{5}$$

This force attracts a solute atom to a dislocation. From (1), (4) and (5), a steady drift velocity of an atom can be obtained as

$$v = \frac{D}{kT}\frac{\mu b(1+\nu)}{3\pi(1-\nu)}\Delta V\frac{\sin\theta}{r^2}\left\{\left[1+\frac{2k_0^2r^2}{a^2}\right]\exp\left(-\frac{k_0^2r^2}{a^3}\right)-1\right\}. \tag{6}$$

For small r the exponential term can be approximated to the first two terms of the series expansion and (6) may be evaluated to give

$$v = \frac{2DA}{kT}(k_0/a)^2, \tag{7}$$

where A is the interaction potential constant and is given by [23]

$$A = [\mu b(1+\nu)\Delta V\sin\theta/3\pi(1-\nu)]. \tag{8}$$

The atoms originally at a distance r from the dislocation reach it in a time given approximately by [23]

$$t = 2\pi r/v \tag{9}$$

Using (7), (9) is rewritten as

$$t = \frac{\pi k T}{DA}(a/k_0)^2 r. \tag{10}$$

Using an elastic interaction potential mentioned above, we have found that the number of defects $n(t)$ which has arrived at a unit length of dislocation at time t is given by

$$n(t) = 4\pi r^2 N_0. \tag{11}$$

From (10) and (11), $n(t)$ is found to be

$$n(t) = \frac{4}{\pi} N_0 (k_0/a)^4 (DAt/kT)^2 \tag{12}$$

where N_0 is the initial number of defects per unit volume. This expression is similar to that of Koehler–Granato–Lücke (KGL) string model [24, 25]. The term k_0/a in (12) comes from the nonlocal elastic interaction between an edge dislocation and a solute atom in low temperature aging process.

The theory of internal friction due to dislocation damping has been studied by numerous authors in the second quarter of this century [24, 25]. In these models it is assumed that the dislocation is fixed at certain places by pinning points and under the influence of external periodic shear stress the free dislocation segments or loops between the pinning points undergo forced vibration. Using the theory for damping of a specimen containing dislocations, an internal friction expression can be written as [24–29]

$$\delta = \Delta \frac{\omega\tau}{1 + (\omega\tau)^2} \tag{13}$$

where Δ is relaxation strength, ω the angular frequency of the applied stress and τ the relaxation time. The relaxation strength is given by

$$\Delta = \frac{16}{\pi^4} \lambda L^2, \tag{14}$$

where λ is dislocation density and L is the loop length of the dislocation line segments. In the case of dislocated martensite, when diffusion of interstitial atoms occurs at low temperatures, the most significant change in the dislocation structure of a specimen is the change in the loop length due to the adding of the point defect pinners and it will affect the value of the internal friction. Thus (13) and (14) can be written directly in terms of the number of pinners added to a dislocation segment during low temperature aging. It can be written as a relationship between L_d, L_0, n_d and n_0 as follows

$$L_d = \frac{L_0}{1 + (n_d/n_0)}, \tag{15}$$

where L_d is the average length with the added pinners, n_d the number of defect pinners added per unit length, n_0 the original number of pinners per unit length of the dislocation line and L_0 the original loop length. Substituting (15) in (14), and taking $D = D_0\exp[-E/kT]$, (14) becomes

$$\Delta = (16/\pi^4)\Lambda L_0^2 \frac{1}{\{1 + [(B_{01}t/kT)\exp(-E/kT)]^2\}^2} \tag{16}$$

where E is the activation energy for the diffusion of the interstitial atoms and

$$B_{01} = (2/\sqrt{\pi})(N_0/n_0)^{1/2}(k_0/a)^2 D_0 A. \tag{17}$$

It can be seen from (16) and (17) that the relaxation strength is the function of the temperature and heating rate and the lattice parameter of the crystal.

For a Debye peak, the following conditions is satisfied at peak temperature T_p

$$\omega\tau = 1 \tag{18}$$

since

$$\omega\tau = \omega\tau_0\exp(Q/kT) \tag{19}$$

where τ_0 is the pre-exponential factor of relaxation time and Q the activation energy. Combining (14), (16), (17) and (19) one could obtain (13) as a function of temperature

$$\begin{aligned}\mathrm{IF} &= \delta/(8\pi^4)\Lambda L_0^2 \\ &= \frac{1}{\{1 + [(C_0'/kT)\exp(-E/kT)]^2\}^2}\,\mathrm{sech}\left[\frac{Q}{k}\left(\frac{1}{T} - \frac{1}{T_p}\right)\right],\end{aligned} \tag{20}$$

where

$$C_0' = B_{01}t. \tag{21}$$

On the other hand, the constant of C_0 in the expression of internal friction in the classical continuum theory is given by [4]

$$C_0 = 3^{3/2}(\pi/2)^{1/2}(N_0/n_0)^{3/2} D_0 At. \tag{22}$$

Comparing (17), (21) and (22), a relationship between C_0' and C_0 may be described by the equation

$$C_0' = (27\pi^2/4)^{-1/2}(n_0/N_0)(k_0/a)^2 C_0, \tag{23}$$

where C_0' and C_0 terms represent the contributions originated from nonlocal elasticity and classical elasticity theory, respectively.

3. Numerical results and comparison

A computer simulation was performed in order to calculate the internal friction peaks of virgin martensite during low temperature aging using classical and nonlocal elastic theory. For this purpose the values of the parameters A, D_0 were taken as one unit. The values of C_0 for $k_0 = 1{\cdot}65$ and $N_0/n_0 = 0{\cdot}86$ were obtained as 5·43 k, 2·17 k, 1·43 k, 0·62 k and 0·28 k at the aging times k, 0·48 k, 0·26 k, 0·12 k and 0·05 k by using (22). Using these parameters and $E = 0{\cdot}90$ k, the internal friction peaks obtained for classical theory are shown in figure 1. It is seen from this figure that the internal friction peaks are situated at temperature units of 1·1, 1·7, 2·1, 2·56 and 4·0. The values of the activation energy Q obtained directly from fittings are about 7·3 k, 5·3 k, 30·8 k, 25·9 k and 33·4 k units for

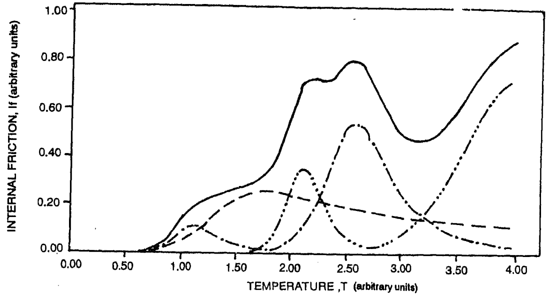

Figure 1. Internal friction temperature behaviour in classical continuum theory.

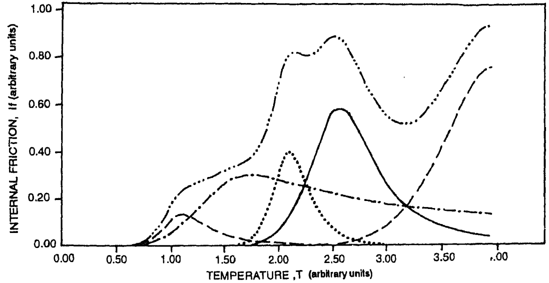

Figure 2. Internal friction temperature behaviour in nonlocal continuum theory. Here the lattice parameter is $a = 0{\cdot}60$. Other parameters are kept as constant.

the peak temperatures mentioned. Figure 2 represents the internal friction peaks obtained from the nonlocal elastic theory at the lattice parameter $a = 0{\cdot}60$ unit. In this case all parameters except lattice parameter in (20), (21) and (23) were kept constant. This figure shows that the values of internal friction are slightly higher than those of figure 1. The internal friction curves obtained from the nonlocal elastic theory were plotted again for various lattice parameters as shown in figure 3. Comparison of the experimental results (figure 4) with figure 3 indicates that $a = 0{\cdot}60$ gives a satisfactory fitting. It is seen from these figures that the shapes of the curves are deformed for the other values of the lattice parameters. The agreement at lower temperatures is reasonable but deviates drastically at higher temperatures. This deviation comes from the assumption in which the $T_p = 2{\cdot}10$ and $2{\cdot}56$ peaks have nearly the same activation energies. However, the results obtained show that the application of the nonlocal elastic theory to the internal friction is successful. The classical continuum theory has

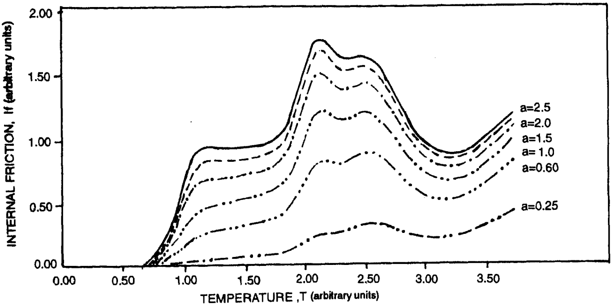

Figure 3. Effect of lattice parameter on internal friction temperature behaviour in nonlocal continuum theory.

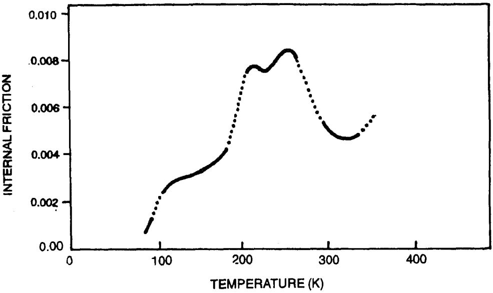

Figure 4. Internal friction of the alloy Fe-28 Ni-0·2C during heating from 82 K to 350 K.

the problem of singularities and gives lower values of the internal friction. The present method, in which the long-range interatomic interactions are taken into account by a nonlocal continuum theory with the dislocation and lattice, overcomes singularities in addition to the early method [3, 4, 17] and gives satisfactory results for internal friction.

4. Results

Based on the process which has been proposed for the low temperature aging of the martensite, solute atoms diffusing to and interacting with dislocations in nonlocal elasticity, a computer simulation of the internal friction peaks of the martensite phase during low temperature aging can be performed. From the results obtained in this study, the following main conclusions can be drawn:

1. Including the nonlocal elastic theory into calculation of the internal friction has given rise to changing of the number of defects $n(t)$ which has been arrived at a unit length of dislocation at time t. In this case the relaxation strength has also been changed.
2. From comparison of the internal friction curves it is seen that the relaxation strength depends on the lattice parameter in addition to temperature and heating rate of the sample.
3. It is found that the peak heights of the internal friction are also changed by the lattice parameter of the sample at the same peak temperatures.

Acknowledgements

The author would like to thank Professors H Holloway, University of Florida and J E Greene, University of Illinois, Urbana, for their valuable critical reviews of the manuscript. Thanks are also due to Y Liu from Helsinki University of Technology, Espoo, Finland, for providing us with a copy of a paper which initiated my interest in this subject.

References

[1] C Prioul and M Carrard, *J. Phys. (Paris) Colloq.* **C5**, Suppl. 10, 1067 (1981)
[2] C Prioul, *J. Phys. (Paris)* **10**, 665 (1985)
[3] Y Liu, K Ullako and J Pietikainen, *Proc. XXIV Annual Conf. Finnish Phys. Soc.* Rep 7–90, 14: 9, Tempere, Finland (1990)
[4] Y Liu, K Ullako and J Pietikainen, *Proc. 6th Int. Conf. on mechanical behaviour of materials*, (Kyoto, Japan, 1991) p. 123
[5] J R Genin and P A Flinn, *Metall. Soc.* **242**, 1419 (1968)
[6] N DeCristofaro, R Kaplow and W S Owen, *Metall. Trans.* **A9**, 821 (1978)
[7] P C Chen, B O Hall and P G Winchell, *Metall. Trans.* **A11**, 1323, (1980)
[8] P C Chen and P G Winchell, *Metall. Trans.* **A11**, 1333 (1980)
[9] S Nagakura and M Toyoshima, *Trans. Jpn. Inst. Met.* **20**, 100 (1979)
[10] K A Taylor, L Chang, G B Olson, G W Smith, M Cohen and J B Vander Sande, *Metall. Trans.* **A20**, 2717 (1989)
[11] C Prioul, M Carrard, L Hyspecka, J Plusquellec and P Azou, *Scr. Metall.* **13**, 523 (1979)
[12] P Grégoire, C Dagbert, P Pahuta, J Galland and L Hyspecka, *Proc. ICOMAT-1990, Sydney*, Australia, Materials Science Forum, Switzerland, 56–58, 213 (1990)
[13] A M Sherman, G T Eldis and M Cohen, *Metall. Trans.* **A14**, 995 (1983)
[14] G B Olson and M Cohen, *Metall. Trans.* **A14**, 1057 (1983)
[15] C A V de A Rodrigues, C Prioul and L Hyspecka, *Metall. Trans.* **A15**, 2193 (1984)
[16] P G Winchell and M Cohen, *Trans Am. Soc. Metals*, **55**, 347 (1962)
[17] Y Liu, *Acta Metall. Mater.* **41**, 3277 (1993)
[18] R Wang, *J. Phys.* **D23**, 263 (1990)
[19] R Wang and K L Pan, *Phys. Status Solidi* **B163**, 75 (1991)
[20] R Wang, G L Chen and Z Q Sun, *Metall. Trans.* **A23**, 3115 (1992)
[21] A Kelly, *Strong solids* (Clarendon Press, Oxford, UK, 1973) 27
[22] J W Christian, *Theory of transformation in metal and alloys; Equilibrium and general kinetic theory*, (Pergamon Press, New York, 1975) part 1
[23] A H Cottrell and B A Bilby, *Proc. Phys. Soc.* **A62**, 49 (1949)
[24] J S Koehler, *Imperfections in nearly perfect crystals*, edited by W Shockley *et al* (John Wiley, New York, 1952)

[25] K Lücke and A V Granato, *Phys. Rev.* **B24**, 6991 (1981)
[26] S Koshimuzu and W Benoit, *J Phys.* (*Paris*), **43**, C4-679 (1982)
[27] A Doğan, Doğa-Tr. *J. Phys.* **16**, 439 (1992)
[28] A Doğan, *Indian J. Phys.* **A67**, 193 (1993)
[29] C M Zener, *Elasticity and anelasticity of metals* (Chicago Press, Chicago, 1948)

PRAMANA
— journal of
physics

© Printed in India

Vol. 44, No. 5,
May 1995
pp. 405–410

Dielectric study of aqueous solution of acetonitrile

S N HELAMBE, M P LOKHANDE, A C KUMBHARKHANE,
S C MEHROTRA and S DORAISWAMY*
Department of Physics, Dr. Babasaheb Ambedkar Marathwada University, Aurangabad 431 004, India
*Chemical Physics Group, Tata Institute of Fundamental Research, Bombay 400 005, India

MS received 2 March 1995

Abstract. Time domain reflectometry method has been used in the frequency range of 10 MHz to 10 GHz to determine dielectric properties of aqueous solutions of acetonitrile in temperature range of 0 °C to 40 °C. The calibration method based on the least squares fit method has been used. The excess permittivity, activation energy, Kirkwood correlation factor and activation energy of acetonitrile-water system have also been determined. The dielectric data show that acetonitrile molecules interact such that the dipoles have a tendency to remain antiparallel.

Keywords. Dielectrics; microwaves; aqueous solutions; acetonitrile; relaxation time; Kirkwood factor.

PACS No. 77·22

1. Introduction

The acetonitrile liquid is a nonhydrogen bonded system with large value of dipole moment. The dielectric data [1–6] show that dipoles of acetonitrile molecules have a tendency to remain antiparallel in liquid state. The system will interact with hydrogen-bonded liquid (such as water) through long-range forces like dipole-dipole interactions. The dielectric relaxation study of acetonitrile-water system should provide information regarding such kind of interactions. Although dielectric studies of the system have been carried out by various groups, they provide information in limited frequency region and temperature. The detailed information about the excess permittivity and thermodynamic properties cannot be obtained by the earlier studies. The objective of the present paper is to report the detailed dielectric work on the system using the time domain technique in temperature range of 0 °C to 40 °C. The Luzar [7] model is also used to get information regarding the interaction in the system.

2. Experimental

Materials:

A spectrograde acetonitrile (MeCN) (E Merc) was used as such without further purification, whereas water was used after double glass distillation and deionization. The solutions were prepared by mixing the MeCN and water in volume. The volume fraction, V_i, of the MeCN was calculated as follows.

$$V_i = \frac{\text{Vol. of MeCN}}{\text{Vol. of MeCN} + \text{Vol. of water}} \tag{1}$$

Apparatus:

The experimental set up used for the study has already been described earlier [8, 9]. In this experimental technique, a 200 mv pulse having rise time 25 ps and repetitive frequency of 1 kHz is generated by tunnel diode pulse generator. The pulse was transmitted through a 3·5 mm coaxial transmission line having characteristic impedance of 50 Ω. The cell has inner and outer dimensions of 1·52 mm and 3·5 mm, respectively. The effective pinlength of inner conductor was 0·486 mm. The reflected pulses with and without sample were digitized with 1024 points in the time window of 5 ns. The recorded pulses were added and subtracted in the oscilloscope memory, and were transferred to PC/XT via GPIB for further numerical analysis.

The complex reflection function ρ^* of the sample liquid was determined through Fourier transforming the measured pulses [8–11].

The dielectric parameters were determined by the method as described earlier [12].

3. Results and discussion

The dielectric parameters obtained are summarized in table 1 alongwith literature values wherever available [6] for comparison. In table 1, the numbers in bracket denote the uncertainty in the last significant digit as obtained by the nonlinear least squares fit method described earlier [9]. This does not include instrumental error which is estimated to be about 2%. The static dielectric constant (ε_0) and relaxation time (τ) for pure acetonitrile are in good agreement with earlier work [5]. In acetonitrile-water system, it is observed that under experimental error the dielectric relaxation can be described by the Debye model ($\alpha = 0$, $\beta = 1$).

The structural information about the liquids by dielectric relaxation parameter, can be obtained either by Kirkwood correlation or excess parameters. It is not possible to obtain correlation parameters in the mixture for both solute and solvent from a single value of permittivity. One may assume the existence of the effective correlation factor, g^{eff} defined as [14]

$$\frac{4\pi N}{9KT}\left(\frac{\mu_a^2\rho_a}{M_a}x_a + \frac{\mu_w^2\rho_w}{M_w}(1-x_a)\right)g^{\text{eff}} = \frac{(\varepsilon_{0\text{m}} - \varepsilon_{\infty\text{m}})(2\varepsilon_{0\text{m}} - \varepsilon_{\infty\text{m}})}{\varepsilon_{0\text{m}}(\varepsilon_{\infty\text{m}} + 2)^2} \tag{2}$$

where μ_a, μ_w are dipole moments of acetonitrile and water molecules, M_a, M_w are corresponding molecular weights, ρ_a, ρ_w are corresponding densities, x_a is the volume fraction of the acetonitrile molecule in the mixture, $\varepsilon_{0\text{m}}$ and $\varepsilon_{\infty\text{m}}$ are permittivities at low and high frequency limits, respectively. The values of g^{eff} are given in table 2. The Kirkwood correlation factor g^{eff} decreases as the concentration of acetonitrile increases. It is interesting to note that the values of g^{eff} are less than one in acetonitrile rich region. This indicates that –CN interacts such that the dipoles in the liquid align in antiparallel direction unlike –OH bond in water.

The excess permittivity ε^{E} is defined [9, 15] as

$$\varepsilon^{\text{E}} = (\varepsilon_0 - \varepsilon_\infty)_{\text{m}} - [(\varepsilon_0 - \varepsilon_\infty)_{\text{a}} x_{\text{a}} + (\varepsilon_0 - \varepsilon_\infty)_{\text{w}}(1 - x_{\text{a}})] \tag{3}$$

where subscripts to the brackets m, a, w correspond to mixtures, acetonitrile and water respectively. Excess permittivity gives an idea regarding interaction between solute and water. The plots of excess permittivity vs concentration of water at different temperatures are shown in figure 1.

Table 1. Dielectric parameters for acetonitrile-water system at different temperatures.

Vol % of MeCN in water V_i	Mole fract. of MeCN	0°C			10°C		
		ε_0	ε_∞	τ(ps)	ε_0	ε_∞	τ(ps)
		0°C				10°C	
0**	0·000	87·9	3·0	17·6	83·9	3·0	12·7
10	0·037	83·1(1)	3·0	17·8(3)	78·9(1)	3·0	13·9(2)
20	0·079	83·2(1)	3·0	18·8(2)	76·0(1)	3·0	13·8(1)
30	0·129	74·6(1)	3·0	18·7(2)	74·0(1)	3·0	13·9(2)
40	0·187	74·7(1)	3·0	19·6(2)	67·7(1)	3·0	14·6(2)
50	0·256	71·0(1)	3·0	18·1(1)	61·0(1)	3·0	13·8(2)
60	0·341	64·7(1)	3·0	15·9(1)	58·7(1)	3·0	12·9(1)
70	0·440	56·8(1)	3·0	14·3(2)	50·4(1)	3·0	10·0(2)
80	0·579	53·1(1)	3·0	12·7(1)	47·4(1)	3·0	9·5(2)
90	0·756	44·6(1)	3·0	9·5(1)	40·0(1)	3·0	6·0(1)
100	1·000	42·8(1)	3·0	8·8(2)	39·2(1)	3·0	3·6(1)
			25°C			40°C	
0*	0·000	78·3	3·0	8·2	73·1(1)	3·0	5·8(1)
10	0·037	76·8(1)	3·0	10·9(2)	73·8(1)	3·0	6·5(1)
20	0·079	74·9(1)	3·0	10·6(1)	70·4(1)	3·0	6·6(1)
30	0·129	69·7(1)	3·0	11·2(1)	68·3(1)	3·0	6·7(1)
40	0·187	66·8(1)	3·0	10·8(1)	65·2(1)	3·0	6·6(1)
50	0·256	54·5(1)	3·0	11·2(2)	60·7(1)	3·0	6·5(1)
60	0·341	52·3(1)	3·0	10·6(1)	52·6(1)	3·0	6·1(1)
70	0·440	52·0(1)	3·0	9·6(1)	50·7(1)	3·0	6·0(1)
80	0·579	47·3(1)	3·0	8·8(1)	46·0(1)	3·0	5·5(1)
90	0·756	41·4(1)	3·0	5·4(1)	34·7(1)	3·0	3·2(1)
100	1·000	37·0(1) 35·9*	3·0	3·4(1) 3·2*	33·1(1)	3·0	2·5(1)

Number in brackets denote the error obtained from least squares fit method. e.g. 37·0(1) means 37·0 ± 0·1.
*Reported in ref. [6]
**The values of ε_0 and τ are taken from Kaatze *et al* [13] for pure water to be used as calibrating liquid.

Figure 1 shows the values of excess permittivity which has a tendency to be negative in acetonitrile rich region and tends to be positive in water rich region. This indicates that there is formation of multimer structure at lower concentration of water in acetonitrile. At these lower concentrations of water, there will be creation of new forms of structures which will include a solvated dimer [15], that will have essentially zero dipole moment and hence will lead to decrease in total permittivity. In water rich region there may be a formation of monomeric structures. The monomeric structures will essentially have dipoles due to which total permittivity increases. The behaviour of structural changes with concentration of water in acetonitrile is similar at different temperatures with some change in magnitude.

The values of enthalpy of activation ΔH at different concentrations are also determined [16] and are given in table 3.

Table 2. Values of g^{eff} for acetonitrile-water system at different temperatures.

Mole fract. of MeCN in water	0°C	10°C	25°C	40°C
0·000	2·64(15)	2·67(16)	2·62(15)	2·48(14)
0·037	2·40(14)	2·40(14)	2·47(14)	2·36(14)
0·079	2·29(13)	2·22(13)	2·31(13)	2·18(13)
0·129	1·97(11)	2·11(12)	2·06(12)	2·04(12)
0·187	1·90(11)	1·86(11)	1·88(11)	1·88(11)
0·256	1·74(10)	1·62(9)	1·76(10)	1·69(10)
0·341	1·53(9)	1·55(9)	1·37(8)	1·47(8)
0·440	1·29(7)	1·33(8)	1·29(7)	1·31(7)
0·579	1·17(7)	1·13(6)	1·10(6)	1·10(6)
0·756	0·94(5)	0·91(5)	0·99(6)	0·87(5)
1·000	0·85(5)	0·87(5)	0·86(5)	0·81(4)

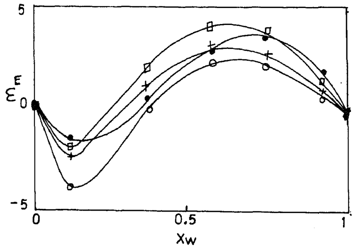

Figure 1. Variation of ε^E vs weight fraction of acetonitrile 40°C; (□), 25°C; (●), 10°C; (○), 0°C; (+).

Table 3. Activation energy for acetonitrile-water system.

Mole fract. of MeCN in water	Activation energy (ΔH) kJ/mol
0·000	17·38(12)
0·037	14·78(54)
0·079	15·45(39)
0·129	14·91(54)
0·187	16·33(38)
0·256	14·82(63)
0·341	13·77(70)
0·440	11·34(76)
0·579	11·08(67)
0·756	15·12(80)
1·000	17·13(17)

The contribution of hydrogen bonds to dielectric properties of the mixture can be studied using the model as suggested by Luzar [7]. He applied the model to water-DMSO system. We have used the same model to explain the static permittivity of the mixture. We found that our experimental data cannot be explained well by the theory because of many limitation assumed in the theory. The different parameters required in the Luzar model are dipole moments of molecules 1 (water) and 2 (acetonitrile), polarizabilities of molecules 1 and 2, energy and enthalpies of (1, 1) and (1, 2) pairs and possible number of bondings with molecule 2, average direction cosine angles between dipoles $\overline{\cos\Phi_{11}}$ and $\overline{\cos\Phi_{12}}$.

In our analysis, the best possible values of above molecular parameters for which experimental and theoretical static permittivity values give reasonably satisfactory agreement are as follows.

Dipole moment of molecule 1, $\mu_1 = 20{\cdot}09$ D
Dipole moment of molecule 2, $\mu_2 = 3{\cdot}58$ D
Polarizability of molecule 1, $\alpha_1 = 1{\cdot}47\,\text{Å}^3$
Polarizability of molecule 2, $\alpha_2 = 3{\cdot}2\,\text{Å}^3$
Bonding energy for (1, 1) pair, $E_{11} = -13{\cdot}3$ kJ/mol
Statistical volume ratio for the pair (1, 1) = 28 Å^3
Bonding energy for (1, 2) pair, $E_{12} = -10$ kJ/mol
Statistical volume ratio for the pair (1, 2) = 41 Å^3

$$\cos\Phi_{11} = \cos\Phi_{12} = 1/3$$

and number of CH_3CN molecules interacting with H_2O, is taken to be one. The values of permittivity obtained from Luzar model using the above parameters are given in table 4 along with the experimental values. It can be seen from the table that the theoretical values are in general smaller than the corresponding experimental values. It is because of the fact that the Luzar theory neglected formation of solute-solute pair. This causes more number of solute-solvant pair as calculated by the theory. It should also be noted that the value of dipole moment of water molecule is taken to be 14·2% higher than the corresponding gas phase value. The larger values of dipoles as determined by

Table 4. Comparison of experimental values of ε_0 with theoretical values obtained from Luzar model.

Mole fraction of MeCN in water	0°C		10°C		25°C		40°C	
	$\varepsilon_0^{\text{exp.}}$	$\varepsilon_0^{\text{the.}}$	$\varepsilon_0^{\text{exp.}}$	$\varepsilon_0^{\text{the.}}$	$\varepsilon_0^{\text{exp.}}$	$\varepsilon_0^{\text{the.}}$	$\varepsilon_0^{\text{exp.}}$	$\varepsilon_0^{\text{the.}}$
0·000	87·9	88·2	83·9	84·3	78·3	78·6	73·1	73·1
0·037	83·1	83·7	78·9	79·9	76·8	74·6	73·8	69·4
0·079	83·2	79·2	76·0	75·7	74·9	70·6	70·4	65·7
0·129	74·6	74·8	74·0	71·4	69·7	66·7	68·3	62·1
0·187	74·7	70·5	67·0	67·3	66·8	62·8	65·2	58·5
0·256	71·0	66·1	61·0	63·1	54·5	58·7	60·7	54·8
0·341	64·7	61·7	58·7	58·6	52·3	54·8	52·6	51·2
0·440	56·8	56·7	50·4	54·3	52·0	50·8	50·7	47·6
0·579	53·1	52·0	47·4	49·7	47·3	46·7	46·0	43·9
0·756	44·6	46·6	40·0	44·7	41·4	42·2	34·7	39·8
1·000	42·8	40·4	39·2	39·0	37·0	37·1	33·1	35·4

the Luzar theory may be due to the Kirkwood–Fröhlich (KF) model adopted in the theory. The KF model does not include the distortion polarization due to molecules present inside the cavity. This distortion polarization will induce a larger local field at the centre of the cavity.

4. Conclusions

The dielectric relaxation parameters for aqueous acetonitrile have been determined at various temperatures by the time domain reflectometry. The calibration process based on the least squares fit method gives reliable values of dielectric parameters. The dielectric data shows that acetonitrile molecules interact such that they remain antiparallel with respect to dipoles. The activation energy of the acetonitrile system is higher than the corresponding value in water. This is because of strong dipole-dipole interaction in acetonitrile. The relaxation time corresponding to acetonitrile system is much smaller than those of water system. The pair energy of acetonitrile-water system using the Luzar model is found to be −10 kJ/mol.

Acknowledgement

The authors thank Drs P B Patil and G S Raju for discussion and helpful suggestions. The financial assistance from UGC is thankfully acknowledged.

References

[1] Y P Borado, Dessertation Kharkar State University (1979)
[2] C Luhrs and G Scheiltz, *Phys. Chem.* **83**, 623 (1979)
[3] G P Gunningham, G A Vidulich and P L Kay, *J. Chem. Engg. Data* **12**, 336 (1967)
[4] G Dourcheret and M Morenas, *C. R. Hebd. Seances Acad. Sci.* **26UC**, 729 (1967)
[5] D Decroocq, *Bull. Soc. Chem.* France **1**, 127 (1967)
[6] J Barthel, K Bachhuber, R Bunchner, J B Gill and M Kleebauer, *Chem. Phys. Lett.* **167**, 63 (1990)
[7] A Luzar, *J. Mol. Liq. Cryst.* **46**, 221 (1990)
[8] S M Puranik, A C Kumbharkhane and S C Mehrotra, *J. Microwave Power and Elect. Energy* **26**, 196 (1991)
[9] A C Kumbharkhane, S M Puranik and S C Mehrotra, *J. Chem. Soc. Faraday Trans.* **87**, 1569 (1991)
[10] D Bertolini, M Cassettari, G Salvetti, E Tombari and S Veronesi, *Rev. Sci. Instrum.* **61**, 450 (1990)
[11] R H Cole, J G Berbarian, S Mashimo, G Chryssikos, A Burns and E Tombari, *J. Appl. Phys.* **66**, 793 (1989)
[12] A C Kumbharkhane, S N Helambe, S Doraiswamy and S C Mehrotra, *J. Chem. Phys.* **99**, 2405 (1993)
[13] U Kaatze and V Uhlendort, *Z. Phys. Chem. Neue. Floge* **126**, 151 (1981)
[14] A C Kumbharkhane, S M Puranik and S C Mehrotra, *J. Mol. Liq. Cryst.* **51**, 261 (1992)
[15] M Tabllout, P Lanceleur and J R Emery, *J. Chem. Soc. Faraday Trans.* **86**, 1493 (1990)
[16] H Eyring, *J. Chem. Phys.* **4**, 283 (1936)

PRAMANA
— journal of
physics

© Printed in India

Vol. 44, No. 5,
May 1995
pp. 411–417

Structural and dielectric properties of $Pb(Li_{1/4}Dy_{1/4}W_{1/2})O_3$

S BERA and R N P CHOUDHARY
Department of Physics, Indian Institute of Technology, Kharagpur 721 302, India

MS received 28 July 1994; revised 24 February 1995

Abstract. The polycrystalline samples of $Pb(Li_{1/4}Dy_{1/4}W_{1/2})O_3$ have been synthesized by high-temperature solid-state reaction techniques. Room temperature X-ray diffraction (XRD) studies of the compound provided preliminary structural data, and hence formation of a single phase desired material was confirmed. Detailed studies of dielectric constant (ε) and loss ($\tan\delta$) as a function of frequency (100 Hz to 10 kHz) at room temperature (298 K) and also as a function of temperature (liquid nitrogen to 403 K) at 10 kHz suggest that the compound undergoes a ferroelectric phase transition of diffuse type.

Keywords. High-temperature solid state reaction; X-ray and dielectric properties; diffuse phase transition.

PACS Nos 77·00; 77·80

1. Introduction

The complex compound, lead-lithium dysprosium tungstate, $Pb(Li_{1/4}Dy_{1/4}W_{1/2})O_3$, (hereafter PLDW) belongs to the perovskite family of general formula ABO_3 (A = mono or divalent, B = tri, tetra, penta or hexavalent ions). Since the discovery of ferroelectricity in $BaTiO_3$ [1], a large number of pure, or complex oxides of different structures have been studied in search of a new material with optimum properties for ferroelectric or related devices [2–7]. Among them, Pb-based compounds such as $PbTiO_3$, $PbZrO_3$, $Pb(ZrTi)O_3$ etc. have been found very useful for wide ranging applications [8–10]. Extensive literature survey on Pb-based ferroelectric compounds revealed that some of the compounds of $Pb(M_{1/4}R_{1/4}X_{1/2})O_3$ (M = alkali ions, R = rare-earth ions, X = W or, Mo) family have ferroelectric property [11], but not much work has been done on those reported and other members of the family. We undertook a study on structural, electrical, thermal and spectroscopic properties of some members of the family [12–14] and found their interesting behaviour. In this paper we report preliminary structural and detailed dielectric properties of PLDW.

2. Experimental

The polycrystalline samples of PLDW were prepared by a standard high-temperature solid-state reaction technique from the raw materials: PbO (99·99% pure, Aldrich Chemical Co.), Li_2CO_3 (99% S.D. Fine chem. Pvt. Ltd., India), Dy_2O_3 (99·99%, Indian Rare-Earth) and WO_3 (AR grade, BDH, England) in a suitable proportion. Those oxides and carbonates were thoroughly mixed in agate-mortar in alcohol for 10 h and dried. The dried powders were calcined in alumina crucible at 873 K for 15 h. The process of calcination and mixing was repeated till fine homogeneous powder of

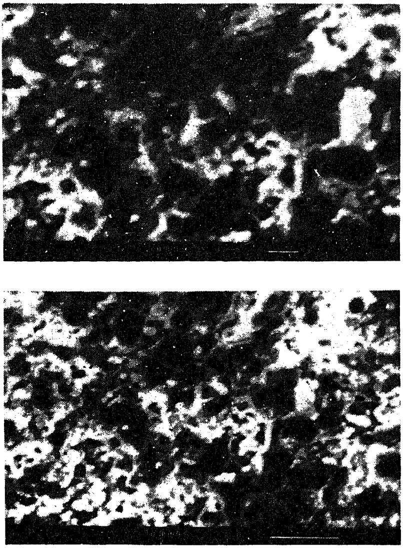

Figure 1. Scanning electron micrograph of PLDW pellet sintered at 900 K for 2 h [(a) 3 μm (b) 10 μm.]

PLDW was obtained. The formation and quality of the compound were checked with X-ray diffraction technique. Some cylindrical pellets of diameter 11·2 mm and thickness 1–2 mm were made under the isostatic pressure (6×10^7 kg/cm^2) using a hydraulic press. These pellets were then sintered in air atmosphere at 893 K for 10 h in alumina crucible. After polishing and grinding, both the flat surfaces of some pellets were electroded with air drying silver paints for electrical measurements. The density of the pellets obtained was approximately 95% of its theoretical value. This is consistent with compactness of the particles as seen in SEM photographs (figure 1), at two different magnifications which helped to estimate the grain size, shape and homogeneity.

The X-ray diffractograms of the FLDW pellet sample were taken with FeK$_\alpha$ radiation ($\lambda = 1{\cdot}9364$ Å) in a wide 2θ range ($20° \leqslant 2\theta \leqslant 110°$) with Philips powder diffractometer (PW 1710, Holland).

The dielectric constant (ε) and loss ($\tan\delta$) were obtained on sintered and electroded pellet samples as functions of frequency (500 Hz to 10 kHz) and temperature (liquid nitrogen to 403 K) using GR-1620 capacitance measuring assembly. The reliability of the data was checked repeating the experiments with different instruments (LCR-High Tester, Hioki 5530 Japan) in the same physical conditions.

Table 1. Comparison of observed and calculated *d*-values (Å) of some reflections of PLDW at room temperature.

h	k	l	d_{obs}	d_{cal}	I/I_0
1	1	1	4·7360	4·7360	11
0	2	0	4·0892	4·0892	3
2	1	1	2·9013	2·9013	100
1	2	4	2·4786	2·4776	6
2	0	4	2·3718	2·3748	3
2	1	5	2·0562	2·0570	20
2	1	7	1·6801	1·6810	25
1	2	8	1·5855	1·5851	2
2	2	8	1·4558	1·4552	7
2	5	3	1·3916	1·3911	1
2	0	10	1·3032	1·3033	7

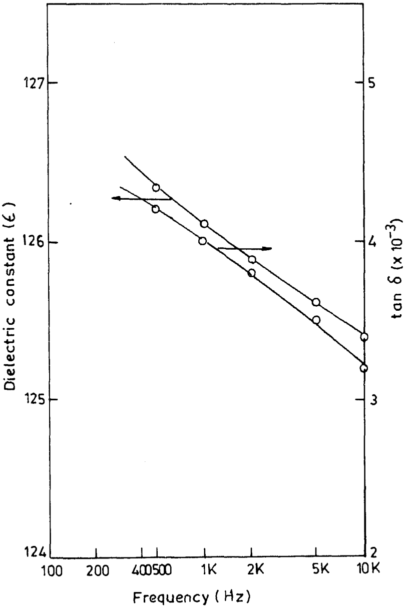

Figure 2. Variation of dielectric constant (ε) and loss ($\tan\delta$) of PLDW as a function of frequency at room temperature (298 K).

3. Results and discussion

All the peak-profiles of the sample were indexed with different cell configuration. Out of them, a suitable cell with its lattice parameters was selected. The lattice parameters were then refined using a least-squares technique. Using refined cell parameters, indexed reflections and wavelength of FeK$_\alpha$ radiation, interplanar spacings (d) of all the reflections were calculated and compared with their observed values (table 1). A good agreement between calculated and observed d-values suggests that the compound is orthorhombic with lattice parameters: $a = 6{\cdot}3582$ (10) Å, $b = 8{\cdot}1786$ (10), $c = 14{\cdot}2888$ (10) Å. It was not possible to find out the space group with very limited data. The linear particle size (L) of the sintered sample, calculated for strong, medium and weak reflections, scattered in wide 2θ range using Scherrer's equation [15] was approximately 25 nm which is consistent with the values obtained from particle size analyser.

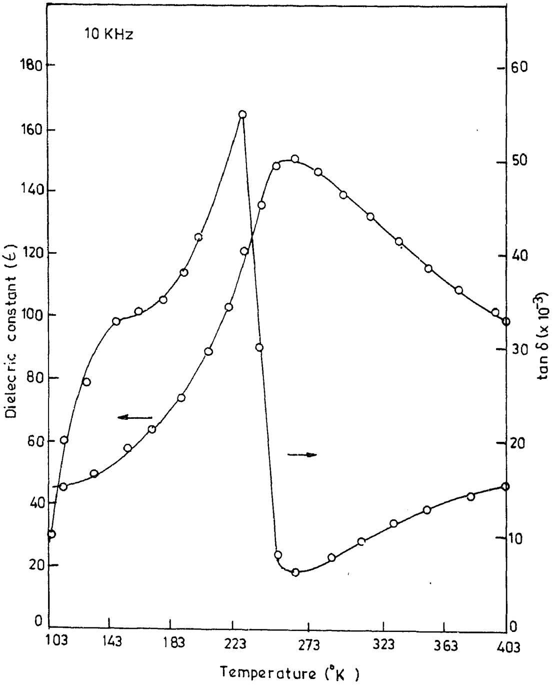

Figure 3. Variation of dielectric constant (ε) and loss (tan δ) of PLDW as a function of temperature at 10 kHz.

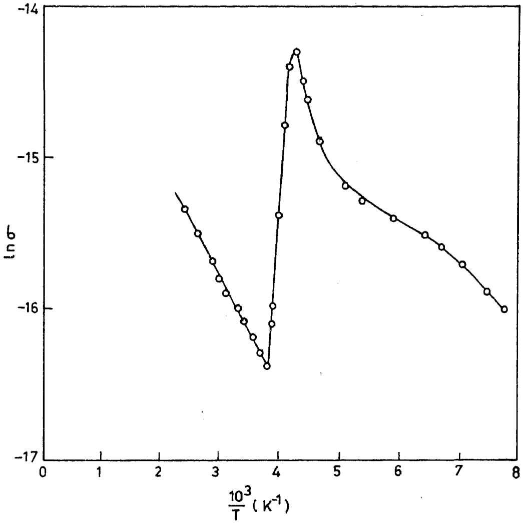

Figure 4. Variation of conductivity (log σ) as a function of inverse of absolute temperature ($1/T$) of PLDW.

Figure 2 gives the variation of ε and tan δ with frequency. Both these parameters show the normal behaviour of dielectrics because they decrease very slowly (from $\varepsilon = 126{\cdot}34$ (at 500 Hz) to 125·38 at 10 kHz), tan $\delta = 0{\cdot}0042$ to 0·003.

Figure 3 shows the variation of ε and tan δ with temperature. The dielectric constant increases asymptotically. With rise in temperature, ε reaches its maximum value of 138 (at 10 kHz) at 263 K and then it starts decreasing almost linearly to 95 at 416 K. But tan δ shows abnormal behaviour. It first increases with its maximum value at temperature 230 K and then it drops to minimum at 253 K and then starts increasing slowly. This type of variation has been observed in $KNbO_3$ ceramics [16] also. As the transition temperature in PLDW was found below room temperature ($T_c = 263$ K), we do not expect any hysteresis loop at room temperature in the paraelectric phase. Further it is not possible to get proper hysteresis loop in our complex lossy ceramic samples in the low temperature phase. However, we have confirmed the reported ferroelectric phase transition in some members of the family on the basis of dielectric anomaly. We have also observed dielectric anomaly in other members of the family [12–14] which is consistent with the ferroelectric phase transition.

Figure 4 shows the variation of ac electrical conductivity (i.e. log σ) with inverse of temperature ($1/T$). It shows the change in slope at 262 K which corresponds to the transition temperature of the sample. The activation energy (E_A) was calculated using the formula $\sigma = \sigma_0 \exp(-E_A/K_B T)$, where K_B is the Boltzman constant of value

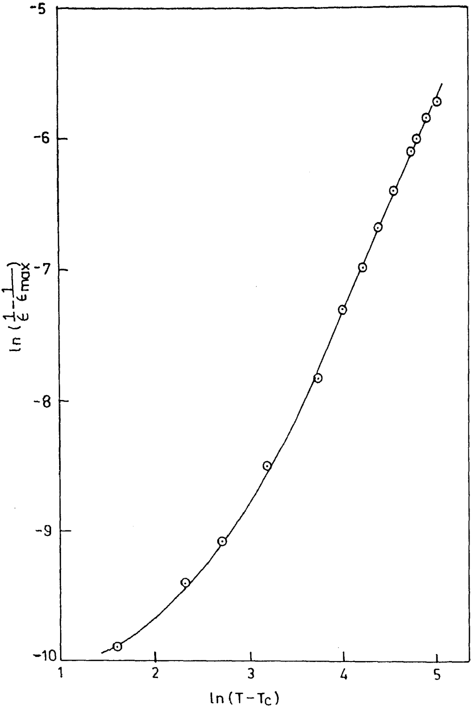

Figure 5. Variation of $\log(1/\varepsilon - 1/\varepsilon_{max})$ with log of temperature difference $(T - T_c)$ of PLDW.

0·06 eV. The value of activation energy is comparable to the other members of this family.

In figure 5, we have plotted log $(1/\varepsilon - 1/\varepsilon_{max})$ vs. $\log(T - T_c)$ which indicates the diffuseness of phase transition. The diffusivity (γ) calculated from formula [17]

$$\left(\frac{1}{\varepsilon} - \frac{1}{\varepsilon_{max}}\right) \propto (T - T_c)^{\gamma}$$

was 1·5 which shows the diffuse/relaxor behaviour of the compound.

Finally it is concluded that the complex compound PLDW has ferroelectric phase transition below room temperature and its dielectric constant and loss of the material are quite different from the other members of the family [12–14].

Acknowledgement

The authors are grateful to Prof. C L Roy for his help during the work.

References

[1] B Wul and L M Goldman, *C. R. Acad. Sci. USSR* **46**, 123 (1945)
[2] M Okuyama and Y Hamakawa, *Ferroelectrics*, **118**, 261 (1991)
[3] K Iijima, Y Tomita, R Takayama and I Ueda, *J. Appl. Phys.* **60**, 361 (1986)
[4] Y Chang, *Appl. Phys.* **A29**, 237 (1982)
[5] G Shirane and A Takeda, *J. Phys. Soc. Jpn.* **7**, 5 (1952)
[6] K L Yadav and R N P Choudhary, *Ferroelectrics*, **141**, 227 (1993)
[7] M Huffman, J P Goral, M M Al-Jassim and C Echer, *J. Vac. Sci. Technol.* **A10**, 1584 (1992)
[8] E Yamaka, H Watanabe, H Kimura, H Kanaya and H Ohkuma, *J. Vac. Sci. Technol.* **46**, 2921 (1988)
[9] K Iijima, I Ueda and K Kugimiya, *Jpn. J. Appl. Phys.* **30**, 2149–51 (1991)
[10] B Jaffe, W R Cork and H Jaffe, *Piezoelectric ceramics* (Academic, New York, 1970) p. 135–183
[11] M E Lines and A M Glass, *Principles and applications of ferroelctrics and related materials* (Oxford Univ. Press, Oxford, 1977) pp. 621
[12] S Bera and R N P Choudhary, *J. Mater. Sci. Lett.*, (in print)
[13] S Bera and R N P Choudhary, *Mater. Lett.* **22** 197 (1995)
[14] S Bera and R N P Choudhary, *Indian J. Pure Appl. Phys.* (in print)
[15] P Scherrer, *Cottin Nachricht* **2**, 98 (1918)
[16] Z I Shapiro, S A Fedulov, Yu N Venevtsev and L C Rigerman, Izvestiya AN SSSR, Seriya *Fizicheskaya*, **29**, 1047 (1965)
[17] M S Pilgrim, E A Sutherland and R S Winzer, *J. Am. Ceram. Soc.* **73**, 3122 (1990)

PRAMANA
— journal of
physics

© Printed in India

Vol. 44, No. 5,
May 1995
pp. 419–427

Phonon properties of rare earth ytterbium pnictides

PRAFULLA K JHA and SANKAR P SANYAL
Department of Physics, C V Raman Building, University of Bhopal, Bhopal 462026, India.

MS received 17 January 1995

Abstract. We report for the first time the complete phonon dispersion curves for the ytterbium pnictide compounds (YbN, YbP and YbAs) using a breathing shell model to establish their predominant ionic nature. The calculated results also show that this group of rare earth compounds does not show any elastic and phonon anomalies which are the characteristic features of other rare earth compounds. We emphasize the need for further Raman and neutron scattering measurements.

Keywords. Phonon dispersion curves; density of states; rare earth; intermediate valence compounds.

PACS Nos **63·10; 63·20**

1. Introduction

Over the last couple of decades, rare earth (RE) pnictides and chalcogenides have evoked considerable interest because of their diverse electronic, magnetic, optical and phonon properties [1–7]. The special feature of these materials is the valence fluctuation due to strong correlation among the ionic radius, the valence and the $4f$ occupation number. The latter is nominally integral for these core level type of localized states. However, a time-averaged non-integral $4f$ occupation number occurs in mixed valence compounds due to the degeneracy of two $4f$ configurations, e.g. $4f^n$ (RE^{2+}) and $4f^{n-1}5d^1$ (RE^{3+}). These two configurations can hybridize into a new ground state, which can be perturbed by either temperature or pressure. Some of these solids for which phonon properties have been studied so far are SmS, $\mathrm{Sm}_x\mathrm{Y}_{1-x}\mathrm{S}$, TmSe, $\mathrm{TmS}_x\mathrm{Se}$ [8–14]. All these studies have revealed that there is a strong electron phonon coupling at the RE ion site due to $4f$–$5d$ hybridization giving rise to anomalies in their phonon dispersion curves [12–14]. Both semiconducting and metallic behaviour have been observed in this wide class of materials. Detailed reviews of phonon anomalies in RE compounds and intermediate valence compounds (IVC) materials can be found in refs [1 and 2].

Recently the elastic, optical and phonon properties of another class of RE-compounds, namely ytterbium pnictides (YbN, YbAs and YbP) have been reported by ETH, Zurich group [15–16]. These authors have measured for the first time the elastic constants using Brillouin scattering and surface acoustic wave (SAW) technique [15] and optical and phonon properties using reflectivity measurements and Raman spectroscopy [16] for large single crystals of RE-pnictide compounds. They have established that these compounds are self compensated semi metals with an indirect overlap of p and d bands. The metallic nature, however, arises because of non-stoichiometric nature of the crystals, a behaviour more prominent in YbN, in comparison to YbAs and YbP. These authors [15,16] have also emphasized that this group of RE-compounds are weakly intermediate valent (or moderate Kondo systems) with semi metallic nature.

While many more investigations are to be carried out to establish the physical properties of the Yb-pnictides, in the present paper we focus on the elastic and phonon properties of these compounds only. An inspection of the measured elastic constants [15] reveals that none of these materials show anomalies in their elastic properties, as are observed in $Sm_xY_{1-x}S$ [14], YS [17], TmSe [13,14] and some of the uranium pnictides and chalcogenides [18,19]. Here, by elastic anomalies, we primarily refer to the negative magnitudes of Poisson ratio and C_{12}, which are the clear indications of valency fluctuation [2,19,20]. On the contrary, the elastic properties are quite similar to those of RE Europium chalcogenides (EuX, X = O, S, Se, Te) which do not exhibit valency fluctuation [21,22].

On the other hand not much can be concluded about metallic and semimetallic nature from the Raman measurements [16] on the optical and phonon properties of these materials. However complete measurements on the phonon dispersion curves by the neutron scattering experiments can lead to some significant results. Thus, it is the juncture to calculate the complete phonon dispersion curves of these compounds with the help of the measured informations provided in refs [15,16] and using suitable theoretical model in order to establish further the physical properties of this group of compounds. We briefly outline the theory in § 2 and present our calculated results in § 3.

2. The theoretical model

In the absence of any measured data on the phonon dispersion curves, except the $\omega_{TO}(\Gamma)$, it is difficult to choose a suitable model to predict them. In selecting the present lattice dynamical model (e.g. breathing shell model), we find the following arguments in our favour: (i) the authors in refs [15,16] have mentioned that the Yb-pnictides are semi-metallic in nature, and therefore a LO-TO splitting is expected. In this respect we expect there will be no anomalous phonon features in PDC, and the PDC will be somewhat similar to those of SmS, rather than TmSe [12–14]. (ii) The measured elastic constants [15] for Yb-pnictides do not exhibit anomalous behaviour, except that C_{12}-C_{44} in YbN is negative while it is positive in YbP and YbAs. Therefore pronounced metallic nature, as is observed in U-pnictides and U-chalcogenides [18,19] is expected to be absent. In view of the above discussion, we have chosen the breathing shell model (BSM) which has been found extremely successful in explaining the phonon anomalies in a wide class of rare earth (RE) compounds [23,24]. The general theory of BSM considers the breathing motion of the electron shells with respect to the core of the RE-ion in the equations of motion [25].

In the adiabatic approximation equations of motion corresponding to BSM are given by

$$\begin{aligned} \omega^2\mathbf{MU} &= (\mathbf{R}+\mathbf{ZCZ})\mathbf{U}+(\mathbf{R}+\mathbf{ZCY})\mathbf{W}+\mathbf{QW} \\ \mathbf{O} &= (\mathbf{R}^+ + \mathbf{YCZ})\mathbf{U}+(\mathbf{R}+\mathbf{G}+\mathbf{YCY})\mathbf{W}+\mathbf{QU} \\ \mathbf{O} &= \mathbf{Q}^+(\mathbf{U}+\mathbf{W})+\mathbf{HV} \end{aligned} \tag{1}$$

where **C** and **R** are the coulomb and repulsive interaction matrices. The breathing matrices **Q**, **H** and **V** are defined as

$$\mathbf{Q}=\begin{vmatrix}\mathrm{O} & \mathrm{G}\\ \mathrm{G} & \mathrm{O}\end{vmatrix},\ \mathbf{H}=\begin{vmatrix}\mathrm{H}(11) & \mathrm{H}(12)\\ \mathrm{H}(21) & \mathrm{H}(22)\end{vmatrix},\ \mathbf{V}=\begin{vmatrix}\mathrm{V}_1\\ \mathrm{V}_2\end{vmatrix} \tag{2}$$

where **G** and **H** are the dynamical matrices corresponding to "shell-breathing" and "breathing-breathing" force constants and **V** is 2-vector breathing amplitude matrix, **G** is a 3-vector breathing matrix, **Q** is a (6×2) matrix. The explict expressions for these force constants are reported elsewhere [26].

The method of determination of the parameters involved in the force constants matrices is quite straight forward. These parameters are related to the bulk properties such as elastic and dielectric constants. In table 1 we present the input constants and in table 2 the derived model parameters for Yb-pnictide compounds.

3. Results and discussion

In deriving the model parameters we have considered only five short-range force constants and four shell model parameters. Due to lack of sufficient macroscopic

Table 1. Input constants for ytterbium pnictides. Elastic constants are in 10^{12} dyn/cm^2, frequency in THz, r_o in Å, α_1 and α_2 in Å^{+3} [15, 16].

Properties	YbN	YbP	YbAs
r_o	2·3905	2·7688	2·8488
C_{11}	3·8500	2·7000	2·5000
C_{12}	1·0800	1·5000	1·4700
C_{44}	1·2900	0·6200	0·4700
ω_{TO}	8·2290	6·2800	5·3100
α_1	0·6000	0·6100	0·7300
α_2	−0·2343	0·7769	1·3689
$\varepsilon_0/\varepsilon_\infty$	12·6500	11·487	7·515

Table 2. Output parameters for Yb-pnictides. All are in units of $e^2/2V$, except Y which is in e and Z (dimension-less).

Parameters	YbN	YbP	YbAs
A_{12}	53·21782	68·18918	76·65823
B_{12}	−11·03196	−9·06572	−4·81384
A_{11}	−1·9070	0·04817	2·28000
B_{11}	1·9945	−2·27000	−6·41569
A_{22}	0·23844	−5·71000	−9·15237
$Y_1 = Y_2$	6·44	7·01	5·70692
G_1	2424·86	3276·89	2058·85
G_2	−4657·9243	2572·71	1097·899
Z	2·60	2·70	2·8

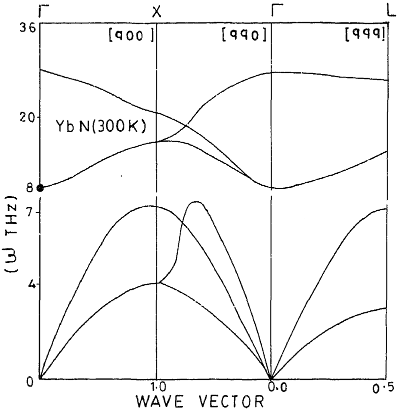

Figure 1. Phonon dispersion curves for YbN using BSM.

properties the shell charges for Yb and pnictide elements are considered to be equal. The calculated phonon dispersion curves (PDC) are plotted in figures 1–3.

In YbN, due to small mass of nitrogen atom, we obtain very large values of longitudinal optical (LO) frequencies. The acoustic branches however remain comparatively small in magnitude and show a smooth variation along all the directions of the Brillouin zone (BZ). Since the present model assumes the Yb-pnictides to behave like ionic crystals, as in Eu-chalcogenides [21, 22], we obtain a large splitting between LO and TO modes. This shows that the ionicity in this compound is large thereby indicating a strong Coulomb interactions. This behaviour is also observed in other two compounds of this series, a characteristic not observed in the PDC of TmSe, SmYS and some other rare earth intermediate valence compounds (REIVC) [12–14, 24]. This is mainly bacause of the fact that the later class of REIVC shows anomalous behaviour in their elastic constants. The ratio of elastic constants C_{11} to C_{12} in REIVC is much larger than that of the Yb-pnictides. In addition this large LO-TO splitting obtained from the present calculations of the PDC of Yb-pnictides could be understood from the electronic density of states and dielectric response measurement, which are, unfortunately not available at present.

A systematic trend of variation of LA phonon in all the three compounds is observed. As the polarizability of pnictide ion increases a hump near the X-point in Δ direction from YbN to YbAs of BZ gradually appears. This hump is maximum in YbAs. It is revealed from figures 1 to 3 that the crossover between TO and LA branches at L-point of the BZ increases from YbP to YbAs due to increase in mass and polarizability of the pnictide ions.

In figure 4, we have plotted two effective radial force constants calculated from the present model as a function of the lattice parameter. The dominance of the Yb-X force constant in all the Yb-pnictides has been observed. In addition, the small (or

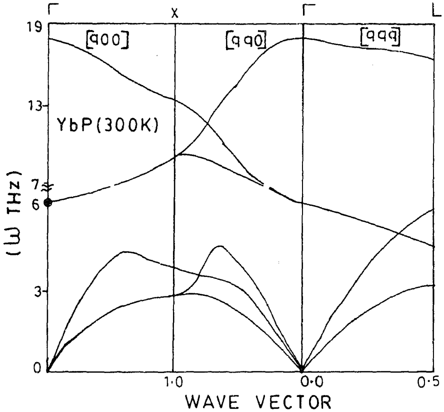

Figure 2. Same as in figure 1 for YbP.

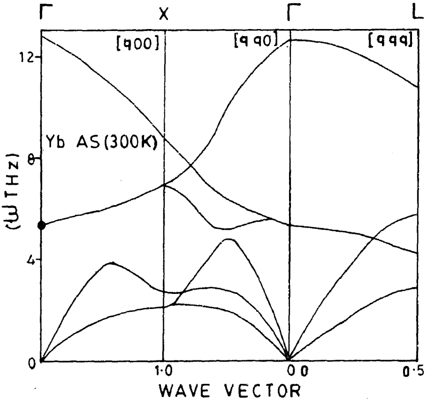

Figure 3. Same as in figure 1 for YbAs.

negative) magnitude of the Yb-Yb force constant shows that the large size of the second neighbour force constants are not significant due to large size of the pnicitide ions. The small magnitudes of Yb-N or Yb-Yb force constants, as compared to those of

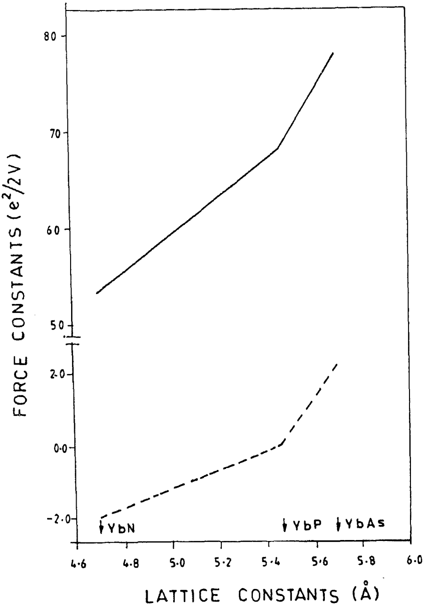

Figure 4. The Yb-X and Yb-Yb radial force constants as a function of lattice parameter. Solid and dashed curves are for Yb-X and Yb-Yb respectively.

other two members of this family reveal that the valence electrons might have some influence on the force constants of YbN.

The phonon density of states is an important dynamical property as its computation needs phonon frequencies in entire Brillouin zone. The one phonon density of states for three ytterbium pnictides have been obtained from BSM and are plotted in figures 5–7. In YbN, the density of states is very small (or nearly zero) in the range of 8 to 10 THz which is in accordance with the PDC. We observe the peaks distributed mainly around three frequency ranges. The distributed peaks between 2 and 7 THz are due to TA(X), LA(X), LA(L) and TA(L) modes. Two peaks with large intensity around 14 THz are also obtained which may be assigned to TO(L) and TO(X) phonons. The peaks between 20 and 26 THz are mainly contributed by the LO phonons at X and L points. The one phonon density of states for YbP and YbAs is plotted in figures 6 and 7 respectively which reveal more or less similar features as observed in YbN. The peaks observed at smaller frequency region are due to TA(X), LA(X) and TA(L), while those in the higher frequency region of the spectrum are due to optical phonons. Since no measurement of Raman and IR spectra has been reported so far, these peaks could not

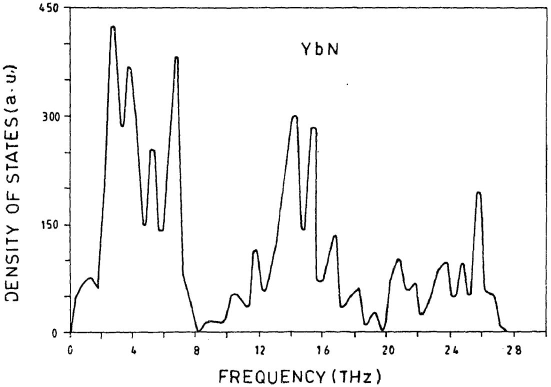

Figure 5. One phonon density of states for YbN.

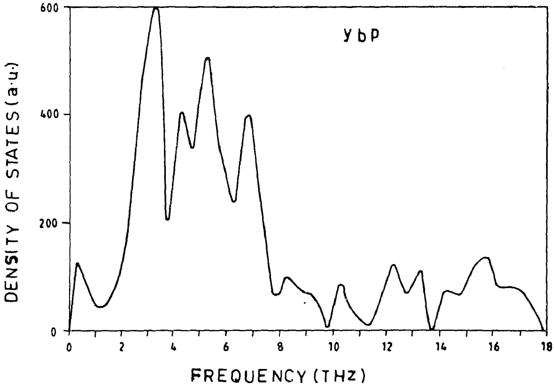

Figure 6. Same as in figure 5 for YbP.

be compared with experiment at present in detail. It is expected that these will be useful when such measurements are carried out.

Finally, we have reported for the first time the complete phonon dispersion curves and one phonon density of states for Yb-pnictides by using the breathing shell model

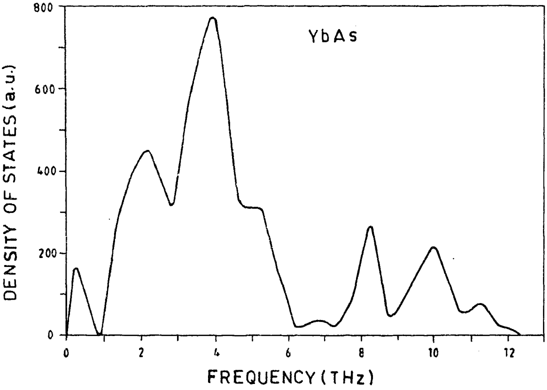

Figure 7. Same as in figure 5 for YbAs.

which incorporates the breathing motion of electron shell. Due to non-availability of sufficient experimental measurements, we could not compare our investigated results on PDC and phonon density of states with observed data. The PDC of Yb-pnictides reveal, in principle, the ionic nature of these rare earth pnictides similar to Eu-chalcogenides [21, 22]. We emphasize the necessity of further Raman and neutron scattering measurements in these compounds.

Acknowledgements

The authors are extremely grateful to Prof. P Wachter, ETH, Zurich for providing the experimental data on elastic properties and Raman measurements. One of them (PKJ) acknowledges the financial support from CSIR, in the form of research associateship. The work of the project was carried out using financial help from DST and DAE.

References

[1] C M Verma, *Rev. Mod. Phys.* **48**, 219 (1986)
[2] R D Parks (ed.) *Valence instabilities and related narrow band phenomena* (Plenum, New York, 1977)
[3] J H Jefferson and K W H Stevens, *J. Phys.* **C11**, 3919 (1978)
[4] J M Robinson, *Rep. Phys.* **51**, 1 (1979)
[5] E Bucher, K Andres, F J Disalve, J P Miata, A C Gossard, A S Cooper and G W Hull Jr, *Phys. Rev.* **B11**, 500 (1975)
[6] L M Falicove, W Hanke and M P Maple, *Valence fluctuations in solids* (North Holland, Amsterdam, 1981)
[7] J A Applebaum and D R Hamann, in *Physics of transition metals*, edited by M J Lee, J M Perz and E Fawcett, *AIP Conf. Proc.* **39** (1978)
[8] A Jayaraman, V Narayanmurti, E Bucher and R G Mains, *Phys. Rev. Lett.* **24**, 1430 (1970)

[9] T Penny, R L Melcher, F Holtzberg and G Guntherodt, *AIP Conf. Proc.* **A2**, 392 (1985)
[10] G Guntherodt, R Merlin, A Frey and M Cardona, *Solid State Commun.* **27**, 551 (1978)
[11] A Triendle and P Wachter, *Solid State Commun.* **32**, 573 (1979)
[12] G Guntherodt, A Jayaraman, H Bilz and W Kress, in *Valence fluctuations in solids*, edited by L M Falicove, W Hanke and M B Maple (North-Holland, Amsterdam, 1981) p. 121
[13] P K Jha and S P Sanyal, *Indian J. Pure Appl. Phys.* **31**, 469 (1993)
[14] H A Mook and F Holtzberg, *Valence fluctuations in solids*, edited by L M Falicove, W Hanke and M B Maple (North-Holland, Amsterdam, 1981) p. 121 and references therein
[15] M Mendik and P Wachter, *Phys. Rev.* **B47**, 6110 (1993); M Mendik and P Wachter, in *Phonon scattering in condensed matter* VIII, edited by M Meissner and R O Pohl (Springer-Verlag, Berlin, 1993) **112**, 469
[16] L Degiorgi, S Teraoka, G Compagmin and P Wachter, *Phys. Rev.* **B47**, 5715 (1993)
[17] P Roedhammer, W Reichardt and F Holtzberg, in *Lattice dynamics*, edited by M Balkanaski, (Flamiron Press, Paris, 1979) p. 84
[18] J A Jackman, T M Holden, W J L Buyers, P De V Duplessis, O Vogt and G Genossar, *Phys. Rev.* **B33**, 7144 (1986)
[19] P K Jha and S P Sanyal, *Phys. Rev.* **B46**, 3664 (1992)
P K Jha, R K Singh and S P Sanyal, *Physica* **B174**, 101 (1991)
[20] H A Mook, D D Mcwhan and F Holtzberg, *Phys. Rev.* **B25**, 4321 (1982)
[21] R Zeyher and W Kress, *Phys. Rev.* **B20**, 2850 (1979)
[22] P K Jha and S P Sanyal, *Indian J. Pure Appl. Phys.* **32**, 824 (1994)
[23] H Bilz, G Guntherodt, W Kleppmann and W Kress, *Phys. Rev. Lett.* **43**, 1998 (1979)
[24] P K Jha and S P Sanyal, *Cond. Matter Mat. Commun.* **1**, 209 (1994)
[25] V Nussulien and U Schroder, *Phys. Status. Solidi.* **B21**, 369 (1967)
[26] R K Singh, *Phys. Rep.* **85**, 259 (1982)

PRAMANA
— journal of
physics

© Printed in India

Vol. 44, No. 5,
May 1995
pp. 429–441

Lattice vibronics of bcc phase metals (Ti, Zr and Hf) at higher temperatures

S K SAXENA, R M AGRAWAL and R P S RATHORE*
Department of Physics and Computer Science, Dayalbagh Educational Institute, Dayalbagh, Agra 282005, India
*Department of Physics, R.B.S. College, Agra 282002, India

MS received 13 December 1994

Abstract. Ashcroft's analytic bare ion pseudopotential form factor with a modified Hartree dielectric function has been employed to represent the temperature dependent interionic potential. This potential includes both direct ion-ion interaction and indirect ion-electron-ion interaction with and without the effects of '*d*' bands, in some scantily studied complex *bcc* metals viz *bcc* Ti, Zr and Hf. The ab initio radial and tangential force constants extending out to 15th nearest neighbours are computed for the metals. The said potential is used for predicting the binding energy, elastic constants and phonon dispersion of the above mentioned metals and the results are satisfactorily compared with the corresponding measured data.

Keywords. Phonon dispersion; second ordered elastic constants; *d*-band electrons.

PACS No. 63·20

1. Introduction

The superconducting metals of groups III and IV namely Ti, Zr and Hf, have attracted attention in recent years on account of the anomalous features in several physical properties. These metals have *hcp* structure at low temperatures, and undergo a phase transition to a *bcc* phase well above room temperature. To understand the systematics of the phase stability of *bcc* metals, it is of fundamental interest to investigate the phonon dispersion i.e. dynamical response to the lattice potentials. The phonon dispersion of the *bcc* phases of Ti at 1293 K, Zr at 1188 K, and Hf at 2073 K are computed.

Recently Wills and Harrison [1] obtained an effective pair potential by taking advantage of the separation between free electron states exhibited in transition metal pseudopotential theory to treat the free electron like states with simple metal theory. The *s*–*s* interaction is treated within the Thomas Fermi approximation. The *d*-electrons have been treated by combining the Harrison and Froyen [2] formulation and a similar treatment has been meted out to the *d* state orthogonality matrix with a simple model of the *d* band density of states. The effective interaction between transition metal ions due to the *d*-electrons in combination with the simple metal repulsion due to the *s*-electrons describes the effect of the ion rearrangement at constant volume reasonably well. In real space, Singh *et al* [3] have taken the damped pair potential in combination with the ion-ion interaction due to *d* electrons obtained by Wills and Harrison [1] to calculate the phonon dispersion, elastic constants and binding energy. The study [3] characterizes (i) freedom from very long range Friedal oscillations (ii) cancellation of the band structure term by the coulomb repulsion in the effective potential and (iii) saving of 9/10 computer time compared to that required to calculate it using wave number space.

The study [3] however, lacks the correct depiction of electron response toward the dynamical state of the metals. The proper behaviour of electron is accurately represented in wave number space. Therefore we have carried out the application of potential in wave number space and sufficient convergence is achieved by taking the interaction system extending up to the 15th shells, more than double the nearest neighbour shells considered by Singh *et al* [3].

The temperature dependent phonon spectra of *bcc* Ti, *bcc* Zr and *bcc* Hf have recently been measured respectively by Petry *et al* [4], Heiming *et al* [5], and Trampenau *et al* [6]. These workers have analyzed their results in terms of the Born–Von Karaman model by fitting twelve force constants of their model to the measured phonon frequencies. Recently Gupta *et al* [7] have applied the model potential of Nand *et al* [8] for some of these metals. The inclusion of interactions due to *d* band electrons, into the phonon dispersion of transition metals [3], as Wills and Harrison [1] have discussed require more elaborate and adequate adoption by the theory.

Most of the dynamical studies [9, 10] make use of the numerous parameters and resort to usual fitting procedure which undermines [11] the credibility and reliability of the model. Model pseudopotential [11–15] on the contrary invariably has a smaller number of fitting parameters.

The indiscriminate use of dielectric screening [16] makes coulombian interaction infructuous. The choice of dielectric screening function invariably leads to the proper adjustment of depth and width of the coupling potential representing the interactions. Fielek [17] has reported the need of incorporating the contribution of dielectric screening, into the elastic constants of the metals, which has so far been generally ignored by almost all the macroscopic studies. In cases where electron *d*-states are close to the valence electron states, the results are not so accurate since the pseudo-potential approach assumes that the cores do not overlap and core-core interactions can be treated using only Madelung terms. It is for this reason that the effect of '*d*' bands, on various structural, vibrational and elastic properties, require to be studied more adequately within the frame-work of pseudopotential studies.

Some earlier workers, Shapiro and Moss [18], Gupta *et al* [19], Singh *et al* [3] and Shyam *et al* [20] have considered the force constants up to 4th, 2nd, 7th and 10th nearest neighbours respectively. In complex metals, however the interatomic forces are found to possess long range character.

Due to these inconsistencies it is necessary to develop an interaction model embodying the following characteristic features:

(1) Present model accounts more appropriately for the repulsive interaction by making the first terms, of (1) and (4) each, $\Phi_{cp}(r)$ and $\Phi_d(r)$ characteristically repulsive
(2) The role of *d*-band electrons has been included in a manner to make the resultant interaction more realistic and appropriate
(3) The temperature dependence of the ensuing interaction has been made adequately effective within the framework of the present model
(4) The dependence of elastic constants on dielectric screening has been sought through the force constants which are expressed as the function of the said screening. This procedure conforms with the requirements set by Fielek [17]

(5) The field corrections due to Sham [21] have been applied to the modified dielectric function resulting in the proper adjustment of electron response to the ionic displacements

(6) The interactions extending out to 15th nearest neighbour have been incorporated a) to account for the long range nature of interactions and b) to arrive at the desired convergence

(7) A single parameter r_c has been fitted to the zone boundary frequency of [111] L mode.

The model is used to predict the binding energy, second order elastic constants (SOECs) and the phonon dispersion in *bcc* metals like Ti, Zr and Hf. The study being one of the first of its kind, reveals fair agreement with the experimental data on the said properties.

2. Theory

2.1 *Screened ion-ion potential*

A second order pseudopotential calculation transforms the interatomic interaction in the central pair wise form [22], i.e.

$$\Phi_{\mathrm{cp}}(r) = Z^2 e^2/r - 2 \cdot Z^2 e^2/\pi \cdot \int G(q) \sin(qr)/qr \, \mathrm{d}q, \tag{1}$$

where Z, is the valence, e the electronic charge and $G(q)$ the normalized energy wave number characteristics, given by

$$G(q) = (4\pi Z e^2/\Omega q^2)^{-2} (W_{\mathrm{b}}^2(q)/1 - \varepsilon(q))(1 - 1/(1 - \varepsilon(q)). \tag{2}$$

with $W_{\mathrm{b}}(q)$ being the bare ion model potential and $\varepsilon(q)$ the modified Hartree dielectric function [23] inclusive of the exchange and correlation effects,

$$\varepsilon(q) = 1 + [(1 - f(q))(4\pi Z e^{*2}/\Omega q^2) 3m^*/\hbar k_{\mathrm{f}}^2] \\ [0{\cdot}5 + ((4k_{\mathrm{f}}^2 + q^2)/8k_{\mathrm{f}} q) \ln|(2k_{\mathrm{f}} + q)/(2k_{\mathrm{f}} - q)|] \tag{3}$$

Table 1. Parameters to the Ashcroft's model potential [25], (All quantities are in atomic units except M, which is given in amu.).

Parameters	Ti	Zr	Hf
r_c	1·191	1·342	1·267
Ω	86·709	109·642	113·81
a_{eff}	0·099	0·098	0·088
m^*	1	1	0
e	1	1	1
r_d	2·042	2·665	2·722
Z	2	2	2
M (amu.)	47·5	91·2	178·2

with

$$e^{*2} = (1 + a_{\rm eff})e^2,$$

$$f(q) = 0{\cdot}5[1 + (k_{\rm f}/q)^2 + (k_s/q)^2]^{-1} \text{ and } k_s^2 = 2k_{\rm f}/\pi \text{ (a.u).}$$

The temperature dependence of two body interaction between ions can be written as:

$$\Phi_t(r) = [\Phi_{\rm cp}(r) + \Phi_d(r)]\cdot\exp[(-\,T\pi k_{\rm b} r/(\hbar v_{\rm f})]. \tag{4}$$

Here, the temperature dependent factor, $\exp(-\,T\pi k_b r/\hbar v_{\rm f})$ has been derived by Takanaka and Yamamoto [24] with $v_{\rm f}(=(\hbar k_{\rm f}/m))$, the Fermi velocity and $k_{\rm b}$ is the Boltzmann constant.

Table 2. Computed radial and tangential force constants (accounting of the d-electrons effect).

Shell (no. of atoms)	Radial force constants (β_i) [10^{-3} Nm^{-1}]			Tangential force constants (α_i) [10^{-3} Nm^{-1}]		
	Ti	Zr	Hf	Ti	Zr	Hf
	1673 K	1188 K	2073 K	1673 K	1188 K	2073 K
1st (8)	20084·7	21097·6	18610·5	5347·7	3118·9	4784·3
2nd (6)	− 11037·1	− 5902·0	− 11011·0	4763·3	3350·0	4095·2
3rd (12)	3421·0	− 2641·0	− 2537·5	194·5	108·0	171·0
4th (24)	257·4	328·0	151·9	22·6	− 8·3	42·7
5th (8)	285·3	362·0	128	33·4	7·7	47·6
6th (6)	− 249·8	− 136·0	− 258·9	29·0	21·6	27·0
7th (24)	− 203·0	− 165·2	− 162·0	5·6	4·8	6·5
8th (24)	− 139·8	− 125·0	− 103·7	1·1	1·1	2·3
9th (24)	50·6	28·0	41·3	− 1·7	− 2·6	1·0
10th (32)	56·6	50·4	32·8	2·0	− 0·04	3·4
11th (12)	− 22·4	− 3·8	− 29·0	3·0	2·39	2·2
12th (48)	− 38·9	− 24·7	− 33	1·1	1·07	1·6
13th (30)	− 37·2	26·5	− 29·8	1·24	0·92	0·8
14th (24)	− 11·9	− 15·0	− 5	− 0·08	0·26	− 0·4
15th (24)	7·3	− 0·28	8·9	− 1·24	− 0·83	0·3

Table 3. Computed radial and tangential force constants (without *d*-electrons effect).

Shell (no. of atoms)	Radial force constants (β_i) [$10^{-3}\mathrm{Nm}^{-1}$]			Tangential force constants (α_i) [$10^{-3}\mathrm{Nm}^{-1}$]		
	Ti	Zr	Hf	Ti	Zr	Hf
	1673 K	1188 K	2073 K	1673 K	1188 K	2073 K
1st (8)	33920	29880	21820·1	2320	1392·7	2407·2
2nd (6)	− 4336·1	− 2101·2	− 5622·0	3476	2655·3	2761·2
3rd (12)	− 2661	− 2245	− 1628·5	61·5	40·6	6·455
4th (24)	520	461·99	476·9	− 22·6	− 30·91	− 14·0
5th (8)	481·4	461·39	371	0·161	− 9·003	5·35
6th (6)	− 177·1	− 100·1	− 167·9	16·128	15·39	11·33
7th (24)	− 164·1	− 145	− 111·0	− 1·035	1·45	− 2·12
8th (24)	− 107	− 108·9	− 60·58	− 4·468	− 1·694	− 4·99
9th (24)	69	36·9	63·3	− 4·677	− 4·00	− 2·83
10th (32)	68	56·7	47·8	0·018	− 1·01	0·88
11th (12)	− 15	− 0·63	− 20·0	1·903	1·8	0·781
12th (48)	− 34	− 22·43	− 27·67	0·298	0·69	0·627
13th (30)	− 33	− 24·39	− 24·8	0·545	0·56	− 0·175
14th (24)	− 9·05	− 13·53	− 1	− 0·568	0·014	− 0·99
15th (24)	9·5	0·849	11	− 1·63	− 1·021	− 0·133

The second potential term $\Phi_d(r)$ in (4) comprises of $\Phi_c(r)$ and $\Phi_b(r)$ i.e.

$$\Phi_d(r) = \Phi_c(r) + \Phi_b(r) \tag{5}$$

where $\Phi_c(r)$, is due to the overlap between *d*-states on different ions and $\Phi_d(r)$, the effects of $s - d$ hybridization are included in an approximate manner as suggested by Wills and Harrison [1].

In the case of effective two body interactions, first and second derivatives of the potential provides for the two independent force constants pertaining to a particular set of neighbour, [21]. We denote the radial force constants $(\mathrm{d}^2\Phi_t(r)/\mathrm{d}r^2)_{ri}$ by β_i and tangential force constants $(r^{-1}\cdot \mathrm{d}\Phi_t(r)/\mathrm{d}r)_{ri}$ by α_i for the *i*th set of neighbours.

Using function $G(q)$, one can easily evaluate the force constants. In this study we proceed with an analytic form for the bare ion pseudopotential form factor first proposed by Ashcroft [25].

The value of r_c, the core radius, Ω the atomic volume, k_f, the Fermi wave vector, Z, the valence, r_d, the d state electron radius and M the ionic mass are enlisted in table 1 for the metals under study. The computed force constants up to 15th set of neighbours are exhibited in tables 2 and 3.

2.2 *Binding energy*

The binding energy for the metals is computed on the lines of Wills and Harrison [1] making use of terms due to free electron gas, core, d-band and band structure components at temperature $T = 0$ K.

2.3 *Phonon dispersion and second order elastic constants (SOECs)*

The phonon frequencies for the present metals are calculated by solving the usual secular determinant.

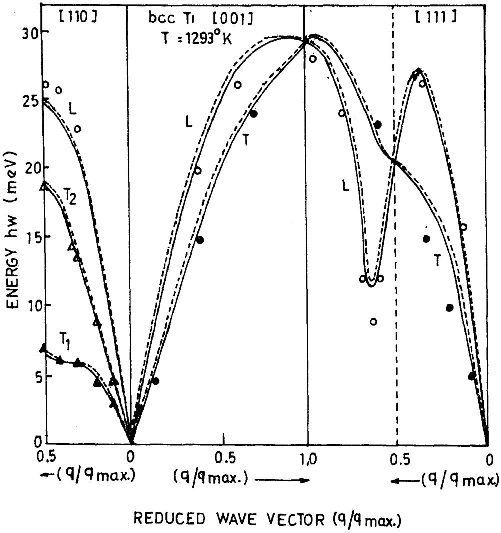

Figure 1. The phonon dispersion curve for the *bcc* Ti at temperature, $T = 1293$ K: present study; (———) with d-band effect, (– – –) without d-band effect. Experimental points are taken from Petry *et al* [4].

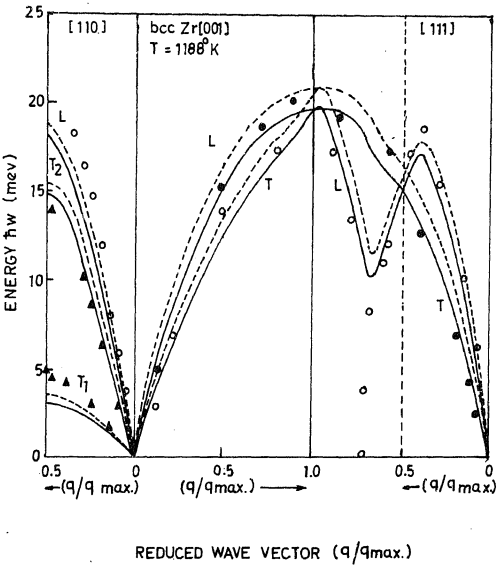

Figure 2. The phonon dispersion curves for the *bcc* Zr at temperature $T = 1188$ K present study; (———) with *d*-band electrons effects and (– – –) without *d*-band effects. Experimental results are taken from Heiming *et al* [5].

In the present microscopic study we have therefore computed the force constants extending up to 15th nearest neighbours and evaluated the dynamical matrix accordingly. The dynamical matrix elements are given in Appendix A.

The expressions for the SOECs of the metals under study are obtained by expanding the secular equation in long wave limits ($q \to 0$) and comparing with the usual Christoffel's relation.

3. Computation and results

The number of electrons *Zs* in the *s*-shell of Ti, Zr and Hf may be equated to 1·5. Obviously the number of electrons in the *d* shell comes out to $(2 - Zs)$. The r_d, the *d*-state radius [1] for the metals cited above is shown in table 1. We obtain the parameter r_c by matching the calculated values of phonon frequencies with experimental results of the L and T mode along [111] direction.

The contribution up to 15th shell have been found sufficient to achieve the needed convergence. The integration term appearing in the usual expressions of radial and

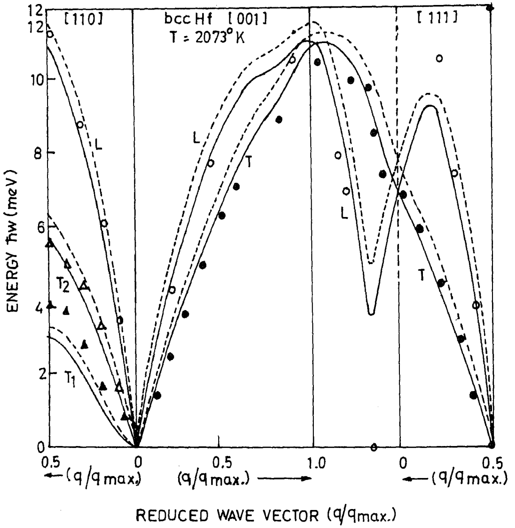

Figure 3. The phonon dispersion curve for the *bcc* Hf at temperature $T = 2073$ K, present study; (———) with the *d*-band effect and (–––) without *d*-band effects, experimental results are taken from Trampenau *et al* [6].

tangential force constants are converged up to 10^{-09}. To achieve this the ranges of wave vector $\mathbf{q}(=10^{-5}k_f$ to $75\,k_f)$ and $(=10^{-05}k_f$ to $100\,k_f)$ are considered for the radial and tangential force constants respectively.

Values of the force constants for the said metals (tables 2 and 3) are fed into the dynamical matrix and then the usual secular equation is solved to obtain the dispersion relations along the three major symmetry directions. The phonon dispersions (reduced wave vector $(q/q_{\max})$ versus energy $\hbar w$ (meV)) so computed are shown in figures (1 to 3) for Ti at 1293 K, Zr at 1188 K, and Hf at 2073 K respectively.

The binding energies, at $T = 0$ K, for the metals under study are computed and shown in table 4 which also displays the experimental values which agree remarkably well with the present results.

The second order elastic constants (C_{11}, C_{12} and C_{44}), at various temperatures, for the metals under study are computed and shown in table 5, along with the calculated values of Petry *et al* [4], Heiming *et al* [5] and Trampenau [6]. These calculated values show fair agreement with those computed herein.

The present temperature dependent model proves to be efficacious in predicting the binding energy, SOECs and the phonon dispersion satisfactorily in *bcc* phase of Ti, Zr and Hf at relatively higher temperatures, which have so far been not studied adequately

Table 4. Binding energy in Ry for bcc Ti, Zr and Hf at $T = 0\,\text{K}$.

Binding-energy	Ti	Zr	Hf
with d-electrons	1·268	1·41	1·45
without d-electrons	1·10	1·20	1·32
experimental	1·361*	1·484*	1·521*

*values are esimated by the relation $E_{\text{bind}}(\text{Exp.}) = -E_{\text{coh}} - E_{\text{I}} - (E_{\text{I}} + E_{\text{II}})/4$, where E_{coh}, is the cohesive energy and E_{I} and E_{II} are first and second ionization energy. And all these data are at $T = 0\,\text{K}$, taken from the Kittel [26].

Table 5. Computed SOECs at different temperatures for *bcc*, Ti, Zr and Hf ($10^{12}\,\text{dyn/cm}^2$).

Metal	Temperature		C_{11}	C_{12}	C_{44}
Ti	1293 K	with d-electrons	1·434	1·244	0·385
		without d-electrons	1·00	1·05	0·3825
		experimental values	$1{\cdot}34^{a}$	$1{\cdot}10^{a}$	$0{\cdot}36^{a}$
Zr	1188 K	with d-electrons	1·21	1·11	0·452
		without d-electrons	1·89	1·75	0·621
		experimental values	$1{\cdot}04^{b}$	$0{\cdot}93^{b}$	$0{\cdot}38^{b}$
Hf	2073 K	with d-electrons	1·41	1·2	0·58
		without d-electrons	1·95	1·92	0·825
		experimental values	$1{\cdot}31^{c}$	$1{\cdot}03^{c}$	$0{\cdot}45^{c}$

where a, b and c data are taken from refs [4], [5] and [6] respectively.

by the theoretical workers. The model however reveals somewhat less pronounced dip in [111] L branch.

The present study establishes that the d-band electrons play a crucial role in the determination of the electronic properties of the transitional metals; phonon frequencies, for the metals by ignoring the d-band electrons contribution, rule over those computed by considering the d-band electrons. The later frequencies, however, lie close to the experimental ones. On the other hand the non-inclusion of the effects of d-band shell in the Zr and Hf leads to less satisfactory result and in the case of Ti, the non-inclusion of these electrons makes, however, little difference.

We have further carried out the computations on the phonon dispersion for the above mentioned metals at different temperatures with and without the inclusion of the interactions due to d-electrons. It was found that the phonon dispersion for each of the said metals at low temperatures in association with the interaction due to d electrons corresponds to those at higher temperatures without the inclusion of the interaction due to d-electrons. It may therefore be concluded that,

(1) The comparison between computed and experimental frequencies improves upon by including the d-band electrons

(2) The inclusion of d-band contribution at lower temperatures leads to the frequencies computed by ignoring the contribution of these electrons at higher temperatures.

It may therefore be inferred that the increase of the lattice temperature freezes down the effect of *d*-band electrons as far as the phonon frequencies are concerned.

Acknowledgements

The authors wish to thank Dr J C Upadhayay for many useful discussions during the course of this work. One of the authors (SKS) is also thankful to the University Grants Commission, New Delhi for providing JRF and financial assistance through the major research project sanctioned to Dr R M Agrawal.

Appendix A

Undefined

$$
\begin{aligned}
D_{11}(q) := {} & \frac{8}{3}\cdot(\beta1-\alpha1)\cdot(1-c1\cdot c2\cdot c3)+8\cdot\alpha1\cdot(1-c1\cdot c2\cdot c3)\\
& +2\cdot(\beta2-\alpha2)\cdot(1-c21)+2\cdot\alpha2\cdot(3-c21-c22-c23)\\
& +2\cdot(\beta3-\alpha3)\cdot(2-c21\cdot c22-c21\cdot c23)+4\cdot\alpha3\cdot(3-c21\cdot c22-c21\cdot c23-c22\cdot c23)\\
& +\frac{8}{11}(\beta4-\alpha4)\cdot(2-c1\cdot c2\cdot c33-c1\cdot c32\cdot c3)+\frac{72}{11}\cdot(\beta4-\alpha4)\cdot(1-c31\cdot c2\cdot c3)\\
& +8\cdot\alpha4\cdot(3-c1\cdot c2\cdot c33-c1\cdot c3\cdot c32-c2\cdot c3\cdot c31)+\frac{8}{3}\cdot(\beta5-\alpha5)\cdot(1-c21\cdot c22\cdot c23)\\
& +8\cdot\alpha5\cdot(1-c21\cdot c22\cdot c23)\\
& +2\cdot(\beta6-\alpha6)\cdot(1-c41)+2\cdot\alpha6\cdot(3-c41-c42-c43)\\
& +\frac{8}{19}\cdot(\beta7-\alpha7)\cdot(1-c1\cdot c32\cdot c33)+\frac{72}{19}\cdot(\beta7-\alpha7)\cdot(2-c31\cdot c2\cdot c33-c31\cdot c32\cdot c3)\\
& +8\cdot\alpha7\cdot(3-c1\cdot c32\cdot c33-c31\cdot c2\cdot c33-c31\cdot c32\cdot c3)\\
& +\frac{4}{5}\cdot(\beta8-\alpha8)\cdot(2-c21\cdot c42-c21\cdot c43)+\frac{16}{5}\cdot(\beta8-\alpha8)\cdot(2-c41\cdot c22-c41\cdot c23)\\
& +4\cdot\alpha8\cdot(6-c21\cdot c42-c21\cdot c43-c41\cdot c22-c41\cdot c23-c22\cdot c43-c23\cdot c42)\\
& +\frac{4}{3}\cdot(\beta9-\alpha9)\cdot(2-c21\cdot c22\cdot c43-c21\cdot c42\cdot c23)+\frac{16}{3}\cdot(\beta9-\alpha9)\cdot(1-c41\cdot c22\cdot c23)\\
& +8\cdot\alpha9\cdot(3-c21\cdot c22\cdot c43-c21\cdot c42\cdot c23-c41\cdot c22\cdot c23)\\
& +\frac{8}{3}\cdot(\beta10-\alpha10)\cdot(1-c31\cdot c32\cdot c33)+\frac{8}{27}\cdot(\beta10-\alpha10)\cdot(2-c1\cdot c2\cdot c53-c1\cdot c52\cdot c3)\\
& +\frac{200}{27}\cdot(\beta10-\alpha10)\cdot(1-c51\cdot c2\cdot c3)\\
& +8\cdot\alpha10\cdot(4-c1\cdot c2\cdot c53-c1\cdot c3\cdot c52-c2\cdot c3\cdot c51-c31\cdot c32\cdot c33)\\
& +2(\beta11+\alpha11)\cdot(2-c41\cdot(c42+c43))+4\cdot\alpha11\cdot(1-c42\cdot c43)
\end{aligned}
$$

$$+(25\cdot\beta12+10\cdot\alpha12)\cdot\frac{8}{35}\cdot(2-c51\cdot(c32\cdot c3+c2\cdot c33))$$

$$+(9\cdot\beta12+26\cdot\alpha12)\cdot\frac{8}{35}\cdot(2-c31\cdot(c52\cdot c3+c2\cdot c53))$$

$$+(\beta12+34\cdot\alpha12)\cdot\frac{8}{35}\cdot(2-c1\cdot(c32\cdot c53+c52\cdot c33))+2\cdot\beta13\cdot(1-c61)$$

$$+2\cdot\alpha13\cdot(2-c62-c63)+\frac{8}{9}\cdot(4\cdot\beta13+5\cdot\alpha13)\cdot(1-c41\cdot c42\cdot c23)$$

$$+\frac{8}{9}\cdot(4\cdot\beta13+5\cdot\alpha13)\cdot(1-c41\cdot c22\cdot c43)$$

$$+\frac{8}{9}\cdot(\beta13+8\cdot\alpha13)\cdot(1-c21\cdot c42\cdot c43)+\frac{4}{10}\cdot(9\cdot\beta14+\alpha14)\cdot(2-c61\cdot(c22+c23))$$

$$+\frac{4}{10}\cdot(\beta14+9\cdot\alpha14)\cdot(2-c21\cdot(c62+c63))+4\cdot\alpha14\cdot(2-c62\cdot c23-c22\cdot c63)$$

$$+4\cdot\alpha14\cdot(2-c62\cdot c23-c22\cdot c63)+\frac{8}{43}\cdot(25\cdot\beta15+18\cdot\alpha15)\cdot(1-c51\cdot c32\cdot c33)$$

$$+\frac{8}{43}\cdot(9\cdot\beta15+34\cdot\alpha15)\cdot(2-c31\cdot c52\cdot c33-c31\cdot c21)$$

$$D_{12}(q):=\frac{8}{3}\cdot(\beta1-\alpha1)s1\cdot s2\cdot c3+2\cdot(\beta3-\alpha3)s21\cdot s22$$

$$+8\cdot(\beta4-\alpha4)s1\cdot s2\cdot c33+\frac{24}{11}\cdot(\beta4-\alpha4)\cdot(s31\cdot s2\cdot c3+s1\cdot s32\cdot c3)$$

$$+\frac{8}{3}\cdot(\beta5-\alpha5)\cdot s21\cdot s22\cdot c23+\frac{24}{19}\cdot(\beta7-\alpha7)\cdot(s1\cdot s32\cdot c33+s31\cdot s2\cdot c33)$$

$$+\frac{72}{19}\cdot(\beta7-\alpha7)\cdot s31\cdot s32\cdot c3+\frac{8}{5}\cdot(\beta8-\alpha8)\cdot(s21\cdot s42+s41\cdot s22)$$

$$+\frac{4}{3}\cdot(\beta9-\alpha9)\cdot s21\cdot s22\cdot c43+\frac{8}{3}\cdot(\beta9-\alpha9)\cdot(s21\cdot s42\cdot c23+s41\cdot s22\cdot c23)$$

$$+\frac{8}{3}\cdot(\beta10-\alpha10)\cdot s31\cdot s32\cdot c33+\frac{8}{27}\cdot(\beta10-\alpha10)\cdot s1\cdot s2\cdot c53$$

$$+\frac{40}{27}\cdot(\beta10-\alpha10)\cdot(s51\cdot s2\cdot c3+s1\cdot s52\cdot c3)+2\cdot(\beta11-\alpha11)\cdot s41\cdot s42$$

$$+\frac{40}{35}\cdot(\beta12-\alpha12)\cdot(s51\cdot(3\cdot s32\cdot c3+s2\cdot c33))$$

$$+\frac{40}{35}\cdot(\beta12-\alpha12)\cdot(s52\cdot(3\cdot c3\cdot s31+c33\cdot s32))$$

$$+\frac{24}{35}\cdot(\beta 12-\alpha 12)\cdot(c53\cdot(s31\cdot s2+s1\cdot s32))$$

$$+\frac{16}{9}\cdot(\beta 13-\alpha 13)\cdot(2\cdot s41\cdot s42\cdot c23+s41\cdot s22\cdot c43+s21\cdot s42\cdot c43)$$

$$+\frac{12}{10}\cdot(\beta 14-\alpha 14)\cdot(s61\cdot s22+s21\cdot s62)$$

$$+\frac{24}{43}\cdot(\beta 15-\alpha 15)\cdot(5\cdot s51\cdot s32\cdot c33+5\cdot s31\cdot s52\cdot c33+3\cdot s31\cdot s32\cdot c53)$$

where

$$s_i := \sin\left[\frac{aq_i}{2}\right] \qquad c_i := \cos\left[\frac{aq_i}{2}\right]$$

$$s_{2i} := \sin[aq_i] \qquad c_{2i} := \cos[aq_i]$$

$$s_{3i} := \sin\left[\frac{3aq_i}{2}\right] \qquad c_{3i} := \cos\left[\frac{3aq_i}{2}\right]$$

$$s_{4i} := \sin[2aq_i] \qquad c_{4i} := \cos[2aq_i]$$

$$s_{5i} := \sin\left[\frac{5aq_i}{2}\right] \qquad c_{5i} := \cos\left[\frac{5aq_i}{2}\right]$$

$$s_{6i} := \sin[3aq_i] \qquad c_{6i} := \cos[3aq_i]$$

with $i = 1, 2, 3, 4, 5$ and 6

References

[1] J M Wills and W A Harrison, *Phys. Rev.* **B28**, 4363 (1983)
[2] W A Harrison and S Froyen, *Phys. Rev.* **B21**, 3214 (1980)
[3] N Singh, N S Banger and S P Singh, *Phys. Rev.* **B38**, (1988) 7415; *Phys. Rev.* **B39**, 3097 (1989)
[4] W Petry, A Heiming, J Trampanuau, M Alba, C Herzig, H R Schober and G Vogl, *Phys. Rev.* **B43**, 10933 (1991)
[5] A Heiming, W Petry, J Trampenau, M Alba, C Herzig, H R Schober and G Vogl, *Phys. Rev.* **B43**, 10948 (1991)
[6] J Trampenau, A Heiming, W Petry, M Alba, C Herzig, W Meikeley and H R Schober, *Phys. Rev.* **B43**, 10963 (1991)
[7] H C Gupta, M M Sinha and B B Tripathi, *Indian J. Pure Appl. Phys.* **30**, 409 (1992)
[8] S Nand, B B Tripathi and H C Gupta, *Phys. Lett.* **A53**, 229 (1975); *J. Phys. Soc. Jpn.* **41**, 1237 (1976)
[9] V K Thakur and T N Singh, *Phys. Status Solidi* **B138**, 407 (1986); *Phys. Status. Solidi* **B135**, 67 (1986)
[10] B L Fielek, *J. Phys.* **F11**, 2381 (1980)
[11] P S Lay, B Szigette and V K Tewari, *Proc. R. Soc. (London)* **A320**, 505 (1971)
[12] K M Ho, C L Fu and B N Harman, *Phys. Rev.* **B29**, 2575 (1984); *Phys. Rev.* **B28**, 6687 (1983)
[13] J A Moriarty, *Phys. Rev. Lett.*, **55**, 1505 (1985)
[14] B N Onwuaga, *Phys. Status Solidi* **B141**, 105 (1987); *Nuovo Cimento* **D10**, 271 (1988); *Can. J. Phys.* **667**, 489 (1989)
[15] A Ramaji Rao and A Rajput, *Phys. Status Solidi* **B147**, K-11 (1988)
[16] R Taylor, *J. Phys.* **F8**, 1699 (1978)

[17] B L Fielek, *J. Phys.* **F14**, 61 (1984)
[18] S M Shapiro and S C Moss, *Phys. Rev.* **B15**, 2726 (1977)
[19] O P Gupta, *Solid State Commun.* **42**, 31 (1982)
[20] R Shyam, S C Upadhyaya and J C Upadhyaya, *Phys. Status Solidi* **B161**, 565 (1990)
[21] L J Sham, *Proc. R. Soc. (London)* **A283**, 33 (1965)
[22] Wei-Mei Shyu and G D Gaspari, *Phys. Rev.* **170**, 687 (1968)
[23] J Hubbard, *Proc. R. Soc. (London)* **A283**, 33 (1965)
[24] K Takanaka and R Yamamoto, *Phys. Status Solidi* **B84**, 813 (1977)
[25] N W Ashcroft, *Phys. Lett.* **23**, 48 (1966); N W Ashcroft and Langreth, *Phys. Rev.* **155**, 682 (1967)
[26] C Kittel, *An introduction to solid state physics*, 5th ed. (Wiley, New York, 1976)

PRAMANA
— journal of
physics

© Printed in India

Vol. 44, No. 5,
May 1995
pp. 443–451

Temperature variation of electric field gradient in scandium metal

B B PANIGRAHI and N C MOHAPATRA*
Department of Physics, Khallikote Autonomous College, Berhampur 760 001, India
*Department of Physics, Berhampur University, Berhampur 760 007, India

MS received 2 February 1995; revised 4 May 1995

Abstract. Electric field gradient (EFG) in scandium metal has been evaluated at temperatures 11 K and 293 K using band wave functions determined in the temperature dependent model potentials. The results of net EFG obtained are $-3{\cdot}756 \times 10^{13}$ esu/cm^3 and $-8{\cdot}009 \times 10^{13}$ esu/cm^3 at 11 K and 293 K respectively. The agreement with available experimental result is reasonably good.

Keywords. Electric field gradient; temperature variation; scandium metal; model potential.

PACS No. 76·60

1. Introduction

Electric field gradient in a solid arises if its charge distribution has lower symmetry than cubic. In non-cubic metals both the localised ions and the itinerant conduction electrons contribute to EFG. The contribution from the localised ions, referred to as the lattice contribution [1], when evaluated in point-ion approximation [2], is expressed as a simple function of lattice parameters. This is particularly true in the hexagonal-close-packed (hcp) solids. The contribution from the conduction electrons, on the other hand, requires a more involved and complex procedure for its evaluation. The standard procedure often used for this purpose is the energy band calculation which provides wave functions for all the occupied electron states. Using these wave functions, EFG is evaluated.

Changes in the temperature bring about changes in both lattice and electron-contribution to EFG. In the point-ion model [1] the effect of temperature variation on the lattice EFG can be included through the change in the lattice parameters. But for electronic contribution, the use of changed lattice parameters is not enough. This is because the potential that determines the electron distribution also changes with temperature. This will not only cause changes in the radial character of the wave function but may also bring about a change in the distribution of electrons in Fermi volume. As a consequence of the latter, electron states which are occupied/(unoccupied) at one temperature may become unoccupied/(occupied) at a different temperature and this may change the contribution to EFG.

One way of getting the changed electron-distribution in Fermi volume due to variation in temperature is by carrying out the energy band calculations with temperature-dependent potential. The latter has been worked out by Kasowski [3]. By treating electron-phonon interaction, he [3] has shown that the Fourier integrals of pseudopotential at two different temperatures are related by some simple relation involving

Debye–Waller factor [3]. Thus, using this formalism it is possible to obtain the Fourier integral of pseudo-potential at any temperature from those available at a known temperature. Once these are determined, they can be used in the energy band calculations to obtain energy and wave functions of occupied electron states at any desired temperature. This procedure has been used in the past for the study of temperature-dependence of Knight-shift [3] and spin susceptibility [4] in metals.

In the present work we have followed the above procedure for evaluating the EFG of the conduction electrons at two temperatures, namely, 11 K and 293 K. Although the procedure is general enough to be applicable for other temperatures, the present work is limited to the above two temperatures because lattice parameters for Sc are currently available [5, 6] only at these two temperatures.

The paper is organized as follows. In § 2 we briefly describe the theory of temperature dependence of EFG. Results and discussion are presented in § 3. Section 4 summarizes the conclusions.

2. Theory

Energy band calculations using non-local model potential are very common. The details of this procedure applied to scandium metal at 293 K are described elsewhere [7, 8]. Here we will briefly go over the necessary theory for the sake of completeness. In atomic units ($e^2 = 2, \hbar = 1, m = \frac{1}{2}$) the Hamiltonian of an electron in a periodic solid is given by

$$H = -\nabla^2 + V_{\mathrm{m}}, \tag{1}$$

where V_{m} is a suitable model potential which, in general, has a local and non-local part. The bare-ion model potential whose parameters are tabulated [9] is screened by the same dielectric function as used in the previous work [7].

The model wave function χ_t, where t denotes the band index, is expanded on the basis of plane waves,

$$|\chi_t(\mathbf{k})\rangle = \sum_{\mathbf{K}} C_t(\mathbf{k},\mathbf{K})|\mathrm{PW}(\mathbf{k}+\mathbf{K})\rangle, \tag{2}$$

where the coefficients $C_t(\mathbf{k},\mathbf{K})$ and the band energy $E_t(\mathbf{k})$ are obtained as solutions of the secular equation,

$$|H_{\mathbf{k}+\mathbf{K},\mathbf{k}+\mathbf{K}'} - E_t(\mathbf{k})\delta_{\mathbf{K},\mathbf{K}'}| = 0. \tag{3}$$

Once the coefficients $C_t(\mathbf{k},\mathbf{K})$ are determined, the true wave function $|\Psi_t(\mathbf{k})\rangle$ is constructed from the model wave function $|\chi_t(\mathbf{k})\rangle$ by orthogonalizing the latter to the core states in the solid, each of which is represented by a single tight binding function $|\Phi_j(\mathbf{k})\rangle$. Thus

$$|\Psi_t(\mathbf{k})\rangle = \sum_{\mathbf{K}} C_t(\mathbf{k},\mathbf{K})[|\mathrm{PW}(\mathbf{k}+\mathbf{K})\rangle - \sum_j \langle\Phi_j(\mathbf{k})| \times \mathrm{PW}(\mathbf{k}+\mathbf{K})\rangle|\Phi_j(\mathbf{k})\rangle] \tag{4}$$

with

$$\Phi_j(\mathbf{k},\mathbf{r}) = \frac{1}{\sqrt{N}}\sum_{\mu} \mathrm{e}^{i\mathbf{k}\cdot\mathbf{R}_\mu} U_j(\mathbf{r}-\mathbf{R}_\mu). \tag{5}$$

In (5) $\mathbf{R}_\mu$ is a direct lattice vector and U_j is the jth atomic core state. The latter, separated into a radial and an angular part is expressed in standard notation by

$$U_{nlm}(\mathbf{r}) = \frac{P_{nl}(r)}{r} Y_{lm}(\theta, \Phi), \tag{6}$$

where the Y_{lm} functions are the standard spherical harmonics. The function $P_{nl}(r)$ is normalized as follows,

$$\int_0^\infty P_{nl}^2(r)\mathrm{d}r = 1. \tag{7}$$

This briefly describes the formalism of obtaining energy and wave functions in the variational procedure using model potential. In the next sub-section we briefly describe the procedure that determines the temperature dependence of the model potential.

2.1 *Temperature-dependence of model potential*

In metals, the Fourier integral of pseudo-potential factorises into two parts; the structure factor and the form factor. The former is a function of the lattice co-ordinates alone while the latter is independent of the lattice co-ordinates. It is this separation which made it possible for Kasowski [3] to express the Fourier integral of the pseudo-potential at temperature T in terms of the corresponding quantity at $T = 0\,\mathrm{K}$ by the simple relation

$$\langle \mathbf{k}+\mathbf{K} |\, V_\mathrm{m} | \mathbf{k} \rangle_T = \langle \mathbf{k}+\mathbf{K} |\, V_\mathrm{m} | \mathbf{k} \rangle_0 \mathrm{e}^{-W_0(\mathbf{K},T)}, \tag{8}$$

where the function $\exp(-2W_0)$ is the usual Debye–Waller [3] factor. The function W_0 which depends on the frequencies $\omega(\mathbf{q}, s)$ of the phonon spectrum of the lattice is given [3] by

$$W_0(\mathbf{K}, T) = \frac{1}{2} \sum_{\mathbf{q},s} \frac{\hbar}{2\,\mathrm{MN}\,\omega(\mathbf{q}, s)} (2\bar{n}(q, s) + 1) |\mathbf{K}, \boldsymbol{\varepsilon}(\mathbf{q}, s)|^2, \tag{9}$$

where the sum is taken over all the branches labelled by s and the wave vectors $\mathbf{q}$ in BZ. $\boldsymbol{\varepsilon}(\mathbf{q}, s)$ is the polarization vector of the phonon in the mode $(\mathbf{q}, s)$, $\bar{n}(\mathbf{q}, s)$ is the average number of phonons in this mode and M is the mass of an atom in the lattice.

In order to evaluate W_0 it is essential to have phonon spectrum of the lattice at the given temperature. In the absence of the phonon spectrum for the discrete lattice, it is a reasonably good approximation to evaluate the sum in (9) using the phonon spectrum in Debye model. In the latter model, W_0 takes the form [10]

$$W_0(\mathbf{K}, T) = \left(\frac{3\hbar^2}{2Mk_\mathrm{B}\theta_\mathrm{D}}\right) K^2 \left(\frac{T}{\theta_\mathrm{D}}\right)^2 \int_0^{\theta_D/T} \left(\frac{1}{\mathrm{e}^x - 1} + \frac{1}{2}\right) x\,\mathrm{d}x, \tag{10}$$

where k_B is the Boltzmann constant and θ_D is the Debye temperature. Using the available Debye temperature, the integral in (10) can be evaluated for any desired temperature T. We wish to remark here that the relation in (8) which was derived for pseudo-potential holds for model potential as well.

For Sc, the phonon spectrum for the discrete lattice is not available. Hence the phonon spectrum from Debye model has been used in the present work to evaluate

$W_0(\mathbf{K}, T)$. Using (8) the Fourier integral of model potential at temperature T_2 is expressed in terms of those at T_1 as

$$\langle \mathbf{k}+\mathbf{K}|\, V_{\mathrm{m}}|\mathbf{k}\rangle_{T_2} = \langle \mathbf{k}+\mathbf{K}|\, V_{\mathrm{m}}|\mathbf{k}\rangle_{T_1} \mathrm{e}^{-[W_0(\mathbf{K},T_2)-W_0(\mathbf{K},T_1)]}. \tag{11}$$

For Sc, the form factors are available [9] at $T_1 = 293\,\mathrm{K}$ and using these the values at $T_2 = 11\,\mathrm{K}$ can be calculated from (11) with W_0 determined in (10).

The band structure calculation described in § 2·1 may be repeated with the temperature dependent model potential discussed above for obtaining energy and eigen functions at the desired temperatures. This makes it possible to determine the Fermi energy and hence the distribution of electrons in Fermi-volume. The latter contributes to EFG. In the following sub-section we derive the expression for the field gradient.

2.2 *Electric field gradient*

Once the true wave functions $\Psi_t(\mathbf{k}, \mathbf{r})$ of all the occupied band states in the full BZ are determined, the field gradient tensor which reduces to a single component, namely, the principal z component for hcp lattice is evaluated using the relation [11],

$$q_{\mathrm{el}} = -\sum_{t,\mathbf{k}} \int \Psi_t^*(\mathbf{k}, \mathbf{r}) \frac{3\cos^2\theta - 1}{r^3} [1 - \gamma(r)] \Psi_t(\mathbf{k}, \mathbf{r}) \mathrm{d}^3 r, \tag{12}$$

where the sum is taken over all the occupied bands t at the $\mathbf{k}$ points in the BZ. The function $\gamma(r)$ is the radially-dependent antishielding factor [12, 13] which accounts for the distortion of the core states of the atom in question by the nuclear quadrupole moment and the remaining charge distribution in solid. r and θ refer to the nucleus in question as the origin and the crystal C-axis as the Z-direction. The negative sign before the sum in (12) is a consequence of the negative charge on electron.

Using (4) in (12) and carrying out a considerable amount of algebra, we obtain the final expression for q_{el} as

$$\begin{aligned}
q_{\mathrm{el}} = {} & \frac{192\pi}{\Omega}\left(\frac{16\pi}{5}\right)^{1/2} \sum_{\mathbf{K}} \omega(\mathbf{k}) \sum_{t} \sum_{\mathbf{K},\mathbf{K}'} C_t^*(\mathbf{k}, \mathbf{K}) C_t(\mathbf{k}, \mathbf{K}') \\
& \times S(\mathbf{K}' - \mathbf{K}) D(|\mathbf{K}' - \mathbf{K}|)\, Y_{20}(\mathbf{K}' - \mathbf{K}) \\
& - \frac{1536}{\Omega}\left(\frac{\pi^5}{5}\right)^{1/2} \sum_{\mathbf{k}} \omega(\mathbf{k}) \sum_{t} \sum_{\mathbf{K},\mathbf{K}'} C_t^*(\mathbf{k}, \mathbf{K}) C_t(\mathbf{k}, \mathbf{K}') S^*(\mathbf{K}) S(\mathbf{K}') \\
& \times \sum_{nlm} \sum_{n'l'm'} (i)^{l'-l}\, Y_{lm}(\mathbf{k}+\mathbf{K})\, Y_{l'm'}^*(\mathbf{k}+\mathbf{K}') I(nl, |\mathbf{k}+\mathbf{K}|) I(n'l', |\mathbf{k}+\mathbf{K}'|) \\
& \times F(nl, n'l') \langle lm|20|l'm'\rangle \\
& + \frac{3072}{\Omega}\left(\frac{\pi^4}{5}\right)^{1/2} \sum_{\mathbf{k}} \omega(\mathbf{k}) \sum_{t} \sum_{\mathbf{K},\mathbf{K}'} C_t^*(\mathbf{k}, \mathbf{K}) C_t(\mathbf{k}, \mathbf{K}') \\
& \times S(\mathbf{K}') S^*(\mathbf{K}) \sum_{\substack{nlm \\ l'm'}} (i)^{l-l'}\, Y_{lm}^*(\mathbf{k}+\mathbf{K}')\, Y_{l'm'}(\mathbf{k}+\mathbf{K}) \\
& \times I(nl, |\mathbf{k}+\mathbf{K}'|) H(nl, l', |\mathbf{k}+\mathbf{K}|) \langle l'm'|20|lm\rangle
\end{aligned} \tag{13}$$

where $\omega(\mathbf{k})$ is the weighting factor assigned to the sample $\mathbf{k}$ point in the BZ, $S(\mathbf{K})$ is the structure factor and i is the imaginary number $\sqrt{-1}$. The symbols I, F, H and D stand for the radial integrals,

$$I(nl, |\mathbf{k}+\mathbf{K}|) = \int_0^\infty P_{nl}(r) j_l(|\mathbf{k}+\mathbf{K}|r) r \, \mathrm{d}r, \tag{14}$$

$$F(nl, n'l') = \int_0^\infty P_{nl}(r) P_{n'l'}(r) \frac{[1-\gamma(r)]}{r^3} \mathrm{d}r, \tag{15}$$

$$H(nl, l', |\mathbf{k}+\mathbf{K}|) = \int_0^\infty P_{nl}(r)(r) j_{l'}(|\mathbf{k}+\mathbf{K}|r) \frac{1-\gamma(r)}{r^2} \mathrm{d}r, \tag{16}$$

$$D(|\mathbf{K}'-\mathbf{K}|) = \int_0^\infty j_2(|\mathbf{K}'-\mathbf{K}|r)[1-\gamma(r)] \frac{1}{r} \mathrm{d}r, \tag{17}$$

where j_l is the spherical Bessel function of order l.

The notation $\langle l_1 m_1 | l_2 m_2 | l_3 m_3 \rangle$ stands for angular integral

$$\langle l_1 m_1 | l_2 m_3 | l_3 m_3 \rangle = \int Y^*_{l_1 m_1}(\theta, \Phi)\, Y_{l_2 m_2}(\theta, \Phi)\, Y_{l_3 m_3}(\theta, \Phi) \sin\theta \, \mathrm{d}\theta \, \mathrm{d}\Phi. \tag{18}$$

The first, second and third $\mathbf{k}$-sums in (13) give contributions from the pure plane wave (PW–PW), the tight binding (TB) and the hybrid (plane wave-tight binding and tight-binding-plane wave) part of Ψ_t respectively.

The contribution to EFG from the lattice ions, evaluated in point-ion approximation [2], is given by

$$q_{\mathrm{latt}} = Z(1-\gamma_\infty)[0{\cdot}0065 - 4{\cdot}4584(c/a - 1{\cdot}633)]/a^3, \tag{19}$$

where a and c are the lattice parameters of hcp lattice, Z is the valency of atom and γ_∞ is the Sternheimer antishielding factor [13]. The contribution, q_{latt} at different temperatures can be computed from (19) by using the lattice parameters a and c at the corresponding temperatures.

3. Results and discussion

The results of EFG in scandium evaluated at 293 K have been published before [7, 8]. In the present work we have followed the same procedure as in the previous work [7, 8] but with the temperature-dependent model potential so that we have now results of EFG both at 293 K and 11 K for comparison. Since the procedure has been discussed in great detail in our previous work [7, 8], we shall briefly deal here only with the salient features of the present work leaving the details to the previous work [7, 8].

In Sc the states $1s$ through $3p$ have been treated as core states, each of which is represented by a single TB function. The atomic core functions used for this purpose are the Hartree-Fock functions of Clementi [14]. Energy and wave functions are calculated at 144 representative $\mathbf{k}$ points in the 1/24th irreducible part of the BZ. For this purpose the triangular prism denoting the irreducible part has been divided into nine equal parts by slicing it along the C-axis in perpendicular direction. Each part is further divided into 16 equal-volume sub-prisms. The centroid of each sub-prism is chosen as the representative **k**-point at which band calculations are carried out. To each **k**-point a weighting factor $\omega(\mathbf{k})$ in proportion to the volume it represents is assigned. For Sc the volumes being equal, the weighting factors are also equal for all the 144 **k**-points. This choice amounts to using 3456 (144×24) **k**-points in the full BZ.

At each **k**-point the model wave function χ_t has been expanded in 23 plane waves corresponding to the shortest 23 wave vectors $|\mathbf{k}+\mathbf{K}|$ for that **k**-point. This makes the size of the matrix 23×23. With this, choice energy and eigen functions are found well converged. The energies of occupied band states have converged to within 0·001 Ry. The band calculation is carried out at both 293 K and 11 K. For the latter temperature, model potential is evaluated using the values at 293 K in (11) after calculating W_0 in Debye model. It may be noted here that W_0 obtained in this model will be a good approximation to its exact value. The latter could not be evaluated as the phonon spectrum of Sc lattice is not available in the literature.

The results of band calculation at 293 K are compared with those of the other works [5]. There is overall agreement between the two calculations. Details of comparison are given in the previous work [7, 8]. Fermi energy is determined by counting the number of occupied band states at all the representative **k**-points such that the total number of conduction electrons are accommodated. This procedure is repeated for both the temperatures. It is found that the Fermi energy changes slightly, but the number of occupied states at each sample **k**-point remains the same at both the temperatures. This is so because the change in energies of band states due to variation of temperature in the range considered is so little that it does not affect the distribution of Fermi-volume electrons. It does however bring about changes in the character of the wave function. With a view to examining the latter, we have compared the coefficients $C_t(\mathbf{k},\mathbf{K})$ of occupied bands at two temperatures at some of the sample **k**-points. We find a very small change in their values. This analysis suggests that the variation of the model potential with temperature is perhaps not significant in the given temperature range. In order to see how much is the change in the form factor due to the temperature variation, we have calculated the ratio of $\langle \mathbf{k}+\mathbf{K}|\, V_{\mathrm{m}}|\mathbf{k}\rangle$ at 11 K to its value at 293 K. This ratio, as can be seen from (11) is equal to $\exp[W_0(\mathrm{K}, 11^\circ) - W_0(\mathrm{K}, 293^\circ)]$, which in view of (10) turns out to be $\exp(0{\cdot}009571\, K^2)$ in case of Sc. The latter is less than 1·01 for the largest **K** used in the calculation. This shows that model potential differs less than by 1% when the temperature is changed from 293 K to 11 K. This is indeed a very small change, which explains why there is marginal change in the character of wave function and no change in the distribution of Fermi-volume electrons. This analysis also leads one to expect a small change in the electron contribution to EFG due to change of temperature from 293 K to 11 K.

We now discuss the field gradient results. Since $\gamma(r)$ for Sc is not available in the literature, we have assumed it as zero while evaluating integrals in (15)–(17). This assumption was also made in our previous work [7, 8] while evaluating EFG in Sc at 293 K. This assumption, as explained in our previous work [7, 8], would significantly affect only the pure plane-wave (PW–PW) part of the contribution to EFG. Its effect on the contribution from the non-plane wave part of Ψ_t is expected to be negligible for reasons explained in the previous work [7, 8]. Although $\gamma(r)$ is put equal to zero, an estimation for the shielded PW–PW contribution has been made in the same way as reported in the previous work [7, 8]. The shielded PW–PW contribution is obtained by enhancing the unshielded ($\gamma(r) = 0$) value by a factor $(1 - \gamma_\infty/2)$. The validity of this assumption is discussed in [7].

The integrals in (14)–(17) are evaluated by generating each integrand at 201 mesh points chosen in a log scale,

$$r_n = r_1 e^{(n-1)h}, \tag{20}$$

where the mesh size $h = 0{\cdot}045$ au and $r_1 = 0{\cdot}00237$ au. The farthest distance up to which integration has been carried out has the value $r_{201} = 19{\cdot}21089$ au. The values of the angular integrals in (18), on the other hand, are taken from the tabulated values [15] for the allowed combinations of angular momentum. The rules of addition of angular momentum suggest that the only allowed combinations in Sc, where there are no *d* cores, are $s-d$, $p-p$ and $p-f$ in spectroscopic notation. The contributions to EFG from these terms are evaluated separately, with a view to finding their relative importance. In addition to these, there is a contribution, referred to 'distant' contribution [7] which arises from the $l=0$ component of electronic charge distribution located on lattice sites other than the one in question. The lattice contribution to EFG has been calculated using (19) for the two temperatures. The electronic and lattice contributions at the two temperatures are summarized in table 1. In the present work as well as in the previous calculation [7, 8] the value of γ_∞ used is $-23{\cdot}104$. It refers to the solid-state value rather than the free-ion value and is taken from the work of Schmidt *et al* [16].

From table 1, it is seen that the change in the electronic contribution due to temperature variation is indeed small as expected. This is due to the small change in model potential in the given temperature range. At each temperature, it is noticed that the $p-p$ contribution has the largest magnitude. This is understandable because the *p*-states give the most asymmetric charge distribution. Comparing the individual components of electronic contribution at the two temperatures, one notices from table 1 that the values at 293 K are systematically lower in magnitude than those at 11 K. This may be explained by the reduction of the strength of potential. In the Kasowski formalism [3], we have seen before that the Fourier integrals of model potential at 11 K are larger than those at 293 K by the factor $\exp(0{\cdot}009571\,K^2)$ in Sc. This suggests that potential at 11 K is stronger than at 293 K. As a result the electron distribution at 293 K is more free-electron-like than at 11 K. Accordingly, *s*-character of charge distribution increases at the expense of the more important *p* character at 293 K and causing a reduction in the magnitude of EFG. The lattice contribution to EFG, on the other hand, changes more significantly than the electronic contribution and this results primarily from the change in the c/a ratio of the lattice due to temperature variation. Adding $q_{\rm el}$ to $q_{\rm latt}$, the net EFG comes to $-8{\cdot}009 \times 10^{13}\,{\rm esu/cm^3}$ and $-3{\cdot}756 \times 10^{13}\,{\rm esu/cm^3}$ at 293 K and 11 K respectively. Results from experiment [17] as well as from other work [18] are available only at 293 K. The experimental result [17] of which the sign is undetermined is: $|q| = 13 \times 10^{13}\,{\rm esu/cm^3}$. The result from Blaha *et al* [18] who have used the linearized-augmented plane wave procedure is $q = 32 \times 10^{13}\,{\rm esu/cm^3}$. As far as the magnitude of EFG is concerned, the present result is more close to experiment [17] than those of Blaha *et al* [18]. But as to the sign of EFG, nothing can be said conclusively until the sign of experimental EFG is determined. The present result is likely to improve if $\gamma(r)$ appropriate to solid state is used in the calculation instead of estimating its effect as has been done in the present work.

It is suggested that attempts be made on the experimental side to measure the EFG in Sc at 11 K so that it would offer a good test for the accuracy of the present result.

Table 1. Electric field gradients in hcp scandium metal at 11 K and 293 K. EFG's are expressed in units of 10^{13} esu/cm^3.

		Present work								
		q_{el}								
T	q_{latt}	PW–PW shielded	$s-d$	$p-p$	$p-f$	dist	Total q_{el}	Net q	Other work* Net q	Expt. $\lvert q\rvert$
11	128·390	−6·200	−4·854	−119·643	−1·346	−0·103	−132·146	−3·756	–	–
293 K	122·176	−5·724	−4·808	−118·231	−1·324	−0·098	−130·185	−8·009	32·0	13·0

*Blaha *et al* [18]

4. Conclusions

Electric field gradients in scandium metal calculated at two temperatures show that the relative change in the electronic contribution is much less than the change in the lattice contribution. The net EFG is found to be $-3{\cdot}756 \times 10^{13}$ esu/cm^3 and $-8{\cdot}009 \times 10^{13}$ esu/cm^3 at 11 K and 293 K respectively. This agrees reasonably well with the available experimental result. For a more meaningful comparison, it is suggested that not only the sign of EFG be determined in experiment but also measurement of EFG at other temperatures including 11 K be made.

References

[1] P Jena, S D Mahanti and T P Das, *Phys. Rev.* **B7**, 975 (1973)
[2] M Pomerantz and T P Das, *Phys. Rev.* **123**, 2070 (1961)
[3] R V Kasowski, *Phys. Rev.* **187**, 891 (1969)
[4] K Kar and N C Das, *Phys. Rev.* **B19**, 441 (1979)
[5] S G Das, *Phys. Rev.* **B13**, 3978 (1976)
[6] R G Barns, F Borsa, S L Segel and D R Torgeson, *Phys. Rev.* **A137**, 1828 (1965)
[7] B B Panigrahi and N C Mohapatra, *Pramana – J. Phys.* **41**, 443 (1993)
[8] B B Panigrahi and N C Mohapatra, *Pramana – J. Phys.* **43**, 407 (1994)
[9] A O E Animalu, *Phys. Rev.* **B8**, 3542 (1973)
[10] R A T Lima and C T Sallis, *Phys. Rev.* **B21**, 458 (1980)
[11] N C Mohapatra, P C Pattnaik, M D Thompson and T P Das, *Phys. Rev.* **B16**, 3001 (1977)
[12] K K P Rao and N C Mohapatra, *Phys. Rev.* **A24**, 10 (1981)
[13] R M Sternheimer, *Phys. Rev.* **115**, 1198 (1959)
[14] E Clementi, *Tables of atomic functions* (IBM, New York, 1965)
[15] M Tinkham, *Group theory and quantum mechanics* (McGraw-Hill, New York, 1964)
[16] P C Schmidt, K D Sen, T P Das and A Weiss, *Phys. Rev.* **B22**, 4167 (1980)
[17] E N Kaufmann and R J Vianden, *Rev. Mod. Phys.* **51**, 161 (1979)
[18] P Blaha, K Schwartz and P H Dederichs, *Phys. Rev.* **B37**, 2792 (1988)

PRAMANA
— journal of
physics

© Printed in India

Vol. 44, No. 5,
May 1995
pp. 453–459

Composite Anderson–Newns model and chemisorption characteristics of nickel-hydrogen system

RAVINDER GULERIA, P K AHLUWALIA and K C SHARMA
Physics Department, Himachal Pradesh University, Shimla 171 005, India

MS received 29 August 1994; revised 19 January 1995

Abstract. The composite Anderson–Newns model and triangular weighted density of states are used to study the electron density of states, magnetic moment and charge transfer of adatoms for a chemisorbed system. The model has been applied to hydrogen chemisorbed on nickel. It has been observed that with the increase in coverage, number of B–AB states as well as bond strength increases, whereas the magnetic moment and adatom charge decrease with coverage. These results match with the experimental data.

Keywords. Chemisorption; density of states; coverage; charge transfer; magnetic moment.

PACS Nos 68·45; 71·20

1. Introduction

Chemisorption of gases on the surface of metals, one of the most interesting problems in solid state physics, has helped us understand various processes that take place on the surfaces of metals, viz. corrosion, hydrolysis and catalysis. At present, there are a number of competing theories for chemisorption based on semi-empirical model Hamiltonian or first principle ab initio method. Considerable progress has been made in ab initio calculations using density functional theory and its local approximation, cluster calculations or coherent potential approximation. Though these methods allow us to carry out high precision calculations of space distribution of electric charge, binding energy, work function changes and other experimental characteristics of an adsorbate-adsorbent system, there are many difficulties when many body effects and correlations in electronic and ionic component of adsorbate are considered.

On the other hand the model Hamiltonian method appears well suited for understanding the experimentally observed features. This is due to the relatively simple microscopic picture of the system used and the possibility of including correlation effects and additional interactions in the adsorbed system by using suitable approximations [1, 2]. Furthermore, equation of motion method can be very useful while including the correlation effects [1]. The first most successful Hamiltonian method proposed by Newns [3] was further improved by many workers [4]. They used Anderson model Hamiltonian for magnetic alloys, to treat the chemisorbed atom as an impurity on the surface, and then solved the problem within the self-consistent Hartree–Fock scheme. A more generalized version of Anderson–Newns model, called the composite Anderson–Ising Model, was proposed by Gavrilenko [5] wherein an attempt was made to incorporate the Coulomb correlations and interactions in the adsorbed system. This model was applied to the case of stochastic arrangement of adatoms on metal surfaces by Gavrilenko *et al* [6] and it was shown that Anderson criteria for impurity magnetism in metals holds for this type of phase transition also. Later, using this model, characteristics of chemisorption were further investigated by Cardena [2]. The calculations were carried out within the framework of Hartree–Fock approximation for electronic component of adsorbate using Bragg–Williams approximation for ionic component. This theoretical study started showing results of density of states (DOS) which were quite close to that obtained from the angular photoemission spectra [7]. However, no systematic attempt has been made so far to analyse the magnetic and non-magnetic case associated with the chemisorption as a function of the coverage using the triangular weighted density of states (WDOS) for nickel-hydrogen system. The triangular WDOS is a better choice as suggested by Kalkestein and Soven as it provides a better fit compared to the semi-elliptical WDOS [8].

We have studied here the changes in electronic DOS, magnetic moment and charge transfer on chemisorption of hydrogen on a transition metal (nickel) using the composite Anderson-Newns model [5] and the triangular WDOS. We solve this model self consistently within the Hartree–Fock scheme.

In § 2 the general formalism and its assumptions are discussed and a basic expression for the DOS, magnetic moment, charge transfer and chemisorption energy is derived. In § 3 the results obtained by numerical analysis are discussed.

2. Basic equations and formalism

Consider a system of N_A adsorbed hydrogen-like atoms (adatoms) distributed over N-active centres (adsorption centres) on the metal surface (substrate). $N_A \leqslant N$. Each atom has a rigid bond with the substrate. The configuration of the adatom arrangment over the adsorption centres is not fixed. In the simplest case, Hamiltonian of this system can be written in the form:

$$H = \sum_{k,\sigma} \varepsilon_k n_{k\sigma} + \sum_{\alpha} N_\alpha \left[\sum_{\sigma} E n_{\alpha\sigma} + U n_{\alpha\uparrow} n_{\alpha\downarrow} + \sum_{k,\sigma} (V_{\alpha k} b^\dagger_{\alpha\sigma} a_{k\sigma} + \text{h.c}) \right]. \qquad (1)$$

Here, sum over α in (1) is over all adsorption centres, the operator $N_\alpha = C^\dagger_\alpha C_\alpha$ has eigen values 0 or 1. $C^\dagger_\alpha$ and C_α are the Fermi amplitude of creation and annihilation operators of adsorption centre, α, ε_k is the energy spectrum of clean substrate, E is the ionization potential of adatom. $n_{k\sigma} = a^\dagger_{k\sigma} a_{k\sigma}$, $n_{\alpha\sigma} = b^\dagger_{\alpha\sigma} b_{\alpha\sigma}$, where $a_{k\sigma}, b_{\alpha\sigma}$ are the electron variables for substrate electron and atoms, respectively, U describes the coulomb interaction of atomic electrons and h.c. means hermitian conjugate.

Here, the difference from the usual form is due to the hopping interactions being proportional to $V_{\alpha k}(V_{k\alpha})$ which takes into account the indirect interactions between the adatoms. Although this model is linear with respect to ion operator N_α it is not equivalent to ideal lattice model due to these interactions and hence Bethe's approximation cannot be used here. To solve this model, only one localized impurity atom is taken. Then $N_\alpha = 1$ if $\alpha = A$ and $N_\alpha = 0$ if $\alpha \neq A$, and using unrestricted Hartree–Fock approximation (which considers the averaged interactions of all adatoms and substrate) the Hamiltonian reduces to the form which can be easily solved [9]. The electronic properties of the system are described by correlators of type $\langle n_{\alpha\sigma} \rangle$, $\langle N_\alpha n_{\alpha\sigma} \rangle$, $\langle N_\alpha b^\dagger_{\alpha\sigma} a_{k\sigma} \rangle, \cdots$, whereas ionic properties are described by correlators of Ising type $\langle N_\alpha \rangle, \langle N_\alpha N_\beta \rangle, \cdots, \langle N_\alpha N_\beta \cdots N_\delta \rangle, \cdots$.

To derive all the related electronic properties of system double time Green's functions are used which are derived by equation of motion method [9]. To derive electronic properties of the system in the final form Bragg-Williams approximation is used which assumes the distribution of the spin as random and considers the interactions only between nearest neighbours. The important feature of this composite model is that it takes care of both the cases and also the intermediate values of coverage. Finally, the density of states (DOS) of this system can be written as [6]:

$$D(\omega) = \sum_{\sigma} D_{\sigma}(\omega)$$

$$= \left(\frac{1}{\theta}\right) \mathrm{Im} \ll N_{\alpha} b_{\alpha\sigma}; b^{\dagger}_{\alpha\sigma} \gg_{\omega - /\theta}.$$

Using the assumptions, we get

$$D_{\sigma}(\omega) = \frac{1}{\theta}\left(\frac{a}{2\pi}\right)^{d} \mathrm{Im} \int \frac{\mathrm{d}\omega}{(\omega - E_{\sigma} + \varepsilon_{F} - (1-\theta) L(\omega) - \theta P_{q}(\omega))_{\omega - /\theta}}. \tag{2}$$

The magnetic moment (m) measured in units of Bohr magneton and electric charge (q) measured in units of electron charge are given by:

$$m = \langle n_{\alpha\uparrow} \rangle - \langle n_{\alpha\downarrow} \rangle, \quad q = 1 - \langle n_{\alpha\uparrow} \rangle - \langle n_{\alpha\downarrow} \rangle,$$

and

$$n_{\alpha} = \int \mathrm{d}\omega\, D_{\sigma}(\omega - \varepsilon_{F}). \tag{3}$$

By definition, the chemisorption energy ΔE is

$$\Delta E = \frac{1}{N_{A}} \left(\langle \mathrm{H} \rangle - \sum_{K,\sigma}^{\mathrm{occ.}} \varepsilon_{K} \right) - E, \tag{4}$$

where H is the Hamiltonian of the system and summation is carried over all occupied states of unperturbed system. We have considered a one dimensional model of periodically arranged atoms with lattice constant $a = 1$ interacting only with its nearest neighbours and taking periodic boundary conditions. Here we have taken energy spectrum, $\varepsilon_{K} = \Gamma \cos(K)$ with respect to the centre of the band. One chemisorption centre per site has also been considered. For this case eq. (2) after some simplifications can be written as:

$$D_{\sigma}(\omega) = \frac{1}{\pi}\left(\frac{a}{2\pi}\right) \int_{-\pi/a}^{\pi/a} \frac{(1-\theta)\,\Delta(\omega)\,\mathrm{d}q}{\left\{\left[\omega - E_{\sigma} + \varepsilon_{F} - (1-\theta)\gamma(\omega) - \left(\frac{\theta \beta^{2}}{\omega - \varepsilon_{q} + \varepsilon_{F}}\right)\right]^{2} + (1-\theta)^{2} \Delta(\omega)^{2}\right\}}, \tag{5}$$

where $\gamma(\omega) + /\Delta(\omega) = L(\omega - /\theta)$, $\Delta(\omega) = \pi\beta^{2} \bar{\rho}(\omega + \varepsilon_{F})$ is the weighted DOS states and $\gamma(\omega)$ is the Hilbert transform of $\Delta(\omega)$-function and is given by:

$$\gamma(\omega) = \int \frac{\Delta(\omega)\mathrm{d}y}{(\omega - y)}, \quad \text{where } -\pi \leqslant \mathrm{arc}\, tg \leqslant \pi.$$

The corresponding equation for ε_F is

$$\frac{1}{N_A}\int_{\varepsilon_F^0}^{\varepsilon_F} \mathrm{d}\omega\, \rho_0(\omega) = \frac{\theta}{\pi}\left(\frac{a}{2\pi}\right)\sum_{\sigma}\int_{-\pi/a}^{\pi/a} \mathrm{d}q$$
$$\times \operatorname{arc} tg\left(\frac{(1-\theta)\bar{\Delta}(\varepsilon_F)}{\varepsilon_F - E_\sigma - (1-\theta)\bar{\gamma}(\varepsilon_F) - (\theta\beta^2/(\varepsilon_F - \varepsilon_q))}\right) + \theta. \tag{6}$$

The functions $\Delta(\omega)$ and $\gamma(\omega)$ are called chemisorption functions, the latter being Hilbert transform of the former. These are related to each other through $G_{\alpha,\sigma}(\omega) = \gamma(\omega) + i\Delta(\omega)$. Here, we take the WDOS to be triangular, a more realistic WDOS, as it reveals the salient features of DOS, e.g. the emergence of split off states at very low coverage [9]. The triangular WDOS is given by

$$\Delta(\omega) = \mathrm{Im}[G(\omega)] = \beta^2[1 - |\omega|] \text{ for } |\omega| < 1 \quad \text{and}$$
$$= 0 \text{ for } |\omega| > 1. \tag{7}$$

The Hilbert transform of $\Delta(\omega)$ is

$$\gamma(\omega) = \mathrm{Re}[G_{\alpha,\sigma}(\omega)] = \beta^2/\pi\left[\ln\left|\frac{1-\omega}{1-\omega}\right| + \omega \ln\left|\frac{(1-\omega)(1+\omega)}{\omega^2}\right|\right], \tag{8}$$

where β is the hybridization parameter, the matrix element of $V_{\alpha\beta}$. This is a measure of the adatom-substrate interaction [2] and the behaviour of a typical system depends on the allowed value of this parameter for a given value of U.

3. Numerical results and discussion

The calculation of electronic DOS, magnetic moment and charge transfer for different coverages has been carried out for both magnetic and non-magnetic cases, using triangular WDOS. In order to calculate these values the basic parameters are: ionization level (E), the electron affinity level ($E + U$), where U is the coulomb's interaction between electrons on impurity level, ε_F^0, the Fermi level, β, the hybridisation parameter and $2\Gamma = (\varepsilon_1 - \varepsilon_0)$ the band width of the unperturbed system where $\varepsilon_1, \varepsilon_0$ are the upper and lower edges of band respectively. There are three situations corresponding to different positions of ionization and affinity level w.r.t. Fermi level parameterised by $\eta = E - \varepsilon_F + U/2$. We shall concentrate on the case $\eta = 0$ corresponding to symmetric Anderson's model. n_α and ε_F are calculated self-consistently using (3), (5) and (6) and all the experimental parameters for nickel are taken ($E = -4{\cdot}789$, $U = 6{\cdot}789$ and $\varepsilon_F = 0{\cdot}926$) from Newns [3]. The value of adatom integral equals 12·9 eV, as it stands for an isolated hydrogen atom. The determination of this quantity in the presence of substrate surface is extremely difficult, therefore we can safely take it to be 12·9 eV, and compare our results with that of others. All energies are measured in terms of half band width (Γ) and the position of energy levels w.r.t. substrate band centre. Also $\varepsilon_F^0 = 0$.

If U/β is large (≈ 20), we have the magnetic case and if U/β is small (≈ 8), the non-magnetic. Figures 1 and 2 give the salient features of the electronic DOS vs ω, for different coverages, for both magnetic and non-magnetic cases respectively.

Some of the common features for both the cases, are (a) At zero coverage there is only one peak, which is quite consistent with the work of Gavrilenko [6]. Of course, it is

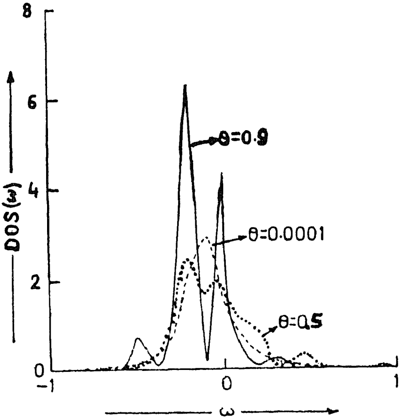

Figure 1. DOS vs ω for different coverages $\theta = 0{\cdot}0001$, $0{\cdot}5$ and $0{\cdot}9$, for coverage stimulated magnetic case.

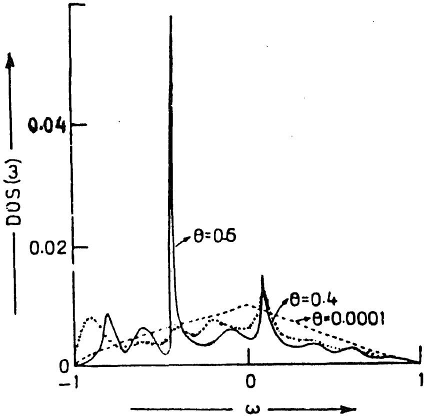

Figure 2. DOS vs ω for different coverages $\theta = 0{\cdot}0001$, $0{\cdot}4$ and $0{\cdot}6$, for coverage stimulated non-magnetic case.

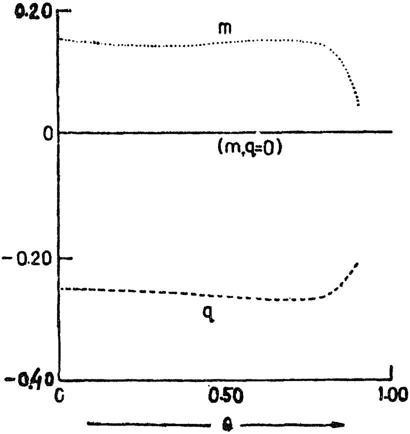

Figure 3. Magnetic moment (m) and charge transfer (q) vs coverage (e), for both magnetic and non-magnetic cases.

apparently sensitive to the choice of parameters, particularly β. (b) With increase in coverage (θ), the height of B–AB peaks increases, which implies an increase in the number of B–AB states. This is also in agreement with the findings of Brenig and schonhammer [11] and Gavrilenko [6]. (c) In both the cases, the distance between the B–AB peaks as well as the depth between the peaks increases with increase in coverage (θ), implying increase in bond strength with coverage. This feature for non-magnetic case is in agreement with other approaches and that of Gavrilenko [6]. Whereas if we take $\beta \approx 1$ in the WDOS, as given by Schrieffer [10], then the behaviour of DOS in this case of nickel-hydrogen system is similar to that discussed here [9]. Thus we conclude that behaviour of DOS is most sensitive to the parameter (β), which takes into account the interaction between adatom and substrate and its value for each system should be determined separately. (d) In both the cases, at high coverage, the number of B–AB peaks also increases which is due to the correlation effects as pointed out by Brenig and Schonhammer [11]. (e) Further, the characteristic features are (i) Comparison of figures 1 and 2 shows that in the magnetic case, the height of B–AB peaks is higher than that in the non-magnetic case, implying, more number of B–AB states in the magnetic case, as expected. (ii) In the magnetic case, there is a considerable decrease in the magnetic moment at large coverages, [figure 3 (upper curve m)], which agrees with the results of density functional approach [12]. The charge transfer to the adatoms remains almost constant up to certain θ and then starts falling off at large θ ($\approx 0{\cdot}9$), showing neutralization of adatoms, [figure 3 (lower curve q)]. This is found consistent with the experimental situation [13], whereas, in the non-magnetic case both magnetic moment and charge transfer are zero for all the coverages, [figure 3 (curve $m, q = 0$)], as was also mentioned by Gavrilenko [6].

References

[1] E Taranko, R Taranko, R Caradena and V K Fedynin, *Vacuum* **45**, 307 (1994)
[2] R Cardena, preprint ICTP December (1989)
[3] D M Newns, *Phys. Rev.* **178**, 1123 (1969)
[4] J P Muscat and D M Newns, *Prog. Surf. Sci.* **9**, 1 (1978)
[5] G M Gavrilenko, *Physica* **A150**, 137 (1988)
[6] G M Gavrilenko, R Cardena and V K Fedyanin, *Surf. Sci.* **217**, 468 (1989)
[7] T L Einstein, J A Hertz and J R Schrieffer, in *Theory of chemisorption,* edited by J R Smith (Springer, Berlin, 1980)
[8] D Kalkestein and P Soven, *Surf. Sci.* **26**, 85 (1971)
[9] R Guleria, P K Ahluwalia and K C Sharma, *Phys. Status, Solidi* **B181**, 397 (1994)
[10] T L Einstein and J R Schrieffer, *Phys. Rev.* **B7**, 3629 (1973)
[11] W Brenig and K Schonhammer, *Z. Phys.* **267**, 201 (1974)
[12] H Ishida and K Terakura, *Phys. Rev.* **B36**, 4510 (1987)
[13] R Taranko, R Cardena, E Taranko and V K Fedyanin, *Surf. Sci.* **238**, 293 (1990)

PRAMANA
— journal of
physics

© Printed in India

Vol. 44, No. 5,
May 1995
pp. 461–470

Vibrational analysis of $NaM_2OH(H_2O)(MoO_4)_2/D_2O$ [M = Ni, Zn]

R RATHEESH, G SURESH and V U NAYAR*
Department of Physics, University of Kerala, Kariavattom, Trivandrum 695 581, India
*to whom correspondence should be addressed

MS received 8 August 1994; revised 6 February 1995

Abstract. The infrared and Raman spectra of $NaNi_2OH(H_2O)(MoO_4)_2$ and $NaZn_2OH(H_2O)(MoO_4)_2$ and their partially deuterated analogues are recorded and analysed on the basis of vibrations of MoO_4^{2-} tetrahedra and H_2O molecules. The MoO_4^{2-} groups are found to be more distorted in $NaNi_2OH(H_2O)(MoO_4)_2$ than in the other compound. Bands indicating the presence of H_3O^+ ions are not observed in $NaZn_2OH(H_2O)(MoO_4)_2$ ruling out the possibility of the formulation of $NaZn_2OHO(MoO_3OH)_2$. Hydrogen bonds of medium strength are present in both the compounds.

Keywords. Infrared spectrum; Raman spectrum; hydrogen bonding.

PACS No. 78·30

1. Introduction

The simple and mixed metal molybdate phases, formed by the reaction of metal molybdates with salts of transition metals are of great importance because of their catalytic and magnetic properties and their spectral features ([1, 2]. X-ray diffraction studies on such phases show that $NaNi_2OH(H_2O)(MoO_4)_2$ is isostructural with $NaZn_2OH(H_2O)(MoO_4)_2$ [3,4]. The Raman and infrared spectra of compounds containing MoO_4^{2-} ions have been investigated by several workers [5–8]. However, there is considerable disagreement in the assignments of the fundamental bending modes, $\nu_2(E)$ and $\nu_4(F_2)$ of these ions. In view of the above facts, IR and Raman spectra of $NaNi_2OH(H_2O)(MoO_4)_2$, $NaZn_2OH(H_2O)(MoO_4)_2$ and their deuterated analogues have been studied to elucidate the dynamics of the crystal and to understand the nature of hydrogen bonding in them.

2. Experimental

The polycrystalline sample of $NaNi_2OH(H_2O)(MoO_4)_2$ (abbreviated as NNHM) was prepared by adding $NiCl_2 \cdot 2H_2O$ (2 M, 100 ml) dropwise to a well stirred boiling solution of $Na_2MoO_4 \cdot 2H_2O$ (2 M, 100 ml) and refluxing it for 15 h [3]. $NaZn_2OH(H_2O)(MoO_4)_2$ (hereafter referred to as NZHM) was prepared by adding $ZnCl_2 \cdot 6H_2O$ (1 M, 100 ml) in a similar way to $Na_2MoO_4 \cdot 2H_2O$ (1 M, 100 ml) and refluxing it for 24 h [4]. The deuterated analogues (NNDM and NZDM) were prepared by dissolving the final products in heavy water. The infrared spectra were recorded using a Perkin-Elmer 577 spectrophotometer using KBr pellet method. A Spex 1401 double monochromator equipped with a Spectra Physics model 165 argon

Table 1. Summary of the factor group analysis of $NaM_2OH(H_2O)(MoO_4)_2$ [M = Ni, Zn].

Factor group species C_{2h}^3	$2MoO_4^{2-}(C_s)$		$H_2O(C_{2h})$		O	H	$2(Ni_2^{2+}/Zn^{2+})$	Na^+	Optical modes	Acoustic modes
	Internal modes	External modes	Internal modes	External modes	(C_{2h})	(C_{2h})	(C_i)	(C_{2h})		
A_g	6	2T, 1R	2	1R	—	—	—	—	12	—
B_g	3	1T, 2R	1	2R	—	—	—	—	9	—
A_u	3	1T, 2R	—	1T	1T	1T	3T	1T	12	1
B_u	6	2T, 1R	—	2T	2T	2T	3T	2T	18	2
	18	6T, 6R	3	3R, 3T	3T	3T	6T	3T	51	3

Table 2. Correlation scheme for the internal vibrations of MoO_4^{2-} in $NaM_2OH(H_2O)(MoO_4)_2$ [M = Ni, Zn].

Free ion symmetry T_d			Site symmetry C_s	Factor group symmetry C_{2h}	
2	(ν_1)	A_1	A′	A_g	6
4	(ν_2)	E		B_g	3
			A″	A_u	3
12	(ν_3, ν_4)	$2F_2$		B_u	6

ion laser was used to record the Raman spectra in the Stokes region with a resolution better than 3 cm^{-1}.

3. Factor group analysis

$NaNi_2OH(H_2O)(MoO_4)_2$ crystallizes in the monoclinic system with space group $C2/m$ (C_{2h}^3) having one formula unit per Bravais cell [3, 9]. There are two crystallographically unique H atoms with one of them occupying half of the available sites, resulting in the presence of water and hydroxyl groups on alternate sites. The MoO_4 units form a tetrahedron with three short Mo-O bonds and the fourth one relatively longer. The coordination of O atoms around Ni atom represents a slightly distorted octahedral arrangement.

The factor group analysis has been carried out on the basis of the correlation method developed by Fateley *et al* [9] to get the irreducible representations. The molybdate ion contributes to 18 internal and 12 external modes, distributed among four factor group species. Water molecules contribute to 3 internal modes. The remaining vibrational degrees of freedom are made up of translational and rotational modes of different ions. The Ni^{2+} and Na^+ ions contribute only to the IR active species A_u and B_u. The results are summarized in tables 1 and 2. The irreducible representations of the title compound in C_{2h} factor group, excluding acoustic modes are:

$$\Gamma_{NNHM} = 12A_g + 9B_g + 12A_u + 18B_u$$

$NaZn_2OH(H_2O)(MoO_4)_2$ is isostructural with the nickel compound and the Zn atoms occupy the positions of Ni atoms [4].

4. Results and discussion

4.1 MoO_4^{2-} vibrations

A free MoO_4^{2-} ion has a tetrahedral symmetry with four normal modes of vibrations: a non-degenerate symmetric stretching mode $\nu_1(A_1)$ at 894 cm^{-1}, a doubly degenerate symmetric bending mode $\nu_2(E)$ at 318 cm^{-1}, triply degenerate asymmetric stretching $\nu_3(F_2)$ and asymmetric bending $\nu_4(F_2)$ modes at 833 and 381 cm^{-1} respectively [10]. All these modes are Raman active whereas ν_1 and ν_2 are IR inactive.

The most intense band in the Raman spectrum of NNHM (table 3) observed at 917 cm^{-1} with a shoulder at 896 cm^{-1} and split components at 942 and 880 cm^{-1} are

Table 3. Spectral data (cm^{-1}) and band assignments of $NaNi_2OH(H_2O)(MoO_4)_2/D_2O$ and $NaZn_2OH(H_2O)(MoO_4)_2/D_2O$.

$NaNi_2OH(H_2O)(MoO_4)_2$		$NaNi_2OD(D_2O)(MoO_4)_2$		$NaZn_2OH(H_2O)(MoO_4)_2$		$NaZn_2OD(D_2O)(MoO_4)_2$		
Raman	IR	Raman	IR	Raman	IR	Raman	IR	Assignments
3498 wbr	3480 –		3520 –					
	2878 sbr		2860 sbr					
		3386 wbr		3350 mbr	3380 –	3356 mbr	3351 –	ν_3, ν_1 H_2O
3290 wbr		3292 wbr			2820 mbr		3138 mbr	
3016 wbr		3119 wbr		3115 wbr		3119 wbr		
		2474 wbr				2510 wbr	2660 –	
		2448 wbr	2240 –				2565 wbr	ν_3, ν_1 D_2O
		2347 wbr	2030 mbr			2327 wbr		
1604 wbr	1618 mbr	1608 wbr	1625 mbr	1618 wbr	1610 w		1620 wbr	ν_2 H_2O
					1570 mbr	1590 wbr	1560 mbr	
		1333 wbr	1380 w			1348 wbr	1389 wbr	ν_2 D_2O
1271 w	1200 m							
		1094 m	1110 m	1136 m	1129 mbr			
				1125 w	1112 mbr		1026 wbr	δMo-O-H/D
942 w		922 w						
917 vs	912 vs	911 vs	920 vs	919 sbr	908 s	918 s	918 s	ν_1 MoO_4^{2-}
896 sh		908 s						
880 vw		893 w						
855 s	849 –	852 s		857 mbr		857 s	857 s	
823 sh	771 sbr	823 sh	863 –	820 mbr	850 –	818 m	840 s	ν_3 MoO_4^{2-}
773 m		770 m	760 sbr	794 w	720 sbr		782 m	
743 m		747 w		768 w		748 wbr		
726 w		737 w						
		721 m						

679 m		675 mbr	690 w					
674 w		670 mbr	672 vw		640 w			$\nu_r H_2O/D_2O$
621 w	610 vw	607 m		609 w	629 w			
556 w		593 m	590 vw		588 vw			
553 w	540 vw	552 m	520 w	578 w	579 vw	538 w		$\nu_t H_2O/D_2O$
	475 vw	471 w		488 vw	494 wbr			
452 w		458 m	460 vw	464 vw	460 w			$\nu_w H_2O/D_2O$
						438 vw	423 w	
401 w	400 m		382 w	418 w		392 w		$\nu_4 MoO_4^{2-}$
		369 w			374 m		384 w	
353 m	350 w	352 m	340 w				366 m	
331 w		333 w	330 w	335 mbr		337 mbr		
	320 m			320 mbr	310 w		302 wbr	$\nu_2 MoO_4^{2-}$
285 w	282 w	283 m	290 w	289 w	290 w	286 w		
				266 m	278 m		270 m	Ni-O & Zn-O stretching
243 w			250 w					
221 w	230 m		239 vw					
184 m		193 m		190 w	218 m	196 w		
		178 w				170 w		External modes
				128 m		132 m		

Relative intensities: w – weak; m – medium; s – strong; br – broad; sh – shoulder assigned to the symmetric stretching (ν_1) mode of the molybdate ion. In NZHM, only a single strong band is observed in this region (*ca.* 919 cm^{-1}). This IR inactive mode appears as an intense band at 912 cm^{-1} in the IR spectrum of NNHM and at 908 cm^{-1} in NZHM. The appearance of the IR inactive mode may be due to the lowering of symmetry of the molybdate ion from T_d to C_1. In the deuterated compounds also, these bands are observed without much change (figures 1 and 2).

The frequencies observed in the 720 to 860 cm^{-1} region in both the compounds are assigned to the triply degenerate asymmetric stretching (ν_3) vibrations of the MoO_4^{2-} ion [11]. The degeneracy of this mode is lifted in both the compounds and additional splitting is observed. NNHM exhibits a larger splitting (around 129 cm^{-1}) than that in NZHM (89 cm^{-1}).

When the Mo-O bond length is 1·759 Å, the MoO_4 tetrahedron is considered to be perfect and Mo-O correlation yields symmetric stretching frequencies at 858 cm^{-1} [12]. But in NNHM the Mo-O bond lengths vary from 1·751 to 1·833 Å whereas in NZHM Mo-O bond lengths vary from 1·737 to 1·839 Å. In both the compounds, the symmetric stretching mode ν_1 shows a shift to higher wavenumbers from the free state values. These higher frequencies for the ν_1 mode and large splitting of ν_3 mode are due to the interaction between the stretching motions of the tetrahedral ions [13].

Discrepancies exist in the assignment of the symmetric bending mode ν_2 and asymmetric bending mode ν_4. Polarization studies by Miller *et al* [14] and comparative study of various potential functions for the MoO_4 species [15] have conclusively proved that $\nu_4 > \nu_2$. Further, from the intensity calculations for ν_2 and ν_4 Muller *et al* [16] have shown that ν_2 has a higher intensity than ν_4 in Raman while ν_4 has a higher intensity in the infrared. The assignment of the internal modes $\nu_2(E)$ and $\nu_4(F_2)$ is however complicated by the presence of lattice modes in the same region.

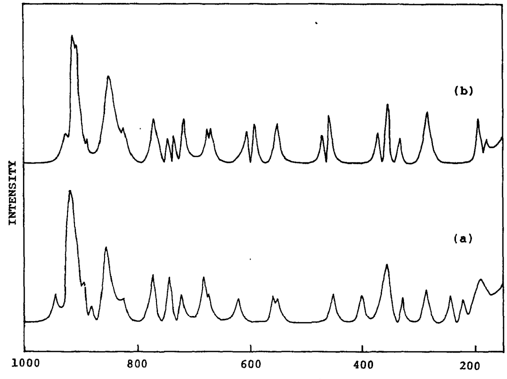

Figure 1. Raman spectra of the internal modes of (a) $NaNi_2OH(H_2O)(MoO_4)_2$ and (b) $NaNi_2OD(D_2O)(MoO_4)_2$ in the 150–1000 cm^{-1} region.

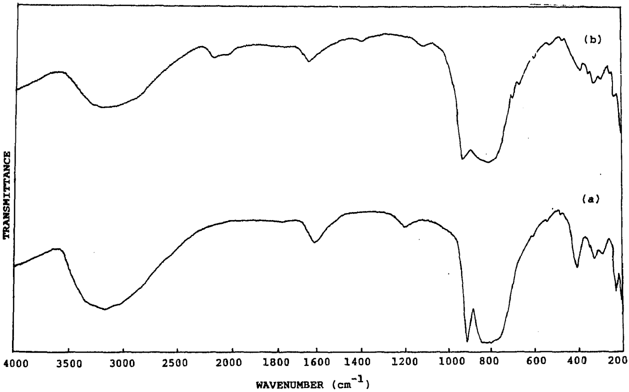

Figure 2. Raman spectra of the internal modes of (a) $NaZn_2OH(H_2O)(MoO_4)_2$ and (b) $NaZn_2OD(D_2O)(MoO_4)_2$ in the 100–1000 cm^{-1} region.

In NZHM, two medium intense broad bands are observed in Raman spectrum in the symmetric bending region (ν_2). The corresponding IR band is a weak line at 310 cm^{-1}. Moreover, asymmetric bending mode ν_4 is observed as a weak band around 418 cm^{-1} in Raman and a medium intense band around 374 cm^{-1} in the IR spectrum in agreement with the intensity criteria suggested by Muller *et al* [16]. But, in NNHM, only a weak band is observed in the symmetric bending mode in the Raman spectrum, while a medium intense band is obtained in the infrared spectrum. The asymmetric bending mode gives a medium intense band at 353 cm^{-1} in the Raman spectrum along with a weak one at 401 cm^{-1}. The corresponding IR band is observed as a medium intense band at 400 cm^{-1} with a weak line at 350 cm^{-1}. Intensity criteria are found to be not obeyed in the nickel compound. Spectra of the deuterated compounds do not show much variation in this region. In both NNHM and NZHM a partial lifting of degeneracy is observed for the bending modes while the degeneracy of the asymmetric stretching mode ν_3 is lifted completely and additional splitting is observed in both the compounds. In addition, the non-degenerate ν_1 mode shows additional weak bands in NNHM. The splitting of the ν_1 mode in NNHM and the departure from the intensity criteria suggested by Muller *et al* [16] show that the distortion of the MoO_4^{2-} ion is more in NNHM than in NZHM.

4.2 *H_2O/D_2O vibrations*

The vibrational frequencies of a free water molecule usually occur at 3756 (ν_3), 3652 (ν_1) and 1595 (ν_2) cm^{-1}. Depending on the hydrogen bond strength, the stretching modes will shift to lower wavenumbers and bending mode to higher wavenumbers [17].

In the Raman spectrum of NNHM, three weak bands are obtained in the stretching mode region of water while a medium intense band at 3350 cm^{-1} and a weak band at

3115 cm^{-1} are observed in NZHM for the corresponding region. The infrared spectrum of the nickel compound shows a strong broad absorption ranging from 2878 to 3480 cm^{-1} while the zinc compound gives medium intense broad band from 2820 to 3380 cm^{-1} in this region. On deuteration, these IR bands are reduced in intensity, showing partial deuteration and a medium intense band is obtained in the 2030–2240 cm^{-1} region for NNDM and in 2565–2660 cm^{-1} region for NZDM. This is assigned to the D_2O stretching modes.

Infrared spectra show a broad band of medium intensity at 1618 cm^{-1} in NNHM and two bands at 1610 (weak) and 1570 (broad, medium intense) cm^{-1} in NZHM for the H_2O bending modes. Corresponding Raman bands are of weak intensity. On deuteration new bands appears in the D_2O bending region. The degree of deuteration is found to be 42% for the nickel compound and 58% for the zinc compound (figures 3–5).

The decrease in frequencies of stretching modes and increase in frequencies of bending mode of water molecules from the free state values show the presence of hydrogen bonds of medium strength in these compounds [17].

In $NaZn_2OH(H_2O)(MoO_4)_2$ Clearfield *et al* [4] have suspected the presence of H_3O^+ ions considering a formulation $NaZn_2OHO(MoO_3OH)_2$. But later Moni *et al* [3] have confirmed the structure of $NaNi_2OH(H_2O)(MoO_4)_2$. In the present study, bands indicating the presence of H_3O^+ ions are not observed in these compounds confirming the structure as suggested in manganese and nickel compounds [18, 19].

The librational modes of water viz. wagging, rocking and twisting, fall in the region of 452–490 cm^{-1}. These modes are assigned in the order $\nu_r > \nu_t > \nu_w$ [20]. The Mo-O-H bending modes are observed at 1200 cm^{-1} in the IR and at 1271 cm^{-1} in the Raman spectrum of NNHM [21]. But, in NZHM, the Raman spectrum gives a medium intense

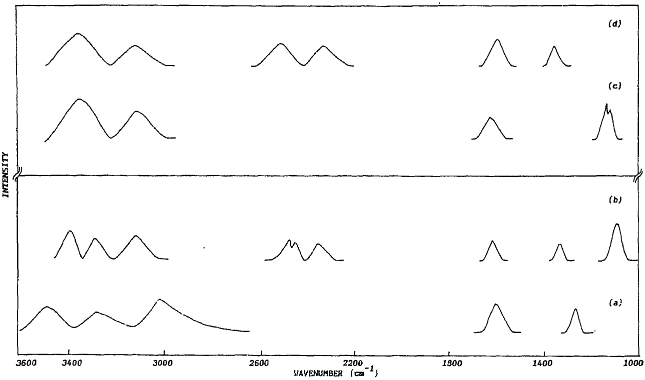

Figure 3. Raman spectra of (a) $NaNi_2OH(H_2O)(MoO_4)_2$, (b) $NaNi_2OD(D_2O)(MoO_4)_2$, (c) $NaZn_2OH(H_2O)(MoO_4)_2$ and (d) $NaZn_2OD(D_2O)(MoO_4)_2$ in the 1000–3600 cm^{-1} region.

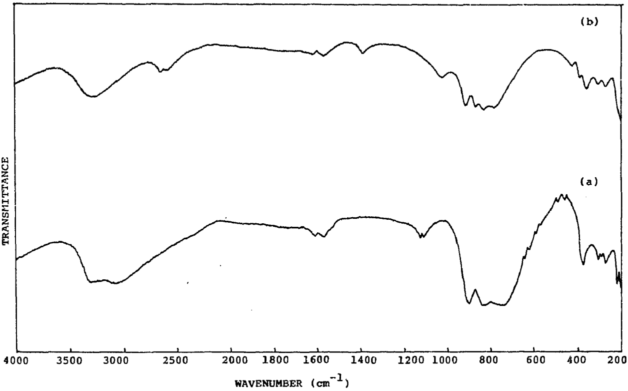

Figure 4. Infrared spectra of (a) $NaNi_2OH(H_2O)(MoO_4)_2$ and (b) $NaNi_2OD(D_2O)(MoO_4)_2$ in the 200–4000 cm^{-1} region.

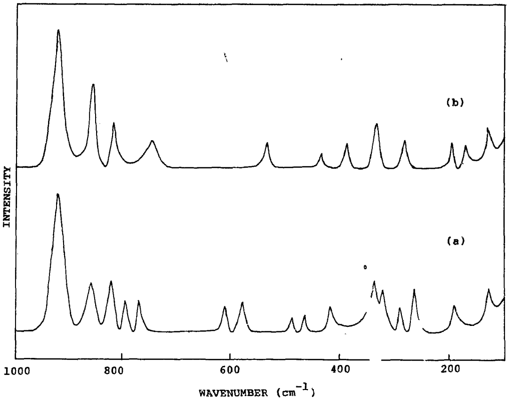

Figure 5. Infrared spectra of (a) $NaZn_2OH(H_2O)($ $oO_4)_2$ and (b) $NaZn_2OD(D_2O)(MoO_4)_2$ in the 200–4000 cm^{-1} region.

band at 1136 cm^{-1} and a weak band at 1125 cm^{-1} in this region. The infrared spectrum gives a doublet with medium intensity.

4.3 *External modes*

The region below 291 cm^{-1} is complicated due to the external modes of the MoO_4^{2-} ion, lattice modes of water and metal oxygen stretching modes. Hence, an unambiguous assignment of the observed bands to each of these modes is not possible. However, Ni-O and Zn-O stretching modes are assigned tentatively taking into account the octahedral coordination of these atoms [22].

5. Conclusions

The MoO_4^{2-} groups in $NaNi_2OH(H_2O)(MoO_4)_2$ are found to be more distorted than that in $NaZn_2OH(H_2O)(MoO_4)_2$. Bands indicating the presence of H_3O^+ ions are not observed in $NaZn_2OH(H_2O)(MoO_4)_2$ ruling out the possibility of the formulation of $NaZn_2OHO(MoO_3OH)_2$. The decrease in frequencies of the stretching modes and the increase in frequencies of the bending mode of water molecules from the free state values show the presence of hydrogen bonds of medium strength in these compounds.

References

[1] L G Van Uitert, R C Sherwood, H J Williams, J J Rubin and W A Ronner, *J. Phys. Chem. Solids* **25**, 1447 (1964)
[2] P Rajaram, V Viswanathan, M V C Sastri and V Srinivasan, *Indian J. Chem.* **12**, 1267 (1974)
[3] A Moni, P R Rudolf and A Clearfield, *Acta Crystallogr.* **C42**, 1667 (1986)
[4] A Clearfield, M J Sims and R Gopal, *Inorg. Chem.* **15**, 335 (1976)
[5] R H Busey and O L Keller Jr., *J. Chem. Phys.* **41**, 216 (1964)
[6] G M Clark and W P Doyle, *Spectrochim. Acta* **22**, 1441 (1966)
[7] J Predhomme and P Tarte, *Spectrochim. Acta* **A28**, 69 (1972)
[8] N Weinstock, H Schulze and A Muller, *J. Chem. Phys.* **59**, 5063 (1973)
[9] W G Fateley, F R Dollish, N T Mc Devitt and F FBentley, *Infrared and Raman selection rules for molecular and lattice vibrations – The correlation method* (Wiley, New York, 1972)
[10] I Kanesaka, M Kirishiki and I Matsuura, *J. Raman Spectrosc.* **23**, 201 (1992)
[11] M Isaac, N Santha and V U Nayar, *J. Raman Spectrosc.* **22**, 237 (1991)
[12] F D Hardcastle and I E Wachs, *J. Raman Spectrosc.* **21**, 683 (1990)
[13] P J Miller, *Spectrochim. Acta* **A27**, 957 (1971)
[14] P J Miller, R K Khanna and E R Lippincott, *J. Phys. Chem. Solids* **34**, 533 (1973)
[15] L J Basile, J R Ferraro, P L B Ville and McWall, *Co-ord. Chem. Rev.* **11**, 211 (1973)
[16] A Muller, E J Baran and R O Carter, *Struct. Bonding* **26**, 81 (1976)
[17] S N Vinogradov and R H Linnel, *Hydrogen bonding* (Reinhold, New York, 1971)
[18] D Philip and G Aruldhas, *Indian J. Phys.* **B64**, 196 (1990)
[19] A Clearfield, A Moni and P R Rudolf, *Inorg. Chem.* **24**, 4606 (1985)
[20] X Mathew and V U Nayar, *Spectrochim. Acta* **A45**, 243 (1989)
[21] S Crouch-Baker and P G Dickens, *Polyhedron* **5**, 63 (1986)
[22] F Cariati, S Bruni, M Martini and G Spinolo, *J. Raman Spectrosc.* **22**, 397 (1991)

PRAMANA
— journal of
physics

© Printed in India

Vol. 44, No. 5,
May 1995
pp. 471–479

Measurement of cross-section of excitation transfer from $3s_2$ to $4s_1$ and $5s_1$ energy levels of neon

R K GARG and VASANT DANDAWATE
National Physical Laboratory, K S Krishnan Marg, New Delhi 110012, India

MS received 16 March 1994; revised 13 February 1995

Abstract. Collision induced non-radiative transitions in neon plasma have been studied using high intra-cavity radiation field of a 633 nm He–Ne laser. The transitions, induced from $3s_2$ energy level to $4s_1$ and $5s_1$ groups of energy levels, have been detected as changes in intensities of the spectral lines originating from these energy levels. From these intensity measurements, the quantities governing the transitions i.e. (i) S_3^e/S_{3RT}, the ratio of the probabilities of electronic deexcitation to the total radiative deexcitation of energy level 3 (ii) $\langle r_{23}^e v_e \rangle$, rate of excitation transfer per particle and (iii) S_{23}^e, the total probability for excitation transfer from level 2 to level 3 at a certain value of electron density have been calculated.

Keywords. Collisional cross-section; excitation transfer.

PACS No. 34·80

1. Introduction

It is known that the different constituents of a plasma viz. electrons, atoms in the ground and excited states and ions exchange their energy during collision. The excited atoms lose their energy by radiative as well as by non-radiative processes. Simultaneously, the population of excited atoms at a particular energy level is replenished by the processes of electron collision and absorption. To understand these processes and to derive the laws governing them, investigations are carried out by selectively exciting a particular energy level of a gas in a plasma using a laser radiation field.

The interaction of a strong laser radiation field with the excited atoms in a particular pair of energy levels, resonant with the incident laser frequency, leads to considerable changes in the population of atoms in these levels. These changes are communicated to other neighbouring energy levels which are connected to the particular pair of energy level by collision induced non-radiative and radiative transitions.

Useful information on interaction among these excited states has been obtained, by analysing the intensity changes in the spontaneous emission from these neighbouring energy levels as a result of interruption of laser radiation. By studying the dependence of these intensity changes on electron density and on pressure of the gas, it is possible to separate out the energy levels connected to electron-atom from those connected to atom–atom collision processes [1].

In an earlier work [2], only the rate of excitation transfer per particle, $\langle r_{23}^e v_e \rangle$, induced by electron-atom collision process from $3s_2$ level to only $4s_1'''$ and ($5s_1'''$ and $5s_1''$) levels of neon was determined.

We present here the data on (i) S_3^e/S_{3RT}, the ratio of the probabilities of electronic deexcitation to the total radiative deexcitation of energy level 3, (ii) $\langle r_{23}^e v_e \rangle$, the rate of excitation transfer per particle and (iii) S^e_{23}, the total probability for excitation transfer from level 2 to level 3 at a certain value of electron density obtained by electron-atom collision between the $3s_2$ level of neon and the close-by energy levels, $4s_1''''$, $4s_1'''$, ($5s_1''''$ and $5s_1''$) and ($5s_1'''$ and $5s_1''$) using the above technique.

We provide here the new data for the three quantities on excitation transfer from $3s_2$ to $4s_1$ and $5s_1$ groups of levels of neon and it also provides data on excitation transfer rate per particle in support of earlier work.

Experimental data on the transition between excited states are low compared to transitions from the ground state of the atoms. The great variety of practical problems calls for knowledge of a large number of quantities. Therefore maximum amount of experimental data on electron-atom collision processes is very essential.

2. Theory

Let us consider an atomic system with two quantum states represented by 2 and 1 having energies E_2 and E_1, with the frequency of radiation ν_{21} obeying the relation $E_2 - E_1 = h\nu_{21}$ as represented in figure 1(a). An incident laser radiation of frequency ν_{21} on such an atomic system will redistribute the population of atoms at the levels 2 and 1 and thus decreases the difference of the population between 2 and 1. If the incident radiation is periodically interrupted, the static population N_1 and N_2 will be modulated with amplitudes ΔN_1 and ΔN_2 with phases opposite to each other.

Atomic levels denoted by 3 and 0 close to 2 and 1 respectively as shown in figure 1(b) may also show modulation in their population as a consequence of transfer of excitation energy from levels 2 and 1 either due to non-radiative transitions involving collisions, or radiative transitions. The magnitude of these modulations at 0 and 3, in general will be determined by the efficiency of excitation transfer from levels 1 and 2 to

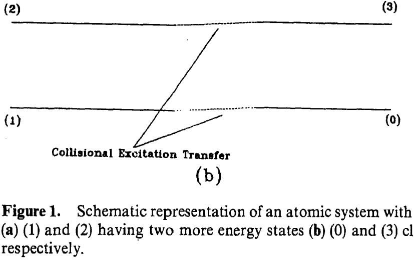

Figure 1. Schematic representation of an atomic system with two quantum states (**a**) (1) and (2) having two more energy states (**b**) (0) and (3) close to each of them respectively.

these levels. The measurements of the amplitude and phases of modulation at levels 0 and 3 provide information on the rates of collisional non-radiative transitions as well as on radiative transitions. The collisional excitation transfer may involve either atom–atom collision or electron-atom collision. Level 3 can be considered free from the cascade radiative transitions from higher energy levels, at least as a result of incident laser radiation. But level 0 will certainly be affected by the cascade radiative transitions from level 2.

Equation 1 gives the relations derived by Khaikin [2] for the excitation transfer process from levels 2 to 3 caused by electron-atom collisions only.

$$\frac{\Delta I_2}{\Delta I_3}=\frac{S_{3RT}}{\langle r^e_{23}v_e\rangle}\frac{A_2\nu_2}{A_3\nu_3}\frac{1}{n_e}+\frac{\langle r^e_3 v_e\rangle}{\langle r^e_{23}v_e\rangle}\frac{A_2\nu_2}{A_3\nu_3} \tag{1}$$

where ΔI_2 and ΔI_3 are the intensity changes of spectral lines originating from levels 2 and 3 respectively, S_{3RT}, is the probability of radiative deexcitation from level 3 to other lower energy levels; $\langle r^e_{23}v_e\rangle$, is the rate of excitation transfer from levels 2 to 3, per particle induced by electron collision; v_e, is the average value of electron velocity; A_2 and ν_2 and A_3 and ν_3, are the Einstein coefficients for spontaneous emission from levels 2 and 3 respectively to some other lower level and the corresponding frequency of emission; n_e, is the electron density; and r^e_3, is the effective cross-section of the non-radiative deexcitation rate of levels 3 to 2 and all other levels by electron collision.

Equation (1) reduces to the form

$$y=ax+b \tag{2}$$

where

$$y=\frac{\Delta I_2}{\Delta I_3}, \tag{2a}$$

$$a=\frac{S_{3RT}}{\langle r^e_{23}v_e\rangle}\frac{A_2\nu_2}{A_3\nu_3}, \tag{2b}$$

$$x=1/n_e, \tag{2c}$$

$$b=\frac{\langle r^e_3 v_e\rangle}{\langle r^e_{23}v_e\rangle}\frac{A_2\nu_2}{A_3\nu_3}. \tag{2d}$$

From (2a–2d), we see that by measuring the modulation in intensities of the spectral line originating from levels 2 and 3 at different values of electron density, we can plot a linear relation between $\Delta I_2/\Delta I_3$ and $1/n_e$. From this linear plot, we determine: S^e_3/S_{3RT}, $\langle r^e_{23}v_e\rangle$ and S^e_{23}.

S^e_3/S_{3RT}, the ratio of the probabilities of electronic deexcitation to the total radiative deexcitation of energy level 3 is obtained from (2b) and (2d) as follows:

$$\frac{S^e_3}{S_{3RT}}=\frac{\langle r^e_3 v_e\rangle}{S_{3RT}}n_e=b/a\,n_e \tag{3}$$

where S^e_3 is the total non-radiative rate of levels 3 to 2 and all other levels by electron collision, a is the slope of linear plot between $\Delta I_2/\Delta I_3$ and $1/n_e$ and b is the intercept on $\Delta I_2/\Delta I_3$ axis.

$\langle r^e_{23} v_e\rangle$, the rate of excitation transfer per particle is obtained by rewriting (2b) as:

$$\langle r^e_{23} v_e\rangle = \frac{A_2 \nu_2}{A_3 \nu_3}\frac{S_{3RT}}{a}, \tag{4}$$

where A_2 is the transition probability of the spectral line originating from level 2; S_{3RT}/A_3 is the ratio of the probability of radiative deexcitation from level 3 to other lower energy levels to the transition probability of the spectral line originating from level 3. These have been taken from theoretical data of Khaikin [2] and Inatsugu and Holmes [4].

S^e_{23}, the total probability for excitation transfer from levels 2 to 3 at a certain value of electron density n_e is obtained as follows:

$$S^e_{23} = \langle r^e_{23} v_e\rangle \times n_e \tag{5}$$

where $\langle r^e_{23} v_e\rangle$ is given by (4).

3. Experimental set-up

The experimental arrangement is shown in figure 2. NPL developed Brewster angle He–Ne laser, of 700 mm length and 1000 mm cavity length was used to generate high intra-cavity laser power by using both the mirrors with reflectivity of 99·8%. This intra-cavity laser radiation passes through a 100 mm long discharge plasma cell placed in a tandem with the laser plasma tube. The laser is operated by a constant current power supply and the laser output power stability is better than 0·1%. As the detecting technique uses a lock-in amplifier, it was observed that 0·1% power stability of the laser power is sufficient for the present study. There is a provision to vary the electric

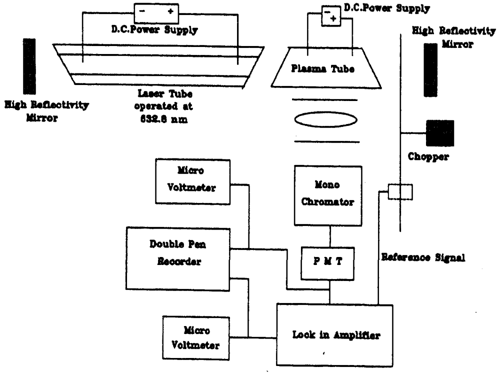

Figure 2. Schematic representation of the experimental set-up.

discharge current through the He–Ne mixture in this cell. Intensity of the spectral lines emitted through the side walls of the discharge cell have been studied using the usual combination of monochromator, a photomultiplier and a microvoltmeter. As the magnitude of the intensity changes induced by laser radiation is very small, a chopper and lock-in amplifier were also used to detect them. The chopping frequency used in this experiment was 34 Hz.

As the response of the detecting system varies with the spectral range, the whole system was calibrated using a light source whose spectral radiant emittance was calibrated against a PTB standard lamp. For determining the electron density value in a He–Ne plasma obtained in a tube diameter of 3 mm at a pressure of 1·2 torr, values obtained by earlier workers [2, 3] based on radio frequency technique were used. These values show that the electron density is linearly dependent on the range of discharge current considered (10 to 100 mA) and its value is $5 \times 10^{10}/\mathrm{cm}^3$ at 10 mA under the above mentioned conditions.

4. Observations

Figure 3 gives some of the energy levels of neon. The 633 nm laser radiation occurs due to transitions of the atoms from $3s_2$ to $2p_4$ states. At the time the laser radiation field is interrupted by the chopper, the stimulation of the atoms in the $3s_2$ state to deexcite to $2p_4$ is stopped and therefore the population of the atoms in the $3s_2$ state increases. It has been experimentally observed that all the spectral lines originating from the $3s_2$ level have shown an increase in intensity. At the same time, the population of the atoms in

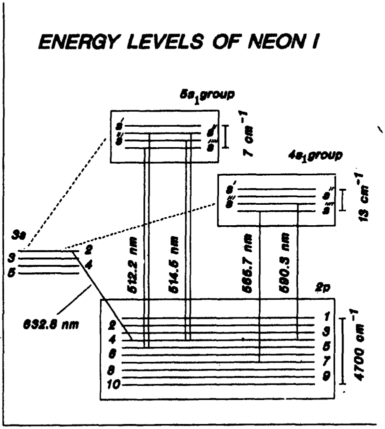

Figure 3. Schematic representation of some of the energy levels of NeI. The energy spacing is only representative and not as per actual values.

the $2p_4$ state has decreased. The percentage change in the intensity of the lines originating from these two levels is about 20. This change in $3s_2$ level population gets communicated to adjoining energy levels and for those within $3500\,\mathrm{cm}^{-1}$ a modulation up to 5% is produced.

If the change in the intensity of a particular line originating from a particular energy level x is denoted as ΔI_x and the change in the intensity of a line from $3s_2$ level as ΔI_{3s_2}, then $\Delta I_x/\Delta I_{3s_2}$ is a measure of the magnitude of the population change that is getting communicated to the level x due to the population change in the level $3s_2$.

Out of the large number of energy levels the $4s_1$ and $5s_1$ groups were selected for detailed study. In the case of $4s_1$ group, only the levels $4s_1''''$ and $4s_1'''$ were connected to $3s_2$ by electron-atom collision process, giving rise to radiations of 565·7 nm and 590·2 nm respectively. However, it was not possible to spectrally isolate a spectral line which would represent the sub-levels of $5s_1$ group; the lines at 512·2 nm and 514·5 nm were taken to represent the two sub-levels ($5s_1''''$ and $5s_1''$) and ($5s_1'''$ and $5s_1''$) respectively. The intensity change $\Delta I_{543\cdot 4}$ of line 543·4 nm originating from $3s_2$ to $2p_{10}$ level has been taken as modulation at $3s_2$ level.

The ratio of the changes in intensity of the line 543·4 nm to the lines under study has been obtained at different values of electron density n_e. A graph between $I_{543\cdot 4}/\Delta I_x$ and $1/n_e$, where x corresponds to the spectral lines under study, gives a linear plot from which the values of quantities a and b in (3) and (4) have been obtained. Such plots obtained for the spectral lines 565·7 nm, 590·2 nm, 512·2 nm and 514·5 nm are given in figures 4a–d respectively.

5. Results

The values of S_3^e/S_{3RT}, $\langle r_{23}^e v_e\rangle$ and S_{23}^e defined in the text, obtained for the above given energy levels $4s_1''''$, $4s_1'''$, ($5s_1''''$ and $5s_1''$) and ($5s_1'''$ and $5s_1''$) of neon are given in table 1. It

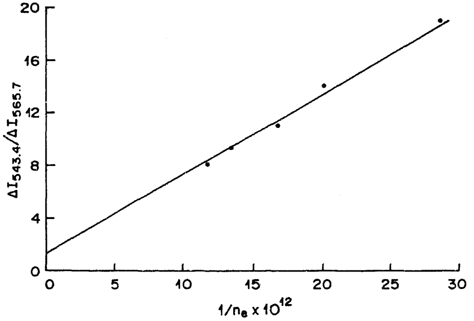

Figure 4(a). Variation of the ratio of intensity changes of two spectral lines at 543·4 and 565·7 nm, representing the two states of neon, $3s_2$ and $4s_1''''$ respectively, with respect to the reciprocal of electron density of the plasma in the cell.

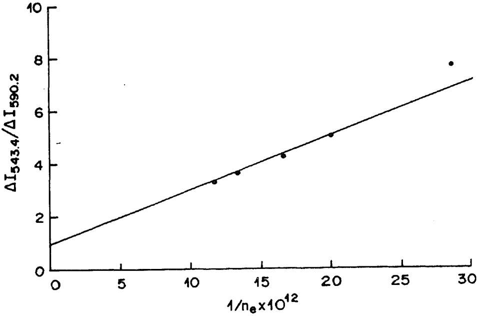

Figure 4(b). Variation of the ratio of intensity changes of two spectral lines at 543·4 and 590·2 nm, representing the two states of neon, $3s_2$ and $4s_1'''$ respectively, with respect to the reciprocal of electron density of the plasma in the cell.

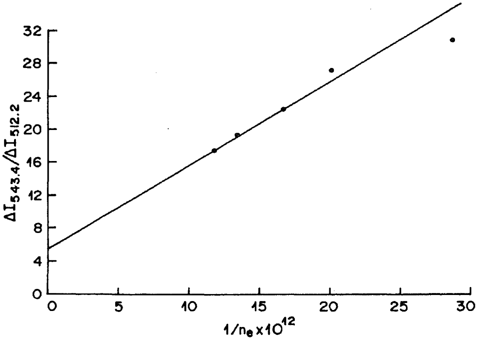

Figure 4(c). Variation of the ratio of intensity changes of two spectral lines at 543·4 and 512·2 nm, representing the two states of neon, $3s_2$ and ($5s_1''''$ and $5s_1''$) respectively, with respect to the reciprocal of electron density of the plasma in the cell.

can be noted that the values of the three quantities for $4s_1''''$ and ($5s_1''''$ and $5s_1''$) energy levels are being reported for the first time.

In table 1 the values of Khaikin [2] for one quantity $\langle r_{23}^e v_e \rangle$ for levels $4s_1'''$ and ($5s_1'''$ and $5s_1''$) are given for comparison. It can be seen that the values obtained by us agree well with this.

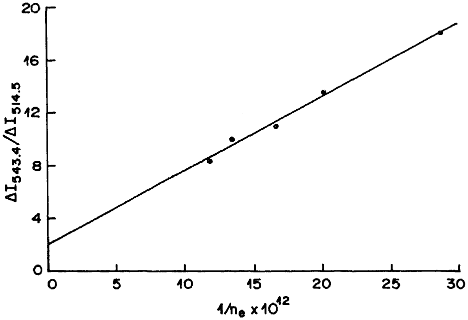

Figure 4(d). Variation of the ratio of intensity changes of two spectral lines at 543·4 and 514·5 nm, representing the two states of neon, $3s_2$ and ($5s_1'''$ and $5s_1''$) respectively, with respect to the reciprocal of electron density of the plasma in the cell.

Table 1. Values of quantities governing the laser induced transitions from intensity measurements.

Energy level (P.N.)* with spectral line (nm)	S_3^e/S_{3RT} at 10 mA	$\langle r_{23}^e v_e \rangle$ cm^3/s ($\times 10^{-8}$)	$S_{23}^e s$ at $n_e = 5 \times 10^{10}$ ($\times 10^7$)	$\langle r_{23}^e v_e \rangle$** cm^3/s ($\times 10^{-8}$)
$4s_1''''$(565·7)	0·11	1420	0·07	—
$4s_1'''$(590·2)	0·19	2150	0·11	2200
$5s_1''''$ and $5s_1''$ (512·2)	0·27	390	0·02	—
$5s_1'''$ and $5s_1''$ (514·5)	0·18	410	0·02	370

*P.N. represents Paschen Notation; **From Khaikin [2]

6. Conclusions and discussion

(1) The values of excitation transfer rate per particle $\langle r_{23}^e v_e \rangle$, obtained experimentally, is quite high ($\approx 10^{-5}$) compared to the typical values of $\langle rv \rangle$ from ground state which are of the order of 10^{-8} cm^3/s.

This is attributed to the fact that (i) the geometrical cross-section of the excited atoms in $4s_1$ and $5s_1$ groups of energy levels exceed by about 2 orders of magnitude to those of the ground state atoms and (ii) because of the small energy discrepancy between the participating levels, this process has a resonance nature and cross-section for such processes high.

(2) The probability of radiative deexcitation of the level $3s_2$ of neon is $2{\cdot}1 \times 10^7$. Now as per table 1 the probability of excitation transfer S_{23}^e from $3s_2$ to say $4s_1$ by electron

collision, is $\approx 10^6$. Even if we add all the probabilities of excitation transfer from $3s_2$ level to all the neighbouring energy levels by electron collision, it may come up to 2×10^6.

It may be thus concluded that the electron impact deexcitation of $3s_2$ level at the usual operating current (10 mA) for the He–Ne laser is about an order of magnitude less than the total radiative transition from it.

(3) From the values of probabilities of deexcitation by electron impact to that by radiative process S_3^e/S_{3RT}, for energy levels $4s_1''''$ and $4s_1''$ and for group $5s_1$, we see that the radiation transition probability exceeds by an order of magnitude to the electron collision deexcitation probability.

Thus it can be seen that, whereas, Khaikin's data on non-radiative transitions between $3s_2$ and the adjoining levels of $4s_1$ and $5s_1$ groups of energy levels is for only one quantity, i.e. $\langle r_{23}^e v_e \rangle$ and for unresolved overlap transitions, our data are for all the three quantities defined in the text belonging to resolved transitions from $4s_1''''$, $4s_1'''$, ($5s_1''''$ and $5s_1''$) and ($5s_1'''$ and $5s_1'$) groups of energy levels.

References

[1] V D Dandawate and R Rai, *J. Phys.* **B17**, 3805 (1984)

[2] A S Khaikin, *Physics of Atomic collisions*, edited by Skobettayn (1971); *Sov. Phys. JETP* **24**, 25 (1967)

[3] E F Labuder and E I Gorden, *J. Appl. Phys.* **35**, 1647 (1964)

[4] S Inatsugu and J R Holmes, *Phys. Rev.* **A8**, 8 (1973)

PRAMANA
— journal of
physics

© Printed in India

Vol. 44, No. 5,
May 1995
pp. 481–488

Fringe formation theory for real-time holographic interferometry using $Bi_{12}SiO_{20}$

C S NARAYANAMURTHY
Department of Physics, Bhavnagar University, Bhavnagar 364 002, India

MS received 3 September 1994; revised 7 February 1995

Abstract. A simple theory has been developed to explain the fringe formation in real-time holographic interferometry using BSO (bismuthsiliconoxide) crystal for interferometric applications. Detailed analysis has been given to choose the optimum size of the crystals.

Keywords. Photorefractive crystals; real-time holography.

PACS No. 42·40

1. Introduction

Photorefractive crystals are increasingly used as a recording medium for real-time holographic interferometry [1–7] due to their several advantages like non-requirement of developing and fixing. Also, the information can be processed in real-time by coupling the output with a computer and above all the medium is reusable unlike the conventional holographic recording media. The popular PR crystals used for real-time holographic interferometry are $Bi_{12}SiO_{20}$ (bismuthsiliconoxide), $Bi_{12}TiO_{20}$ (bismuthtitaniumoxide) and $Bi_{12}GeO_{20}$. Among these both BSO and BTO are used widely for real-time holographic interferometry since the former is very sensitive to bluish green (typically argon-ion laser wavelength) region and the latter to popular red wavelength region. These two PR crystals utilise anisotropic self-diffraction phenomena in which the diffracted beam polarization is rotated with respect to the transmitted beams. Many geometries have been proposed for recording real-time holograms in these crystals based on four-wave mixing and two-beam coupling. The four-wave mixing technique needs read out beam and some times with a different frequency and more optics but the two-beam coupling requires only simple geometry. The most efficient real-time holographic interferometry geometry was proposed by Kamshalin *et al* using BTO crystal sandwiched between two polarizers in a two-beam coupling geometry [4]. This geometry utilizes the anisotropic self-diffraction phenomena and later this was successfully implemented by Troth and Dainty using a BSO crystal for real-time holographic interferometry [7]. The theoretical explanation for hologram formation inside PR crystals was developed by many authors using Kogelnik's coupled mode theory utilizing volume hologram phenomena [2]. However no theory has been proposed so far for the fringe formation for real-time holographic interferometry in a PR crystal. This paper reports a fringe formation theory for real-time holographic interferometry utilizing anisotropicself-diffraction phenomena in BSO. This theory also predicts the optimum size of the crystals to be used for real-time holographic interferometric applications.

2. Fringe formation theory

The proposed fringe formation theory is derived in two ways. First by considering optical activity and secondly by ignoring it. For both the analyses a BSO crystal sandwiched between two polarizers as shown in figure 1 is considered. The BSO crystal is cut in the (110) crystal orientation with its $[1\bar{1}0]$ crystal direction parallel to the plane of incidence illuminating radiation.

2.1 *Consideration of optical activity of the crystal*

Let $E_0 e^{i\phi_0}$ be the object wave and $E_r e^{i\phi_r}$ be the reference wave forming the writing beams which incident on the BSO crystal. These two writing beams interfere inside the crystal to form the necessary phase grating which in turn produces the necessary refractive index change through diffusion mechanism. The transfer matrix for such a photorefractive crystal can be written as [3],

$$M^1_{tr} = |\tilde{E}_0 + \tilde{E}_r| \begin{vmatrix} \cos At - i\sin\psi_0 \sin At & -\sin At\cos\psi_0 \\ \cos\psi_0 \sin At & \cos At + i\sin\psi_0 \sin At \end{vmatrix} \tag{2.1}$$

where, t is the thickness of the crystal; $A = [\rho^2 + \{(\Delta n)^2/4\}]^{1/2}$; $\psi = \tan^{-1}(\Delta n/2\rho)$; ρ is the optical activity per unit length and Δn is the birefringence per unit length.

The value of Δn for BSO crystal used in this analysis is $1{\cdot}49 \times 10^{-5}$ (calculation is shown in appendix).

The anisotropic self-diffraction phenomenon occurs in BSO/BTO type of crystals of sillenite family whenever the writing beams interfere in the crystal. Figure 2 shows both the diffraction phenomena namely isotropic and anisotropic self-diffraction. In BSO crystal the relative intensity of two writing beams creates a space charge field which in turn produces a refractive index grating $\pi/2$ phase shifted relative to the intensity. This also induces axes of linear birefringence with refractive indices $n_0 + \Delta n$ and $n_0 - \Delta n$. After the formation of hologram inside the crystal to read out, one of the writing beams itself is used by assuming that the other writing beam i.e. the signal beam is turned off. This assumption can be considered since the phase grating will exist for a time due to inherent inertia of the photo refractive effect. Figure 3 shows that the reference wave polarization (assuming it is vertical at the centre of the crystal) is decomposed into two components polarized in the c_1 and c_2 directions. These orthogonal components will diffract off the grating polarized in the same directions, but with a phase delay between them. Consider the phase delays of the c_1 and c_2 relative to the reading wave. The refractive index that the c_1 and c_2 components of the read out wave see is different, due to induced birefringence, and are equal in magnitude but opposite in sign. Thus the phase difference between the two orthogonal components of diffraction is $+\pi/2 - (-\pi/2) = \pi$. Referring to figure 3, supposing that the polarization component of the reference wave in the c_1 direction $E_r(c_1)$ diffracts from the $n_0 - \Delta n$ grating with the same sense of polarization $E_r(c_1)$ at a particular instant. But, the polarization component in the c_2 direction $E_r(c_2)$ which is out of phase by π with respect to $E_r(c_1)$. The net resultant polarization of the diffracted reference wave is orthogonal to the input polarization. This is not so in the case of conventional holographic reconstruction. The advantage of such diffraction phenomenon is that it eliminates completely the background noise while forming the hologram. The above phenomenon can be derived from eq. (1) in the following way. Let the reference wave $E_r e^{i\phi_r}$ reads out the recorded

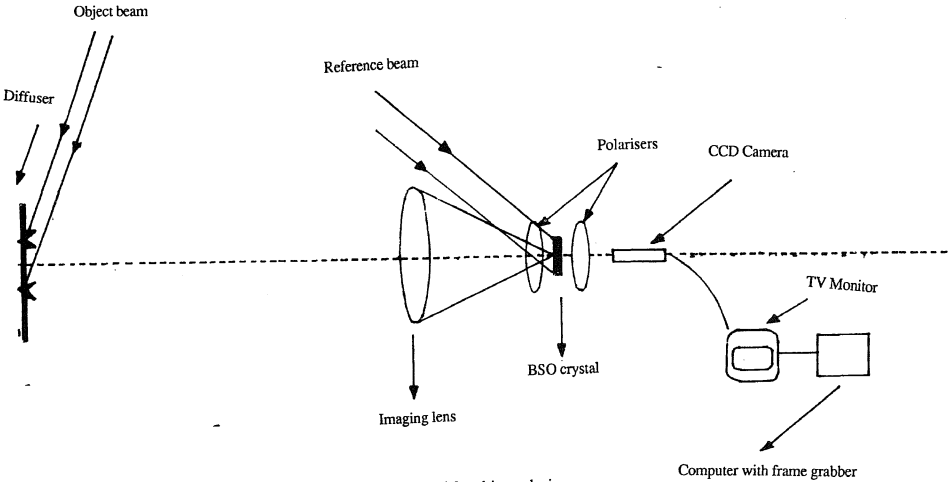

Figure 1. Shows the schematic of the experimental set-up used for this analysis.

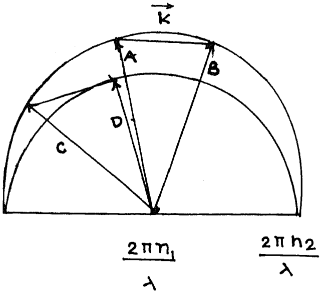

Figure 2. A, B shows the diagram of the isotropic diffraction and C, D shows the anisotropic self-diffraction phenomena.

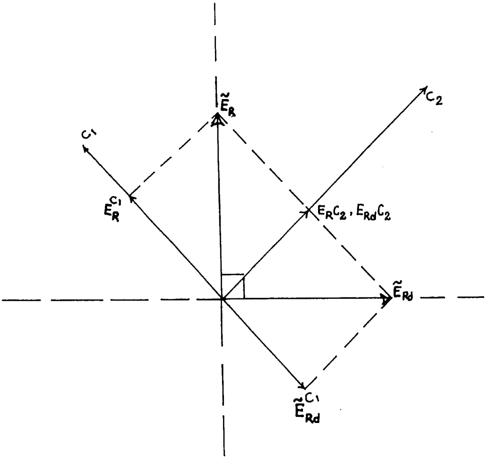

Figure 3. Shows the read out mechanism of anisotropic self-diffraction.

hologram (phase grating) with its vertical polarization at the centre of the crystal and assuming the signal beam is turned off momentarily. The output beam immediately after the crystal and just before the output polarizer is,

$$E^1_{Rd} = |\tilde{E}_0 + \tilde{E}_r| \begin{vmatrix} \cos At - i\sin\psi_0\sin At & -\sin At\cos\psi_0 \\ \cos\psi_0\sin At & \cos At + i\sin\psi_0\sin At \end{vmatrix} \begin{vmatrix} 0 \\ \tilde{E}_r \end{vmatrix}. \qquad (2.2)$$

The amplitude of the transmitted residual beam just outside the crystal is,

$$E^1_{Rd} = \begin{vmatrix} 0 & 0 \\ 0 & \cos \mathbf{A}t + i \sin \psi_0 \sin \mathbf{A}t \end{vmatrix} (E_0^2 + E_r^2) E_r e^{i\phi_r} + \begin{vmatrix} -\sin \mathbf{A}t \cos \psi_0 (E_0 e^{i\phi_0} + E_0 e^{-i\phi_0}) & 0 \\ 0 & 0 \end{vmatrix}. \tag{2.3}$$

Where the first term is the diffracted beam and the second term is the transmitted residual amplitude part. To obtain the transmitted residual amplitude the input and output polarizers are to be crossed and mathematically this can be written from (2.3) as,

$$E^1_{Rd} = \left(\begin{vmatrix} 0 & 0 \\ 0 & \cos \mathbf{A}t + i \sin \psi_0 \sin \mathbf{A}t \end{vmatrix} (E_0^2 \tilde{E}_r + E_r^2 \tilde{E}_r) \right) \begin{vmatrix} 1 & 0 \\ 0 & 0 \end{vmatrix} + \left(\begin{vmatrix} -\sin \mathbf{A}t \cos \psi_0 [(E_0 e^{i\phi_0}) + (E_0 e^{-i\phi_0})] & 0 \\ 0 & 0 \end{vmatrix} \right) \begin{vmatrix} 1 & 0 \\ 0 & 0 \end{vmatrix}. \tag{2.4}$$

The residual transmitted amplitude of the object beam can be written from the above matrix as,

$$|E^1_{Rd}| = (\sin \mathbf{A}t \cos\psi_0) E_0 e^{i\phi_0}. \tag{2.5}$$

Equation (2.5) represents the holographic image of the object alone and in real-time holographic interferometry, there will be a change in the phase of the object beam due to deformations/displacements of the test object as soon as the holographic image is formed then, in such a case eq. (2.5) will become,

$$|E^{11}_{Rd}| = (\sin \mathbf{A}t \cos\psi_0) E_0 e^{i\phi'_0} \tag{2.6}$$

Adding (2.5) and (2.6) the resultant transmitted residual intensity after complete cancellation of the diffracted beams is,

$$I_{Rd} = 2E_0^2 \sin^2 \mathbf{A}t \cos^2 \psi_0 (1 + \cos^2 \delta_0) \tag{2.7}$$

where $\delta_0 = (\phi_0 - \phi'_0)$.

The maximum intensity for the holographic interferometric fringes in conventional holographic interferometry depends upon the values of δ_0, that is the phase changes occurring in the object beam before and after in the ambient state of the object. In dynamic holographic interferometric case, it is clear from (2.7) that in addition to the value of δ_0 the intensity of the interferometric fringes depends upon the values of optical activity (ρ) and the birefringence value of the crystal. Figure 4 shows the plot between the thickness of the crystal and the visibility of the holographic interferometric fringes. Visibility is defined as $V = (\mathrm{I}_{\mathrm{rd\,max}} - \mathrm{I}_{\mathrm{rd\,min}})/(\mathrm{I}_{\mathrm{rd\,max}} + \mathrm{I}_{\mathrm{rd\,min}})$ for holographic interferometric fringes and the maximum value is one. It is clear from figure 4 that for obtaining maximum visibility the optimum thickness of the PR crystal (here BSO) should be between 1·5 mm and 3·5 mm for different values of optical activity in addition to the value of δ_0 where it should be $m\pi$ (m is an integer).

2.2 *Ignoring optical activity of the crystal*

The fringe formation theory can be derived by ignoring the optical activity of the

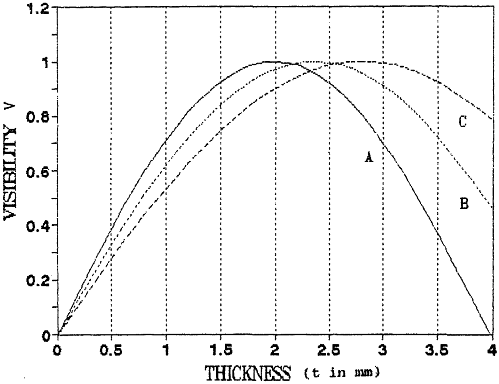

Figure 4. Shows the plot between visibility V and the thickness t of the BSO crystal for a constant value of $\lambda = 514$ nm. Curve A, $\rho = 45°/\text{mm}$; curve B, $\rho = 38°/\text{mm}$ and curve C, $\rho = 32°/\text{mm}$.

crystal. The transfer matrix of eq. (1) after neglecting the value of optical activity will be,

$$M_{\text{tr}}^2 = |\tilde{E}_0 + \tilde{E}_r| \begin{vmatrix} \cos \mathrm{A}t & -\sin \mathrm{A}t \\ \sin \mathrm{A}t & \cos \mathrm{A}t \end{vmatrix} \tag{3.1}$$

where $\rho = 0$, $\mathrm{A} = \{(\Delta n)^2/4\}^{1/2}$ and $\Delta n =$ the birefringence per unit length. Now when the read out beam enters the crystal the output beam just before the output polarizer is,

$$E_{Rd}^2 = \begin{vmatrix} 0 & 0 \\ 0 & \cos \mathrm{A}t \end{vmatrix} (E_0^2 + E_r^2)\tilde{E}_r + \begin{vmatrix} -\sin \mathrm{A}t(E_0 e^{i\phi_0} + E_0 e^{-i\phi_0}) & 0 \\ 0 & 0 \end{vmatrix}. \tag{3.2}$$

The transmitted residual amplitude of the object beam after rotating the output polarizer will be

$$|E_{Rd}^2| = E_0 \sin \mathrm{A}t e^{i\phi_0}. \tag{3.3}$$

The final resultant transmitted intensity after the phase changes in the object beam is

$$I_{Rd}^2 = 2E_0^2 \sin^2 \mathrm{A}t(1 + \cos^2 \delta_0) \tag{3.4}$$

The maximum intensity of the residual transmitted intensity can be obtained only when $\mathrm{A}t = \pi/2$ in addition to the value of δ_0. Substituting the value of A and assuming $\delta_0 = \pi$, the thickness of the BSO crystal needed is high to get the maximum visibility of the holographic interferometric fringes. This contradicts our earlier theoretical prediction by considering the optical activity that the optimum thickness of the crystal required is about 1·5 mm to 3·5 mm. Also, Troth *et al* [9] have reported that the thickness of the

BSO crystal used in their experiment on holographic interferometry to study the noise and sensitivity is 2·25 mm for a value of optical activity $\rho = 38{\cdot}7^\circ\,\mathrm{mm}^{-1}$ for $\lambda = 514$ nm and this agrees with the theory. Another important point is that the maximum thickness of commercially available and good optical quality BSO and BTO crystals (which are commonly used for holographic interferometry) is between 1·5 mm and 3·5 mm. The above results show that the optical activity of the PR crystal is very important in BSO/BTO type of crystals to do real-time holographic interferometry. The results also show that even by considering the optical activity, the BSO crystal acts as a birefringent/half wave plate.

3. Conclusion

A simple theory to obtain real-time holographic interferometric fringes using BSO crystal sandwiched between two polarizers is given and this theory also predicts the optimum size of the crystal required. This theory also shows that by ignoring optical activity the BSO crystal will act as a birefringent plate only when the size of the crystal is large.

Acknowledgements

The author dedicates this paper to Prof. J C Dainty of Imperial College, London and acknowledges his help and for providing facilities to carry out this work. The author acknowledges the DST, Government of India for awarding the BOYSCAST fellowship to carry out this work. The author wishes to thank the referee for his valuable comments.

Appendix

Calculation for finding Δn for the BSO crystal is used in this analysis. The formula for Δn following [2, 8] is,

$$\Delta n = n_0^3 r_{41}\left[\sqrt{\beta_0}\frac{\varepsilon_D \varepsilon_q}{(\varepsilon_q + \varepsilon_D)(1+\beta_0)}\right]$$

$$\varepsilon_D = \frac{K_B T K_g}{e}, \quad \varepsilon_q = \frac{e N_A}{\varepsilon \varepsilon_0 K_g} \tag{A1}$$

where K_B is the Boltzmann constant, T the temperature in Kelvin, e the electric charge of an electron, ε and ε_0 are the unperturbed permittivity of the material and the permittivity of the free space respectively and N_A is the trap number density in the crystal volume, r_{41} is the non-zero electro optic coefficient for crystals of sillenite family, β_0 is the signal to reference beam intensity ratio, n_0 is the unperturbed refractive index and K_g is grating spatial frequency.

The values of the constants are,

$n_0 = 2{\cdot}165$, $r_{41} = 4{\cdot}51$ pm/V, $K_\mathrm{B} = 1{\cdot}380 \times 10^{-23}$ J/K,

$T = 300$ K, $N_\mathrm{A} = 1{\cdot}27 \times 10^{22}/\mathrm{m}^3$, $e = 1{\cdot}602 \times 10^{-19}$ C,

$K_\mathrm{g} = 12{\cdot}6\,\mu\mathrm{m}^{-1}$, $\varepsilon_0 = 8{\cdot}854 \times 10^{-12}$ F/m, $\varepsilon = 56$,

$\beta_0 = 1$.

Substituting the values of constants in (A1) the value of $\Delta n = 1{\cdot}49 \times 10^{-5}$.

References

[1] J P Huignard, J P Herriau and T Valentin, *Appl. Opt.* **16**, 2796 (1977)
[2] H Kogelnik, *Bell Syst. Tech. J.* **48**, 2909 (1969)
[3] J P Herriau, J P Huignard and P Aubourg, *Appl. Opt.* **17**, 1851 (1978)
[4] A A Kamshilin, E V Mokrushina and P P Petrov, *Opt. Eng.* **28**, 580 (1989)
[5] F M Kuchel and H J Tiziani, *Opt. Commun.* **38**, 17 (1981)
[6] J P Huignard and A Marracki, *Opt. Lett.* **6**, 622 (1981)
[7] R C Troth and J C Dainty, *Opt. Lett.* **16**, 53 (1991)
[8] N V Kukhtarev, V B Markov, S Godulov, M S Soskin and V L Vinetskii, *Ferroelectrics*, **22**, 949 (1979)
[9] R C Troth, S L Sochava and S I Stepanov, *Appl. Opt.* **30**, 3756–61 (1991)

RAMAN RESEARCH INSTITUTE LIBRARY BANGALORE
21 JUL 1995

PRAMANA
— journal of physics
© Printed in India
Vol. 44, No. 6,
June 1995
pp. 489–493

Quantal behaviour of magnetically kicked electron

A K SIKRI and M L NARCHAL
Department of Physics, Punjabi University, Patiala 147 002, India

MS received 19 October 1994; revised 20 January 1995

Abstract. The problem of a free electron periodically kicked by a magnetic field has been solved. The system shows a transition from quantum recurrence to instability at $\omega T = 2$ where ω is the Larmor frequency and T is the period of the kick. The existence of recurrent behaviour amounts to the confinement of the electron by magnetic kicking. Since the theory holds for all types of charged particles, it has many practical applications.

Keywords. Quantum recurrence; magnetic confinement; Quantum instability wave function.

PACS No. **05·45**

1. Introduction

It is now well-known that the behaviour of a quantum system subject to time periodic potential is dependent on the nature of its quasienergy spectrum. If the quasienergy spectrum is discrete, the system is quantum mechanically recurrent whereas if the spectrum is continuous the quantal behaviour of system is unstable characterized by unbounded growth of energy [1–2]. There exist systems whose quasienergy spectrum makes a transition from discrete to continuous at a certain value of system parameter. Such systems are characterized by a transition from quantum mechanically recurrent to non-recurrent behaviour [3–5]. The non-recurrent behaviour is particularly interesting since it is here one may expect quantum instability. Some criteria have already been discussed according to which one may distinguish between quantum irregularity and quantum chaos. In the former the quasienergy spectrum is absolutely continuous whereas in the latter it is singularly continuous [6–7]. However most of the studies reported has so far been confined to one-dimensional systems [8–9].

It is obvious that more interesting possibilities are expected in systems having more than one degree of freedom. The different modes of such systems can be recurrent or unstable individually or collectively depending on the separability of the problem which in turn would depend on the choice of appropriate coordinate system. If the problem is not separable then one could imagine mixing between unstable and recurrent modes leading to newer types of behaviour. This has sufficient motivation for the study of more than one-dimensional problems. There are a very few such problems which find discussion in literature [10]. In the following sections we consider the two-dimensional problem of a magnetically kicked free electron. It has been shown that the quasienergy spectrum is determined by the product ωT where ω is Larmor frequency and T is the time period of the kick. The solution results in the magnetic confinement of the electron through appropriate kicking.

2. Wave function of electron after N kicks

Consider an electron of charge e and mass m subject to steady magnetic field $\mathbf{H}$. It is described by the Hamiltonian

$$\hat{H} = \frac{p_x^2 + p_y^2}{2m} + \left[\frac{e^2A^2}{2mc^2} - \frac{e}{2mc}(\mathbf{A}\cdot\mathbf{p} + \mathbf{p}\cdot\mathbf{A})\right] \tag{1}$$

where $\mathbf{p}$ is the linear momentum of free electron, $\mathbf{A}$ is the vector potential corresponding to magnetic field $\mathbf{H}$.

The first term represents the free particle Hamiltonian whereas the second term is the contribution of the magnetic field. We consider an electron in which the second term appears in the form of δ function kicks so that

$$\hat{H} = \frac{p_x^2 + p_y^2}{2m} + \left[\frac{e^2A^2}{2mc^2} - \frac{e}{2mc}(\mathbf{A}\cdot\mathbf{p} + \mathbf{p}\cdot\mathbf{A})\right]\sum_n \delta(t - nT) \tag{2}$$

where T is the time period of the kick. Assuming that the magnetic field is in z direction, (2) can be written in Coulomb gauge as

$$\hat{H} = \frac{p_x^2 + p_y^2}{2m} + \left[\frac{1}{2}m\omega^2(x^2 + y^2) - \omega L_z\right]\sum_n \delta(t - nT) \tag{3}$$

where $\omega = eH/2mc$ is the Larmor frequency of electron and L_z is the z component of orbital angular momentum.

The time evolution of the system is governed by one step Floquet operator

$$U = \exp\left[-\frac{i(p_x^2 + p_y^2)T}{2m\hbar}\right]\exp -\frac{iT}{\hbar}\left[\frac{1}{2}m\omega^2(x^2 + y^2) - \omega L_z\right]. \tag{4}$$

Using the technique developed by Blumel *et al* [3], it can be shown that

$$U = \exp -\left(\frac{iG_xT}{\hbar}\right)\exp -\left(\frac{iG_yT}{\hbar}\right)\exp\left(\frac{i\omega L_zT}{\hbar}\right) \tag{5}$$

where

$$G_x = \lambda\left[\frac{p_x^2}{2m} + \frac{1}{2}m\omega^2x^2 + \omega^2T(xp_x + p_xx)\right] \tag{6}$$

$$\lambda = \sin^{-1}(r\omega T)/r\omega T \tag{7}$$

$$r^2 = 1 - \omega^2T^2/4. \tag{8}$$

The wave function $|\psi_N\rangle$ of the system after N kicks is given by

$$|\psi_N\rangle = U^N|\psi_0\rangle \tag{9}$$

where $|\psi_0\rangle$ is the wave function of the electron at time $t = 0$. Since G_x, G_y and L_z are commuting operators, we may write (9) as

$$|\psi_N\rangle = \exp\left(\frac{iN\omega TL_z}{\hbar}\right)\exp\left(-\frac{iNG_xT}{\hbar}\right)\exp\left(-\frac{iNG_yT}{\hbar}\right)|\psi_0\rangle. \tag{10}$$

It can be further written as

$$|\psi_f\rangle = \exp\left(-\frac{iNG_x T}{\hbar}\right)\exp\left(-\frac{iNG_y T}{\hbar}\right)|\psi_0\rangle \tag{11}$$

where

$$|\psi_f\rangle = \exp\left(-\frac{iN\omega T L_z}{\hbar}\right)|\psi_N\rangle \tag{12}$$

In the position representation (11) may be written as

$$\psi_f(x,y) = \int_{-\infty}^{\infty}\int_{-\infty}^{\infty} K(x,y;x',y')\psi_0(x',y')\mathrm{d}x'\mathrm{d}y' \tag{13}$$

where

$$K(x,y;x',y') = \left\langle x,y\left|\exp\left(-\frac{iNG_x T}{\hbar}\right)\exp\left(-\frac{iNG_y T}{\hbar}\right)\right|x',y'\right\rangle \tag{14}$$

is the propagator for the system and contains all information about the system.

The matrix element on the right side of (14) can be easily evaluated using well-known techniques and it turns out to be

$$K(x,y;x',y') = \left(\frac{mr\omega}{2\pi i\hbar\sin\eta}\right)\exp\left[\frac{-imr\omega}{2\hbar\sin\eta}(x^2+y^2+x'^2+y'^2)\cos\eta\right.$$
$$\left. -2(xx'+yy')\right]\exp[ib(x^2+y^2-x'^2-y'^2)] \tag{15}$$

where

$$b = m\omega^2 T/4\hbar, \tag{16}$$

$$\eta = N\sin^{-1}(r\omega T). \tag{17}$$

We represent the free electron by two-dimensional wave packet of width σ at $t=0$ by

$$\psi_0(x',y') = \frac{1}{(2\pi\sigma^2)^{1/2}}\exp\left[-\frac{(x'^2+y'^2)}{4\sigma^2}\right]\exp[i(k_x x'+k_y y')] \tag{18}$$

Using (18) and (15) in (13) and performing the integration in plane polar coordinates (ρ,ϕ) we obtain

$$\psi_f(\rho,\phi) = \left(-\frac{v}{2\pi\sigma^2}\right)^{\frac{1}{2}}\exp\left[-\frac{4\rho^2}{4\sigma^2}\right]\exp\left[-\frac{4\rho\sin\eta}{4br\sigma^2}(k_\rho\cos\phi+k_\phi\sin\phi)\right]$$
$$\times\exp\left[-\frac{k^2 v\sin^2\eta}{16b^2r^2\sigma^2}\right]\exp[-if(\rho,\phi)] \tag{19}$$

where

$$v = r^2\left[\frac{\sin^2\eta}{16b^2\sigma^4}+\left(r\,\mathrm{con}\,\eta+\frac{\omega T}{2}\sin\eta\right)^2\right]^{-1} \tag{20}$$

$$f(\rho,\phi) = bd\rho^2 - \frac{\rho va\sin\eta}{r}(k_\rho\cos\phi+k_\phi\sin\phi)$$
$$+\tan^{-1}(4\sigma^2 ba) - k^2 va\sin^2\eta/4br^2 \tag{21}$$

Table 1. Variation of position vector of electron with kicks.

η	0	$\pi/3$	$2\pi/3$	π
ρ	$1{\cdot}54 \times 10^{-12}$	$10{\cdot}36 \times 10^{-31}$	$10{\cdot}36 \times 10^{-31}$	$1{\cdot}54 \times 10^{-12}$

$$d = a(1 - v) - \omega T \tag{22}$$

$$a = r \cot \eta + \omega T/2. \tag{23}$$

3. Energy and position of electron after N kicks

The energy of electron after N kicks is given by

$$E_N = \langle \psi_f | \hat{H}_0 | \psi_f \rangle \tag{24}$$

where

$$\hat{H}_0 = \frac{p_x^2 + p_y^2}{2m} \tag{25}$$

is free electron Hamiltonian.

Substituting the value of $\hat{H}_0$ in (24) we obtain

$$E_N = \frac{\hbar^2}{2m}\left[\frac{v}{2\sigma^2} + \frac{4b^2 d^2 \sigma^2}{v} + \frac{2k^2 \sin^2 \eta}{r^2}(av + d)^2\right]. \tag{26}$$

For $\omega T < 2$ the energy oscillates showing quantum recurrence whereas for $\omega T > 2$ the energy grows exponentially with a time scale proportional to the kicking strength.

The position of the electron after N kicks is given by

$$\langle \rho \rangle = \langle \psi_f | \rho | \psi_f \rangle. \tag{27}$$

Using (19) it takes the form

$$\langle \rho \rangle = \frac{\sqrt{\pi \sigma}}{(2v)^{1/2}} \exp\left(-\frac{k^2 v \sin^2 \eta}{8b^2 r^2 \sigma^2}\right) {}_1F_1\left(\frac{3}{2}, 1, -\frac{k^2 v \sin^2 \eta}{8b^2 r^2 \sigma^2}\right) \tag{28}$$

where ${}_1F_1$ is the degenerate hypergeometric function.

Table 1 shows the numerical values of ρ corresponding to different values of η for $\omega T = 1$. It is clear that ρ is periodic with period π.

4. Conclusions

The behaviour of the electron kicked magnetically has been investigated using Floquet theory. The propagator of electron after N kicks has been explicitly evaluated and it has been utilized to calculate the wave function after N kicks in plane polar coordinates. This wave function has been further used to find the energy and position vector of the electron.

It has been found that time evolution of electron is determined by the product of Larmor frequency ω and time period T of the kick. The energy of electron oscillates for $\omega T < 2$. This is a manifestation of phenomenon of quantum recurrence. This phenomenon of quantum recurrence is equivalent to magnetic confinement of electron.

The position vector of electron has been evaluated numerically for $\omega T = 1$ and $H = 10^4$ gauss. It has been found to be periodic function of η with period π. It deviates significantly from its original position during the first kick and then returns to its original after third kick. Similiar behaviour occurs for other values of $\omega T < 2$. This implies that electron can be localized magnetically by proper kicking.

References

[1] T Hogg and B A Huberman, *Phys. Rev.* **A28**, 22 (1983)
[2] J Bellissard, in *Trends and developments in the eighties*, edited by S Albeverio and Ph Blanchard (World Scientific, Singapore 1985)
[3] R Blumel, R Mier and U Smilansky, *Phys. Lett.* **A103**, 353 (1984)
[4] J V Jose and R Cordery, *Phys. Rev. Lett.* **56**, 290 (1986)
[5] A K Sikri and M L Narchal, *Pramana – J. Phys.* **41**, 509 (1993)
[6] B Milek and P Seba, *Phys. Rev.* **A42**, 3213 (1990)
[7] J M Luck, H Orland and U Smilansky, *J. Stat. Phys.* **53**, 551 (1988)
[8] G Casati, B V Chirikov, F M Izrailev and J Ford, in *Stochastic behaviour in classical and quantum Hamiltonian systems*, edited by G Casati and J Ford, Lecture Notes in Phys. (Springer, Berlin, 1979) Vol 93
[9] A Cohen, S Fishman, *Int. J. Mod. Phys.* **B2**, 103 (1988)
[10] F Haake, M Kus and R Scharf, *Z. Phys.* **B65**, 3812 (1987)

PRAMANA
— journal of
physics

© Printed in India

Vol. 44, No. 6,
June 1995
pp. 495–500

Higher dimensional spherically symmetric inhomogeneous cosmological model with heat flow

SUBENOY CHAKRABORTY and MD. FIROJ SHAH[†]
Department of Mathematics, Jadavpur University, Calcutta 700 032, India
[†]Uttar Akhratala S. M. Institution, P.O. Chaital, North 24 Parganas, West Bengal, India

MS received 2 August 1994; revised 14 February 1995

Abstract. We study spherically symmetric inhomogeneous cosmological model with heat flow in higher dimensional space-time and present a class of solutions in which the velocity field is shear-free. Some of these solutions are analogous to the known solutions in 4-dimension while some are totally new.

Keywords. Cosmology; heat flux; higher dimension; spherically symmetric solutions.

PACS Nos 04·20; 95·30

1. Introduction

In the usual space-time dimension, Bergmann [1] initiated the study of cosmological solutions with an energy flux. Then several authors (see for example, Maiti [2], Modak [3], Banerjee *et al* [4], Deng [5]) have found other solutions for 4-dimensional space-time. The reason to study cosmological solutions with heat flow is that one can get a general picture of gravitational collapse of stars, considering dissipation in the form of radial heat flow in simple adiabatic fluid. Also thermodynamically, one can relate non-uniformity of temperature to heat flux. So a non-zero heat flux means a temperature gradient as may be expected to occur following the formation of a gravitational condensation. Further, heat conduction ensures entropy production on general thermodynamic grounds.

As far as our knowledge goes, there has been no study so far in higher dimensions considering heat flux. In this paper, we have found some cosmological solutions with heat flux in $(D+2)$-dimensional space-time. The idea behind the consideration of higher dimensional space-time is to consider the effect of heat flux at the very early Universe when the higher dimensional theory is very important. The paper is organized as follows: Section 2 deals with basic equations and the field equations are solved in different situations to obtain different sets of cosmological solutions. In § 3, we consider solutions corresponding to the isotropy of pressure. The paper ends with a short discussion and concluding remarks.

2. Basic field equations and their solutions

The metric for a higher dimensional, spherically symmetric non-static space-time can be taken in isotropic form as

$$dS^2 = e^{\gamma} dt^2 - e^{\omega}(dr^2 + r^2 d\Omega_D^2), \tag{1}$$

where $\mathrm{d}\Omega_D^2$ is the metric on the D-sphere in polar co-ordinates with expression

$$\mathrm{d}\Omega_D^2 = \mathrm{d}x_1^2 + \sin^2 x_1 \mathrm{d}x_2^2 + \sin^2 x_1 \cdot \sin^2 x_2 \mathrm{d}x_3^2 + \cdots$$

and

$$\gamma = \gamma(r, t), \quad \omega = \omega(r, t).$$

So, here space-time is $(D+2)$-dimensional. The energy-momentum tensor for a fluid with heat flux is expressed in the standard form as

$$T_\mu^\gamma = (\rho + p) v_\mu v^\gamma - p \cdot \delta_\mu^\gamma + q^\gamma \cdot v_\mu + q_\mu \cdot v^\gamma, \tag{2}$$

where q^μ stands for heat flow vector, orthogonal to the velocity vector v^μ. In co-moving co-ordinate system $v^\mu = e^{-\gamma/2}\delta_0^\mu$, this ensures that the velocity field is shear-free. In the present spherically symmetric case the only non-vanishing component of heat flow vector is q^1, along the radial direction. The non-trivial components of the Einstein field equation

$$R_\mu^\gamma - \tfrac{1}{2} R\, \delta_\mu^\gamma = -8\pi\, T_\mu^\gamma,$$

for the metric (1) are [6]

$$e^{-\omega}\frac{D(D-1)}{2r^2} + e^{-\gamma}\frac{D(D+1)}{8}\dot{\omega}^2 - e^{-\omega}\left[D\left(\frac{\omega''}{2} + \frac{1}{r^2}\right) + \frac{D(D+1)}{2}\left(\frac{\omega'}{2} + \frac{1}{r}\right)^2 - \frac{D\omega'}{2}\left(\frac{\omega'}{2} + \frac{1}{r}\right)\right] = 8\pi\rho, \tag{3}$$

$$e^{-\gamma}\left[D\frac{\ddot{\omega}}{2} - D\frac{\dot{\omega}\dot{\gamma}}{4} + \frac{D(D+1)}{8}\dot{\omega}^2\right] + e^{-\omega}\frac{D(D-1)}{2r^2} - e^{-\omega}\left[D\frac{\gamma'}{2}\left(\frac{\omega'}{2} + \frac{1}{r}\right) + \frac{D(D-1)}{2}\left(\frac{\omega'}{2} + \frac{1}{r}\right)^2\right] = -8\pi p, \tag{4}$$

$$e^{-\gamma}\left[\frac{D\dot{\omega}}{2} + \frac{D(D+1)}{8}\dot{\omega}^2 - \frac{D\dot{\omega}\dot{\gamma}}{4}\right] + e^{-\omega}\frac{(D-1)(D-2)}{2r^2} - e^{-\omega}\left[\frac{\gamma''}{2} + \frac{\gamma'^2}{4} + (D-1)\left(\frac{\omega''}{2} - \frac{1}{r^2}\right) + \frac{D(D-1)}{2}\left(\frac{\omega'}{2} + \frac{1}{r}\right)^2 + \frac{(n-1)}{2}(\gamma' - \omega') \times \left(\frac{\omega'}{2} + \frac{1}{r}\right) - \frac{\omega'\gamma'}{4}\right] = -8\pi p, \tag{5}$$

and

$$\frac{D}{2}(\dot{\omega}' - \dot{\omega}\gamma'/2)e^{-\omega} = 8\pi q^1 \cdot v_0. \tag{6}$$

Here, differentiation with respect to r and t are denoted by prime and overhead dot respectively. Let us define a pair of variables (u, v) as follows:

$$u = [e^{\omega} \cdot r^2]^\alpha \quad \text{and} \quad v = \ln r, \tag{7}$$

α is an arbitrary constant. Then (3) has the following compact form using the new variables from (7):

$$\frac{\mathrm{d}^2u}{\mathrm{d}v^2}=\frac{(D-1)^2}{4}u-\frac{(D-1)}{2D}u^{(D+3)/(D-1)}\left[8\pi\rho-\frac{D(D+1)}{8}e^{-\gamma}\dot{\omega}^2\right] \tag{8}$$

provided the arbitrary constant α is taken to be $(D-1)/4$. Now, in order to integrate (8) in close form, let us assume an expression for ρ in the form

$$8\pi\rho=\frac{D(D+1)}{8}e^{-\gamma}\dot{\omega}^2+\beta u^l, \tag{9}$$

where $\beta=\beta(t)$ and l are arbitrary. The elimination of ρ from (8) and (9) gives rise to the second order differential equation in u

$$\frac{\mathrm{d}^2u}{\mathrm{d}v^2}=au+bu^m \tag{10}$$

with

$$a=4\alpha^2,\quad m=1+l+1/\alpha,\quad b=-\beta\frac{(D-1)}{2D},\quad \alpha=\frac{D-1}{4}.$$

This can be solved at once to give the explicit form for ω as

$$e^{\omega}=R/[1+Kr^{\alpha}]^{4/\alpha}, \tag{11}$$

where R depends on α, l and K and $K=K(t)$ is arbitrary. To obtain the other metric coefficient we first eliminate p from (4) and (5) and then using (11) for ω the differential equation in γ is

$$\gamma''+\frac{\gamma'^2}{2}+\frac{\gamma'}{r}\frac{(3Kr\alpha-1)}{1+Kr^{\alpha}}+4\frac{K(D-1)(2-\alpha)r^{\alpha-2}}{(1+Kr^{\alpha})^2}=0. \tag{12}$$

In general, this cannot be integrated at once for arbitrary values of $\alpha(D)$ and K. So we shall study solutions for particular values of $\alpha(D)$ and K.

Case I: $\alpha=2$, K is arbitrary i.e. the space-time is 11-dimensional

In this case (12) can be solved easily to obtain

$$e^{\gamma}=\left[1+\frac{\gamma_0}{1+K\gamma^2}\right]^2, \tag{13}$$

γ_0 is an arbitrary function of t alone. This solution is analogous to the 4-dimensional solution of Modak [3]. The expressions for physical quantities namely ρ, p, q^1 and θ for the above solution are

$$8\pi\rho=\frac{180K}{R}+\frac{45}{4}\left[\frac{\dot{R}}{R}-\frac{2\gamma^2\dot{K}}{1+K\gamma^2}\right]^2\left(1+\frac{\gamma_0}{1+K\gamma^2}\right)^{-2},$$

$$8\pi p=\frac{144K}{R}-\frac{2\gamma_0K}{R}\left(\frac{1-K\gamma^2}{1+K\gamma^2}\right)\left(1+\frac{\gamma_0}{1+K\gamma^2}\right)^{-1}$$
$$-\frac{45}{4}\left(\frac{\dot{R}}{R}-\frac{2\gamma^2\dot{K}}{1+K\gamma^2}\right)^2\left(1+\frac{\gamma_0}{1+K\gamma^2}\right)^{-2}$$

$$-\frac{27}{8}\left[\frac{\dot{R}}{R}-\frac{2\gamma^2\dot{K}}{1+K\gamma^2}\right]^{-1}\frac{\partial}{\partial t}\left\{\left[\frac{\dot{R}}{R}-\frac{2\dot{K}\gamma^2}{1+K\gamma^2}\right]^2\left(1+\frac{\gamma_0}{1+K\gamma^2}\right)^{-2}\right\}, \tag{14}$$

$$8\pi q'=-\frac{18\dot{K}\gamma}{R}\left(1+\frac{\gamma_0}{1+K\gamma^2}\right)^{-1}+\frac{9\gamma_0K\gamma}{R}\left(\frac{\dot{R}}{R}-\frac{2\dot{K}\gamma^2}{1+K\gamma^2}\right)\left(1+\frac{\gamma_0}{1+K\gamma^2}\right)^{-1}.$$

Similar to the analysis of Modak [3] for 4-dimensional space-time one can interpret that the parameter K measures the $(D+1)$-space scalar curvature and γ_0 measures the deviation of the integral curves of the velocity vector field to be geodesics.

Another set of solutions can be obtained for $K=0$ i.e. for flat space-time. This is almost identical to those of Modak [3] for 4-dimensional space-time. So we shall not present it here.

Case II: When K is large i.e. $(D+1)$-dimensional spatial hypersurface has large curvature

Here we assume K to be infinitely large in such a manner that the metric coefficient e^{ω} is a finite (non-zero) quantity. Then (12) can be approximated by the equation (assuming $1/K$ to be very small so that second and higher powers are neglected)

$$\gamma''+\frac{\gamma'^2}{2}+\frac{3\gamma'}{r}-\frac{4\gamma'}{Kr^{\alpha+1}}+\frac{4(D-1)(2-\alpha)}{Kr^{\alpha+2}}=0. \tag{15}$$

To solve this equation, let us assume

$$\gamma=\bar{\gamma}+h, \tag{16}$$

where $\bar{\gamma}$ satisfies

$$\bar{\gamma}''+\frac{\bar{\gamma}'^2}{2}+\frac{3\bar{\gamma}'}{r}=0 \tag{17}$$

and the small correction h (assuming square and higher powers of the derivative of h are neglected) follows

$$h''+\frac{3h'}{r}=\frac{4\gamma'}{Kr^{\alpha+1}}-\frac{4(D-1)(2-\alpha)}{Kr^{\alpha+2}}, \tag{18}$$

Now, (17) can be solved easily to obtain

$$\begin{aligned} e^{\bar{\gamma}} &= \left(1-\frac{1}{4cr^2}\right)^2, \quad c\neq 0 \\ &= \frac{1}{r^4}, \quad c=0 \end{aligned} \tag{19}$$

where $c=c(t)$ is the integration constant. Hence from (18) one can write the integral form

$$h'=\frac{4}{Kr^3}\int\frac{r^{-\alpha+1}}{(cr^2-1/4)}\mathrm{d}r-\frac{4(D-1)}{Kr^{\alpha+1}}. \tag{20}$$

So γ can be expressed in close form only for $c = 0$, the expression is

$$\gamma = -4\ln r + \frac{16}{K}\left[1 + \frac{1}{\alpha(2-\alpha)}\right]r^{-\alpha}. \tag{21}$$

Case III: When the spatial curvature is very small (K is small so that K^2 and higher powers are neglected)

In this case, (12) reduces to

$$\gamma'' + \frac{\gamma'^2}{2} + \frac{\gamma'}{r}(4Kr^{\alpha} - 1) + 4K(n-1)(2-\alpha)r^{\alpha-2} = 0. \tag{22}$$

So proceeding to the previous case we get,

$$\gamma = \gamma_0 \ln(r^2 + c_0) + H \tag{23}$$

with

$$H' = 8K\gamma_0 r \int \frac{r^{\alpha-1}}{r^2 + c_0}\mathrm{d}r + 16\alpha K r^{\alpha-1}. \tag{24}$$

The only solution, which is in close form for $c_0 = 0$, is the following

$$\gamma = \gamma_0 \ln r^2 + 8K((\alpha/\alpha - 2)\cdot\gamma_0 + 2)r^{\alpha}. \tag{25}$$

One can add to this solution a second degree polynomial in r with arbitrary coefficients, which are functions of t alone.

3. Alternative solution by Glass and Bergmann

The condition of pressure isotropy in co-moving co-ordinates, following Glass [7] and Bergmann [1], gives rise to a second order partial differential equation

$$F\frac{\partial^2 A}{\partial x^2} + 2\frac{\partial F}{\partial x}\frac{\partial A}{\partial x} - \frac{A}{(D-1)}\frac{\partial^2 F}{\partial x^2} = 0. \tag{26}$$

Here $A = e^{\gamma/2}$, $F = e^{\omega/2}$ and $x = r^2$. This partial differential equation is very similar to that in the 4-dimensional case. So one can get solutions analogous to those of Bergmann [1], Modak [3], Maiti [2], Banerjee *et al* [4] and Deng [5]. So we shall not discuss these types of solutions here. Only we shall present here solutions which are different from those mentioned above.

Let us assume the following polynomial relation between the metric coefficients:

$$F = \mu A^n, \quad \mu \text{ and } n \text{ are arbitrary.} \tag{27}$$

Now substituting in (26) one obtains

$$A\frac{\partial^2 A}{\partial x^2} + \lambda\left(\frac{\partial A}{\partial x}\right)^2 = 0, \tag{28}$$

with

$$\lambda = \frac{n(2D - n - 1)}{(D - n - 1)}.$$

Hence the solution is

$$A = [a_0 r^2 + b_0]^{1/(\lambda+1)},$$
$$F = \mu[a_0 r^2 + b_0]^{n/(\lambda+1)}, \tag{29}$$

where $a_0 = a_0(t)$ and $b_0 = b_0(t)$ are arbitrary. This solution is different from the above mentioned solutions.

4. Discussion

In the present paper, we have presented cosmological solutions with heat flux in higher dimensions. Some of the solutions are analogous to those present in the literature for 4-dimensional case. Also we get a few solutions which are totally new. As the arbitrary parameter K is related to the spatial curvature, the solutions with K large and small correspond to the cases where the gravitational effect is large and small respectively. Also, in the case of the pressure isotropy condition we obtain a different solution from the standard solutions in 4-dimensions.

The higher dimensional study of heat flux does not show any special character compared to the 4-dimensional case. So we may conclude that the dimension of space-time has very little effect on heat flux.

Acknowledgement

The authors are thankful to the members of Relativity and Cosmology Research Centre, Department of Physics, Jadavpur University for helpful discussion.

References

[1] O Bergmann, *Phys. Lett.* **A82**, 383 (1981)
[2] S R Maiti, *Phys. Rev.* **D25**, 2518 (1982)
[3] B Modak, *J. Astrophys. Astron.* **5**, 317 (1984)
[4] A Banerjee, S B Dutta Chaudhury and B K Bhui, *Pramana – J. Phys.* **34**, 397 (1990)
[5] Y Deng, *Gen. Relativ. Gravit.* **21**, 503 (1989)
[6] A Banerjee, S B Dutta Chaudhury and S Chatterjee, *Gen. Relativ. Gravit.* **24**, 991 (1992)
[7] E N Glass, *J. Math. Phys.* **20**, 1508 (1979); *Phys. Lett.* **A86**, 351 (1981)

PRAMANA
— journal of
physics

© Printed in India

Vol. 44, No. 6,
June 1995
pp. 501–509

Supersymmetry in complex space-time

SHUCHI BORA and B S RAJPUT*
Department of Physics, Kumaun University, Nainital, 263 002, India
*Present address: H N B Garhwal University, Srinagar 246 174, India

MS received 19 September 1994

Abstract. An interconnection between superluminal transformation and supersymmetric transformations has been investigated in complex C^3-space and the evolution of bosonic and fermionic subspaces in such space has been undertaken. Introducing the suitable anticommuting operators to induce grading in Poincare group in C^3-space in terms of components of complex angular momentum operator, the supersymmetric algebra connecting bradyonic and tachyonic bosons and fermions has been constructed and it has been demonstrated that the difference between scales of bosonic and fermionic subspaces in C^3-space increases quickly in spite of their closeness initially.

Keywords. Supersymmetry; bradyons; tachyons; complex space.

PACS Nos 03·30; 11·30; 11·60.

1. Introduction

Basic algebraic structure underlying the notion of supersymmetry is a graded Lie algebra which involves both commutation and anticommutation relations and plays a unique role in particle physics providing a fusion between space-time and internal symmetries overcoming no-go theorem [1]. In the history of diversified ways of the study of various space-time symmetries and their fusion with internal symmetries, one of the convenient methods has been to place emphasis on homogeneous Lorentz group (HLG) which leads to the study of the irreducible representations of Poincare group used as Lie algebra in super-symmetric theories. Keeping in view the importance of reconstruction and investigation of the representations of SL (2, C) group, universal covering group of which is HLG, a compact operator formulation has been developed [2] in explicit continuable form to reformulate the Gel'fand–Naimark theory [3]. Though the space-time representations of Poincare group have made their appearance in several investigations of mathematical and physical nature [4, 5], the space-like objects have been shown [6, 9] to suffer with the problem of proper representation and localization in usual four-dimensional space $R^4(\mathbf{r}, t)$ and it has been demonstrated [10] that the relativistic extension to superluminal phenomena and the building of unified theory of bradyons [11] and tachyons [12] are possible only in a pseudo-Euclidean higher dimensional space-time $D^8 = R^4(\mathbf{r}, t) \times T^4(\mathbf{r}, t)$, with equal number of spatial and temporal constituents. Such higher dimensional symmetrical space has been complexified by various authors [13–15] and it has been demonstrated that the transformation in the complex space C^3, consisting of real, spatial and temporal three vectors are related to the group SU(3) of unitary intrinsic symmetries of elementary particles and law of trichromatism.

Justification for the need of complex space-time was put forward by various authors in special relativity [16], general relativity [17] and Twistor theory [17, 18]. In our recent work [19] we have analysed subluminal and superluminal Lorentz transformations in such a complex C^3-space, constructed [20] the complex angular momentum operators for bradyons and tachyons and derived [21] the realizations of HLG for non-zero real mass, zero mass and imaginary mass (i.e. bradyons, photons and tachyons) systems. An attractive interconnection of such an extended manifold with superluminal theories makes the perspective to invoke a variety of ideas of many dimensional schemes as the basis for unified theory of all physical interactions in space-time of non-trivial topology. Separation of extra time-like dimensions from space-like ones leads to the connection of superluminal transformations and supersymmetric transformations [22, 23], where, the former tranforms bradyonic objects into tachyonic ones and vice versa, and the latter transforms boson states into fermionic states.

In the present paper, the interconnection between superluminal transformations and supersymmetric transformations has been investigated in complex C^3-space and the study of evolution of bosonic and fermionic subspaces has been undertaken. Introducing the suitable anticommuting operators to induce grading in Poincare group in C^3-space in terms of components of complex angular momentum operator, the supersymmetric algebra connecting bradyonic and tachyonic bosons and fermions has been constructed in terms of spinorial charges giving rise to close system of commutation and anticommutation relations. Introducing eight dimensional theory with supersymmetric coordinates in C^3-space, the study of evolution of bosonic and fermionic subspaces and their interaction has been undertaken and it has been demonstrated that the difference between scales of bosonic and fermionic subspaces in C^3-space increases quickly in spite of their closeness initially.

2. Generators of Lorentz group in complex space

In complex three-space C^3, consisting of symmetrical, spatial and temporal components, an event A is specified by three complex coordinates,

$$\{A\} = (z^1, z^2, z^3) \tag{2.1}$$

where

$$z^j = x^j + it^j, \quad (j = 1, 2, 3) \tag{2.2}$$

Using natural units $c = \hbar = 1$, and the convention that $x^j = -x_j$, $t^j = t_j$, the interval between two events in this space may be written as,

$$ds^2 = \mathrm{Re}(dz^j \cdot dz_j^*) \tag{2.3}$$

where Re denotes the real part and * denotes the complex-conjugate. The generalized linear momentum corresponding to translation in C^3-space may be defined as

$$\mathbf{P} = \mathbf{p} + i\mathbf{E} \tag{2.4}$$

where the usual vector momentum $\mathbf{p}$, denotes translations along spatial coordinates and the vector energy $\mathbf{E}$, denoting the translations along the temporal coordinates, is directed tangentially to the time trajectory. Generalized angular momentum operator, corresponding to relations in C^3-space, may be constructed in the following manner:

$$\hat{\mathcal{Z}} = \hat{J} + i\hat{K} \tag{2.5}$$

where $\hat{J}$ generates pure rotations (spatial as well as temporal) and $\hat{K}$ generates space-time rotations (boosts). The Hamiltonian of a free particle in C^3-space may be constructed as

$$\hat{H} = \frac{\hat{P}^2}{2|M_c|} \tag{2.6}$$

where the proper mass M_c of the particle in C^3-space is also a complex quantity

$$M_c = m + i\mu. \tag{2.7}$$

Assuming the orthogonality between vectors **p** and **E** in (2.4), we may write the modulus of this Hamiltonian as

$$|H| = (p^2 - E^2)/2|M_c| \tag{2.8}$$

which reduces to following forms, respectively, in the four-spaces $R^4(\mathbf{r}, t)$ with $t = (t_1^2 + t_2^2 + t_3^2)^{1/2}$ and, $T^4(\mathbf{t}, r)$ with $r = (x_1^2 + x_2^2 + x_3^2)$;

$$H_{\mathrm{B}} = p^2/2m$$

and

$$H_{\mathrm{T}} = -E^2/2\mu \tag{2.9}$$

where B and T denotes bradyons and tachyons with the natural spaces for their physical specifications as R^4 and T^4 respectively.

Operators $\hat{P}$, $\hat{\mathcal{Z}}$ and $\hat{H}$ given by (2.4), (2.5) and (2.6) constitute generalized Poincare group in C^3-space and satisfies the following commutation rule,

$$\begin{aligned} &[\hat{H}, P] = 0; \quad [\hat{H}, \hat{Z}_j] = 0, \quad [H, \mathcal{Z}^2] = 0 \\ &[\hat{\mathcal{Z}}_j, \hat{\mathcal{Z}}_k] = i\varepsilon_{jkl} Z_l. \end{aligned} \tag{2·10}$$

3. Global supersymmetry in C^3-space

Basic algebraic structure underlying the notation of supersymmetry is graded Lie algebra which is a graded extension of Poincare group. This grading makes a distinction between even and odd elements where, even elements, belonging to Lie algebra, obey commutation relations and the odd elements which are responsible for the grading, obey anticommutation relations among themselves and commutation relations with the even elements. The representation of Lie algebra in terms of odd elements is known as grading representation. For the Poincare group specified by (2.10) in C^3-space, let us introduce grading by the anticommuting operators

$$Q'_\alpha = Q_\alpha + i q_\alpha \tag{3.1}$$

such that

$$\begin{aligned} \{Q_\alpha, Q_\beta\} &= -2(\gamma^j k^{-1})_{\alpha\beta} P_j \\ \{q_\alpha, q_\beta\} &= -2i(\gamma^j k^{-1})_{\alpha\beta} E_j \\ \{q_\alpha, Q_\beta\} &= 0 \end{aligned} \tag{3.2}$$

where k is the charge conjugation matrix. Substituting the usual relation

$$\bar{Q} = \tilde{Q}\gamma^0$$

equations (3.2) may be written as

$$\begin{aligned} &\{Q_\alpha, Q_\beta\} = -2\gamma^j_{\alpha\beta} p_j; \\ &\{q_\alpha, \bar{q}_\beta\} = 2i\gamma^j_{\alpha\beta} E_j \\ &\{q_\alpha, \bar{Q}_\beta\} = 0; \quad \{\bar{q}_\alpha, Q_\beta\} = 0. \end{aligned} \tag{3.3}$$

Then we may construct the following graded algebra ($N = 1$ supersymmetry) as the graded extension of generalized Poincare group defined by (2.10);

$$\begin{aligned} &[Q'_\alpha, \not{Z}^l] = i\sigma^{jk}_{\alpha\beta} Q'_\beta \\ &[Q'_\alpha, \bar{Q}'_\beta] = -2\gamma^j_{\alpha\beta} P_j \\ &[P_j, Q'_\alpha] = 0 \end{aligned} \tag{3.4}$$

where $\sigma^{jk} = 1/4\,[\gamma^j, \gamma^k]$, and $j,k,l = 1,2,3$ with $j,k \neq l$. These equations lead to

$$\begin{aligned} &[p_j, Q_\alpha] = 0; \quad [P_j, q_\alpha] = 0 \\ &[E_j, q_\alpha] = 0; \quad [E_j, Q_\alpha] = 0 \\ &[q_\alpha, \not{Z}^l] = i\,\sigma^{jk}_{\alpha\beta} q_\beta - i\sigma^{01}_{\alpha\beta} Q_\beta \\ &[Q_\alpha, \not{Z}^l] = i\,\sigma^{jk}_{\alpha} Q_\beta - \sigma^{01}_{\alpha\beta} Q_\beta \end{aligned} \tag{3.5}$$

which may be further reduced to the graded algebras in R^4 and T^4 spaces separately. The graded algebra (3.4) may therefore be treated as supersymmetry which connects bradyonic and tachyonic, bosonic and fermionic fields. This supersymmetry of bosons and fermions, with bradyons and tachyons on equal footing, is generated by charges transforming like spinors under generalized Poincare group defined by (2.10). These spinorial charges give rise to a closed system of commutation and anticommutation relations (3.5) and (3.3) which may be called as pseudo-Lie algebra. Any linear representation of supersymmetric generators of (3.4) contains both fermions (bradyonic as well as tachyonic) and bosons (bradyonic as well as tachyonic) which have equal masses (magnitudes) if the symmetry is unbroken.

4. Evolution of supersymmetric subspaces in C^3-space

Many different dimensional schemes are thought to be the basis for building the unified theory of all physical interactions (including the tachyonic ones). In these extended manifolds the signs of metrical coefficients are interchanged on passing horizon [24] and there are many dimensional regions of such representation in which time-like and space-like coordinates are taken into account in unified symmetrical way. The introduction of additional (extra) dimensions with the unified consideration of bradyonic and tachyonic subspaces, R^4 and T^4 respectively in C^3-space, allows to overcome some problems of trivial construction with time-like coordinates in extra space-time manifolds. Let us consider the eight dimensional theory with supersymmetric coordinates in C^3-space to study the evolution of bosonic and fermionic subspaces and their interactions on the basis of general relativity (with supersymmetry between four-dimensional subspaces R^4 and T^4). The bosonic and fermionic dimensions form the global eight dimensional space-time manifold,

$$(M,N)=(t,z^1,z^2,z^3,\bar{t},\bar{z}^1,\bar{z}^2,\bar{z}^3) \tag{4.1}$$

where

$$t=(t_x^2+t_y^2+t_z^2)^{1/2},$$

and

$$z^j=x^j+it^j, \quad (j=1,2,3)$$

and the fermionic coordinates $(\bar{t},\bar{z}_i)$ are transformed from the bosonic one (t,z_i) by means of the following transformation

$$\bar{z}^j\bar{z}^j=z^\alpha h_{\alpha\beta}z^\beta \tag{4.2}$$

with

$$h=\begin{bmatrix}\sigma_2 & & \\ & \ddots & \\ & & \sigma_2\end{bmatrix} \tag{4.3}$$

σ_2 being the Pauli matrix. Matter dynamics may be investigated in this model by using the uniform and isotropic spherical symmetrical metric for subspaces which are reduced to the Friedmann–Robertson Walker metric in the four-dimensional case. It admits either matter or field in the right part of Einstein–Maxwell equations. Thus we have,

$$G_{MN}=\begin{bmatrix}-1 & & & \\ & g_{ij}R^2 & & \\ & & +1 & \\ & & & g_{mn}\bar{R}^2\end{bmatrix} \tag{4.4}$$

where R and $\bar{R}$ are maximally symmetric subspaces.

The line element may be written as follows,

$$\begin{aligned}\mathrm{d}s^2 = &-\mathrm{d}t^2+\mathrm{d}\bar{t}^2+b^2\,\mathrm{d}z^\alpha\mathrm{d}z^{*\alpha}(1+|z|^2/4)^{-2}\\ &-f^2\,\mathrm{d}\bar{z}^\alpha\mathrm{d}\bar{z}^{*\alpha}(1+|\bar{z}|^2/4)^{-2}\end{aligned} \tag{4.5}$$

while b and f denote the bosonic and fermionic scale factors. This line element may be written as follows in the supersymmetric representation

$$\mathrm{d}s^2=E^M G_{MN}E^{*N}$$

where Vielbein E^M is given by

$$E^1=\mathrm{d}t, \quad E^5=-\mathrm{d}t$$

$$(E^\alpha,E^\alpha)=\frac{(d_z^\alpha b,\mathrm{d}\bar{z}^{\alpha f})}{[1+|z|^2/4]^2} \tag{4.6}$$

The non-zero components of G_{MN} are

$$G_{00} = 1, \quad G_{\alpha\alpha} = 1, \quad G_{55} = +1, \quad G_{\alpha\beta} = h_{\alpha\beta}$$

and we get the curvature invariant as

$$\begin{aligned} R/3 = {} & 2(\ddot{b}/b - \ddot{f}/f) - 2\dot{b}^2/b^2 + 6\dot{b}\dot{f}/bf - 4\dot{f}^2/f^2 \\ & - 1/4[|z|^2 + |\bar{z}|^2 + 1][b^{-2} + f^{-2}] \end{aligned} \tag{4.7}$$

Then action is giving by

$$S = \int \mathrm{d}^8 y g^{1/2} R = \int \mathrm{d}t\, L \tag{4.8}$$

where L is Lagrangian and $d^8 y$ is the element

$$\mathrm{d}t\, \mathrm{d}\bar{t}\, \mathrm{d}z_1\, \mathrm{d}z_2\, \mathrm{d}z_3\, \mathrm{d}\bar{z}_1\, \mathrm{d}\bar{z}_2\, \mathrm{d}\bar{z}_3.$$

Let us introduce the following parameters in terms of bosonic and fermionic scale factors,

$$Q = 1/2 \log(bf)$$

and

$$q = \log(b/f) \tag{4.8a}$$

then the action given by (4.8) yields the following equations of motion

$$\begin{aligned} & 3q + 27/4\dot{q}^2 + 3/2\dot{q}\dot{Q} + 3/2\exp(-2Q)\sinh q = 0 \\ & \ddot{q} + 3\dot{q}^2 + 2\exp(-2Q)\sinh q = 0 \\ & \ddot{q} - 1/3\ddot{Q} + 3/2\dot{q}^2 + 1/3\exp(-2Q)[3\sinh q + \cosh q] = 0 \end{aligned} \tag{4.9}$$

These non-linear differential equations determine the evolution laws for bosonic and fermionic subspaces. An exact complete solution of these equations is very difficult by analytical methods. Let us consider the following approximate solutions without any loss of generality:

(a) Power law approximation

In a general case, (4.9) can also be written as,

$$\ddot{q} - 6\dot{q}^2 - 2\dot{q}\dot{Q} - 4q = 0 \tag{4.10}$$

and

$$\ddot{Q} + 9\dot{q}^2 + (6\sinh q - 2\cosh q)\exp(-2Q) = 0. \tag{4.11}$$

Let us assume the following power law dependence on time

$$\begin{aligned} & q = Bt^{n_1} - Ft^{n_2} \\ & Q = 1/2[Bt^{n_1} + Ft^{n_2}] \end{aligned} \tag{4.12}$$

where B and F are positive constants and n_1 and n_2 are integer constants. Then (4.10) becomes

$$Bn_1(n_1-1)t^{n_1-2}-7B^2n_1^2t^{2(n_1-1)}-4Bt^{n_1}-Fn_2(n_2-1)t^{n_2-2}$$
$$-5F^2n_2^2t^{2(n_2-1)}+4Ft^{n_2}+12n_1n_2BFt^{n_1+n_2-2}=0 \tag{4.13}$$

and (4.11) becomes

$$Bn_1(n_1-1)t^{n_1-2}+9n_1^2B^2t^{2(n_1-1)}+n_2(n_2-1)Ft^{n_2-2}$$
$$+9n_2^2F^2t^{2(n_2-1)}-18n_1n_2BFt^{n_1+n_2-2}-2e^{-2Ft^{n_1}}-4e^{-2Bt^{n_2}}=0. \tag{4.14}$$

For $n_1=n_2=1$, (4.13) gives

$$B=F$$

or

$$5F-7B=4t. \tag{4.15}$$

Substituting relations (4.8a) and (4.12) into (4.15), we get

$$b=f$$

or

$$f/b=b^{2/5}e^{4/5}t^2 \tag{4.16}$$

Conditions (4.15) and (4.16) show that either the bosonic and fermionic scales remain the same in time or the difference in scales of fermionic and bosonic subspaces increases with time (i.e. the ratio of f and b increases in time). This connection between these subspaces enables us to determine the properties of one subspace (fermionic) through another (bosonic) subspace. For this case (i.e. $n_1=n_2=1$), (4.14) reduces to

$$9B^2+9F^2-18BF=2[e^{-2Ft}+2e^{-2Bt})$$

which gives

$$b/f=\exp[(\sqrt{2}t)/(3bf)(b^2+2f^2)^{1/2}] \tag{4.17}$$

which also gives the above mentioned connection between fermionic and bosonic subspaces in time. For the choice $n_1=n_2=2$, (4.13) reduces to

$$(B-F)/2=[B-F+7B^2+5F^2+12BF]t^2 \tag{4.18}$$

which also gives a simple connection between B and F. It may also be written as,

$$(F-B)/(F+B)=2(7B+5F)[2-1/t^2]^{-1} \tag{4.19}$$

showing an increase in difference of bosonic and fermionic scales, when time increases beyond $t=1/\sqrt{2}$. At sufficiently large time ($t\to\infty$), this difference maintains a constant value. Initially, for $t=0$, $F=B$, i.e. bosonic and fermionic scales are identical.

For this choice, we have

$$B=1/t^2\log b$$

and

$$F=1/t^2\log f$$

and hence (4.18) may also be written as

$$\frac{\log b/f}{\log(bf)} = \frac{2}{1-2t^2}\log(b^7 f^5) \tag{4.20}$$

showing the same increase in the difference of scales of bosonic and fermionic subspaces with the increase in time in the interval $0 < t < 1/\sqrt{2}$.

(b) Approximation for small difference in b and f.

Let the difference of bosonic and fermionic scales be very small i.e.

$$q \gg \dot{q}.$$

Then (4.10) reduces to

$$\ddot{q} - 6\dot{q}^2 - 2\dot{q}\dot{Q} = 0 \tag{4.21}$$

Let us assume its solution in term of zeroth approximation for Q, i.e.

$$Q = \log c + D\log t \tag{4.22}$$

which yields

$$bf = c_1 t^{\gamma_1} \tag{4.23}$$

where $c_1 = c^2$ and $\gamma = 2D$, both are positive constants. Then (4.21) becomes

$$\ddot{q} - 6\dot{q}^2 - 2\dot{q}D/t = 0 \tag{4.24}$$

Let its solution be

$$q = \log c_2 + \log t^{\gamma} \tag{4.25}$$

which yields

$$b/f = c^2 t^{\gamma}.$$

Substituting this solution into (4.24) we get

$$\gamma = 0 \quad \text{or} \quad \gamma = -[(2D+1)/6] = -\gamma_2$$

where $\gamma_2 = (\gamma_1 + 1)/6$ is non-zero positive. For $\gamma = 0$ we may set $b = f$ which gives the initial stage. At a later time we have

$$b/f = c_2 t^{-\gamma_2}, \tag{4.26}$$

Combining solutions (4.23) and (4.26) we have

$$b = \sqrt{c_1 c_2}\, t^{(\gamma_1 - \gamma_2)/2}$$

and

$$f = \sqrt{\frac{c_1}{c_2}}\, t^{(\gamma_1 + \gamma_2)/2} \tag{4.27}$$

showing that the difference between bosonic and fermionic scales increases quickly in spite of their closeness initially. It shows the similarity of bosonic and fermionic evolution in time. Thus (4.27) shows that supersymmetry is broken rather weakly.

The unobservability of more than four-dimensions of space-time may be associated with the event horizon effect ($R^4 \leftrightarrow T^4$) taking into account the interconnection between boson–fermion symmetry and bradyon–tachyon transformations. Supersymmetric connections in higher dimensions ought to be perspective in order to invoke the deeply developed theory of supersymmetry in realistic physics. It may also be used for the explanation of absence of many supersymmetric partners for ordinary particles since various ions and *s*-quarks may possibly exist in additional dimensions and can manifest themselves only in the regions where different dimensions are mixed.

References

[1] S Coleman and J Mandula, *Phys. Rev.* **159**, 1251 (1967)
[2] B S Rajput and K N Joshi, *J. Math. Phys.* **21**, 1579 (1980)
[3] I M Gel'fand and M A Naimark, *Izu Akad. Nauk USSR*, **11**, 411 (1947)
[4] E C G Sudarshan, *Arkin Fysik*, **39**, 585 (1969)
[5] T T Wu and C N Yang, *Phys. Rev.* **D14**, 437 (1976)
[6] B S Rajput and O P S Negi, *J. Math. Phys.* **23**, 1964 (1982)
[7] L Marchildon, A F Antippa and A S Evertt, *Phys. Rev.* **D27**, 1740 (1983)
[8] E Recami, *Rev. Nuovo Cimento.* **9**, 1 (1986) and references therein
[9] E A B Cole, *Nuovo Cimento.* **A40**, 171 (1977); **B44**, 157 (1978); **B85**, 105 (1985)
[10] B S Rajput and H C Chandola, *J. Math. Phys.* **26**, 208 (1985); *Nuovo Cimento.* **B72**, 21 (1982); *Prog. Theor. Phys.* **80**, 277 (1988)
[11] Bradyons: Particles which always move with a velocity lesser than that of light
[12] Tachyons: Hypothetical particles which always move with velocity greater than that of light
[13] B S Rajput and H C Chandola, *Can. J. Phys.* **67**, 485 (1989); *Indian J. Pure Appl. Phys.* **22**, 301 (1984)
[14] C Raman and E P Rauscher, *Found. Phys.* **10**, 661 (1980)
[15] Y Yaccarini, *Lett. Nuovo Cimento.* **9**, 354 (1974)
[16] G Ramchandran, S G Tagore and A S Kalaskar, *Lett. Nuovo Cimento.* **4**, 140 (1972)
[17] E T Newman, *J. Math. Phys.* **14**, 774 (1973); *Gen. Relativ. Gravit.* **63**, 361 (1975)
[18] R Penrose and M A H MacCallum, *Phys. Rep.* **c6**, 245 (1973)
[19] B S Rajput, S Bora and H C Chandola, *Indian J. Pure Appl. Phys.* **28**, 221 (1990)
[20] B S Rajput, S Bora and H C Chandola, *Indian J. Pure Appl. Phys.* **29**, 1 (1991)
[21] B S Rajput, S Bora and H C Chandola, *Can. J. Phys.* **68**, 59 (1990)
[22] S Hamomoto, *Prog. Theor. Phys.* **48**, 1073 (1972); **51**, 1977 (1974)
[23] V S Gurin, *Nuovo Cimento.* **A88**, 253 (1985)
[24] B S Rajput, H C Chandola, R Sagar and R C Verma, *Indian J. Pure Appl. Phys.* **24**, 51 (1986)

PRAMANA
— journal of
physics

© Printed in India

Vol. 44, No. 6,
June 1995
pp. 511–518

Cosmic strings in Bianchi III spacetime: Integrable cases

S D MAHARAJ[1,2], P G L LEACH[1,2,3] and K S GOVINDER[1,2,3]
[1]Department of Mathematics and Applied Mathematics, University of Natal, Private Bag X10, Dalbridge 4014, South Africa
[2]Visiting: Inter-University Centre for Astronomy and Astrophysics, Post Bag 4, Ganeshkhind, Pune 411 007, India
[3]Current address: Department of Mathematics, University of the Aegean, Karlovassi 83 200, Greece

MS received 28 February 1995

Abstract. We investigate the integrability of cosmic strings in Bianchi III spacetime using a symmetry analysis. The behaviour of the model is reduced to the solution of a single second order nonlinear differential equation. We show that this equation has a rich structure and admits an infinite family of solutions. Our class of solutions extends special cases previously obtained by Tikekar and Patel [*Gen. Relativ. Gravit.* **24**, 397 (1992)].

Keywords. Cosmology; strings; integrable.

PACS Nos 04·20; 98·90

1. Introduction

The study of cosmic strings is of considerable importance because it may generate density perturbations thereby leading to the formation of galaxies. (For details the reader is referred to the paper by Zel'dovich [1].) It has been noted that the presence of strings in the early universe does not contradict present day observations of the universe [2]. There is no direct evidence of strings in the present day universe; our models must therefore evolve from an era dominated by strings to an era dominated by particles which may possess remnants of strings. Cosmic strings have stress energy and couple in a simple way to the gravitational field. Most analyses are concerned with the gravitational effects which arise from the presence of strings.

Vilenkin [3], Gott [4] and Garfinkle [5] made pioneering analyses of the features of strings. The general relativistic formalism of cosmic strings is due to Letelier [6] and Stachel [7]. Subsequently, a number of general relativistic exact solutions were obtained in models of different Bianchi types. Krori *et al* [8] considered models with Bianchi types II, VI_0, VIII and IX. Bianchi type I string cosmological models were studied by Banerjee *et al* [9]. More recently a number of exact solutions, in the presence of a magnetic field and also with vanishing electromagnetic tensor, in Bianchi III spacetimes were obtained by Tikekar and Patel [10].

In this paper we consider other classes of string solutions in Bianchi III spacetime, thereby extending the Tikekar and Patel [10] solution. Essentially the solution of the field equations reduces to solving a single second order nonlinear ordinary differential equation. We show that this equation has a rich structure and admits an infinite number of solutions, some of which may lead to physically viable models. In § 2 we briefly outline the general field equations governing the behaviour of strings. The second order equation that has to be integrated is generated in § 3. The Lie symmetries of this equation are obtained and we demonstrate that it is transformable to the Emden–Fowler equation. In § 4 the field variables are presented in a general form. A comprehensive analysis is performed in § 5 of the fundamental integral constraint that underpins this analysis. Some concluding remarks are made in § 6. Throughout we follow the notations and conventions of Tikekar and Patel [10].

2. The field equations

We consider the general Bianchi III type spacetime with the line element

$$\mathrm{d}s^2 = \mathrm{d}t^2 - A^2(t)\mathrm{d}x^2 - B^2(t)\mathrm{e}^{-2ax}\mathrm{d}y^2 - C^2(t)\mathrm{d}z^2, \tag{2.1}$$

where a is a constant. The energy-momentum tensor is given by

$$T_{ik} = \rho u_i u_k - \lambda w_i w_k + \frac{1}{4\pi}\left[-g^{lm}F_{il}F_{km} + \frac{1}{4}g_{ik}F_{lm}F^{lm}\right] \tag{2.2}$$

for a cloud of string dust with a magnetic field along the z-direction. In (2.2) ρ, the proper energy density for a cloud of strings, and λ, the string tension density, are related by

$$\rho = \rho_{\mathrm{p}} + \lambda, \tag{2.3}$$

where ρ_{p} is the particle density of the configuration. The quantity u^i is the four-velocity of the particles and w^i represents the direction of the string; these satisfy

$$u^i u_i = -w^i w_i = 1, \quad u^i w_i = 0.$$

We consider a comoving coordinate system so that

$$u^i = (0,0,0,1), \quad w^i = (0,0,1/C,0).$$

Tikekar and Patel [10] were concerned with Bianchi III symmetry and so made the assumption $A = B$.

As the magnetic field is along the z-direction, Maxwell's equations imply that

$$F_{12} = K\mathrm{e}^{-ax}, \tag{2.4}$$

where K is a constant, is the only nonzero component of the electromagnetic field tensor F_{ik}. We are now in a position to generate the Einstein field equations

$$R_{ik} - \tfrac{1}{2}Rg_{ik} = -8\pi T_{ik} \tag{2.5}$$

explicitly with the assistance of (2.2) and (2.4) for the line element (2.1). The field equations (2.5) reduce to the system

$$8\pi\rho = 2\frac{\dot{A}\dot{C}}{AC} + \frac{\dot{A}^2}{A^2} - \frac{a^2}{A^2} - \frac{K^2}{A^4} \tag{2.6}$$

$$8\pi\lambda = 2\frac{\ddot{A}}{A} + \frac{\dot{A}^2}{A^2} - \frac{a^2}{A^2} - \frac{K^2}{A^4} \tag{2.7}$$

$$0 = \frac{\ddot{A}}{A} + \frac{\ddot{C}}{C} + \frac{\dot{A}\dot{C}}{AC} + \frac{K^2}{A^4}. \tag{2.8}$$

The particle density is given by

$$8\pi\rho_p = -2\frac{\ddot{A}}{A} + 2\frac{\dot{A}\dot{C}}{AC}. \tag{2.9}$$

Note that (2.3) and (2.9) are consistent. We generate an infinite family of solutions to (2.6–2.8) in subsequent sections.

3. The model equation

The three nonvanishing field equations (2.6–2.8) contain the four dependent field variables ρ, λ, A and C. To enable explicit solutions determination a constraint must be imposed. Tikekar and Patel [10] take

$$C = A^n, \tag{3.1}$$

where n is a real constant, so that (2.8) becomes

$$(n+1)\frac{\ddot{A}}{A} + n^2\frac{\dot{A}^2}{A} + \frac{K^2}{A^4} = 0 \tag{3.2}$$

for which they were able to provide some solutions. It is a trivial matter to show that (3.1) is the most general constraint on the relationship between A and C for (2.8) to reduce to (3.2). Tikekar and Patel obtained exact solutions for the cases $n = 0$, $n = (3 \pm \sqrt{21})/2$, $n = (3 \pm \sqrt{33})/4$ and $n = 1 \pm \sqrt{3}$.

By inspection (3.2) is seen to have the two Lie point symmetries

$$G_1 = \frac{\partial}{\partial t} \tag{3.3}$$

$$G_2 = 2t\frac{\partial}{\partial t} + A\frac{\partial}{\partial A} \tag{3.4}$$

and it can be quickly verified (for example by the use of Program LIE [11]) that these are the only two Lie point symmetries except for the particular values $n = 0$, $(3 \pm \sqrt{21})/2$ and -1 for which the numbers of point symmetries are three, eight and infinity respectively. The existence of the additional symmetries is not necessary for the reduction of (3.2) to quadratures via the normal subgroup, G_1. (Since $[G_1, G_2] = G_1$, where $[G_1, G_2] = G_1G_2 - G_2G_1$ is the standard Lie Bracket, G_1 is the normal subgroup and this is the symmetry which should be used to reduce the order of (3.2) [12, p 148]. Reduction via G_2 leads to an Abel's equation of the second kind from which little joy can be expected.)

A more satisfactory solution is obtained if (3.2) is transformed to the autonomous Emden–Fowler equation (13, 15] of index ν, viz.

$$Y'' = \tfrac{1}{2}\varepsilon(\nu + 1)Y^\nu, \tag{3.5}$$

where $\varepsilon = \pm 1$ and the constant $(\nu + 1)/2$ is introduced with the advantage of hindsight. The algebra of G_1 and G_2 is A_2 in the Mubarakzyanov classification scheme [16]. Since it is solvable and $G_1 \not\subset G_2$, the algebra is that of Lie's Type IV [17, p 424]. However, we do not use the standard representation of a second order differential equation invariant under a type IV algebra since the form (3.5) is more suitable for the present discussion. The necessary tranformation is

$$t = \alpha X, \quad A = Y^{(n+1)/(n^2+n+1)}, \tag{3.6}$$

where

$$\alpha^2 = -\frac{\varepsilon(n+1)^2(n^2-n-1)}{2K^2(n^2+n+1)^2}, \quad \nu = \frac{n^2-3n-3}{n^2+n+1}. \tag{3.7}$$

The case $\nu = -1$ is special and (3.7a) must be replaced by

$$\alpha^2 = -\frac{\varepsilon(n+1)^2}{K^2(n^2+n+1)}. \tag{3.8}$$

The equation is

$$Y'' = \varepsilon Y^{-1}. \tag{3.9}$$

In (3.5), $\varepsilon = -1$ for $n^2 - n - 1 \geqslant 0$ and $\varepsilon = +1$ for $n^2 - n - 1 \leqslant 0$. The latter applies to the interval $n \in ((1-\sqrt{5})/2, (1+\sqrt{5})/2)$. The asymptotic value of ν is 1. It takes a minimum value of -3 at $n = 0$. This corresponds to a special case of the Ermakov–Pinney equation [18, 19]. The maximum value of $7/3$ is attained when $n = -2$. The parameter ν can take on all values in $[-3, 7/3]$. We shell see that in this interval there are many values of ν, hence n, for which the reduction of (3.2) to quadrature can be taken the further step of evaluation of the quadrature. The particular values of n given by Tikekar and Patel [10] for which explicit integration is possible correspond to $\nu = -3, 0, -3/5$ and $-1/3$. The case $n = -1$ is trivial.

The reduction of (3.5) to quadrature is elementary. The first integral is

$$I = \begin{cases} \frac{1}{2}Y'^2 - \frac{1}{2}\varepsilon Y^{\nu+1} \\ \frac{1}{2}Y'^2 - \log Y, \quad \nu = -1. \end{cases} \tag{3.10}$$

The solution is found by inversion of the result obtained after performance of the integration

$$X - X_0 = \begin{cases} \int [2I + \varepsilon Y^{\nu+1}]^{-1/2} \mathrm{d}Y \\ \int [2I - 2\log Y]^{-1/2} \mathrm{d}Y, \quad \nu = -1. \end{cases} \tag{3.11}$$

4. General results

Whatever the outcome of the quadratures in (3.11) we can write down some general results. (We omit the special case $\nu = -1$ to avoid what is virtually repetition.) Thus the metric (2.1) is

$$\begin{aligned} \mathrm{d}s^2 = \mathrm{d}t^2 &- \left[Y\left(\frac{t}{\alpha}\right)\right]^{2(n+1)/(n^2+n+1)} \mathrm{d}x^2 \\ &- \mathrm{e}^{-2\alpha x}\left[Y\left(\frac{t}{\alpha}\right)\right]^{2(n+1)/(n^2+n+1)} \mathrm{d}y^2 \\ &- \left[Y\left(\frac{t}{\alpha}\right)\right]^{2n(n+1)/(n^2+n+1)} \mathrm{d}z^2, \end{aligned} \tag{4.1}$$

the energy density (2.6) is

$$8\pi\rho = -\frac{K^2[2(2n+1)+(n^2-n-1)]}{(n^2-n-1)\,Y^{4(n+1)/(n^2+n+1)}} - \frac{4K^2 I(2n+1)}{\varepsilon(n^2-n-1)\,Y^2} - \frac{a^2}{Y^{2(n+1)/(n^2+n+1)}}, \tag{4.2}$$

the string tension (2.7) is

$$8\pi\lambda = \frac{4IK^2(2n^2-n-1)}{\varepsilon(n+1)(n^2-n-1)\,Y^2} - \frac{K^2(n^2-n-3)}{(n^2-n-1)\,Y^{4(n+1)/(n^2+n+1)}} - \frac{a^2}{Y^{2(n+1)/(n^2+n+1)}} \tag{4.3}$$

and the particle density (2.9) is

$$8\pi\rho_p = -\frac{8IK^2 n(2n+1)}{\varepsilon(n+1)(n^2-n-1)\,Y^2} - \frac{4K^2(n+1)}{(n^2-n-1)\,Y^{4(n+1)/(n^2+n+1)}}. \tag{4.4}$$

The expansion scalar is

$$\begin{aligned}\theta &= 2\frac{\dot{A}}{A} + \frac{\dot{C}}{C}\\ &= \frac{2K(n+2)}{[-2\varepsilon(n^2-n-1)]^{1/2}}\left[\frac{2I}{Y^2} - \frac{\varepsilon}{Y^{4(n+1)/(n^2+n+1)}}\right]^{1/2}\end{aligned} \tag{4.5}$$

and the shear scalar is

$$\begin{aligned}\sigma^2 &= \frac{2}{3}\left[\frac{\dot{C}}{C} - \frac{\dot{A}}{A}\right]^2\\ &= -\frac{4K^2(n-1)^2}{3\varepsilon(n^2-n-1)}\left[\frac{2I}{Y^2} + \frac{\varepsilon}{Y^{4(n+1)/(n^2+n+1)}}\right].\end{aligned} \tag{4.6}$$

The expressions (4.1–4.6) give the physical parameters of interest once Y is known. We note the appearance of the constant of integration, I. In (3.10) we can take $I=0$ as a special case when $\varepsilon=+1$ which occurs for $n^2-n-1\leqslant 0$, i.e. $n\in((1-\sqrt{5})/2, (1+\sqrt{5})/2)$. This corresponds to $\nu\in[-3,-1]$. (Recall that ν takes its minimum at $n=0$.) Thus (3.10) reduces to

$$Y'^2 = Y^{\nu+1}. \tag{4.7}$$

We assume that $A(t)$ and $Y(X)$ are non-negative. Then (4.7) is easily integrated to

$$Y = \left[\frac{1-\nu}{2}(X-X_0)\right]^{2/(1-\nu)} \tag{4.8}$$

provided $\nu\neq -2$. (For the general discussion we have already excluded $\nu=-1$.) This gives a range of solutions for the field variables for n in the interval specified.

5. Solutions of the governing equation

The solution of the field equations (2.6–2.8) and the evaluation of the field variables etc. (4.1–4.6) have been reduced under the assumption (3.1) to the evaluation of the integral (3.11), viz.

$$X - X_0 = \begin{cases} \int [2I + \varepsilon Y^{\nu+1}]^{-1/2} \mathrm{d}Y \\ \int [2I - 2\log Y]^{-1/2} \mathrm{d}Y, \quad \nu = -1. \end{cases} \tag{5.1}$$

It is well-known that (5.1b) cannot be evaluated in closed form under any circumstances since it is a variant of the exponential-integral function [20, p 93]. However, (5.1a) is known to be evaluable as a standard integral for $\nu = -3, -2, 0, 1, 2, 3$ (the corresponding values for n are $0, (1 \pm \sqrt{13})/6, (3 \pm \sqrt{21})/2, -1, (-5 \pm \sqrt{5})/2, (-3 \pm i\sqrt{3})/2$.

The two cases given by Tikekar and Patel [10] which are not included in this list correspond to $\nu = -3/5$ ($n = (3 \pm \sqrt{33})/4$) and $\nu = -1/3$ ($n = 1 \pm \sqrt{3}$). These values give a hint to one sequence for which (5.1a) can be evaluated in closed form. Let

$$\nu = -\frac{m}{m+2}, \quad m \in \mathscr{Z}. \tag{5.2}$$

Then (5.1a) is

$$X - X_0 = \int [2I + \varepsilon Y^{2/(m+2)}]^{-1/2} \mathrm{d}Y. \tag{5.3}$$

For $m + 2 \geqslant 0$ the first nontrivial value of m is $m = 1$. For $m \geqslant 1$, $\nu \in (-1, -1/3)$. Over this interval $\varepsilon = -1$. The appropriate substitution is

$$Y = [(2I)^{1/2} \sin u]^{m+2} \tag{5.4}$$

so that (5.3) becomes

$$(X - X_0) = (m+2)(2I)^{(m+4)/2} \int^{u(Y)} \sin^{m+1} u \mathrm{d}u \tag{5.5}$$

which can be evaluated in closed form for all integral $m \geqslant 1$. Inversion is not generally possible apart from locally. The one exception is $m = 2$ ($n = (5 \pm \sqrt{85})/6$). However, (5.4) with (5.5) does define a parametric solution. It is a simple matter to express (4.1–4.6) in terms of the parameter u through (5.4)

For $m + 2 \leqslant 0$ we replace m by $-p-2$, $p \in \mathscr{Z}^+$. Then (5.3) becomes

$$X - X_0 = \int [2I + \varepsilon Y^{-2/p}]^{-1/2} \mathrm{d}Y \tag{5.6}$$

and

$$\nu = -\frac{p+2}{P} \tag{5.7}$$

so that $\varepsilon = +1$ for all admissible values of p. We rewrite (5.6) as

$$X - X_0 = \int Y^{1/p} [2I\, Y^{2/p} + 1]^{-1/2} \mathrm{d}Y \tag{5.8}$$

and the integral is evaluated in closed form by the substitution

$$Y = [(2I)^{-1/2} \sinh u]^p. \tag{5.9}$$

Finally we note that there is another set of values of v for which (3.5) is integrable. If

$$v = \frac{p+2}{p}, \quad p \in \mathscr{Z}^+, \tag{5.10}$$

(3.5) possesses the Painlevé Property [21] and is integrable in the sense of Painlevé [22]. Unfortunately the evaluation of the quadrature is by no means obvious. As a matter of curiosity we note that when v is given by (5.7), the negative of (5.10), (3.5) does not possess the Painlevé Property in its present form, but the quadrature of (3.11) is straightforward.

6. Conclusion

In this paper we have shown, using symmetry arguments, how the equation governing the behaviour of cosmic strings in Bianchi III spacetime may be reduced to the quadrature (3.11). A detailed analysis of (3.11) was performed. Those cases for which (3.11) is evaluable as a simple integral, from standard handbooks of integrals, are given; particular cases reported previously in [10] are identified. In addition, we present a particular sequence for which the integral may be evaluated in closed form. In general for this sequence the solution can only be put into parametric form and inversion is only possible locally. Few closed form solutions to the Einstein equations for cosmic strings have been reported in the literature. Our analysis is an attempt to obtain more exact solutions so that our understanding of these objects may be improved. It is hoped that some of the solutions presented here will provide the basis for a detailed physical analysis of cosmic strings in the gravitational context.

Acknowledgements

Authors thank the Foundation for Research Development of South Africa and the University of Natal for their continued support. Authors thank the Foundation for Research Development of South Africa and the University of Natal for their continued support.

References

[1] Ya B Zel'dovich, *Mon. Not. R. Astron. Soc.* **192**, 663 (1980)
[2] T W S Kibble, *J. Phys.* **A9**, 1387 (1976)
[3] A Vilenkin, *Phys. Rev.* **D24**, 2982 (1981)
[4] J R Gott, *Astrophys. J.* **288**, 422 (1985)
[5] D Garfinkle, *Phys. Rev.* **D32**, 1323 (1985)
[6] P S Letelier, *Phys. Rev.* **D20**, 1294 (1979)
[7] J Stachel, *Phys. Rev.* **D21**, 2171 (1980)
[8] K D Krori, T Chaudhuri, C R Mahanta and A Mazumdar, *Gen. Relativ. Gravit.* **22**, 123 (1990)
[9] A Banerjee, A K Sanyal and S Chakrabarty, *Pramana – J. Phys.* **34**, 1 (1990)
[10] Ramesh Tikekar and L K Patel, *Gen. Relativ. Gravit.* **24**, 397 (1992)
[11] A K Head, *Comp. Phys. Commun.* **77**, 241 (1993)
[12] Peter J Olver, *Applications of Lie groups to differential equations*, second edition (New York, Springer-Verlag, 1993)
[13] I J Homer Lane, *Am. J. Sci. Arts* **4**, 57 (1869–1870)

[14] R Emden, *Gaskugeln, Anwendungen der mechanischen Warmen-theorie auf Kosmologie und meteorologische Probleme*, Leipzig, Teubner (1907)
[15] R H Fowler, *Q. J. Math.* **45**, 289 (1914);
R H Fowler, *Mon, Not. R. Astron. Soc.* **91**, 63 (1930)
[16] J Patera and P Winternitz, *J. Math. Phys.* **18**, 1449 (1977)
[17] S Lie, *Differentialgleichungen*, (New York, Chelsea, 1967)
[18] V Ermakov, *Univ. Izv. Kiev Ser. III* **9**, 1 (1880)
[19] Edmund Pinney, *Proc. Am. Math. Soc.* **1**, 681 (1950)
[20] I S Gradshteyn and I M Ryzhik, *Table of integrals, series and products.* fourth edition, edited by Allan Jeffrey (Academic Press, San Diego, 1980)
[21] K S Govinder and P G L Leach, *Integrability analysis of the Emden–Fowler equation,* Preprint: Department of Mathematics, University of the Aegean (1994)
[22] P Painlevé, *Acta Math.* **25**, 1 (1902)

PRAMANA
— journal of
physics

© Printed in India

Vol. 44, No. 6,
June 1995
pp. 519–534

Static and dynamic properties of pseudoscalar mesons

D K CHOUDHURY*⁺, PRATIBHA DAS**, D D GOSWAMI*** and
J K SARMA*
*Department of Physics, Gauhati University, Guwahati 781 014, India
**Department of Physics, Nalbari College, Nalbari 781 335, India
***Department of Physics, North Lakhimpur College, North Lakhimpur 787 001, India
⁺ Present address: International Centre for Theoretical Physics, P.O. Box 586, 34100 Trieste, Italy

MS received 20 May 1994; revised 14 November 1994

Abstract. We report the results of form factors, charge radii and decay constants of both light and heavy flavoured pseudoscalar mesons in a QCD inspired quark model. We use the quantum mechanical perturbation theory and discuss its limitations in the present problem. Several predictions are also made for bottom and top flavours.

Keywords. Meson wave function; form factors; decay constants; charged radii.

PACS No. **12·40**

1. Introduction

Study of hadron wave functions and their phenomenology is an important topic in quantum chromodynamics [1]. Constraints on the baryon and meson distribution amplitudes have been obtained in recent years within the framework of QCD sum rules [2] and lattice QCD [3].

In the more phenomenological approach of non-relativistic potentials however, attention is paid for enumerating the spectra of hadrons rather than the wave function structures since the classical work of De Rujula *et al* [4]. Even in most recent analysis [5], harmonic oscillator basis for the trial wave functions are considered rather than the exact wave functions themselves. The reason is easily understandable; the spin dependent terms of the Fermi–Breit Hamiltonian [4, 6] are more singular than r^{-2} and are therefore illegal operators in the Schrödinger equation.

The application of QCD potentials to light quark systems is rather handicapped due to their relativistic modifications. In the works referred to earlier [5], ad hoc smearing functions as well as momentum dependent strengths are considered as such possible relativistic modifications.

However, it is impossible to solve the eigen functions and eigen energies of the Hamiltonian with such terms directly from the Schrödinger equation. This has resulted in the use of the variational method [5] rather than the perturbation theory.

The aim of the present paper is to report an analysis based on perturbation theory which uses the variational method as well to extract the modification due to spin effect. Specifically, we use the two-body Schrödinger equation and obtain the first order perturbed wave function of the potential using Dalgarno's method [7]. We then incorporate relativistic effects at the wave function level by introducing standard Dirac modifications [8, 9] rather than full covariantization as in Bethe–Salpeter approach [10–12].

In order to test the wave function, one needs to calculate the properties of mesons such as form factors, decay constants and charge radii. This paper attempts to derive them within the present formalism. In §2 we include a discussion on QCD inspired quark model, formulate the wave function and analyse the properties of pseudoscalar mesons. Section 3 contains the summary and conclusions.

2. Theory

2.1 *The non-relativistic QCD inspired quark model*

The non-relativistic QCD inspired quark model has its origin in the work of ref. [4]. Since then, it has been applied to explain schematically the vast body of information available on mesons and baryons [11–13]. However, the non-relativistic treatment of light quark systems is clearly inadequate and needs improvement.

On the other hand, the Fermi–Breit Hamiltonian [4] which is the basis of the QCD inspired quark model has terms which are more singular than γ^2 and hence is not exactly soluble.

Godfrey and Isgur [5] improved upon the model by postulating a relativistic potential $V(\mathbf{p},\mathbf{r})$ which differs from its non-relativistic limit in two ways (i) the coordinate $(\mathbf{r})$ becomes smeared at over distances of the order of the inverse quark mass and (ii) the coefficients of the various potentials become dependent on the momentum of the interacting quarks. The smearing of the potentials results in taming of all their singularities. Specifically, the smearing function between two quarks of masses m_i, m_j is taken as

$$\rho_{ij}(r_i - r_j) = \frac{\sigma_{ij}^3}{\pi^{3/2}} \exp[-(\sigma_{ij}^2(r_i - r_j)^2)] \tag{1}$$

with the prescription

$$\sigma_{ij}^2 = \sigma_0^2\left[\frac{1}{2} + \frac{1}{2}\left(\frac{4m_i m_j}{(m_i + m_j)^2}\right)^4\right] + S^2\left(\frac{2m_i m_j}{m_i + m_j}\right)^2, \tag{2}$$

where σ_0 and S are the relativistic parameters determined from data. Similarly, the momentum dependence introduced in relativistic treatment transforms mass function $(1/m_i)$ of the potentials into energies $1/(m_i^2 + p_i^2)^{1/2}$.

Such a method although claimed to be phenomenologically successful, is crude enough to warrant alternate route of improving the non-relativistic QCD inspired quark model. In the present paper, we improve upon the model without additional free parameters, unlike [5]. To that end we use perturbation theory [7] and parameter-free Dirac modification.

2.2 *Fermi–Breit Hamiltonian*

We take the non-relativistic two body Schrödinger equation as our basis, i.e.

$$H|\psi\rangle = (\hat{H}_0 + \hat{H}')|\psi\rangle = E|\psi\rangle, \tag{3}$$

where H_0 is the free Hamiltonian for two quarks of masses m_i and m_j and three-momenta $\mathbf{P}_i$ and $\mathbf{P}_j$. H_0 is defined as

$$H_0 = \frac{p_i^2}{2m_i} + \frac{p_j^2}{2m_j}, \tag{4}$$

and H is the Fermi–Breit Hamiltonian with confinement which is defined as

$$H(r) = H^{\text{conf}}(r) + H^{\text{hyp}}(r) + H^{\text{S.O.}}(r). \tag{5}$$

Here,

$$H^{\text{conf}}(r) = +\left(-\frac{\alpha_s(r)}{r} + \frac{3}{4}br + \frac{3}{4}c\right)(F_i \cdot F_j) \tag{6}$$

$$H^{\text{hyp}}(r) = \frac{-\alpha_s(r)}{m_i m_j}\left[\frac{8\pi}{3}\mathbf{S}_i \cdot \mathbf{S}_j \delta^3(r) + \frac{1}{r^3}\left\{\frac{3(\mathbf{S}_i \cdot \mathbf{r})(\mathbf{S}_j \cdot \mathbf{r})}{r^2} - \mathbf{S}_i \cdot \mathbf{S}_j\right\}\right](\mathbf{F}_i \cdot \mathbf{F}_j) \tag{7}$$

$$H^{\text{S.O.}}(r) = H^{\text{S.O.(c.m.)}} + H^{\text{S.O.(t.p.)}} \tag{8}$$

$$H^{\text{S.O.(c.m.)}} = \frac{\alpha_s(r)}{r^3}\left(\frac{1}{m_i} + \frac{1}{m_j}\right)\left(\frac{\mathbf{S}_i}{m_i} + \frac{\mathbf{S}_j}{m_j}\right)\mathbf{L}(\mathbf{F}_i \cdot \mathbf{F}_j) \tag{9}$$

$$H^{\text{S.O.(t.p.)}}(r) = -\frac{1}{2r}\frac{\partial H^{\text{conf}}}{\partial r}\left(\frac{\mathbf{S}_i}{m_i^2} + \frac{\mathbf{S}_j}{m_j^2}\right)\mathbf{L}. \tag{10}$$

Here, $\mathbf{S}_i$ and $\mathbf{S}_j$ are the spins of the ith and jth quarks separated by a distance r. For ground state ($l = 0$), only the contact term $\propto \delta^3(r)$ contributes and the Hamiltonian takes the simpler form

$$H = \frac{4\alpha_s}{3}\left[-\frac{1}{|r|} - \frac{8\pi}{3}\delta^3(\mathbf{r})\frac{\mathbf{S}_i \cdot \mathbf{S}_j}{m_i m_j}\right] + br + c. \tag{11}$$

2.3 *Formulation of wave function*

Neglecting the δ-function in (11) the spin-independent Hamiltonian is

$$H = -\frac{4\alpha_s}{3r} + br + c \tag{12}$$

so that

$$H'(r) = br + c \tag{13}$$

can be treated as the perturbation to the unperturbed Hamiltonian

$$H_0 = \frac{p_i^2}{2m_i} + \frac{p_j^2}{2m_j} - \frac{4\alpha_s}{3r}. \tag{14}$$

Let us now calculate the first order perturbed eigen function $\psi^{(1)}$ and eigen energy $W^{(1)}$ using the relation [7]

$$H_0 \psi^{(1)} + H\psi^{(0)} = W^{(0)}\psi^{(1)} + W^{(1)}\psi^{(0)} \tag{15}$$

where

$$W^{(1)} = \langle \psi^{(0)} | H' | \psi^{(0)} \rangle. \tag{16}$$

From (15), we calculate $\psi^{(1)}$ by Dalgarno's method and obtain

$$\psi^{(1)}(r) = -\frac{1}{2\sqrt{\pi a_0^3}}\mu b a_0 r^2 \exp(-r/a_0), \tag{17}$$

where μ is the reduced mass defined as

$$\mu = \frac{m_i m_j}{m_i + m_j} \tag{18}$$

and

$$a_0 = (4/3\mu\alpha_s)^{-1}, \tag{19}$$

α_s being the strong coupling constant.

The normalized wave function with coulomb plus linear potential will be

$$\begin{aligned}\psi(r) &= \psi^{(0)}(r) + \psi^{(1)}(r)\\ &= \frac{1}{[\pi a_0^3(1 - 3\mu b a_0^3 + (45/8)\mu^2 b^2 a_0^6)]^{1/2}}\left(1 - \frac{1}{2}\mu b a_0 r^2\right)\exp(-r/a_0).\end{aligned} \tag{20}$$

Its momentum transform is

$$\psi(Q) = \left[\frac{2^3}{\pi^3(1 - 3\mu b a_0^3 + (45/8)\mu^2 b^2 a_0^6)}\right]^{1/2}\sum_i e_i\left(1 - \frac{6\mu b a_0^3(1 - a_0^2 Q_i^2)}{(1 + a_0^2 Q_i^2)^2}\right) \tag{21}$$

where Q_i's are defined as

$$Q_i = \sum_{j\neq i} m_j Q \Big/ \sum_i m_i. \tag{22}$$

2.4 *Status of confinement as perturbation*

The question naturally arises about the validity and consequences of treating linear confining potential as perturbation. The reason is understandable: linear confining potential being strong, is expected to be more dominant than the coulombic piece. However the confinement potential is operative within the characteristic size of a hadron. The characteristic distance of heavy flavour mesons is taken to be of the order of $\frac{1}{2}m_Q$, m_Q being the mass of heavy quark [16]. Even for heavy light meson, the corresponding distance is of the order of quarkonium size, smaller than the hadronic scale $\Lambda_{\mathrm{QCD}}^{-1}$. A similar observation has been done in QCD sum rules approach as well [17, 18]. If such an observation is taken seriously, treating confinement potential as perturbation appears to be justified for mesons containing at least one heavy flavour. For light mesons however, such argument does not hold good. We therefore assume it to be an ansatz to obtain explicit mesonic wave functions for light quark systems. The validity or otherwise of it will then be tested through available data.

If confinement is to be treated as perturbation, then from (21)

$$\left|\sum_i e_i \frac{6\mu b a_0^3(1 - a_0^2 Q_i^2)}{(1 + a_0^2 Q_i^2)^2}\right| < 1. \tag{23}$$

Equation (23) does not hold good for very low Q^2 with $b = 0{\cdot}183\,\mathrm{GeV}^2$ [19]. As a result, the present perturbation method breaks down for low $Q^2, Q^2 \leqslant Q_0^2$ where Q_0^2 is determined from the condition

$$\sum e_i \frac{6\mu b a_0^3(1 - a_0^2 Q_0^2)}{(1 + a_0^2 Q_0^2)^2} = 1. \tag{24}$$

Values of Q_0^2 are different for different mesons due to the quark mass dependence occurring in Q_i. In table 1 we record the values of Q_0^2 for several light and heavy flavoured mesons. As $b \to 0$, the value of Q_0^2 will be decreased so that the formalism works for lower Q^2 range. It is thus clear that for fixed Q^2, perturbation works for smaller b.

We note that α_s as occurred in Q_0 [eq. 19] is Q^2 dependent. However as the dependence is only logarithmic, for our numerical analysis (table 1), we have assumed it to be approximately constant. For the Q^2 range under study, such variation is indeed found to be quantitatively small [5]. We also note that justification for neglecting the running of α_s for qualitative and numerical analysis has recently been advocated in other areas of QCD as well [20, 21].

2.5 *Relativistic effects*

The relativized version of (20) is [8, 9]

$$\psi^{\mathrm{Rel}}(r) = \frac{N}{\sqrt{\pi a_0^3}}\left(1 - \frac{1}{2}\mu b a_0 r^2\right)\left(\frac{r}{a_0}\right)^{-\varepsilon} \exp(-r/a_0) \tag{25}$$

Table 1. Values of Q_0^2 (in GeV^2) for different mesons above which linear potential can be treated as perturbation for $b = 0{\cdot}183\,\mathrm{GeV}^2$.

	Non-relativistic version (eq. (23))		Relativistic version (eq. (31))		
Particles	$\alpha_s = 0{\cdot}5$	α_s determined from meson mass	$\alpha_s = 0{\cdot}65$	$\alpha_s = 0{\cdot}6$	$\alpha_s = 0{\cdot}5$
$\pi^\pm$	6·4	0·3	3·6	4·2	5·6
$K^\pm$	5·5	0·3	3·1	3·6	4·8
k^0	28·3	15·0	13·0	18·0	23·8
$D^\pm$	6·2	0·2	3·5	4·1	5·5
D^0	4·0	3·0	2·2	2·6	3·3
$D_s^\pm$	6·3	4·0	3·5	4·2	5·8
$B^\pm$	2·6	2·0	1·4	1·7	2·3
B_d^0	6·0	5·0	3·4	3·9	5·0
B_s^0	6·9		3·9	4·4	5·5
$B_c^\pm$	0·5		0	0·4	2·0
T_u^0	2·6		1·5	1·7	2·1
$T_d^\pm$	4·5		2·5	3·0	4·0
$T_s^\pm$	4		3·3	2·9	27·0
T_c^0	5·9		0	0	0

where N is the normalization constant and ε is defined by

$$\varepsilon = 1 - \sqrt{1-(4\alpha_s/3)}. \tag{26}$$

The corresponding momentum transform is

$$\psi^{\mathrm{Rel}}(Q) = \frac{N\sqrt{2a_0}\,\Gamma(2-\varepsilon)}{\pi Q_i} \times \left[\frac{\sin(2-\varepsilon)\theta_i}{(1+a_0^2Q_i^2)^{(2-\varepsilon)/2}} - \frac{\mu b\, a_0^3(3-\varepsilon)(2-\varepsilon)(4-\varepsilon)\theta_i}{2(1+a_0^2Q_i^2)^{(4-\varepsilon)/2}}\right], \tag{27}$$

where

$$\theta_i = \sin^{-1}\frac{Q_i}{\left(\frac{1}{a_0^2}+Q_i^2\right)^{1/2}} \tag{28}$$

and Q_i is defined in (22)

For small Q^2, (i.e. for small Q_i)

$$\sin^{-1}\frac{Q_i}{\left(\frac{1}{a_0^2+Q_i^2}\right)^{1/2}} \cong \frac{Q_i}{\left(\frac{1}{a_0^2}+Q_i^2\right)^{1/2}}, \tag{29}$$

implying that θ_i defined in (28) will be small for small Q_i. Hence, for low Q^2, corresponding to small value of Q_i, $\psi^{\mathrm{Rel}}(Q)$ reduces to

$$\psi^{\mathrm{Rel}}(Q) = \sum \frac{N a_0^{3/2}\sqrt{2}(2-\varepsilon)\Gamma(2-\varepsilon)}{\pi(1+a_0^2Q_i^2)^{(3-\varepsilon)/2}}\left[1 - \frac{(4-\varepsilon)(3-\varepsilon)\mu b\, a_0^3}{2(1+a_0^2Q_i^2)}\right]. \tag{30}$$

In this case, confinement will be perturbation only if

$$\sum_i e_i \frac{(4-\varepsilon)(3-\varepsilon)\mu b\, a_0^3}{2(1+a_0^2Q_i^2)} \ll 1. \tag{31}$$

The value of Q_0^2 is now dependent on ε besides quark flavour as recorded in table 1.

2.6 *Spin effect*

It is observed that the masses of the hadrons with same quark content but different in spin are different. For instance the vector mesons (ρ, K^* etc.) are heavier than the pseudoscalar mesons (π, K etc.) despite having the same quark content. The difference in their masses must be attributed to a spin–spin interaction, the QCD analog to hyperfine splitting in the ground state of hydrogen. In our approach, we attempt to incorporate spin effect from the observed meson masses in the spirit of variation method [22].

The energy shift of mass splitting due to spin interaction in the perturbation theory reads [23],

$$\Delta E = \int \psi^* \left\{\frac{32\pi\alpha_s}{9}\delta^3(r)\frac{\mathbf{S}_i\cdot\mathbf{S}_j}{m_i m_j}\right\}\psi\, d^3r \tag{32}$$

leading to

$$\Delta E = \frac{32\pi\alpha_s}{9m_i m_j}(\mathbf{S}_i \cdot \mathbf{S}_j)|\psi(0)|^2. \tag{33}$$

Taking this energy shift into account, the pseudoscalar meson mass is expressed as [24]

$$M_P = m_i + m_j - \frac{8\pi\alpha_s}{3m_i m_j}|\psi(0)|^2 \tag{34}$$

$$\text{since } (\mathbf{S}_i \cdot \mathbf{S}_j) = -\tfrac{3}{4} \text{ for pseudoscalar mesons} \tag{35}$$

Let us now estimate the effect of spin in $\psi(0)$ and construct $\psi(r)$ using the variation method. The wave function (20) can be rewritten as

$$\psi(r) = \psi(0)\left(1 - \frac{1}{2}\mu b a_0 r^2\right)\exp(-r/a_0) \tag{36}$$

where

$$\psi(0) = \frac{1}{[\pi a_0^3(1 - 3\mu b a_0^3 + (45/8)\mu^2 b^2 a_0^6)]^{1/2}}. \tag{37}$$

The spin effect can then be incorporated in (35) by modifying the value of α_s through a_0,

$$a_0^P = \frac{1}{4/3\mu\alpha_s^P} \tag{38}$$

so that

$$\psi(0) = \frac{1}{[\pi a_0^{P^3}(1 - 3\mu b a_0^{P^3} + (45/8)\mu^2 b^2 a_0^{P^6}]^{1/2}}. \tag{39}$$

α_s^P is then obtained from the fitting of $\psi(0)$ to the pseudoscalar meson mass equation (34), which is different for different mesons.

The spin modified wave function therefore takes the form

$$\psi^P(r) = \frac{1}{[\pi a_0^{P^3}(1 - 3\mu b a_0^{P^3} + (45/8)\mu^2 b^2 a_0^{P^6}]^{1/2}} \times \left(1 - \frac{1}{2}\mu b a_0^P r^2\right) \cdot \exp(-r/a_0^P). \tag{40}$$

2.7 *Spin-cum-relativistic effects*

The spin effect depends on the wave function at the origin, $\psi(0)$. But as $r \to 0$, relativistic wave function (25) develops a $r^{-\varepsilon}$ behaviour for fixed α_s. As a result, in the fixed α_s approximation used in the present work, $\psi^{\mathrm{Rel}}(0)$ is undefined and hence spin effect cannot be introduced together with its relativistic counterpart. We consider it as an inherent limitation of the present formalism.

In order to circumvent the problem, we use the additional ansatz that due to asymptotic freedom $\varepsilon \to 0$ as $r \to 0$, so that relativity does not modify the wave function at the origin and $\psi(0)$ is finite. To see the effect of spin in such a constrained wave function, we again use the variation method discussed earlier. If the spin modified value a_0^P in (38) is such that $\alpha_s^P > \frac{3}{4}$, then ε [eq. (26)] becomes complex and the formalism might even break down.

We will study such possibilities in our subsequent analysis and discuss critically its limitations.

2.8 *Properties of mesons*

2.8.1 *Form factors*: The elastic charge form factor for a charged system of point quarks [25] is defined as

$$F(Q^2)=\frac{1}{e}\int\psi^{+}(\tau)\sum_{i=1}^{n}e_i\exp(i\mathbf{Q}_i\mathbf{r}_i)\psi(\tau)\mathrm{d}\tau \tag{41}$$

in which e is the total charge, e_i and r_i are the charge and position vector of the ith quark, and $\psi(\tau)$ is the model eigenvector solution, collectively denoting all internal coordinates. Equation (41) can be recast in a simplified form [26]:

$$eF(Q^2)=\sum_i\frac{e_i}{Q_i}\int_0^{\infty}r|\psi(r)|^2\sin Q_i r\,\mathrm{d}r. \tag{42}$$

With eq. (20), (42) becomes

$$eF(Q^2)=\frac{4N^2}{a_0^3}\sum_i\frac{e_i}{Q_i}\int_0^{\infty}\left(1-\frac{1}{2}\mu b a_0 r^2\right)\exp(-2r/a_0)r\sin(Q_i r)\mathrm{d}r \tag{43}$$

which after normalization, becomes

$$\begin{aligned}eF(Q^2)=\sum_i&\frac{e_i}{(1-3\mu b a_0^3+(45/8)\mu^2b^2a_0^6)}\\&\times\left[\frac{1}{(1+(a_0^2Q_i^2/4))^2}-\frac{3\mu b a_0^3(1-(a_0^2Q_i^2/4))}{(1+(a_0^2Q_i^2/4))^4}\right.\\&\left.+\frac{15\mu^2b^2a_0^6}{8(1+(a_0^2Q_i^2/4))^4}\left(3-\frac{4a_0^2Q_i^2}{(1+(a_0^2Q_i^2/4))}-\frac{a_0^4Q_i^4}{(1+(a_0^2Q_i^2/4))^2}\right)\right]\end{aligned} \tag{44}$$

Spin effect will modify a_0 to a_0^P as noted earlier.

Incorporating relativistic effect, (43) becomes

$$eF(Q^2)=\sum\frac{4N'^2e_i}{Q_ia_0^{3-2\varepsilon}}\int_0^{\infty}\left(1-\frac{1}{2}\mu b a_0 r^2\right)^2r^{1-2\varepsilon}\sin(Q_ir)\exp(-2r/a_0)\mathrm{d}r \tag{45}$$

where N' is the normalization constant. After performing the integration, it has the form

$$\begin{aligned}eF(Q^2)=\frac{N'^2}{a_0 2^{-2\varepsilon}}\sum_i\frac{e_i}{Q_i}&\left[\frac{\Gamma(2-2\varepsilon)\sin(2-2\varepsilon)\theta_i}{(1+(a_0^2Q_i^2/4))^{(1-\varepsilon)}}\right.\\&-\frac{1}{4}\mu b a_0^3\frac{\Gamma(4-2\varepsilon)\sin(4-2\varepsilon)\theta_i}{(1+(a_0^2Q_i^2/4))^{(2-\varepsilon)}}\\&\left.+\frac{1}{64}\mu^2b^2a_0^6\frac{\Gamma(6-2\varepsilon)\sin(6-2\varepsilon)\theta_i}{(1+(a_0^2Q_i^2/4))^{(3-\varepsilon)}}\right].\end{aligned} \tag{46}$$

As noted in (29) small θ_i corresponds to low Q^2. In this limit, (46) becomes

$$eF(Q^2) \simeq \sum \frac{N^2 e_i}{2^{-2\varepsilon}} \left[\frac{\Gamma(2-2\varepsilon)(2-2\varepsilon)}{2(1+a_0^2 Q_i^2/4))^{(3/2-\varepsilon)}} - \frac{1}{4}\mu b a_0^3 \frac{\Gamma(4-2\varepsilon)(4-2\varepsilon)}{2(1+(a_0^2 Q_i^2/4))^{(5/2-\varepsilon)}} + \frac{1}{64}\mu^2 b^2 a_0^6 \frac{\Gamma(6-2\varepsilon)(6-2\varepsilon)}{2(1+(a_0^2 Q_i^2/4))^{(7/2-\varepsilon)}} \right]. \tag{47}$$

In perturbative QCD, the running coupling constant $\alpha_s(Q^2)$ is defined as

$$\alpha_s(Q^2) = \frac{12\pi}{(33-2N_f)\ln Q^2/\Lambda^2} \tag{48}$$

where N_f = number of flavours.

For very low $Q^2, Q^2 \to 0$, (48) diverges and hence several extrapolated forms have been proposed in recent literature. In the work of Godfrey and Isgur [5], $\alpha_s(Q^2)$ is defined as,

$$\alpha_s(Q^2) = 0{\cdot}25 e^{-Q^2} + 0{\cdot}15 e^{-Q^2/10} + 0{\cdot}2 e^{-Q^2/1000} \tag{49}$$

so that $\alpha_s \leqslant 0{\cdot}6$ yielding $\varepsilon \leqslant 0{\cdot}4$.

There is another hypothesis for such extrapolation of $\alpha_s(Q^2)$ for low Q^2. With the idea of "frozen coupling constant" Ji and Amiri [27] as well as Cornwall [28] assume

$$\alpha_s(Q^2) = \frac{4\pi}{(33-2N_f)\ln[(Q^2+4m_g^2)/\Lambda^2]} \tag{50}$$

where m_g is interpreted as an effective dynamical gluon mass. With a value of m_g about 0·5 GeV/C and Λ of the order of 0·2 GeV [29], $\alpha_s(0) \sim 0{\cdot}5$ and $\varepsilon \sim 0{\cdot}25$.

On the other hand, if $(Q^2)^{-1}$ fall is expected [30, 31] one needs $\alpha_s \sim 0{\cdot}65$ which leads to $\varepsilon \sim 0{\cdot}5$.

Equation (47) shows that confinement effect invariably introduces higher power of $1/Q^2$ in the form factor and modify the nonasymptotic behaviour. In figure 1 we show the prediction of (44) for pion form factor with $b = 0, 0{\cdot}07, 0{\cdot}1$ and $0{\cdot}183\ \text{GeV}^2$ and using $a_0^\pi = 3{\cdot}03\ \text{GeV}^{-1}$. Data are taken from Amendolia *et al* [32]. It shows that the present formalism falls short of accommodating reasonably large confinement effect in form factor. In figure 2 we show similar analysis for kaon using $a_0^K = 2{\cdot}91\ \text{GeV}^{-1}$ and compare with more recent data of Amendalia *et al* [33]. The results are similar to figure 1.

2.8.2 *Charge radii.* The average charge radii square for mesons can be obtained using the relation

$$\langle r^2 \rangle = -6 \frac{\mathrm{d}F(Q^2)}{\mathrm{d}Q^2}\bigg|_{Q^2=0} \tag{51}$$

which yields for masses m_i and m_j

$$\langle r^2 \rangle = \frac{3n}{2} a_0^2 g_{conf} \left(\frac{e_i}{(1+(m_i/m_j))^2} + \frac{e_j}{(1+(m_j/m_i))^2} \right) \tag{52}$$

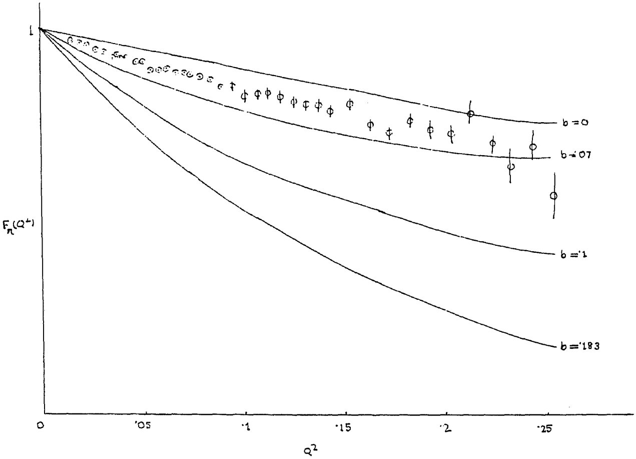

Figure 1. $F_\pi(Q^2)$ vs Q^2 for confinement parameter for $b = 0, 0{\cdot}07, 0{\cdot}1$ and $0{\cdot}183\,\mathrm{GeV}^2$ using (41) and $a_0^\pi = 3{\cdot}03\,\mathrm{GeV}^{-1}$. Data are taken from Amendolia *et al* [32].

when $n = 1$, $1{\cdot}1$ and $1{\cdot}25$ correspond to $\varepsilon = 0{\cdot}5$, $0{\cdot}4$ and $0{\cdot}25$ respectively. In non-relativistic case, $n = 2$ and $a_0 \to a_0^P$. In (52) g_{conf} is the confinement factor given by

$$g_{\mathrm{conf}} = \frac{1 - (15/2)\mu b a_0^3 + (105/4)\mu^2 b^2 a_0^6}{1 - 3\mu b a_0^3 + (45/8)\mu^2 b^2 a_0^6} \quad (n = 2) \tag{53a}$$

$$= \frac{1 - 3\mu b a_0^3 + (45/8)\mu^2 b^2 a_0^6}{1 - (3/2)\mu b a_0^3 + (15/8)\mu^2 b^2 a_0^6} \quad (n = 1) \tag{53b}$$

$$= \frac{1 - 3{\cdot}35\mu b a_0^3 + 6{\cdot}76\mu^2 b^2 a_0^6}{1 - 1{\cdot}76\mu b a_0^3 + 2{\cdot}4\mu^2 b^2 a_0^6} \quad (n = 1{\cdot}1) \tag{53c}$$

$$= \frac{1 - 3{\cdot}72\mu b a_0^3 + 8{\cdot}45\mu^2 b^2 a_0^6}{1 - 2{\cdot}19\mu b a_0^3 + 3{\cdot}38\mu^2 b^2 a_0^6} \quad (n = 1{\cdot}25) \tag{53d}$$

With spin effect, a_0 of (53a) changes to a_0^P [eq. (38)], using the variational method [20]. For (53b–d), however, such modification is not possible as the present formalism falls short of accommodating spin and relativity simultaneously, as discussed earlier.

In figure 3 we plot g_{conf} vs b for pion using eqs (53a–d). The dashed region correspond to the allowed range of g_{conf} using the data of [25], which suggests $b \leqslant 0{\cdot}07\,\mathrm{GeV}^2$. A similar analysis for kaon in figure 4 suggests $b \leqslant 0{\cdot}05\,\mathrm{GeV}^2$ using data of [33]. Hence as in our previous analysis of form factors, charge radii too severely constrain confinement parameter b.

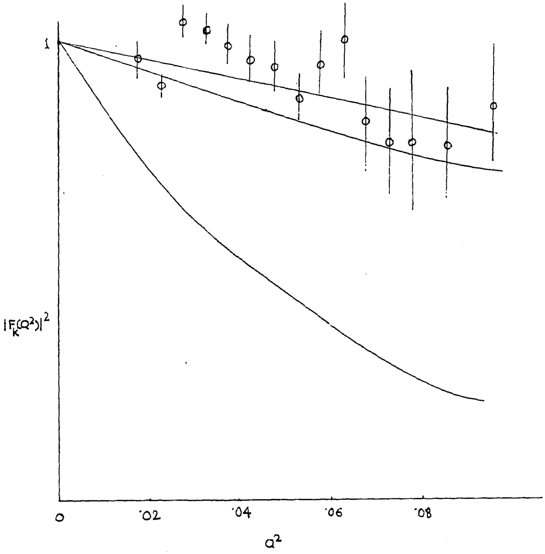

Figure 2. $|F_k(Q)|^2$ vs Q^2 for confinement parameter $b = 0$, 0·05 and 0·183 GeV^2 with $a_0^K = 2{\cdot}91\,\mathrm{GeV}^{-1}$ compared to data of Amendolia *et al* [33].

2.8.3 *Decay constants*: The standard expression for pseudoscalar meson decay constant in non-relativistic quark model [34] is

$$f_P = \sqrt{\frac{12}{M_P}|\psi(0)|^2} \tag{54}$$

where $\psi(0)$ is the wave function at $r = 0$ and M_P is the mass of the pseudoscalar meson. The wave function at the origin is given by (39). Using spin averaged meson masses from [35, 36] in (54) and taking $0 \leqslant b \leqslant 0{\cdot}07\,\mathrm{GeV}^2$, we obtain

$$151 \geqslant f_\pi \geqslant 109\,\mathrm{MeV} \tag{55}$$

while for $0 \leqslant b \leqslant 0{\cdot}05\,\mathrm{GeV}^2$, we get

$$119 \geqslant f_k \geqslant 99\,\mathrm{MeV}. \tag{56}$$

Equations (55) and (56) show that confinement effect decreases the decay constants, the upperbound corresponding to $b = 0$.

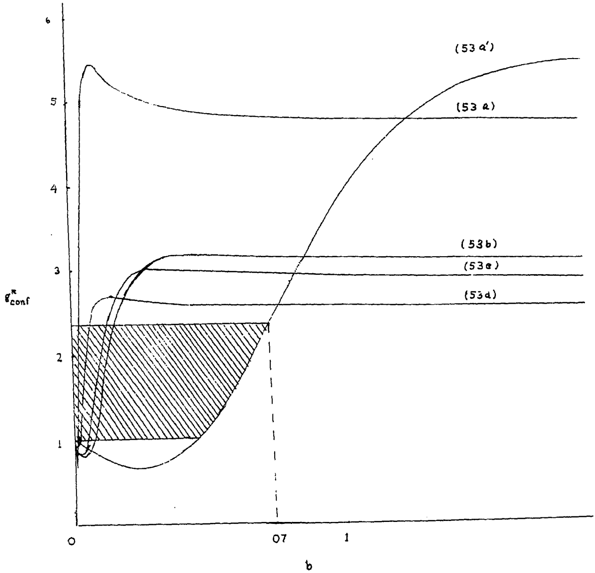

Figure 3. $g^{\pi}_{\rm conf}$ vs b for pion defined in (50a–d). (50a′) means a_0 changes to a_0^P. Data used are from ref. [25].

The weak decay constant f_{D_s} is presently a topical problem in heavy flavour physics [35, 37, 38]. Taking the physical mass $M_{D_s} \cong 1{\cdot}9688$ GeV in (54), we obtain $f_{D_s} \leqslant 237$ MeV, upper limit again corresponding to $b = 0$ to be compared with the results of other authors [5, 34, 38–52] as given in table 2. Recent experiment reported average of f_{D_s} and $f^*_{D_s}$ as [35]

$$f_{D_s}(\cdot) \approx 267 \pm 28 \text{ MeV}. \tag{57}$$

However there are no data on $\langle r^2 \rangle_{D_s}$ to constrain b as in pion or kaon. The experimental limit $f_D \leqslant 310$ MeV [53] also cannot yield $f_D \leqslant 209$ MeV, the upper limit corresponds to $b = 0$. It is to be compared with the results of other authors [27, 34, 38–41, 44, 52, 54, 55] as given in table 3.

There are no reliable data on f_B as well. In calculating $B^0_d - \bar{B}^0_d$ mixing parameter, widely accepted value of f_B is [56]

$$100 < f_B < 200 \text{ MeV}. \tag{58}$$

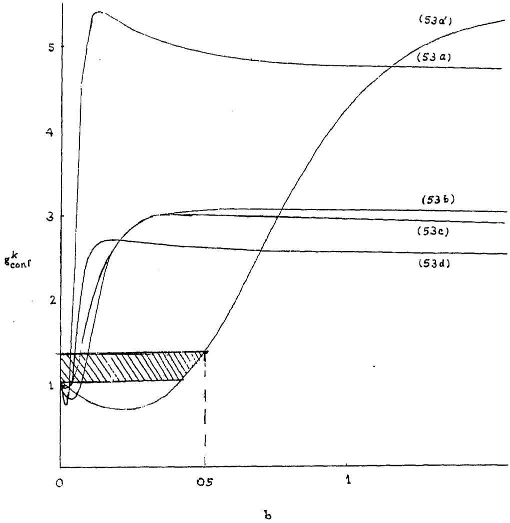

Figure 4. g^{K}_{conf} vs b for kaon using data of ref. [33].

Table 2. Compilation of some theoretical estimates for the weak decay constants f_{D_s} from potential models, bag models, sum rules and lattice calculations. The values are given in MeV.

Potential model	Bag model	Sum rules	Lattice
260 [34]	166 [43]	~232 [44]	215 ± 17 [48]
149 [39]		276 ± 13 [45]	157 ± 11 [49]
210 [40]		218 ± 20 [46]	234 ± 72 [50]
380–590 [38]		200 ± 15 [47]	280 [51]
356 [41]			209 ± 18 [52]
199 [42]			
290 ± 20 [5]			

However, several theoretical estimates of f_B have been made within potential models, lattice QCD, factorization and QCD sum rule approach as compiled in table 4. Taking $M_B \sim 5{\cdot}2786\,\text{GeV}$ in (54) we obtain $f_B \leqslant 107\,\text{MeV}$; upper limit again corresponds to $b = 0$.

Table 3. Compilation of some theoretical estimates for the weak decay constant f_D from potential models, sum rules and lattice calculations. The results are given in MeV.

Potential model	Sum rules	Lattice
112–141 [36]	290 [43]	198 ± 17 [52]
200 [34]	170 ± 30 [35]	
139 [39]		
112–137 [40]		
360–580 [38]		
281 [41]		
150 [54]		

Table 4. Compilation of some theoretical estimates for the weak decay constant f_B from potential models, QCD sum rules, factorization, lattice QCD calculations. The values are given in MeV.

Potential model	Sum rules	Factorization	Lattice
120 [34]	290 [44]	150 ± 50 [59]	366 ± 22 ± 55 [52]
93 [39]	190 ± 50 [55]		205 ± 40 [60]
75–114 [40]	200 ± 35 [57]		310 ± 25 ± 50 [61]
260–300 [38]	170 ± 20 [58]		233 ± 42 [61]
229 [41]	140 [45]		
< 100 [54]			

3. Summary and conclusion

In this paper, we have studied the form factors, charge radii and decay constants of pseudoscalar mesons within a chromodynamic potential model discussed in the text. We have also attempted to incorporate spin, relativity and confinement within our analysis. While, relativity and spin could not be introduced simultaneously, only mild confinement effects are found permissible within our formalism.

However, while confronting with experiments, we observe that two variants of the models still survive: the non-relativistic one with spin effect and the relativistic one with negligible confinement effect ($b \sim 0$) but having a large α_s, $\alpha_s \sim 0{\cdot}65$.

There are arguments against the dominance of perturbative QCD over soft, non-perturbative effects in exclusive processes at currently available range of Q^2 [32, 62, 63]. Within the present formalism, nonperturbative effects can be attributed to a large value of coupling constant α_s as Q^2 small or large value of string constant b. However, for large b the formalism itself breaks down. As a result, the low Q^2 limit of α_s is the only effective measure of nonperturbative effects in the present formalism. The analysis of the present paper indicates that invariably a large value of $\mathrm{Lt}_{Q^2 \to 0}\alpha_s(Q^2)$ is needed to make the relativistic version of the theory compatible with present experiments. It presumably hints the presence of such effect in the present analysis.

Acknowledgement

Two of the authors (PD and JKS) gratefully acknowledge financial support from UGC, New Delhi.

References

[1] S J Brodsky, SLAC-PUB-5013 (1989)
[2] V L Chernyak and J R Zhitnisky, *Phys. Rep.* **112**, 1783 (1984)
[3] G Martinelli and C T Sachrajda, *Phys. Lett.* **B190**, 151 (1987); **B196**, 184 (1987); **B217**, 319 (1989)
[4] A De Rujula, H Georgi and S L Glashow, *Phys. Rev.* **D12**, 147 (1975)
[5] S Godfrey and N Isgur, *Phys. Rev.* **D32**, 189 (1985)
[6] F E Close, in *An introduction to quarks and partons*, (Academic Press, London, 1979) p. 374
[7] A K Ghatak and S Lokanathan, in *Quantum mechanics: theory and applications* (Macmillans, Madras, 1986), p. 255
[8] J J Sakurai, in *Advanced quantum mechanics* (Massachusetts, Addison-Wesley Publishing Company, 1967) p. 128
[9] C Itzykson and J Zuber, in *Quantum field theory* (International Student Edition, McGraw Hill, Singapore, 1986) p. 79
[10] H A Bethe and E E Salpeter, *Phys. Rev.* **82**, 309 (1951)
[11] A N Mitra, in *Quarks, few body systems and relativity in few methods – Principles and applications*, edited by T K Lim *et al* (World Scientific, Singapore, 1986) p. 777
[12] A N Mitra and I Santhanam, *Few-body systems* **12**, 41 (1992) and references therein
[13] N Isgur *Proc. of the XVI International School of subnuclear physics*, Erica 1978 edited by A Zichichi (Plenum, New York, 1980) p. 107
[14] A J G Hey and R Kelley, *Phys. Rep.* **C96**, 71 (1983)
[15] O W Greenberg, *Ann. Rev. Nucl. Part. Phys.* **28**, 327 (1976)
[16] D Kharzeev and H Satz, CERN-TH-7274/94; BI-TP 94/24
[17] M A Shifman, A I Vainshtein and V I Zakharov, *Phys. Lett.* **B65**, 255 (1976)
[18] V A Novikov, M A Shifman, A I Vainshtein and V I Zakharov *Nucl. Phys.* **B136**, 125 (1978)
[19] E Eichten *et al*, *Phys. Rev. Lett.* **34**, 369 (1975); *Phys. Rev.* **D17**, 3090 (1978); **21**, 203 (1980)
[20] A D Martin, Durham Report, DTP/93/66 (1993)
[21] J Bartels and H Lotter, DESY Report, DESY 93–027 (1973)
[22] L Pauling and E B Wilson, in *Introduction of quantum mechanics* (McGraw Hill, Tokyo, 1935) p. 180
[23] D Griffiths, in *Introduction to elementary particles* (John Wiley, New York, 1987) p. 151
[24] F Halzen and A D Martin, in *Quarks and Leptons* (John Wiley, New York, 1984) p. 65
[25] D P Stanley and D Robson, *Phys. Rev.* **D21**, 3180 (1980); **26**, 223 (1982)
[26] S Flugge, in *Practical quantum mechanics* (Springer-Verlag, New York, Heidelberg, Berlin, 1974)
[27] C R Ji and F Amiri, *Phys. Rev.* **D42**, 3764 (1990)
[28] M Cornwall, *Phys. Rev.* **D26**, 1453 (1982)
[29] V Khoze, in *XIV Int. Conf. on HEP*, Munich Aug. (1988)
[30] S J Brodsky and G P Lepage, SLAC-PUB-2294 (1979)
[31] N Isgur and C H Llewellyn Smith, *Phys. Lett.* **B217**, 535 (1989); CERN-TH 5013/88
[32] S R Amendolia *et al*, *Phys. Lett.* **B146**, 116 (1984); *Nucl. Phys.* **B277**, 168 (1986)
[33] S R Amendolia *et al*, *Phys. Lett.* **B178**, 435 (1986)
[34] V O Galkin, A Yu Mishrurov and R P Fauslav, *Sov. J. Nucl. Phys.* **53**, 1026 (1991)
[35] Z Dziembowski, *Phys. Rev.* **D37**, 2030 (1988) and references therein
[36] C R Ji and S R Cotanch, *Phys. Rev.* **D41**, 2319 (1990)
[37] H Albrecht *et al*, DESY report, DESY 91–121 (1991)
[38] D Silverman and H Yao, *Phys. Rev.* **D38**, 214 (1988)
[39] H J Munczek and P Jain, *Phys. Rev.* **D46**, 438 (1992)
[40] H Krassemann, *Phys. Lett.* **B96**, 397 (1980); M Suzzuki, *Phys. Lett.* **B162**, 392 (1985)

[41] S N Sinha, *Phys. Lett.* **B178**, 110 (1986)
[42] P Cea *et al*, *Phys. Lett.* **B206**, 691 (1988)
[43] E Golowich, *Phys. Lett.* **B91**, 271 (1980)
[44] V S Mathur and M T Yamazaki, *Phys. Rev.* **D29**, 2057 (1984)
[45] C A Dominguez and N Paver, *Phys. Lett.* **B197**, 423 (1987); *Phys. Lett.* **B199**, 596(E) (1987)
[46] S Narisson, *Phys. Lett.* **B198**, 104 (1987)
[47] M A Shifman, *Sov. Phys. Ups.* **30**, 91 (1987)
[48] M B Gavela *et al*, *Phys. Lett.* **B206**, 113 (1988)
[49] T A DeGrand and R D Loft, *Phys. Rev.* **D38**, 954 (1988)
[50] C Bernard *et al*, *Phys. Rev.* **D38**, 3540 (1988)
[51] R M Woloshyn *et al*, *Phys. Rev.* **D39**, 978 (1989)
[52] C Alexandrou *et al*, *Phys. Lett.* **B256**, 60 (1991)
[53] M Aguilar-Benitez *et al*, *Phys. Rev.* **D45**, 1 (1992)
[54] S Bhatnagar, D S Kulshrestha and A N Mitra, *Phys. Lett.* **B263**, 485 (1991)
[55] M Neubert, *Phys. Rev.* **D45**, 2451 (1992)
[56] C Q Geng and P Turcotte, *Phys. Lett.* **B278**, 330 (1992)
[57] M Neubert, *Phys. Rev.* **D46**, 1076 (1992)
[58] L J Reinders, *Phys. Rev.* **D38**, 947 (1988)
[59] C S Kim, J L Rosner and C P Yuan, *Phys. Rev.* **D42**, 96 (1990)
[60] A Abada *et al*, *Nucl. Phys.* **B376**, 172 (1992)
[61] C Alton *et al*, *Nucl. Phys.* **B349**, 598 (1991)
[62] C J Bebek *et al*, *Phys. Rev.* **D17**, 1693 (1978)
[63] S Dubnicka and L Martinovic, *J. Phys.* **G15** 1349 (1989)

PRAMANA
— journal of
physics

© Printed in India

Vol. 44, No. 6,
June 1995
pp. 535–544

Measurement and analysis of alpha particle induced reactions on gold

D J SHAH, H B PATEL, N L SINGH, S MUKHERJEE* and
S N CHINTALAPUDI**
Physics Department, M. S. University, Baroda 390 002, India
*School of studies in Physics, Vikram University, Ujjain 456 010, India
**IUC-DAEF Calcutta Centre, 3/LB-8 Bidhan Nagar, Calcutta 700 091, India

MS received 30 August 1994; revised 20 February 1995

Abstract. Stacked foil activation technique and Ge(Li) gamma ray spectroscopy have been used for the measurement of excitation functions of ^{197}Au(α, xn) $(x = 1-3)$, ^{197}Au$(\alpha, 2pn)$ and ^{197}Au$(\alpha, \alpha n)$ reactions up to 50 MeV. The experimental cross-sections were compared with the predictions of pre-equilibrium hybrid model, as well as with the more recent index model. A general agreement was found in all reactions using initial exciton number $n_0 = 4(4p0h)$ except for ^{197}Au(α, n) reaction, where index model gives fairly good agreement with $n_0 = 5(5p0h)$.

Keywords. Nuclear reactions; ^{197}Au$(\alpha, xnypz\alpha)$; stacked foil activation technique; $E_\alpha \leqslant 50$ MeV; hybrid and index models.

PACS No. 25·60

1. Introduction

Statistical model code which combine precompound and compound decay channels has proven to be successful in a wide range of projectile energies. Most of these models are semiclassical and have been used with considerable success in describing experimental data pertaining to the equilibration process, mainly the forward peaked hard component observed in the continuous spectra of light ejectiles and the high energy tail seen in the excitation functions. Apart from these semi-classical models [1–10], work is in progress to give a full quantum mechanical picture in the framework of multistep direct and multistep compound nucleus theories proposed by Feshbach *et al* [11] and others [12–15]. Quantum mechanical theories are not applied to routinely measurable pre-equilibrium cross-sections but they support the foundations on which the classical models are built. As a result, a number of formulations, the hybrid model of Blann [4], the exciton model of Gadioli *et al* [5], index model of Ernst *et al* [10] and many other models [16, 17] have emerged as descendents to Griffin's statistical model of intermediate structure. All these models have the common feature that they group the many body states of equilibrating system according to the exciton numbers and particle-hole densities to estimate the occurrence of configuration capable of pre-compound particle emission. There are some conceptual differences between the hybrid and exciton models. The long-standing controversy on the basic viewpoints was resolved by Bisplinghoff [18] on the basis of configuration mixing and reported different physics and approximations. In the hybrid model no intrinsic configuration mixing is assumed while full configuration mixing is inherent in the exciton model. On the other hand Ernst *et al* [10] proposed a model of independently interacting excitons, known as index model in which it is shown that each generation in the framework of exciton model predicts the exclusive emission spectra which can easily be converted into residual nucleus population probabilities. It is shown that three stages are sufficient to describe the single and multinucleon emissions to all the orders of practical importance.

Two of the many models discussed above received greater attention because of their simplicity and transparency and have been improved over the years by their proponents. These are hybrid [4] and index models [10]. In both these model codes, at the end of the precompound stages, the equilibrated compound nucleus is calculated using the Weisskopf–Ewing formalism [19] and added incoherently to the pre-equilibrium contributions, so that the theoretical excitation function can be directly compared with the experimental ones.

Indeed large experimental data are available in literature [20–23] for alpha induced reactions on gold mostly using Ge(Li) detectors but there are large discrepancies in the cross-section values for the same reaction. In this context the present investigation was undertaken with two aims. (1) To improve the quality of existing data. (2) To compare the experimental results so obtained with the theoretical predictions based on the up-dated hybrid as well as index models.

2. Experimental procedures

Excitation functions for the reaction residues ^{200}Tl, ^{199}Tl, ^{198}Tl, ^{198}Au and ^{196}Au in the alpha particle induced reaction on ^{197}Au, were measured using stacked foil activation technique and Ge(Li) gamma ray spectroscopy (2·0 keV FWHM for 1332 keV photons of ^{60}Co). Spectroscopically-pure gold foils of purity greater than 99·99% and thickness 24 mg/cm^2 have been used as target in the stacks together with aluminium degraders of varying thicknesses to reduce the beam energy to desired levels. Two independent irradiations were carried out at the VECC Calcutta, India using 40 MeV and 50 MeV alpha particles respectively. Copper foils of thicknesses 23 mg/cm^2 and 8·9 mg/cm^2 were used as flux monitor [24]. The average beam energy incident upon a given foil, degrader and monitor was calculated from the stopping power tables of Williamson *et al* [25]. The beam is totally stopped in the electrically insulated foil stack which is itself serving as a Faraday-cup. The beam currents on the targets were kept of the order of 250 nA. The residual nuclei were identified using their characteristic gamma rays as

Table 1. Nuclear data used for the identification of residual nuclei [26].

Reaction	Q-value (MeV)	Half life $T_{1/2}$	Gamma ray energy E_γ(keV)	% Abundance (θ_γ)
^{197}Au$(\alpha, n)^{200}$Tl	− 9·73	26·1 h	368	88·0 ± 0·9
^{197}Au$(\alpha, 2n)^{199}$Tl	− 17·80	7·42 h	455	12·0 ± 0·6
^{197}Au$(\alpha, 3n)^{198}$Tl	− 25·87	5·3 h	676	10·4 ± 0·7
^{197}Au$(\alpha, 2pn)^{198}$Au	− 23·78	2·69 d	412	95·5 ± 1·8
^{197}Au$(\alpha, \alpha n)^{196}$Au	− 8·00	6·15 d	356	87·0 ± 1·1
Monitor reaction				
^{65}Cu$(\alpha, 2n)^{67}$Ga	− 14·1	78·26 h	300	19·03 ± 1·39

mentioned in table 1 [26]. The energy and efficiency calibration of the detector were performed with a calibrated ^{152}Eu multigamma source obtained from the Radio-Chemistry Division at VECC, Calcutta. The formula used for the determination of cross-section is given in our earlier papers [27, 28]

$$\sigma = \frac{A_\gamma A_{\text{gm}} \lambda}{\Phi \theta_\gamma p_\gamma w_i p_i N_{\text{av.}} (1 - e^{-\lambda t_i}) e^{-\lambda t_w} (1 - e^{-\lambda t_c})}$$

where, σ is the cross-secion, A_γ is the photo peak area of the characteristic gamma ray of the residual nucleus, A_{gm} is the gram atomic weight of the target element, λ is the disintegration constant of the residual nucleus, Φ is the flux of the incident particle, w_i is the weight per unit area of the target foil in g/cm^2, p_i is the fractional abundance by weight of the target isotope of interest, θ_γ is the fractional abundance of characteristic gamma rays emitted per decay of the residual nucleus, p_γ is the photopeak efficiency of the gamma ray, t_i, t_w and t_c are the periods of irradiation, waiting and counting respectively.

3. Results and discussion

The measured cross-section of the reactions ^{197}Au$(\alpha, xn)^{201-x}$Tl$(x = 1-3)$, ^{197}Au$(\alpha, 2pn)^{198}$Au and ^{197}Au$(\alpha, \alpha n)^{196}$Au have been listed in table 2. The total error in the experimental cross-section is contributed by photo peak area (1–4%), detector efficiency (3–4%), uniformity of the foil thickness (1–2%), spectroscopic data (1–7%) and standard deviation (10%) of the monitor cross-section from which the flux is deduced. The relative errors which affect the shape of the excitation function is about 6%, the absolute errors on the magnitude of the cross-section is thus less than 13% in the present measurement.

Five reactions studied in gold are compared with previous measurements [20–23] as shown in figures 1–5. Lanzafame and Blann [20] used both NaI crystal and Ge(Li)

Table 2. Cross-section of the alpha-induced reaction on ^{197}Au.

E_α(MeV)	σ(mb)	σ(mb)	σ(mb)	σ(mb)	σ(mb)
Target nucleus	^{197}Au	^{197}Au	^{197}Au	^{197}Au	^{197}Au
Reaction	(α, n)	$(\alpha, 2n)$	$(\alpha, 3n)$	$(\alpha, 2pn)$	$(\alpha, \alpha n)$
Product nucleus	^{200}Tl	^{199}Tl	^{198}Tl	^{198}Au	^{196}Au
19·5	13·2 ± 1·5	44·8 ± 5·41			
20·9	19·5 ± 2·22	110·0 ± 13·28			
24·7	15·8 ± 1·8	332·0 ± 40·10			
27·0	12·3 ± 1·4	580·0 ± 70·06			
31·9	6·8 ± 0·77	310·0 ± 37·74	380·0 ± 47·42		4·18 ± 0·46
32·2	6·1 ± 0·69	297·0 ± 35·87	470·0 ± 58·65		5·33 ± 0·59
37·8	4·4 ± 0·5	125·0 ± 15·10	1110·0 ± 138·52	1·25 ± 0·15	16·20 ± 1·81
38·0	4·2 ± 0·47	110·0 ± 13·28	1050·0 ± 131·04	1·30 ± 0·15	17·40 ± 1·94
42·8	3·3 ± 0·37	82·4 ± 9·95	760·0 ± 94·84	2·10 ± 0·25	34·20 ± 3·83
47·2	2·9 ± 0·33	53·7 ± 6·48	315·0 ± 39·31	3·40 ± 0·40	43·50 ± 4·87

detector for measurement of gamma activities and the reported uncertainty in their measurement was quoted as 20%. Kurz *et al* [21] studied reactions up to 43 MeV, employing a small volume (7 cc) Ge(Li) detector with a resolution of 4·2 keV for the 1332 keV photons of ^{60}Co. The experimental errors in the cross-section were mentioned as less than 10%, but it is not mentioned whether or not this includes the uncertainty in the monitor cross-section used for flux measurement as well as the errors in spectroscopic data. Whereas excluding the above mentioned errors the uncertainty in the present measurement becomes about 6%. Capurro *et al* [22] measured the reactions up to 55 MeV using an intrinsic Ge-detector. The overall error in their measurement varied in the range 24 to 37%. Bhardwaj *et al* [23] measured the reactions up to 40 MeV using HPGe detector. The reported values of Capurro *et al* and Bhardwaj *et al* differ by more than 50% around 30 MeV and the deviation is larger at higher energies.

4. Pre-equilibrium model predictions

The basic concepts of pre-equilibrium theory rest on the intranuclear cascade (INC) model of Goldberger [29] and Metropolies *et al* [30] and the statistical model of intermediate structure (SMIS) of Griffin [1]. Much effort has been devoted to combining both into a single one capable of calculating absolute pre-equilibrium emission cross-sections. In hybrid model [4] the pre-equilibrium emission spectra are given by simple closed formed expressions. However, the index model [10] involves more complex recursion relations. The index model, which is an acronym for *ind*ependently interacting *ex*citon model, has a somewhat different philosophy than the hybrid model. Both the models constitute significantly different approaches and yield different results for the pre-equilibrium emission but still they are built on the same basic assumption concerning the physics of the reaction.

The principal idea incorporated in the index model is nearly the same as in the hybrid model. The deexcitation cascade followed by individual excitons is independent of each other. However, the corresponding use of single particle state lifetimes implies a different statistical treatment for the higher stages of the nuclear equilibration than in the hybrid model. As far as particle emission is neglected, the internal collisions of all excitons of the initial configuration $n_0(p_0, h_0)$ lead to $n_1 = 3n_0$ excitons in the next stage, since each decaying exciton at a particular excitation energy loses part of its energy to create an additional particle-hole pair. The particle and hole number becomes $p_1 = 2p_0 + h_0$ and $h_1 = p_0 + 2h_0$. Due to this multiplicative proliferation factor three, instead of the additive constant two in the hybrid model, the number of excitons quickly increases from stage to stage so that two or three stages suffice to yield the total pre-equilibrium cross-section. The particle and hole densities of subsequent stages are derived from preceding stages using recursion relations.

The observed excitation functions show a high energy tail following the usual compound nucleus bump at low energy. The calculation starts with an initial number of excitons, i.e. particles above and holes below the fermi level, induced by the primary interaction and proceeds to states with an increasing exciton number. For each of these states the emission probability for the particles is calculated and finally the integrated spectra yield the cross- sections for the individual reactions. The statistical part of the codes (Overlaid Alice) can account for a large variety of reaction types. Besides evaporation of neutrons and protons [19] also clusters such as deuteron and alpha particles can be considered.

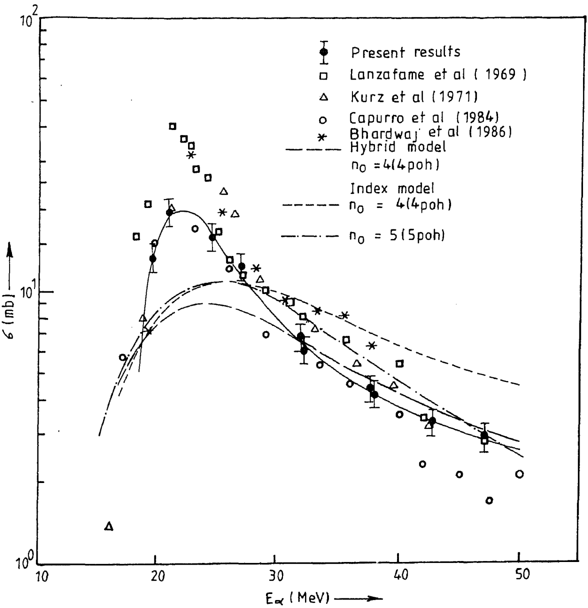

Figure 1. Excitation function of ^{197}Au$(\alpha, n)^{200}$Tl reaction.

A short description of the option chosen is given below. The nuclear masses were calculated from the Myers–Swiatecki mass formula [31] considering liquid drop with shell correction term without pairing, i.e. the level density pairing shift absorbed in binding energies. The inverse cross-sections were calculated by an optical model subroutine included in the code, where the optical model parameters were those of Becchetti and Greenless [32]. The fermi level density used is of the form

$$\rho(u) \propto (u-\delta)^{-5/4} \exp[2\sqrt{a(u-\delta)}]$$

where u is residual nucleus excitation, a is the level density parameter taken as A/8 MeV^{-1} which is the default option of the code and $\delta = 11/\sqrt{A}$ MeV the pairing energy shift.

In the *a priori* formulation of the hybrid and index models, the intra-nuclear transition rates are calculated either from the imaginary part of the optical model or from the free nucleon-nucleon scattering cross-section [33]. The use of optical potential in calculating intra-nuclear transition rates for pre-equilibrium decay models offers distinct advantages at least in principle over the nucleon-nucleon scattering approach.

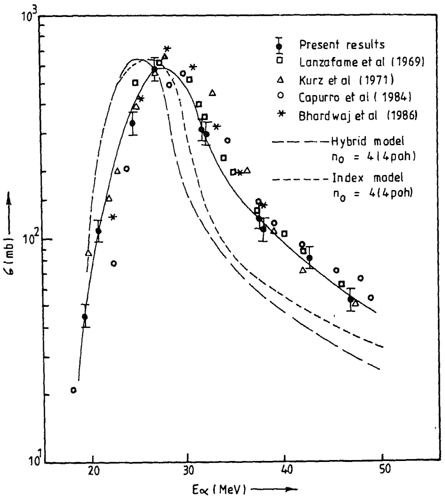

Figure 2. Excitation function of $^{197}Au(\alpha, 2n)^{199}Tl$ reaction.

Specifically, the parameters of the optical potential have been determined from the results and trends of a large body of experimental data. The mean free path values are therefore based on experimental measurements in nuclear matter as opposed to the extrapolation of free scattering cross-sections to the nuclear environment. Secondly the question of possible errors in nucleon-nucleon scattering approach due to inability to consider recoil momentum effects are avoided by using the optical potential. Becchetti and Greenless [32] have analysed large amount of data to find a best set of optical model parameters for nucleon induced reactions. But for particle energies exceeding 55 MeV the optical model parameters of Becchetti and Greenless are no longer applicable and thus at higher energies the calculation of the mean free path for intra-nuclear transitions is done from nucleon-nucleon scattering cross-sections.

The mean free path multiplier K which is a kind of free parameter introduced by Blann [34] to account for the transparency of nuclear matter in the lower density nucleus periphery was kept as unity.

The initial exciton number $n_0(p_0 h_0)$ plays an important role because it governs the entire cascading process of the binary collisions and thereby influences the shape of the hard component in the particle spectra. A good guess would be the number of nucleons in the projectile or an additional particle/hole or both [10, 27, 28, 35]. This view is quite consistent with the basic physics of the pre-equilibrium decay that only a small number of degrees of freedom is initially excited in nuclear reactions at moderate energies. So, we have made the theoretical calculations using $n_0 = 4(4p0h)$, $n_0 = 5(5p0h)$ and

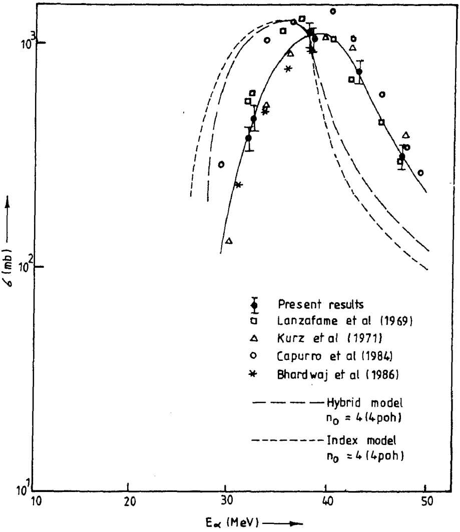

Figure 3. Excitation function of $^{197}Au(\alpha, 3n)^{198}Tl$ reaction.

$n_0 = 6(5p1h)$ as initial configurations. In view of this, a set of six theoretical excitation functions is calculated for each reaction using the three values of n_0, in the framework of two models. All these are tested against the experimentally measured excitation function to pick out the best out of them and to draw inferences based on these comparisons individually for each reaction at first. In general, it was found that $n_0 = 4(4p0h)$ gives by far the best results for both models. The prediction of the $n_0 = 5(5p0h)$ and $n_0 = 6(5p1h)$ configurations were lower than those obtained with $n_0 = 4(4p0h)$.

Figures 1–3 and 5 show a comparison of the present experimental results with hybrid and index models predictions. The lines (i.e. solid, broken and dashed lines) are drawn only to guide the eye. It can be seen from figure 1 that Au(α, n) reaction is fairly well reproduced by hybrid model, whereas index model makes an overestimation by a factor of two using $n_0 = 4(4p0h)$ in the high energy region (30–50 MeV) where the pre-equilibrium effect is predominant. It is observed that the index model gives fairly good account of high energy region with initial exciton configuration $n_0 = 5(5p0h)$, but both the models failed to account the compound nucleus part. The excitation functions of reactions Au$(\alpha, 2n)$ and Au$(\alpha, 3n)$ are shown in figures 2 and 3. It can be seen that the theoretical shape of excitation function using initial exciton configuration $n_0 = 4(4p0h)$ agrees well with the experimental shape of excitation function, there is a systematic underestimation by about 30 to 40% of the experimental cross-sections at high energy region.

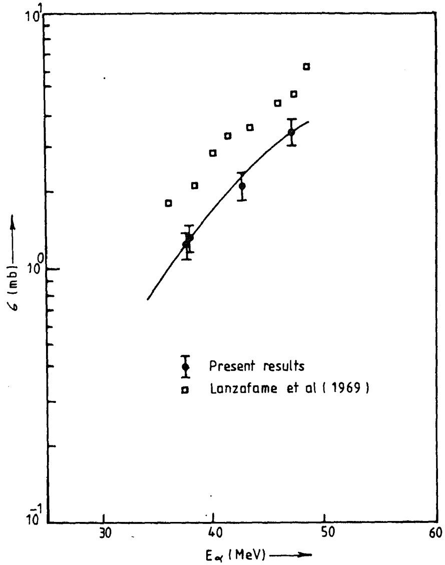

Figure 4. Excitation function of ^{197}Au(α, 2pn)^{198}Au reaction.

It is well-known that value of a shows local variations, particularly in the vicinity of magic numbers, thereby affecting the compound nucleus part of the cross-section dominating at lower energies. Consequently, the maximum in the experimental excitation function occurring due to the compound nucleus is matched with theoretical Weisskopf–Ewing estimate by adjusting the value of the level density parameter approximately. We varied level density a as A/7, A/8, A/9, A/10, A/11 and A/12 MeV^{-1} to reproduce the compound nucleus peaks respectively after fixing the initial exciton configuration n_0. However, all the six values of level density parameter are not able to match the experimental compound nucleus peak of excitation function (figure 1). The variation is only about 10%. Based on these considerations, the value of the level density parameter a for theoretical calculations was chosen as the global parameter A/8 MeV^{-1}.

As far as ^{197}Au(α, 2pn) reaction is concerned, (figure 4) the observed experimental cross-sections between 30 and 50 MeV cannot be accounted for either by equilibrium or pre-equilibrium mechanisms using hybrid and index models.

Figure 5 shows the excitation function of the ^{179}Au(α, αn) reaction. There is a radical difference in the shape of theoretical and experimental excitation functions, as well as severe underestimation of the theory by two orders of magnitude. This is of course not very surprising because, neither the hybrid model nor the index model, is designed to

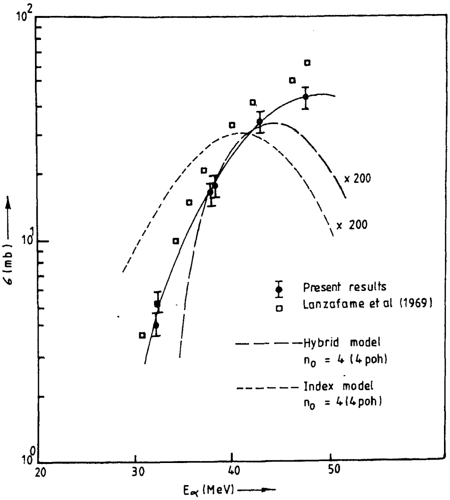

Figure 5. Excitation function of ^{197}Au($\alpha, \alpha n$)^{196}Au reaction.

deal with alpha particle emission in the pre-equilibrium phase, which is quite likely at moderate energies.

Further, as seen in the figures there is a slight shift in the energy between the theoretical and experimental compound nucleus peak. Generally such shifts are ascribed due to the complete neglect of angular momentum effects in the Weisskopf–Ewing theoretical calculations provided in the codes. More elaborate computations, using Hauser–Feshbach theory [36] may bring about a better agreement.

5. Conclusion

From the present study of the excitation functions for ^{197}Au($\alpha, xnypz\alpha$) reactions, it is concluded that there is a qualitative agreement between our experimental results and the theoretical ones. In the observed high-energy tail of the excitation functions of the (α, xn) reactions, there are the veritable signatures of pre-equilibrium decay, irrespective of any model or theory. The basic tenet that only a small number of degrees of freedom is excited in pre-equilibrium reactions is amply borne out by the satisfactory agreement observed between the experimental results and the pre-equilibrium hybrid and index models predictions for an initial exciton number $n_0 = 4(4p0h)$ except for (α, n) reaction whereas index model with exciton number $n_0 = 5(5p0h)$ gives fairly good agreement. Comparatively speaking, the former model is better than the latter.

It can be seen from figures that there is a clear shift in energy between theoretical and experimental compound nucleus peaks. Generally such shifts are ascribed to the complete neglect of angular momentum effects in the Weisskopf–Ewing theoretical calculations of the compound nucleus contribution.

Acknowledgements

The authors are thankful to the entire staff of IUC-DAEF, Calcutta Centre and VECC Calcutta for their co-operation in the present investigation. They also wish to thank Prof. J Rama Rao and Prof. D R S Somayajulu for stimulating discussions. This work is supported by University Grants Commission, New Delhi.

References

[1] J J Griffin, *Phys. Rev. Lett.* **17**, 478 (1966)
[2] G D Harp, J M Miller and B J Berne, *Phys. Rev.* **165**, 1166 (1968)
[3] M Blann, *Ann. Rev. Nucl. Sci.* **25**, 123 (1975)
[4] M Blann and H K Vonach, *Phys. Rev.* **C28**, 1475 (1983)
M Blann code ALICE/85/300, UCID-20169 (1984)
[5] E Gadioli, E Gadioli-Erba and P G Sona, *Nucl. Phys.* **A217**, 589 (1973)
[6] J Ernst and J Rama Rao, *Z. Phys.* **A281**, 129 (1977)
[7] G Mantzouranis, D Agassi and H A Weidenmueller, *Z. Phys.* **A27**, 145 (1976)
[8] H Machner, *Phys. Lett.* **B86**, 129 (1979)
[9] J M Akkermans, H Gruppelaar and G Reffo, *Phys. Rev.* **C22**, 73 (1980)
[10] J Ernst, W Friedland and H Stockhorst, *Z. Phys.* **A328**, 333 (1987); **A333**, 45 (1989)
[11] H Feshbach, A Kerman and S Koonin, *Ann. Phys.* **125**, 429 (1980)
[12] D Agassi, H A Weidenmueller and G Mantzouranis, *Phys. Rev.* **22**, 145 (1975)
[13] T Tamura, T Udagawa, D H Feng and K K Kan, *Phys. Lett.* **B68**, 109 (1977)
[14] L Avaldi, R Bonetti and L Colli Milazzo, *Phys. Lett.* **B94**, 463 (1980)
[15] G M Field, R Bonetti and P E Hodgson, *J. Phys.* **G12**, 93 (1986)
[16] C K Cline, *Nucl. Phys.* **A210**, 590 (1973)
[17] E Betak and J Dobes, *Z. Phys.* **A279**, 319 (1976)
[18] J Bisplinghoff, *Phys. Rev.* **C33**, 1569 (1986)
[19] V F Weisskopf and D H Ewing, *Phys. Rev.* **57**, 472 (1940)
[20] F M Lanzafame and M Blann, *Nucl. Phys.* **A142**, 545 (1970)
[21] H E Kurz, E W Jasper, K Fischer and F Hermes, *Nucl. Phys.* **A168**, 129 (1971)
[22] O A Capurro, M de la Vega Vedoya, C Wasilevsky and S J Nassiff, *J. Radioanal. Nucl. Chem.* **89/2**, 519 (1985)
[23] H D Bhardwaj and R Prasad, *Nucl. Instrum. Methods* **A242**, 286 (1986)
[24] H P Graf and H Muenzel, *J. Inorg. Nucl. Chem.* **36**, 3647 (1974)
[25] C E Williamson, J P Boujot and J Picard, *CENS Report*, CEA-R 3042 (1966)
[26] C M Lederer and V S Shirley, *Table of isotopes*, 7th edn. (John Wiley, New York, 1978)
[27] N L Singh, S Agarwal and J Rama Rao, *Can. J. Phys.* **71**, 115 (1993)
[28] N L Singh, B J Patel, D R S Somayajulu and S N Chintalapudi, *Pramana – J. Phys.* **42**, 349 (1994)
[29] M L Goldberger, *Phys. Rev.* **74**, 1269 (1948)
[30] N Metropolis, R Bivins, M Storm, A Turkevich, J M Miller and G Friedlander, *Phys. Rev.* **110**, 185, 204 (1958)
[31] W D Myers and W J Swiatecki, *Nucl Phys.* **81**, 1 (1966)
[32] F D Becchetti and F W Greenless, *Phys. Rev.* **182**, 1190 (1969)
[33] M Blann, *Nucl. Phys.* **A213**, 570 (1973)
[34] M Blann, *Phys. Lett.* **27**, 337 (1971)
[35] M Blann and T T Komoto, *Phys. Rev.* **C29**, 1678 (1984)
[36] W Hauser and H Feshbach, *Phys. Rev.* **87**, 366 (1952)

PRAMANA
— journal of
physics

© Printed in India

Vol. 44, No. 6,
June 1995
pp. 545–553

Elastic scattering of 81 keV γ rays by aluminium, nickel, tantalum, gold and lead

G BASAVARAJU[1], P P KANE[1], LYNN KISSEL[2,*] and R H PRATT[2]
[1] Department of Physics, Indian Institute of Technology, Powai, Bombay 400 076, India
[2] Department of Physics and Astronomy, University of Pittsburgh, Pittsburgh, PA 15260, USA
*Permanent address: Computational Physics Group, Lawrence Livermore National Laboratory, Livermore, CA 94550, USA

MS received 5 December 1994; revised 18 March 1995

Abstract. A recently reported study [*Phys. Rev.* **A49**, 3664 (1994)] of elastic scattering of 81 keV γ rays in the angular range from 60° to 133° has been extended to smaller and larger angles. Previously reported S matrix calculations of atomic Rayleigh scattering have been shown to require a subtraction of contributions from spurious resonances. Most of the experimental data are in agreement with the calculations. Calculations (MF + ASF) based on a combination of relativistic modified form factors (MF's) and angle independent anomalous scattering factors (ASF's) are found to be inadequate for an explanation of experimental cross-sections in the case of high Z elements at angles larger than about 120°.

Keywords. Germanium detector; anomalous scattering; S matrix.

PACS No. 32·80

1. Introduction

Recently, a study of elastic scattering of 81 keV γ rays has been reported [1] in the angular range from 60° to 133°. The experimental results were found to be in reasonable agreement with the then reported relativistic second order S matrix calculations of atomic Rayleigh scattering, but, at large angles in the case of high Z elements, were in poorer agreement with (MF + ASF) calculations based on a combination of relativistic modified factors (MF's) and angle independent anomalous scattering factors (ASF's). As expected for photon energies close to or less than target K shell binding energies, ε_K, a simple treatment based on only MF's was shown to fail in the case of gold and lead with ε_K values of 80·723 and 88·006 keV, respectively.

The experimental cross-sections at 133° in the case of tantalum and gold, and at 120° and 133° in the case of lead were found to be significantly smaller than (MF + ASF) calculations. The present studies at 145° confirm the same trend at a larger angle. The cross-sections for the elastic scattering of 81 keV γ rays increase rapidly below about 90° with decreasing angle θ, whereas the cross-sections for the production of $K\beta'_2$ X-rays are independent of angle. Thus, in the case of gold with $K\beta'_2$ X-rays having energies from about 80·08 to 80·72 keV, the determination of the 81 keV elastic scattering counts from a composite pulse height distribution in the 80 to 81 keV range was expected to become easier at smaller angles of scattering. On the other hand, on account of decreasing Compton shifts, a separation of the elastic and the broad Compton peaks becomes increasingly more difficult as θ decreases. An angle of 45° was found to be optimal from these considerations.

Previously reported S matrix calculations were shown to require a subtraction of contributions from "spurious" resonances, which are particularly significant when the photon energy is close to an inner shell threshold. These features and the new calculations are described in § 2. Important details relevant to the new measurements are mentioned in § 3. The experimental and theoretical results at six angles from 45° to 145°, including some of the earlier ones, are presented in § 4.

2. Theoretical calculations

The elastic scattering cross-sections have been calculated for isolated atoms, since solid state environment effects are not expected to be significant for values of the momentum transfer parameter $x[= \sin(\theta/2)/\lambda(\text{Å})]$ larger than about 2·5 relevant for the present study. The relativistic calculations have been performed in the independent particle approximation for bound electrons. The scattering amplitude for each atomic electron is evaluated separately and is summed so as to obtain the atomic Rayleigh amplitude. In the second order S matrix treatment, the contribution of each electron involves a sum over a complete set of intermediate states (bound and continuum) of the single particle Hamiltonian. As pointed out in [2], transitions to intermediate bound states correspond to resonances in the individual electron amplitude. The resonant contribution from an electron in a bound state (a) involving an intermediate occupied state (b) is cancelled by the resonance in the amplitude for scattering from an electron in state (b) involving the intermediate state (a). These cancelling resonances are called "spurious" resonances. The scattering amplitude of an electron is small below the resonance regime and is proportional to the square of the photon energy in the low energy limit. When the photon energy is larger than the photoionization threshold associated with a given electron, the scattering amplitude for that electron is close to r_0 in the forward direction but generally becomes small for scattering vectors [= (momentum transfers)/$\hbar$] large compared to the inverse of the radius of the orbital. Here, r_0 is e^2/mc^2, e is the electron charge, m is the mass of an electron, c is the speed of light and $h[= 2\pi\hbar]$ is Planck's constant. Note that the amplitude is not small in the vicinity of a real or a spurious resonance.

The scattering amplitude at a given finite angle due to weakly bound outer electrons generally drops rapidly with increasing photon energy, hν. Thus approximate estimates of outer electron contributions are adequate and are frequently obtained in the relativistic modified form factor (MF) approximation, whereas it is necessary to treat inner electron shells by S matrix methods. Such a procedure was adopted in many earlier calculations [e.g. 1, 2].

However, the (MF) approximation omits spurious resonances and hence does not provide the proper cancellation with the spurious resonances of the S matrix calculation for the inner shells. The resulting errors become particularly significant when the photon energy is close to an inner shell threshold. Under these circumstances, it is better to first subtract the spurious resonances in the inner shell contributions and to ensure that the amplitude for each shell is finite except for real observable resonances at transitions into unfilled shells. The bound-bound resonant term in each amplitude is calculated with the help of the formulae given in § 2.1 of ref. [2]. Further, as described in ref. [1], it is necessary to adopt a photon energy shifting procedure near an inner shell threshold in order to correctly position the anomalous scattering regime with a rapidly varying amplitude. As in ref. [1], the inner subshells with binding energies larger than hν/300 were treated by S matrix methods and the (MF) approximation was used for the outer shells.

Table 1. Cross-sections for elastic scattering of 81 keV γ rays in $10^{-24}\mathrm{cm}^2/\mathrm{sr}$. The theoretical values are obtained by the coherent addition of nuclear Thomson and atomic Rayleigh contributions. The values (MF + ASF) in column 2 have been obtained on the basis of a combination of relativistic modified form factors (MF) and angle independent anomalous scattering factors (ASF). The cross-sections calculated by the relativistic second order S matrix treatment after subtraction of contributions of spurious resonances are given in column 3. The term SR indicates these contributions. The experimental cross-sections σ_{expt} along with errors $\pm\Delta$ appear in column 4. Note that the experimental values marked with a * for angles between 60° and 133° are the same as those in ref. [1]. If σ_s is the calculated S matrix cross-section in column 3 and $\chi_s = (\sigma_{\mathrm{expt}} - \sigma_s)/\Delta$, χ_s^2 is listed in the last column. The average values of χ_s^2 for Al, Ni, Ta, Au and Pb are 0·46, 2·9, 0·09, 0·52 and 1·2, respectively. The average values of similarly defined $(\chi_{\mathrm{MF+ASF}})^2$ are 0·46, 4·2, 1·5, 1·7 and 6·5, respectively.

θ (deg)	Calculated cross section (b/sr)		σ_{expt}(b/sr)	χ_s^2
	(MF + ASF)	S matrix (after SR, subtraction)		
Al				
45	0·0577	0·0573	0·0550 ± 0·0038	0·37
60	0·0241	0·0238	0·0222 ± 0·0026*	0·38
90	0·00510	0·00504	0·00582 ± 0·00070*	1·2
120	0·00237	0·00235	0·00263 ± 0·00033*	0·72
133	0·00206	0·00203	0·00196 ± 0·00030*	0·05
145	0·00190	0·00186	0·00183 ± 0·00033	0·01
Ni				
45	0·409	0·401	0·480 ± 0·034	5·4
60	0·147	0·141	0·125 ± 0·011*	2·1
90	0·0571	0·0544	0·0570 ± 0·0043*	0·37
120	0·0501	0·0477	0·0505 ± 0·0040*	0·49
133	0·0524	0·0495	0·0397 ± 0·0042*	5·4
145	0·0549	0·0514	0·0430 ± 0·0043	3·8
Ta				
45	6·31	6·12	6·05 ± 0·42	0·03
60	2·49	2·35	2·35 ± 0·20*	0·00
90	0·907	0·839	0·843 ± 0·096*	0·00
120	0·836	0·761	0·741 ± 0·082*	0·06
133	0·893	0·799	0·783 ± 0·083*	0·04
145	0·953	0·838	0·788 ± 0·079	0·40
Au				
45	4·15	4·03	4·18 ± 0·46	0·11
60	1·43	1·35	1·26 ± 0·19*	0·22
90	0·445	0·393	0·386 ± 0·058*	0·01
120	0·496	0·423	0·549 ± 0·082*	2·4
133	0·579	0·481	0·461 ± 0·069*	0·08
145	0·663	0·537	0·495 ± 0·074	0·32
Pb				
45	6·74	6·43	6·30 ± 0·44	0·09
60	2·71	2·50	2·21 ± 0·17*	2·9
90	0·588	0·523	0·518 ± 0·045*	0·01
120	0·399	0·349	0·314 ± 0·033*	1·1
133	0·400	0·344	0·304 ± 0·030*	1·8
145	0·409	0·346	0·310 ± 0·031	1·3

But unlike in ref. [1], spurious resonances in inner shell amplitudes were subtracted off. This procedure is efficient in terms of computation time and is also reliable [3].

The differences between cross-sections calculated before and after subtraction of spurious resonances depend on scattering angle and are of the order of 0·1%, 0·2%, 0·6% and 1·5% for Al, Ni, Ta and Pb, respectively. However, the differences are as much as 13% at 60° in the case of gold with the value of ε_K within 275 eV of hν.

The sensitivity of the new calculations to the value of $(h\nu - \varepsilon_K)$ was checked in the case of gold. For $(h\nu - \varepsilon_K)$ of (275 ± 10) eV, the calculated cross-sections differed at most by $\pm 0{\cdot}9\%$. As seen from table 1, the (MF + ASF) results in column 2 are systematically larger than the S matrix values in column 3. The differences between columns 2 and 3 increase with increasing angle of scattering, and at 145° are about 2·2%, 7·0%, 14%, 23% and 18% for Al, Ni, Ta, Au and Pb, respectively.

The (MF) cross-sections have been shown graphically in [1] over an extensive angular range, and are enormously larger than experimental values for gold and lead. For these reasons, these calculations are not listed in table 1.

3. Measurements

A thin ^{133}Ba source of about 20 mCi strength and 0·1 cm diameter provided 81 keV γ rays, a stronger intensity of 356 keV γ rays and weaker intensities of γ rays of 53·2, 79·6, 160·6, 223·1, 276·4 and 383 keV [4]. A cylindrical brass shell of 15·5 cm diameter and 18 cm length contained lead shielding with the source at its centre. The γ rays from the source emerged through a collimator of 0·8 cm diameter and 10 cm length (figure 1). The heavy source assembly was mounted on a robust arm which could be rotated on a graduated base plate B of 45 cm radius about the vertical direction through the target centre. The source assembly could be moved horizontally along guiding rails towards or away from the target and vertically by screw-jacks. The beam line was more than 25 cm above the base plate. The source-target distance was 23 cm and 31 cm for 45° and 145° measurements, respectively. The 2·54 × 2·54 cm targets of better than 99·5% purity were thin enough to ensure with the adopted orientations, a transmission larger than 0·55 for elastically scattered γ rays.

The distance from the target to the centre of the planar high purity germanium (HpGe) detector was fixed at 23 cm. The HpGe detector supplied by EG & G ORTEC had a diameter of 1·6 cm and a thickness of 1·0 cm, and was cooled in a cryostat with a 0·0127 cm thick beryllium entrance window. A cylindrically symmetric brass shell containing tightly packed tungsten carbide powder was used as the shield around the detector. The opening in front of the detector had a diameter of 2 cm. The detector shield was positioned horizontally on a thick brass plate which could be moved vertically by screw-jacks. The different mechanical parts were fabricated in the workshop of the Department of Physics in Indian Institute of Technology, Bombay.

The pulse height spectrum of γ rays of energies near 81 keV scattered by a 0·360 g/cm^2 nickel target is shown in figure 2. Note that the intensity of 79·6 keV γ rays is only about 8·14% of that of 81 keV γ rays [4]. A weak continuum due to higher energy γ rays underlying the 81 keV photopeak was subtracted in order to determine the net 81 keV elastic scattering counts N_{el} which were about 20 per hour at 145° in the case of aluminium and as high as 500 per hour at 45° in the case of nickel, whereas background counts varied from about 20 per hour at 145° to about 45 per hour at 45°. The error in the estimation of the continuum was combined with the statistical error in order to determine the error in N_{el}. The procedures for the determination of elastic

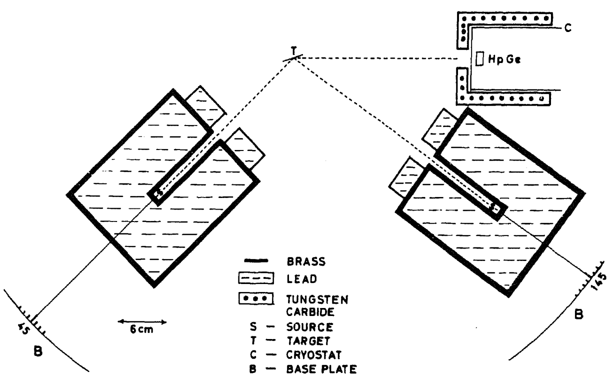

Figure 1. Geometrical arrangement for the scattering experiment (see also § 3). The brass-lead shielding surrounding the source S and the brass-tungsten carbide shielding around the HpGe detector cryostat C are shown. The detector along with its shielding was kept fixed, whereas the distance of the source from the target T was varied from 23 cm for 45° measurements to 31 cm for 145°. The orientation of the target during 45° measurements is shown. But the angle between the incident beam direction and the target plane during 145° measurements was 55° and is not indicated in the interest of clarity of the figure. The source shielding was mounted on a robust arm which could be rotated on the graduated plate B around the vertical direction through the target centre. The height of the beam line above the base plate was larger than 25 cm.

scattering cross-sections have been described in detail [1, 5] but are summarized below in the interest of quick accessibility.

The elastic scattering counts, N_{el}, obtained with a target under study were compared with the Compton scattering counts, N_{Comp}, measured at the same angle with an aluminium target of the same area in order to determine the elastic scattering cross-sections σ_{expt}. This procedure eliminated the need for the determination of the source strength, solid angles, and absolute values of detection efficiency and of target transmissions. The elastic scattering cross-sections were obtained with the help of (1).

$$\frac{N_{\mathrm{el}}}{N^{\mathrm{Al}}_{\mathrm{Comp}}} = \frac{M^t}{M^{\mathrm{Al}}}\frac{A^{\mathrm{Al}}}{A^t}\frac{T_{81}}{T^{\mathrm{Al}}_{\mathrm{Comp}}}\frac{\varepsilon_{81}}{\varepsilon_{\mathrm{Comp}}}[\mathrm{d}\sigma^{\mathrm{Al}}_{\mathrm{Comp}}/\mathrm{d}\Omega]^{-1}\frac{\mathrm{d}\sigma_{\mathrm{el}}}{\mathrm{d}\Omega}, \qquad (1)$$

where M^t and M^{Al} are the masses of the target under study and of aluminium, respectively, A^t and A^{Al} are the atomic weights of the target and of aluminium, T_{81} and $T^{\mathrm{Al}}_{\mathrm{Comp}}$ are the transmissions for 81 keV elastic scattering with the target and for corresponding Compton scattering with aluminium, ε_{81} and $\varepsilon_{\mathrm{Comp}}$ are the photopeak detection efficiencies for 81 keV and for the energy after Compton scattering, and $\mathrm{d}\sigma^{\mathrm{Al}}_{\mathrm{Comp}}/\mathrm{d}\Omega$ is the Compton scattering cross-section of an aluminium atom for 81 keV γ rays. Since the binding energies of electrons in aluminium are much smaller than 81 keV, the last mentioned cross-section is obtained reliably [6] through the use of the

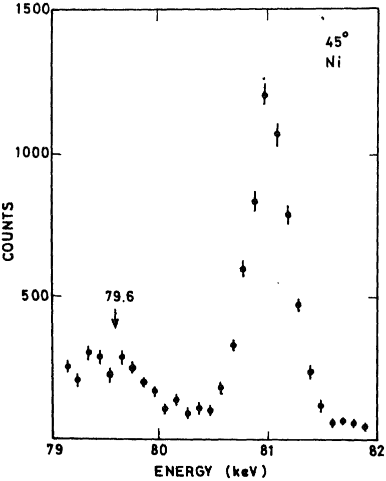

Figure 2. Net counts in the neighbourhood of 81 keV obtained at 45° with a nickel target in 9 h. The small peak corresponding to elastic scattering of the weak 79·6 keV γ ray intensity is indicated by an arrow.

incoherent scattering function $S(x, Z)$, where Z is the atomic number of the scattering atom and x is given by (2).

$$x = \sin(\theta/2)/\lambda(\text{Å}), \tag{2}$$

where θ is the angle of scattering and $\lambda(\text{Å})$ is the wavelength of the incident radiation in Å. In the case of aluminium, we get

$$\frac{d\sigma^{\text{Al}}_{\text{Comp}}}{d\Omega} = \frac{d\sigma^{\text{KN}}}{d\Omega} S(x, Z = 13), \tag{3}$$

where $d\sigma^{\text{KN}}/d\Omega$ is the differential cross-section for Compton scattering by a free and stationary electron according to the well-known Klein–Nishina formula. The shift of the Compton peak from the elastic scattering peak in the pulse height spectrum was used to confirm the scattering angle within about ±0·25°. The Compton peak is broader than the elastic scattering peak on account of finite angular acceptance, ±2° in this experiment, and the momentum distribution of electrons in aluminium. The full width at half maximum of the Compton peak was about 1·7 keV. So a correction for the intensity of the weak 79·6 keV Compton component had to be estimated from the relative emission probability of 8·14%, and from the product of values of $T^{\text{Al}}_{\text{Comp}}$, $\varepsilon_{\text{Comp}}$ and $d\sigma^{\text{Al}}_{\text{Comp}}/d\Omega$ appropriate for 79·6 keV Compton scattering relative to the similarly defined product for 81 keV. The three factors vary slowly with energy and in

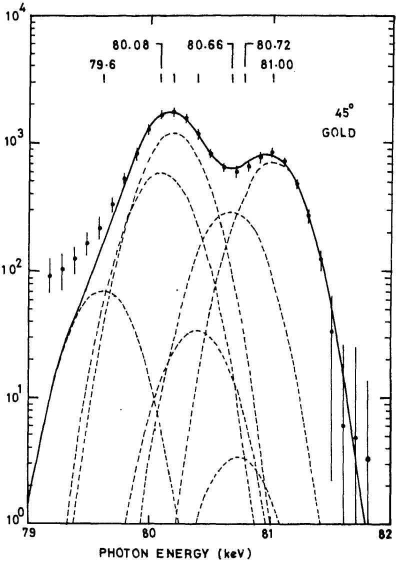

Figure 3. Net counts arising at 45° from gold $K\beta'_2$ X-rays, and elastically scattered 79·6 keV and 81·0 keV γ rays in 40 h. The continuous curve represents the best fit obtained by a least-squares-fitting procedure, the seven dashed curves indicating the corresponding individual contributions as described in § 3. Note the logarithmic scale for counts.

a partially compensating manner. Thus the intensity of the 79·6 keV Compton peak was estimated to be about 8·2% of that in the case of 81 keV Compton scattering and was allowed for in the determination of $N^{\rm Al}_{\rm Comp}$ in (1). The statistical error in $N^{\rm Al}_{\rm Comp}$ was less than 1% but the combined error arising from statistics, and from uncertainties associated with subtraction of the continuum and of the 79·6 keV contribution was conservatively estimated to be ± 5%.

The transmission factors were calculated with the help of attenuation coefficients interpolated between the values tabulated by Storm and Israel [7]. The error in the ratio of T factors for thin targets in reflection geometry turned out to be about ± 1·5%. The relative efficiencies of the HpGe detector in the energy range of interest were measured with the help of relative intensities of $K\alpha_2$, $K\alpha_1$, $K\beta'_1$ and $K\beta'_2$ X-rays obtained separately with tantalum, gold and lead targets. As in [1], the errors in the ratio $\varepsilon_{81}/\varepsilon_{\rm Comp}$ were about ± 3%. The errors in the different ratios in eq. (1) were combined in quadrature in order to determine the errors in $d\sigma_{\rm el}/d\Omega$.

The pulse height data obtained at 45° with the 25·2 mg/cm^2 gold target are displayed in figure 3. The 81 keV elastic scattering cross-section in the case of gold at 45° is about seven times larger than that at backward angles. So at 45°, the 81 keV elastic scattering component is quite visible even in the presence of gold $K\beta'_2$ X-rays of energies between 80·08 and 80·72 keV. The relative transition probabilities for the five main $K\beta'_2$ components turn out to be nearly independent of details of different relativistic theoretical models [8, 9]. So a least-squares-fitting procedure employing the known intensity ratios of the different $K\beta'_2$ components and a common but adjustable pulse height FWHM was used to separate the gold data into seven Gaussians representing contributions from elastic scattering of 81 and 79·6 keV γ rays and gold $K\beta'_2$ X-rays. The fitted individual contributions are indicated by dashed curves. The smooth curve indicating the composite distribution is seen to be in good agreement with experimental data in the energy range of interest above 79·6 keV, the corresponding χ^2 per degree of freedom being 0·7. Note that the fit to experimental data below 79·5 keV is poor on account of the tail of the stronger $K\beta'_1$ X-ray components of lower energy not included in the fitting procedure.

Independent checks of the fitting procedure were also made. For example, a similar analysis of the pulse height data spanning gold $K\alpha_2$ and $K\alpha_1$ X-rays of 66·990 and 68·805 keV, respectively, led to a value of $0{\cdot}585 \pm 0{\cdot}012$ for the intensity ratio of $K\alpha_2$ to $K\alpha_1$ X-rays, which is in agreement with theoretical calculations [8] and previous experiments [10]. Another experiment was performed with 88·03 keV γ rays of a ^{109}Cd source in order to excite only the five gold $K\beta'_2$ X-ray components in the energy range from 79·6 to 81 keV. As expected in this case, only five Gaussians representing the $K\beta'_2$ components were adequate to give excellent fits to the pulse height distributions.

A summary of experimental and theoretical results for cross-sections is presented in table 1. The (MF + ASF) values and S matrix results σ_s obtained with subtraction of spurious resonances are given in columns 2 and 3, respectively. The experimental cross-sections σ_{expt} along with errors $\pm\Delta$ are given in column 4 of table 1. The nature of agreement between σ_{expt} and σ_s is indicated by values of χ_s^2 in column 5, where $\chi_s = (\sigma_{\text{expt}} - \sigma_s)/\Delta$. Average values for the different targets of χ_s^2 and of similarly defined $(\chi_{\text{MF+ASF}})^2$ are given at the end of the caption of table 1.

4. Results

The experimental results for aluminium ($\varepsilon_K = 1{\cdot}56$ keV) are in good agreement with the different calculated values which differ from each other by less than 2·2%. The values of σ_{expt} for nickel at a few angles show unexpected deviations from the (MF + ASF) or the S matrix calculations. There is good agreement between experiment and S matrix calculations in the case of tantalum and of even gold with a value of ε_K within about 275 eV of the γ energy. The experimental cross-sections for lead ($\varepsilon_K = 88{\cdot}006$ keV) are in fair agreement with S matrix calculations. The (MF + ASF) calculations show significant deviations from experiment in high Z cases at large angles. Except in the case of aluminium, the average values of $(\chi_{\text{MF+ASF}})^2$ are larger than unity and are much larger than the corresponding values of χ_s^2, indicating a noticeably poorer agreement of experiment with (MF + ASF) calculations than with calculations based on the S matrix treatment.

Acknowledgement

The work was supported in part by Grant Nos INT-91 02053 and INT-90 19385 of the US National Science Foundation under the Special Foreign Currency programme, also in part by NSF Grant No. Phy-93 07478, and in part under the auspices of the US Department of Energy by Lawrence Livermore National Laboratory under Contract No. W-7405-ENG-48.

References

[1] G Basavaraju, P P Kane, Lynn D Kissel and R H Pratt, *Phys. Rev.* **A49**, 3664 (1994)

[2] P P Kane, Lynn Kissel, R H Pratt and S C Roy, *Phys. Rep.* **140**, 75 (1986)

[3] The reliability has been tested in a study of elastic scattering of 88·03 keV γ rays by lead for which the value of $(h\nu - \varepsilon_K)$ is only (27 ± 7)eV and the resonant contributions are consequently much larger than the ones in the present study. The test was performed as follows. Extending the S matrix treatment by successive stages to (K), $(K+L)$, $(K+L+M)$ and $(K+L+M+N)$ shells, removing at each stage uncancelled spurious resonances and adding (MF) contributions of remaining electrons, the scattering cross-sections for 125° at $(K+L)$ and $(K+L+M)$ stages were found to differ from the final value at the $(K+L+M+N)$ stage by less than 2·4% and 0·6%, respectively. Further, the cross-section calculated by an S matrix treatment of all occupied shells, requiring an enormously longer computation time but automatically ensuring cancellation of spurious resonances, differed by less than 0·2% from that calculated at the above mentioned $(K+L+M+N)$ stage.

[4] C M Lederer and V S Shirley, *Table of Isotopes*, 7th edn. (Wiley, New York, 1978)

[5] G Basavaraju and P P Kane, in *Proceedings of the eighth symposium on radiation measurements and applications* held at Ann Arbor, Michigan, USA, May 16–19, 1994, *Nucl. Instrum. Methods* **A353**, 209 (1994)

[6] J H Hubbell, Wm J Veigele, E A Briggs, R T Brown, D T Cromer and R J Howerton, *J. Phys. Chem. Ref. Data* **4**, 471 (1975); **6**, 615E (1977)

[7] E Storm and H I Israel, *Nucl. Data Tables* **A7**, 565 (1970)

[8] J H Scofield, *At. Data Nucl. Data Tables* **14**, 121 (1974)

[9] J H Scofield, *Phys. Rev.* **A9**, 1041 (1974)

[10] W Bambynek, B Crasemann, R W Fink, H U Freund, H Mark, C D Swift, R E Price and P V Rao, *Rev. Mod. Phys.* **44**, 716 (1972)

[redacted]

PRAMANA
— journal of
physics

© Printed in India

Vol. 44, No. 6,
June 1995
pp. 555–562

Collision cross-sections for scattering of electrons from NO molecule

ARVIND KUMAR JAIN, PRADEEP KUMAR and A N TRIPATHI
Department of Physics, University of Roorkee, Roorkee 247 667, India

MS received 10 November 1994

Abstract. Electron–NO scattering is investigated in the energy range 2–1000 eV by using a parameter-free spherical complex optical potential (SCOP) approach in the fixed nuclei approximation. The real part of the optical potential consists of three potentials namely, the static, the exchange and the polarization. For the imaginary part of the SCOP, we employ a semi-empirical model absorption potential. The molecular charge density function is calculated from a single-configuration molecular orbital based on Slater type orbitals. The various potential terms are then determined from these charge density functions. Calculations of the elastic (with and without absorption effects), total absorption, momentum transfer and differential cross-sections are obtained and compared with the available theoretical results and experimental measurements.

Keywords. Electron; charge density; potential; scattering.

PACS Nos 34·80; 34·90; 52·20

1. Introduction

The electron scattering from NO molecules plays an important role in many applied sciences, for example its role in the catalytic destruction of ozone in atmospheric studies is very well known. There is a paucity of theoretical and experimental electron impact cross-section data for this molecule. The total cross-section measurements on the e–NO system are available due to [1–4]. The experimental elastic e–NO differential cross-sections (DCS) at low energies (5, 10 and 20 eV) were reported by Kubo *et al* [5]. However, recently Brunger *et al* [6] have also reported their experimental DCS at these energies. Electron transmission experiments have observed strong resonance features in the low energy e–NO scattering [7]. The resonance positions and width for e–NO scattering using *R*-matrix method has been calculated by Tennyson and Noble [8]. Very recently Lee *et al* [9] have also investigated the elastic DCS due to low energy electron impact using a Born-closure Schwinger variational method (BCSVM) and its variants.

It is a well known fact that low energy electron molecule scattering is very sensitive to the treatment of short-range correlation (electron exchange and relaxation of bound orbitals due to impinging electron) and long-range polarization effects. In a model potential approach, the non-local nature of exchange and polarization effect is approximated by local forms [10].

Further, it should be noted that for the evaluation of total cross-section (σ_t) the optical potential of the interacting system must be complex; the imaginary part of the complex potential (known as absorption potential) takes into account the flux going into all possible inelastic channels, such as ionization, electronic excitation and dissociation etc. It is because of this reason, the complex optical potential approach has been found very successful for predicting σ_t in the intermediate and high energy region collisions. There are a few *ab initio* techniques (e.g. see [11, 12]) available where electron-molecule problems can be pursued at rigorous level. Nevertheless such methods are very difficult from the computational point of view. It is always desirable to look for simple, local and parameter-free models which yield reliable scattering parameter with respect to experimental or more accurate theoretical results.

In this paper, we calculate the various scattering parameters i.e. DCS, elastic cross-section (σ_{el}), absorption cross-section (σ_{abs}), total (elastic + inelastic) cross-section (σ_t), momentum transfer cross-section (σ_m) and elastic cross-section without absorption effects (σ'_{el}) for electron scattering from NO molecules using a parameter-free spherical complex model potential in the energy range of (2–1000 eV). In the next section we give a brief description of theoretical methodology, while § 3 presents a discussion of the results and concluding remarks.

2. Theoretical methodology

The ground-state electronic configuration of NO is $1\sigma^2 2\sigma^2 3\sigma^2 4\sigma^2 1\pi^2 5\sigma^2 2\pi, X^2\pi$. The SCF molecular wavefunction of NO is taken from the compilation of Cade and Huo [13]. All calculations are performed for the bond lengths fixed as the equilibrium value $R_{\text{N-O}} = 2{\cdot}1747 a_0$. Within the framework of the fixed-nuclei approximation, the interaction of the electron molecule system can be represented by a local optical potential, i.e.

$$V_{\text{opt}}(\mathbf{r}) = V_R(\mathbf{r}) + i V_{\text{abs}}(\mathbf{r}) \tag{1}$$

where V_R, the real part of the total interaction, consists of three spherical local interactions, i.e.

$$V_R(\mathbf{r}) = V_{\text{st}}(\mathbf{r}) + V_{\text{ex}}(\mathbf{r}) + V_{\text{pol}}(\mathbf{r}). \tag{2}$$

Here the static potential (V_{st}) is the average over the ground-state molecular charge distribution of the electrostatic interaction of the electron and molecule. The V_{pol} represents approximately the short-range correlation and long-range polarization effects, while V_{ex} term accounts for electron exchange interaction and V_{abs}, is the absorption potential. All the potential terms (V_{st}, V_{ex}, V_{pol} and V_{abs}) are functions of charge density. In order to generate the target charge density and static potential, we employ a near Hartree–Fock wavefunction in terms of Slater type orbitals as given by Cade and Huo [13] following the VLAM and ALAM codes as given by Schmid *et al* [14] and Morrison [15] respectively. For example, the static potential in terms of legendre projections, v_λ, is given as

$$V_{\text{st}}(\mathrm{r}) = \sum_{\lambda=0}^{\lambda_{\max}} v_\lambda^{\text{st}}(\mathrm{r}) P_\lambda(\cos\theta). \tag{3}$$

We have taken about $\lambda_{\max} = 20$ and 40 for electronic and nuclear contributions, respectively, in the expansion of the static potential. The static potential (V_{st}) is augmented by a parameter-free model of correlation polarization interactions which has a simple dependence of charge density and polarizability (see [16, 17]. For the present calculation, the value of dipole polarizability is taken as 11·47 a.u. [18].

The exchange effect is incorporated through the Hara free electron gas exchange (HFEGE) [19] and modified semi-classical exchange (MSCE) [20]. The V_{abs} in (1) is the absorption potential which represents approximately the combined effect of all the inelastic channels. Here we employ a semi-empirical absorption potential as discussed by Staszewska *et al* [21]. The V_{abs} is the function of molecular charge density, incident electron energy and the mean excitation energy (Δ) of the target. Here we have taken Δ to be the ionization potential (I.P.) of the molecule. After generating the full optical potential eq. (1) of a given electron-molecule system, we treat it exactly in a partial wave analysis following a variable-phase-approach (VPA) (for details see, [10]). The various scattering parameters i.e. DCS, σ_{el}, σ_{abs}, σ_t, σ'_{el}, and σ_m are then easily obtained from the complex S-matrix at each energy.

3. Results and discussion

We have calculated several models with and without absorption potential. They are abbreviated as follows: S, pure static only; SH, S plus HFEGE potential; SHP, SH plus the correlation polarization potential; SE, S plus MSCE potential; SEP, SE plus the correlation polarization potential; and SHPa, SHP plus the absorption potential. Figures 1–4 show our DCS at 20, 30, 100 and 200 eV. In figures 1 and 2 we have shown our DCS in SHPa, SHP and SEP models at 20 and 30 eV, respectively, alongwith the measurements of Brunger *et al* [6] and Kubo *et al* [5]. We have also shown the results of recent calculations of Lee *et al* [9] using both BCSVM and SVIM approaches. It is seen that the present results of both models SEP and SHP yield similar DCS in the

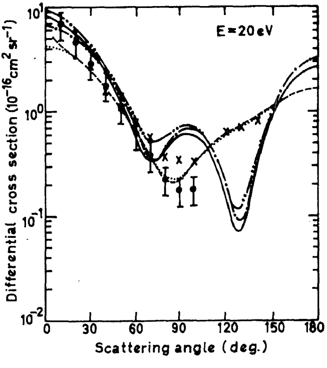

Figure 1. Differential cross-sections for e–NO scattering at 20 eV. Present calculations: ——, SHPa model; —•—, SHP model; —••—, SEP model (for notations see text); – – –, theoretical BCSVM results of Lee *et al* [9]; ......, theoretical SVIM results of Lee *et al* [9]. Experimental data: ⧱, Brunger *et al* [6]; ×, Kubo *et al* [5].

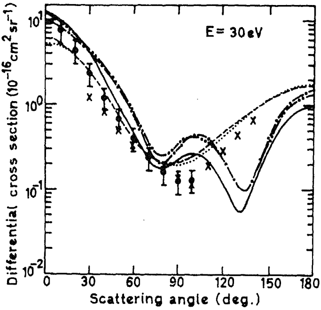

Figure 2. Same legend as in figure 2 except at 30 eV.

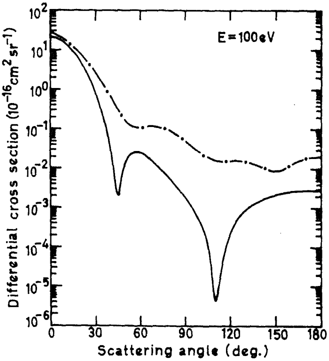

Figure 3. Differential cross-sections for e–NO scattering at 100 eV. Present calculations: ——, SHPa model; —•—, SHP model (for notations see text).

entire angular region, both giving the forward peak ($\theta < 20°$) compared to the *S* model and therefore we have displayed our results only in the SHP model in subsequent figures 3 and 4. Further, we also see that the results in SHPa model exhibit the forward peaking and are similar in shape to the results in SHP model in the entire angular region.

At these energies of 20 eV and 30 eV, the new measurements due to Brunger *et al* [6] are available at smaller scattering angles i.e. in the range of 5° to 100° whereas Kubo *et al*'s are in the range of 30° to 140°. At lower angles $\theta < 40°$, we find a good quantitative

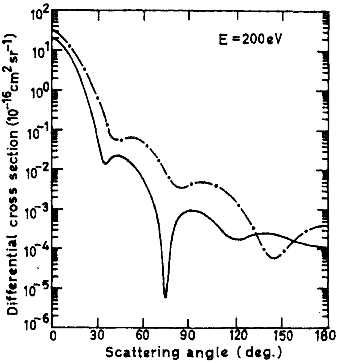

Figure 4. Same legend as in figure 3 except at 200 eV.

agreement between our theory and the data of Brunger *et al* [6]. Further, we see here that the DCS curves in SHPa model compare better with the measured results relative to the corresponding DCS in SHP model. The calculation of Lee *et al* [9] underestimates the cross-section almost by a factor of two at these angles. The disagreement between our results and the calculation of Lee *et al* [9] is probably due to neglect of polarization effects. Tennyson and Noble [8] have also observed that the inclusion of polarization is quite important for low energy elastic scattering for such molecules. Further, the present DCS exhibit dips around 65° and 130° accompanied by a shallow peak at 90° in between the two dips and thereafter, it shows a large backward peaking at large scattering angles, whereas the calculated results of Lee *et al* [9] reproduce the position of dip better compared to the present calculations as observed in the measurements. It is also to be noted that the measurements of Bruger *et al* [6] and Kubo *et al* [5] differ in the magnitude of cross-section values and the position of the dip. These variations in the angular distribution with respect to the experiment and theory narrow down with the increase in the impact energy (see figure 2). In figures 3 and 4, we show our calculated DCS for incident energies 100 and 200 eV only in SHPa and SHP models. At these higher energies, the DCS curves in SHPa model are rich in structure, in particular, the structure of dips and humps, both in magnitude and width, and change significantly relative to the DCS in SHP model. These oscillations show the typical characteristic of electron diffraction in the calculated DCS, a similar feature is also noticed in the recent calculation of Lee *et al* [9].

Finally, in figures 5 and 6, we have plotted our total (σ_t) and momentum transfer cross-sections (σ_m) in SHPa, SHP and SEP models in the energy regime (2–1000 eV) respectively. The results for the corresponding σ_t in this energy region is also compiled in table 1. For comparison, we have also displayed on the curve, the recent available experimental measurements of Szmytkowski and Maciag [4] in the energy region (1–160 eV). The important feature of the experimental result is an oscillatory structure at an incident energy below 2 eV and a broad hump with a maximum close to 16 eV.

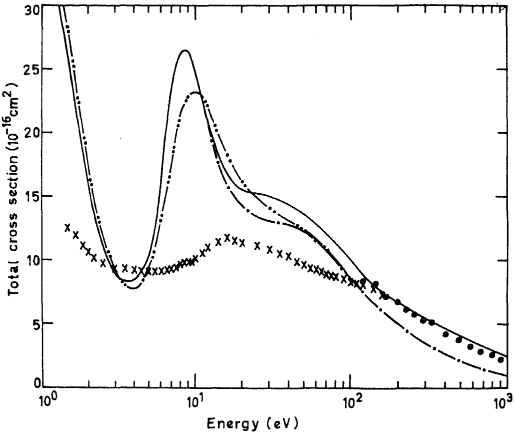

Figure 5. Total cross-sections for e–NO scattering as a function of electron energy, Present calculations: ——, SHPa model; —•—, SHP model; —••—, SEP model (for notations see text); Experimental data: ×, Szmytkowski and Maciag [4]; ●, Dalba *et al* [2].

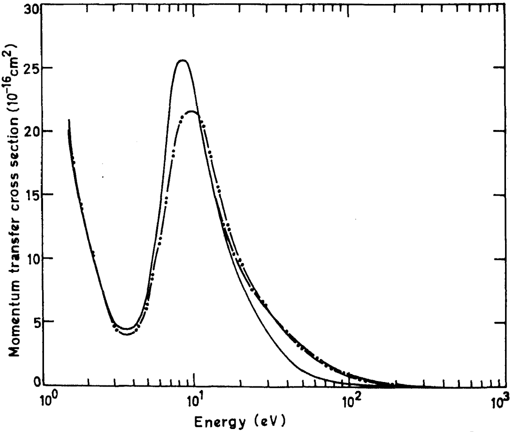

Figure 6. Momentum transfer cross-sections for e–NO scattering as a function of electron energy. Present calculations: ——, SHPa model; —•—, SHP model; —••—, SEP model (for notations see text).

Table 1. Elastic (σ_{el}), absorption (σ_{abs}), and total (σ_t) cross-sections in units of $10^{-16}\,cm^2$ in SHP model with absorption effects. σ'_{el} is the elastic scattering cross-section without absorption effects (for notations see text).

Energy (eV)	σ'_{el}	σ_{el}	σ_{abs}	σ_t	Expt. Szmytkowski and Maciag [4]
2·00	16·59	16·59	0·00	16·59	10·7
5·00	10·81	10·81	0·00	10·81	9·22
10·00	24·80	24·80	0·01	24·81	10·1
20·00	14·29	13·79	1·74	15·53	11·4
30·00	13·25	11·69	3·54	15·23	10·8
40·00	12·90	10·33	4·55	14·88	10·3
50·00	12·40	9·10	5·04	14·14	9·59
60·00	11·70	7·95	5·25	13·20	9·30
70·00	10·91	6·98	5·29	12·27	8·96
80·00	10·14	6·27	5·21	11·48	8·75
90·00	9·43	9·53	5·15	10·68	8·58
100·00	8·79	5·22	4·97	10·19	8·48
110·00	8·23	4·51	4·94	9·45	8·29
120·00	7·72	4·05	4·85	8·90	8·13
140·00	6·86	3·45	4·63	8·08	7·76
160·00	6·16	2·99	4·43	7·42	7·44
200·00	5·09	2·62	4·04	6·66	—
300·00	3·52	2·18	3·35	5·53	—
400·00	2·68	1·87	2·89	4·76	—
500·00	2·16	1·63	2·54	4·17	—
700·00	1·55	1·28	2·05	3·33	—
1000·00	1·09	0·99	1·59	2·58	—

Further, the experimental results available from other groups [3] are in good accord with respect to the position of maxima near the oscillatory structure but they all differ with the recent measurements of Szmytkowski and Maciag (SM) [4]. The calculated values in the present models SHP and SEP exhibit almost similar variation with the maximum centred around 10 eV which is at lower energies compared to experimental measurements (around 16 eV). Our calculated results are higher by a factor of two compared to the recent available data of SM. The disagreement between our results and the experimental data with respect to magnitude of the cross-section values around 2 eV is consistent with earlier calculations in the e–CO scattering [22]. For energies above 100 eV, a comparison for the total cross-section is presented with the measured values of Dalba *et al* [2]. Our values in SHP model are smaller by 40% than those of Dalba *et al* [2]. On the contrary, the results of SHPa model show a very good agreement with the measured values of Dalba *et al* [2]. It clearly shows that the agreement with the experimental data with the inclusion of absorption effect in the calculation is better than the usual calculation without absorption effects at higher impact energies where inelastic channels become important. Figure 6 shows our σ_m cross-sections in the same energy region, where the shape of the cross-section is very similar to the σ_t curve of figure 5. To the best of our knowledge, no theoretical or experimental data are available in the literature for comparison of σ_m values.

We have presented differential, elastic (with and without absorption effects), total and momentum transfer cross-sections for electron scattering from NO molecule in the energy range of 2–1000 eV. A parameter-free spherical complex optical potential is treated exactly in the partial wave scheme to obtain the various scattering parameters. Various choices of exchange, a parameter-free correlation polarization and static potentials are derived from the *ab initio* molecular charge density. The inclusion of absorption effects is important at higher impact energies. All the salient features in the cross-sections, observed in various measurements for both the differential and total cross-sections are reproduced well by the present theoretical model.

Acknowledgement

This research is funded by the Department of Science and Technology, New Delhi, India under the project No. SR/SY/P-16/90.

References

[1] E Bruche, *Ann. Phys. Lpz.* **83**, 1065 (1927)
[2] G Dalba, P Fornasini, R Grisenti, G Ranieri and A Zecca *J. Phys.* **B13**, 4695 (1980)
[3] A Zecca, I Lazzizzera, M Krauss and C E Kuyatt, *J. Chem. Phys.* **61**, 4560 (1974)
[4] C Szmytkowski and K Maciag, *J. Phys.* **B24**, 4273 (1991)
[5] M Kubo, D Matsunaga, T Suzuki and H Tanaka *Proc. 12th Int. Conf. on the Phys. of Electronic and Atomic Collisions (Gatlinburg)* (North-Holland, Amsterdam, 1981) p. 360
[6] M J Brunger *et al* (1993) *Private communication to the author*
[7] M Tronc, G C King and F H Read, *J. Phys.* **B13**, 999 (1980)
[8] J Tennyson and C J Noble, *J. Phys.* **B19**, 4025 (1986)
[9] M-T Lee, M Fujimoto, S E Michelin, L E Machado and L M Brescansin, *J. Phys.* **B25**, L505 (1992)
[10] A Jain and K L Baluja, *Phys. Rev.* **A45**, 202 (1992)
[11] P G Burke and J B West eds. *Electron molecule scattering and photoionization* (Plenum: New York, 1987)
[12] A Herzenburg, *Aspects of electron–molecule scattering and photoionization* (AIP: New York, 1990)
[13] P E Cade and W M Huo, *At. Data Nucl. Data Tables* **15**, 2 (1975)
[14] G B Schmid, D W Norcross and L A Collins *Comput. Phys. Commun.* **21**, 79 (1980)
[15] M A Morrison, *Comput. Phys. Commun.* **21**, 63 (1980)
[16] N T Padial and D W Norcross, *Phys. Rev.* **A29**, 15 (1984)
[17] F A Gianturco, A Jain and L C Pantano, *J. Phys.* **B20**, 571 (1987)
[18] T M Miller, *CRC Handbook of Chemistry and Physics* (Boca Raton F L, Chemical Rubber, 1984)
[19] S Hara, *J. Phys. Soc. Jpn.* **22**, 710 (1967)
[20] F A Gianturco and S Scialla, *J. Phys.* **B20**, 3171 (1987)
[21] G Staszewska, D W Schwenke and D G Truhlar, *Phys. Rev.* **A29**, 3078 (1984)
[22] A Jain and D W Norcross, *Phys. Rev.* **A45**, 1644 (1992)

PRAMANA
— journal of
physics

© Printed in India

Vol. 44, No. 6,
June 1995
pp. 563–568

Electron impact ionization of Ba, Ba^+ and Ba^{2+}

GOPALJEE, S K SHRIVASTAVA and B N ROY
Department of Physics, B R Ambedkar Bihar University, Muzaffarpur 842 001, India

MS received 22 November 1994

Abstract. The binary encounter approximation has been used to investigate the effect of charge state of the target atom (ion) on the electron impact excitation autoionization cross-sections. Roothan–Hartree–Fock (RHF) velocity distribution for the bound electrons has been used throughout the calculations. The present results give a good account of the experimental observations.

Keywords. Electron impact ionization; binary encounter approximation; excitation-autoionization; Roothan–Hartree–Fock velocity distribution.

PACS No. 34·80

1. Introduction

Collisions involving electrons with atoms and ions are one of the most fundamental interactions in physics. These events are basic to a variety of processes such as plasma physics, radiation physics and astrophysics. Electron-impact is also the most common form of ionization in commercial mass spectrometers and is used as an analytical tool for measuring species concentrations in gaseous samples. Total ionization cross-sections are necessary data in modelling and understanding the various environments.

Excitation-autoionization and resonant excitation double autoionization processes are the important indirect physical mechanisms for ionization which received considerable theoretical and experimental attention in recent years. In the excitation-autoionization, an inner shell electron is excited to a level above the ionization threshold which can subsequently decay by autoionization. The inner shell excitation can cause significant rise in the ionization function near the excitation threshold [1–4].

We have used the binary encounter (BE) description of excitation-autoionization contributing to the electron impact ionization [5, 6] for systems Ba, Ba^+ and Ba^{2+}. Systematic studies of these systems may provide some generalization for the dependence of excitation-autoionization on the charge state of the target system.

In quantal approximations, it is difficult to investigate ionization due to the involvement of a large number of states that are to be taken in mathematical formulations. In fact, usually, excitation cross-sections are calculated in different quantal approximations and then added either to the scaled ionization cross-sections of McGuire (7) or to the cross-sections obtained using semiempirical formulae of Lotz [8, 9 see also 10–12]. On the other hand, the binary encounter approximation (BEA) in the case of electron impact ionization of atoms and ions, is quite suitable for the reliable estimation of ionization cross-sections for atoms and ions [5, 6].

In the present work Vriens' [13] expressions for electron impact ionization and excitation cross-sections including exchange and interference have been used throughout the calculations. The effect of the residual ionic field of the target ions (in the case of ions) has been incorporated along the line suggested by Thomas and Garcia [14] [see also 15, 5].

2. Theoretical consideration

Following Gopaljee *et al* [6] (and references therein), Vriens' expressions for electron impact ionization and excitation cross-sections incorporating the effect of residual ionic field of target ion can be written in terms of dimensionless variables,

$$Q_i(s,t) = \frac{(s+s')^2}{s^2(s'^2+t^2+1)}\left[\frac{s'^2-1}{U^2 s'^2} + \frac{2t^2}{3}\left(\frac{s'^2-1}{U^2 s'^4}\right) - \frac{\varphi'}{U^2(s'^2+1)} l_n s'^2\right](\pi a_0^2) \tag{1}$$

and

$$\begin{aligned} Q_E(s,t) = {} & \frac{(s+s')^2}{s^2(s'^2+t^2+1)}\left[\frac{1}{U}\left(\frac{1}{U_n} - \frac{1}{U_{n+1}}\right) + \frac{2}{3}t^2\left(\frac{1}{U_n^2} - \frac{1}{U_{n+1}^2}\right)\right. \\ & + \frac{1}{U}\left(\frac{1}{s'^2U + U - U_{n+1}} - \frac{1}{s'^2U + U - U_n}\right) \\ & + \frac{2}{3}t^2\left(\frac{1}{(s'^2U + U - U_{n+1})^2} - \frac{1}{(s'^2U + U - U_n)^2}\right) \\ & \left. - \frac{\varphi''}{(s'^2+1)U} l_n\left(\frac{U_{n+1}(s'^2u + U - U_n)}{U_n(s'^2U + U - U_{n+1})}\right)\right](\pi a_0^2), \quad s'^2U \geqslant U_{n+1} \\ = {} & \frac{(s+s')^2}{s^2(s'^2+t^2+1)}\left[\frac{1}{U}\left(\frac{1}{U_n} - \frac{1}{s'U}\right) + \frac{2}{3}t^2\left(\frac{1}{U_n^2} - \frac{1}{(s'^2U)^2}\right)\right. \\ & + \frac{1}{U}\left(\frac{1}{U} - \frac{1}{s'^2U + U - U_n}\right) + \frac{2}{3}t^2\left(\frac{1}{U^2} - \frac{1}{(s'^2U + U - U_n)^2}\right) \\ & \left. - \frac{\varphi''}{(s'^2+1)U} l_n\left(\frac{s'^2(s'^2U + U - U_n)}{U_n}\right)\right](\pi a_0^2), \quad U_n \leqslant s'^2U \leqslant U_{n+1}. \end{aligned} \tag{2}$$

The expressions for ionization and excitation cross-sections have been integrated over the Roothan–Hartree–Fock velocity distribution for the bound electrons. Roothan–Hartree–Fock radial functions given by McLean and McLean [16] have been used to construct the momentum distribution function. In case of Ba^{2+}, due to non-availability of RHF radial functions, hydrogenic velocity distribution has been used. For the calculation of ionization and excitation cross-sections, in the case of Ba, the modifications made in Vriens' expressions (1) and (2) to incorporate the effect of residual ionic field of the target ion have been dropped off.

In excitation-autoionization calculations, as there is usually abrupt increase in cross-section at the autoionization thresholds, we have assumed that the probability of decay into the continuum is unity, when the electron is excited to an autoionizing level.

3. Results and discussion

Electron impact ionization cross-sections for Ba have been plotted as a function of the incident energy in figure 1. The figure includes, in addition to the present cross-sections

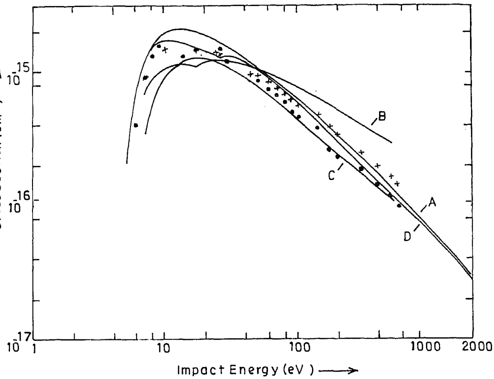

Figure 1. Electron impact ionization cross-sections for Ba; (**A**) Present calculation including contributions from inner shells and excitation-autoionization; (**B**) Calculation of Lotz [17]; (**C**) Calculation of McGuire [18]; (**D**) Present calculation (including contributions from inner shells) excluding excitation-autoionization. (●) Experiment of Dettmann and Karstensen [19]; (×) Experiment of Okudaira [20]

(including and excluding contributions from excitation autoionization), the theoretical results of Lotz [17] and McGuire [18] and experimental observations of Dettmann and Karstensen [19] and Okudaira [20]. We have used the transition $5p^6s^2$—$5p^5 6s^2 5d^1$ occurring at the energies 12·0–15·0 eV to calculate the excitation-autoionization cross-sections. Our direct calculation of ionization cross-sections incorporates the contribution from the inner shells 5p, 5s and 4d. The calculated cross-sections (including contributions of excitation-autoionization) are always within a factor 2 of the experimental observations at all impact energies. It is observed that the indirect process i.e. excitation-autoionization, significantly enhances the cross-sections near excitation threshold and our cross-sections slightly overestimate the experimental value. The first peak which can be attributed to the excitation-autoionization appears at near 100 eV in both the experiments, whereas the corresponding peak appears at 120 eV in our calculations. Our cross-sections are in better agreement with both the experiments below the energy range 100 eV than those of Lotz [17] and McGuire [18]. In the energy region above 100 eV, our cross-sections correspond well with the experimental observations of Okudaira [20] whereas McGuire's results are in closer agreement with the experimental observations of Detmann and Karstensen [19].

The calculated and experimental cross sections for Ba$^+$ have been shown in the figure 2. For comparison with other theory, we have also plotted the only theoretical results of Bely *et al* [21]. Transitions $5p^5 5d(^3p)6s^2 p_{1/2,3/2}$–$5p^5 5d(^1p)^2 p_{1/2,3/2}$ [22a, b] appearing at the energies 15·96 eV and 21·05 eV, respectively, have been used to calculate the excitation-autoionization cross-sections. Our calculated cross-sections are always within a factor 2 of the experimental observations of Peart and Dolder [23] and Feeny

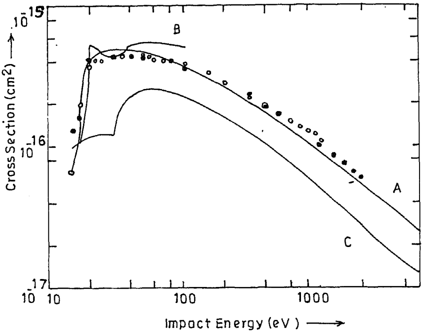

Figure 2. Electron impact ionization cross-sections for Ba^+; (**A**) Present calculation including contributions from inner shells and excitation-autoionization; (**B**) Calculation of Bely *et al* [21]; (**C**) Present calculation (including contributions from inner shells) excluding excitation-autoionization. (●) Experiment of Peart and Dolder [23]; (○) Experiment of Freney *et al* [24]

et al [24] throughout the energy range investigated except at excitation-autoionization threshold. The peak (at 20 eV) due to excitation-autoionization in our calculation corresponds well the experimental peak in both the experiments. The present cross-sections are in better agreement with experiments than those of Bely *et al* [21] in the energy range 20–100 eV, whereas the results of Bely *et al* [21] are close to the experiments below 20 eV. As there is no other theoretical work in the energy range larger than 100 eV, we are unable to compare our results with others. In this energy range, our cross-sections are in excellent agreement with both the experiments.

Theoretical as well as experimental cross-sections for Ba^{2+} have been shown in figure 3 and we have used the transitions $5s^2 5p^6 - 5s5p^6 nl - 5s^2 5p^5 + e$ and $4d^{10} 5s^2 5p^6 - 4d^9 5p^6 4f$ appearing at energies 40·9 eV–42·1 eV and 90·7 eV–118·0 eV, respectively, to calculate the excitation-autoionization cross-sections. Our calculated cross sections are always within a factor 2 of the experimental observations of Tinschert *et al* [3] throughout the energy range investigated except below the excitation-autoionization threshold. The peak corresponding to excitation-autoionization shifts left on the energy axis. This may be attributed to the fact that the hydrogenic velocity distribution of the bound electrons for Ba^{2+} has been used. As the Hartree–Fock velocity distribution reduces the cross-section in low energy range and enhances in high energy range compared to the hydrogenic velocity distribution, the use of HF velocity distribution may improve our calculation both in lower and higher energy ranges. In high energy range, our results underestimate the experiments. Plane wave (PW) calculations [3] available in the energy range 40–200 eV are certainly in better agreement with experiments than the present ones.

It is observed that the direct total ionization cross-section decreases appreciably with increase in the charge state of the target atom (ion). On the other hand the excitation-autoionization cross-section increases significantly with increase in the charge state.

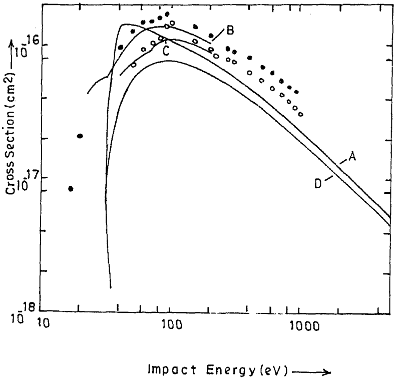

Figure 3. Electron impact ionization cross-sections for Ba^{2+}; **(A)** Present calculation including contributions from inner shells and excitation-autoionization; **(B)** D W calculation for direct ionization of 5p and 5s in metastable state [3]; **(C)** D W calculation for direct ionization of 5p and 5s in ground state [3]; **(D)** Present calculation (including contributions from inner shells) excluding excitation-autoionization; (●) Experiment of Tinschert *et al* [3] employing Penning ion-source; (○) Experiment of Tinschert *et al* [3] employing hot ECR ion source.

The decrease in the total ionization cross-section with increase in charge state can be understood in terms of the fact that the binding energies for the shells of the atom (ions) increase remarkably with increase in charge state. The same fact is probably responsible for the increasing excitation-autoionization cross-sections with increase in charge state of atom (ion) which we have observed in our calculations. In the case of greater charge state of target ion, the binding energies of inner shells are larger and the electron getting excitation there from may go into the autoionization level well above the first ionization limit [see 25 and references therein]. This leads to greater probability to decay into the continuum. The overestimation near excitation-autoionization threshold is a general feature [see 5 and references therein]. However, the overestimation can be reduced to some extent by multiplying the excitation cross-section by the branching ratio $(A_a/A_a + A_r)$, A_a and A_r being the transition probabilities for autoionization and radiative decay, respectively.

Acknowledgement

One of us (SKS) is grateful to CSIR, New Delhi for the award of the Research Associateship.

References

[1] S S Tayal and R J W Henry, *Phys. Rev.* **A39**, 3890 (1989)
[2] B Peart, J W G Thompson and K Dolder, *J. Phys.* **B24**, 489 (1991)

[3] K Tinschert, A Muller, G Hofmann, E Salzborn and S M Younger, *Phys. Rev.* **A43**, 3522 (1991)
[4] N D Juric, E W Bell, E Daniel and G H Dunn, *Phys. Rev.* **A46**, 270 (1992)
[5] S K Shrivastava and B N Roy, *J. Phys.* **B17**, 4935 (1984)
[6] Gopaljee, S K Shrivastava and B N Roy, *Pramana – J. Phys.* **40**, 321 (1993)
[7] E J McGuire, *Phys. Rev.* **A16**, 6273 (1977)
[8] W Lotz, *Z. Phys.* **216**, 241 (1968)
[9] W Lotz, *Z. Phys.* **220**, 466 (1969)
[10] P G Burke, A E Kingston and A Thompson, *J. Phys.* **B16**, L385 (1983)
[11] S M Younger, *Phys Rev.* **A23**, 1138 (1981)
[12] W T Rogers, G Stefani, R Camilloni, G H Dunn, A Z Meezane and R J W Henry, *Phys. Rev.* **A25**, 737 (1982)
[13] L Vriens, *Proc. Phys. Soc.* **89**, 13 (1966)
[14] B K Thomas and J D Garcia, *Phys. Rev.* **179**, 94 (1969)
[15] A Kumar and B N Roy, *J. Phys.* **B12**, 3979 (1979)
[16] A D McLean and R S McLean, *At. Data. Nucl. Data Tables* **26**, 206 (1981)
[17] W Lotz, Z. *Phys.* **20**, 232, 101 (1970a)
[18] E J McGuive, *Phys. Rev.* **A20**, 445 (1979)
[19] J M Dettmann and F Karstensen, *J. Phys.* **B15**, 287 (1982)
[20] S Okudaira, *J. Phys. Soc. Jpn.* **29**, 409 (1970)
[21] O Bely, S B Schwartz and J L Val, *J. Phys.* **B4**, 1482 (1971)
[22a] J E Hansen, *J. Phys.* **B7**, 1902 (1974)
[22b] J E Hansen, *J. Phys.* **B8**, 2759 (1975)
[23] B Peart and K T Dolder, *J. Phys.* **B1**, SER 2, 872 (1968)
[24] R K Feeney, J W Hooper and M T Elford, *Phys. Rev.* **A4**, 1469 (1972)
[25] D K Rai and Rajesh Srivastava, *Proceedings of the IV National Workshop on Atomic and Molecular Phys.* held at IACS Jadavpur, Edited by S C Mukherjee **P72**, (1984)

SUBJECT INDEX

General and Mathematical Physics

A new computation scheme for triangular quantum billiards *Paolo Bellomo* 85–108

On the accuracy of wavefunctions obtained by the Fourier grid Hamiltonian method *P Dutta and S P Bhattacharyya* 109–119

Conversion of a chaotic attractor into a strange nonchaotic attractor in an one dimensional map and BVP oscillator *S Rajasekar* 121–131

Patterned chaos in a system of three coupled identical unidirectional ring lasers *J Jose and S Dutta Gupta* 281–293

Invariants of chaotic Hamiltonian systems *B R Sitaram* 295–302

Charge screening in a two potential theory of electromagnetism *C Wolf* 323–332

Quantal behaviour of magnetically kicked electron *A K Sikri and M L Narchal* 489–493

Supersymmetry in complex space-time *Shuchi Bora and B S Rajput* 501–509

Relativity and Gravitation

Wormholes in higher dimensions with Gauss–Bonnet terms *B C Paul, A Beesham and S Mukherjee* 133–144

On singularity-free spacetimes *Naresh Dadhich, L K Patel and R Tikekar* 303–316

Exact solutions of Einstein and Einstein-scalar equations in $2+1$ dimensions *K S Virbhadra* 317–322

Dual nature of Ricci scalar and creation of spinless particles *K P Sinha and S K Srivastava* 333–345

Higher dimensional spherically symmetric inhomogeneous cosmological model with heat flow *Subenoy Chakraborty and Md. Firoj Shah* 495–500

Cosmic strings in Bianchi III spacetime: Integrable cases
S D Maharaj, P G L Leach and K S Govinder 511–518

Particle Physics

Magnetic moments of decuplet baryons in an independent particle potential model *N Barik, P Das and A R Panda* 145–152

Momentum- and energy-dependence of J/ψ suppression in relativistic heavy ion collisions *R S Kaushal and S K Karn* 167–176

Two-loop Majorana neutrino mass and magnetic moment in a gauge model *Jyoti Dhar, Umesh Pandey and S Dev* 347–356

S-wave baryons in an equally mixed scalar-vector square root potential model of independent quarks *S N Jena and M R Behera* 357–374

Static and dynamic properties of pseudoscalar mesons
D K Choudhury, Pratibha Das, D D Goswami and J K Sarma 519–534

Nuclear Physics

A new approach for heavy ion fusion spin distribution
S V S Sastry, A K Mohanty and S K Kataria 153–166

Deep inelastic collisions of ^{32}S + ^{27}Al reaction at 130 MeV bombarding energy *R K Choudhury, D M Nadkarni, V S Ambekar, B V Dinesh, A Saxena, M S Samant, D C Biswas and L M Pant* 177–182

Trinucleon system with Reid soft core potential by hyperspherical harmonics expansion method
Satadal Bhattacharyya and Tapan Kumar Das 183–200

Shape transitions in even Mo and Sm isotopes: Study in a new microscopic interacting boson model scheme
Subrata Sarangi and Jitendra C Parikh 375–391

Measurement and analysis of alpha particle induced reactions on gold
D J Shah, H B Patel, N L Singh, S Mukherjee and S N Chintalapudi 535–544

Atomic and Molecular Physics

Measurement of cross-section of excitation transfer from $3s_2$ to $4s_1$ and $5s_1$ energy levels of neon *R K Garg and Vasant Dandawate* 471–479

Elastic scattering of 81 keV γ-rays by aluminium, nickel, tantalum, gold and lead *G Basavaraju, P P Kane, Lynn Kissel and R H Pratt* 545–553

Collision cross-sections for scattering of electrons from NO molecules
Arvind Kumar Jain, Pradeep Kumar and A N Tripathi 555–562

Electron impact ionization of Ba, Ba^+ and Ba^{2+}
Gopaljee, S K Shrivastava and B N Roy 563–568

Lasers, Optics and Spectroscopy

A comparative study of laser second harmonic generation in some crystals *G C Bhar, A M Rudra, P K Datta, U N Roy, V K Wadhawan and T Sasaki* 45–53

Anomalous variation of thermal lens signal with concentration from rhodamine B in methanol solution
C V Bindhu, S S Harilal, Riju C Issac, Geetha K Varier, V P N Nampoori and C P G Vallabhan 225–229

Pulsed photoacoustic technique to study nonlinear processes in liquids: Results in toluene *C V Bindhu, S S Harilal, Riju C Issac, Geetha K Varier, V P N Nampoori and C P G Vallabhan* 231–235

Analysis of mode-locked internally frequency doubled broad-band continuous wave lasers
H K T Kumar, K Appaji Gowda and K P J Reddy 237–248

Self tapering and uptapering of a self guided laser beam in an absorbing/gain medium with nonlinearity
Sarang Medhekar, S Konar and Rajkamal 249–256

Fringe formation theory for real-time holographic interferometry using $Bi_{12}SiO_{20}$ *C S Narayanamurthy* 481–488

Plasma Physics

Dynamics of a collisional ion sheath *S Mukherjee and P I John* 55–66

The evolution of the resonant mode in plasma-maser interaction
Bipuljyoti Saikia and S Bujarbarua 257–262

Dynamic sheath expansion and ion current in transient ion sheath experiments *S Mukherjee, K Avinash and P I John* 263–270

Static structure factor of electrons around a heavy positively charged impurity in a one component quantum rare plasma
S P Tewari and Hira Joshi 271–277

Condensed Matter Physics

Effect of size and charge on ordering of a highly charged concentrated macroions in suspension *R K Pandey and D N Tripathi* 1–7

Transient currents in discharge mode in cellulose acetate: polyvinyl acetate blend films *P K Khare, R S Chandok and A P Srivastava* 9–18

Microwave conductivity studies on some semiconductors
V Subramanian, V R K Murthy and J Sobhanadri 19–32

Dielectric relaxation and related studies of 4-ethylphenol-methanol mixtures using time domain reflectometry
R H Fattepur, M T Hosamani, D K Deshpande, R L Patil and S C Mehrotra 33–44

Phonons and fractons in sol–gel alumina: Raman study
Anushree Roy and Ajay K Sood 201–209

Thermally stimulated luminescence and electron paramagnetic resonance studies on uranium doped $K_2Ca_2(SO_4)_3$
T K Seshagiri, V Natarajan and M D Sastry 211–217

Structural, spectroscopic and dielectric properties of KVO_3
N K Misra, R N P Choudhary and K L Yadav 219–224

Effect of nonlocal elasticity on internal friction peaks observed during martensite transformation *Ali Dogân* 397–404

Dielectric study of aqueous solution of acetonitrile
S N Helambe, M P Lokhande, A C Kumbharkhane, S C Mehrotra and S Doraiswamy 405–410

Structural and dielectric properties of $Pb(Li_{1/4}Dy_{1/4}W_{1/2})O_3$
S Bera and R N P Choudhary 411–417

Phonon properties of rare earth ytterbium pnictides
Prafulla K Jha and Sankar P Sanyal 419–427

Lattice vibronics of bcc phases metals (Ti, Zr and Hf) at higher temperatures *S M Saxena, R M Agrawal and R P S Rathore* 429–442

Temperature variation of electric field gradient in scandium metal
B B Panigrahi and N C Mohapatra 443–451

Composite Anderson–Newns model and chemisorption characteristics of nickel-hydrogen system
Ravinder Guleria, P K Ahluwalia and K C Sharma 453–459

Vibrational analysis of $NaM_2OH(H_2O)(MoO_4)_2/D_2O[M = Ni, Zn]$
R Ratheesh, G Suresh and V U Nayar 461–470

Experimental Techniques and Instrumentation

Instrumentation for beam-foil spectroscopic studies in the UV-visible region *Tapan Nandi, V Nanal, W A Fernandes, C A Desai, M B Kurup, K G Prasad, P M R Rao and S Padmanabhan* 67–76

Subject index 573

Rapid Communications

Gap states in a doped Mott–Hubbard insulator *Prasenjit Sen, Saurabh Basu and Avinash Singh* L77–L83

Giant magnetoresistance in bulk samples of $LaMnO_3$ with varying Mn^{4+} content *R Mahendiran, R Mahesh, A K Raychaudhuri and C N R Rao* L393–L396

Corrigendum

New answer to the solar neutrino problem *Marc Dixmier* 279

AUTHOR INDEX

Agrawal R M
  see Saxena S K 429
Ahluwalia P K
  see Guleria Ravinder 453
Ambekar V S
  see Choudhury R K 177
Gowda K Appaji
  see Kumar H K T 237
Avinash K
  see Mukherjee S 263

Barik N
  Magnetic moments of decuplet baryons in an independent particle potential model 145
Basavaraju G
  Elastic scattering of 81 keV γ-rays by aluminium, nickel, tantalum, gold and lead 545
Basu Saurabh
  see Sen Prasenjit L77
Beesham A
  see Paul B C 133
Behera M R
  see Jena S N 357
Bellomo Paolo
  A new computation scheme for triangular quantum billiards 85
Bera S
  Structural and dielectric properties of $Pb(Li_{1/4}Dy_{1/4}W_{1/2})O_3$ 411
Bhar G C
  A comparative study of laser second harmonic generation in some crystals 45
Bhattacharyya Satadal
  Trinucleon system with Reid soft core potential by hyperspherical harmonics expansion method 183
Bhattacharyya S P
  see Dutta P 109
Bindhu C V
  Anomalous variation of thermal lens signal with concentration from rhodamine B in methanol solution 225
  Pulsed photoacoustic technique to study nonlinear processes in liquids: Results in toluene 231
Biswas D C
  see Choudhury R K 177
Bora Shuchi
  Supersymmetry in complex space-time 501
Bujarbarua S
  see Saikia Bipuljyoti 257

Chakraborty Subenoy
  Higher dimensional spherically symmetric inhomogeneous cosmological model with heat flow 495
Chandok R S
  see Khare P K 9
Chintalapudi S N
  see Shah D J 535
Choudhury D K
  Study of static and dynamic properties of pseudoscalar mesons 519
Choudhury R K
  Deep inelastic collisions of $^{32}S+^{27}Al$ reaction at 130 MeV bombarding energy 177
Choudhury R N P
  see Misra N K 219
  see Bera S 411

Dadhich Naresh
  On singularity-free spacetimes 303
Dandawate Vasant
  see Garg R K 471
Das P
  see Barik N 145
Das Pratibha
  see Choudhury D K 519
Das Tapan Kumar
  see Bhattacharyya Satadal 183
Datta P K
  see Bhar G C 45
Desai C A
  see Nandi Tapan 67
Deshpande D K
  see Fattepur R H 33
Dev S
  see Dhar Jyoti 347
Dhar Jyoti
  Two-loop Majorana neutrino mass and magnetic moment in a gauge model 347
Dinesh B V
  see Choudhury R K 177
Dixmier Marc
  Corrigendum 279
Dogân Ali
  Effect of nonlocal elasticity on internal friction peaks observed during martensite transformation 397

Doraiswamy S
  see Helambe S N 405
Dutta Gupta S
  see Jose J 281
Dutta P
  On the accuracy of wavefunctions obtained by the Fourier grid Hamiltonian method 109

Fattepur R H
  Dielectric relaxation and related studies of 4-ethylphenol-methanol mixtures using time domain reflectometry 33
Fernandes W A
  see Nandi Tapan 67

Garg R K
  Measurement of cross-section of excitation transfer from $3s_2$ to $4s_1$ and $5s_1$ energy levels of neon 471
Gopaljee
  Electron impact ionization of Ba, Ba$^+$ and Ba^{2+} 563
Goswami D D
  see Choudhury D K 519
Govinder K S
  see Maharaj S D 511
Guleria Ravinder
  Composite Anderson–Newns model and chemisorption characteristics of nickel-hydrogen system 453

Harilal S S
  see Bindhu C V 225, 231
Helambe S N
  Dielectric study of aqueous solution of acetonitrile 405
Hosamani M T
  see Fattepur R H 33

Issac Riju C
  see Bindhu C V 225, 231

Jain Arvind Kumar
  Collision cross sections for scattering of electrons from NO molecules 555
Jena S N
  S-wave baryons in an equally mixed scalar-vector square root potential model of independent quarks 357
Jha Prafulla K
  Phonon properties of rare earth ytterbium pnictides 419
John P I
  see Mukherjee S 55, 263
Jose J
  Patterned chaos in a system of three coupled identical unidirectional ring lasers 281
Joshi Hira
  see Tewari S P 271

Kane P P
  see Basavaraju G 545
Karn S K
  see Kaushal R S 167
Kataria S K
  see Sastry S V S 153
Kaushal R S
  Momentum- and energy-dependence of J/ψ suppression in relativistic heavy ion collisions 167
Khare P K
  Transient currents in discharge mode in cellulose acetate: polyvinyl acetate blend films 9
Kissel Lynn
  see Basavaraju G 545
Konar S
  see Medhekar Sarang 249
Kumar H K T
  Analysis of mode-locked internally frequency doubled broadband continuous wave lasers 237

Kumar Pradeep
  see Jain Arvind Kumar 555
Kumbharkhane A C
  see Helambe S N 405
Kurup M B
  see Nandi Tapan 67

Leach P G L
  see Maharaj S D 511
Lokhande M P
  see Helambe S N 405

Maharaj S D
  Cosmic strings in Bianchi III spacetime: Integrable cases 511
Mahendiran R
  Giant magnetoresistance in bulk samples of LaMnO$_3$ with varying Mn^{4+} content L393
Mahesh R
  see Mahendiran R L393
Medhekar Sarang
  Self tapering and uptapering of a self guided laser beam in an absorbing/gain medium with nonlinearity 249
Mehrotra S C
  see Fattepur R H 33, 405
Misra N K
  Structural, spectroscopic and dielectric properties of KVO$_3$ 219
Mohanty A K
  see Sastry S V S 153

Mohapatra N C
see Panigrahi B B 443
Mukherjee S
Dynamics of a collisional ion sheath 55
see Paul B C 133
Dynamic sheath expansion and ion current in transient ion sheath experiments 263
see Shah D J 535
Murthy V R K
see Subramanian V 19

Nadkarni D M
see Choudhury R K 177
Nampoori V P N
see Bindhu C V 225, 231
Nanal V
see Nandi Tapan 67
Nandi Tapan
Instrumentation for beam-foil spectroscopic studies in the UV-visible region 67
Narayanamurthy C S
Fringe formation theory for real-time holographic interferometry using $Bi_{12}SiO_{20}$ 481
Narchal M L
see Sikri A K 489
Natarajan V
see Seshagiri T K 211
Nayar V U
see Ratheesh R 461

Padmanabhan S
see Nandi Tapan 67
Panda A R
see Barik N 145
Pandey R K
Effect of size and charge on ordering of a highly charged concentrated macroions in suspension 1
Pandey Umesh
see Dhar Jyoti 347
Panigrahi B B
Temperature variation of electric field gradient in scandium metal 443
Pant L M
see Choudhury R K 177
Parikh Jitendra C
see Sarangi Subrata 375
Patel H B
see Shah D J 535
Patel L K
see Dadhich Naresh 303
Patil R L
see Fattepur R H 33
Paul B C
Wormholes in higher dimensions with Gauss–Bonnet terms 133
Prasad K G
see Nandi Tapan 67
Pratt R H
see Basavaraju G 545

Rajasekar S
Conversion of a chaotic attractor into a strange nonchaotic attractor in an one dimensional map and BVP oscillator 121
Rajkamal
see Medhekar Sarang 249
Rajput B S
see Bora Shuchi 501
Rao C N R
see Mahendiran R L393
Rao P M R
see Nandi Tapan 67
Ratheesh R
Vibrational analysis of $NaM_2OH(H_2O)(MoO_4)_2/D_2O[M = Ni, Zn]$ 461
Rathore R P S
see Saxena S K 429
Raychaudhuri A K
see Mahendiran R L393
Reddy K P J
see Kumar H K T 237
Roy U N
see Bhar G C 45
Roy Anushree
Phonons and fractions in sol–gel alumina: Raman study 201
Roy B N
see Gopaljee 563
Rudra A M
see Bhar G C 45

Saikia Bipuljyoti
The evolution of the resonant mode in plasma-maser interaction 257
Samant M S
see Choudhury R K 177
Sanyal Sankar P
see Jha Prafulla K 419
Sarangi Subrata
Shape transitions in even Mo and Sm isotopes: Study in a new microscopic interacting boson model scheme 375
Sarma J K
see Choudhury D K 519
Sasaki T
see Bhar G C 45
Sastry S V S
A new approach for heavy ion fusion spin distribution 153
Sastry M D
see Seshagiri T K 211

Saxena A
  see Choudhury R K 177
Saxena S K
  Lattice vibronics of bcc phases metals (Ti, Zr and Hf) at higher temperatures 429
Sen Prasenjit
  Gap states in a doped Mott–Hubbard insulator L77
Seshagiri T K
  Thermally stimulated luminescence and electron paramagnetic resonance studies on uranium doped $K_2Ca_2(SO_4)_3$ 211
Shah Md. Firoj
  see Chakraborty Subenoy 495
Shah D J
  Measurement and analysis of alpha particle induced reactions on gold 535
Sharma K C
  see Guleria Ravinder 453
Shrivastava S K
  see Gopaljee 563
Sikri A K
  Quantal behaviour of magnetically kicked electron 489
Singh Avinash
  see Sen Prasenjit L77
Singh N L
  see Shah D J 535
Sinha K P
  Dual nature of Ricci scalar and creation of spinless particles 333
Sitaram B R
  Invariants of chaotic Hamiltonian systems 295
Sobhanadri J
  see Subramanian V 19
Sood Ajay K
  see Roy Anushree 201
Srivastava A P
  see Khare P K 9
Srivastava S K
  see Sinha K P 333
Subramanian V
  Microwave conductivity studies on some semiconductors 19
Suresh G
  see Ratheesh R 461

Tewari S P
  Static structure factor of electrons around a heavy positively charged impurity in a one component quantum rare plasma 271
Tikekar R
  see Dadhich Naresh 303
Tripathi A N
  see Jain Arvind Kumar 555
Tripathi D N
  see Pandey R K 1

Vallabhan C P G
  see Bindhu C V 225, 231
Varier Geetha K
  see Bindhu C V 225, 231
Virbhadra K S
  Exact solutions of Einstein and Einstein-scalar equations in 2 + 1 dimensions 317

Wadhawan V K
  see Bhar G C 45
Wolf C
  Charge screening in a two potential theory of electromagnetism 323

Yadav K L
  see Misra N K 219

RAMAN RESEARCH INSTITUTE
BANGALORE - 80.
CLASS NO.
ACC NO. 26998